Doctoral School in Environmental Engineering

Effects of rigid stems on sediment transport

Valentina Cavedon

UNIVERSITÀ DEGLI STUDI DI TRENTO
Dipartimento di Ingegneria Civile
e Ambientale

Based on the Doctoral Thesis in Environmental Engineering (XXIV Cycle) defended in April 2012 at the Faculty of Engineering, University of Trento, Italy

Effects of rigid stems on sediment transport, Doctoral thesis in Environmental Engineering, XXIV cycle

Supervisor: Prof. A. Armanini

February 2012

Al mio tempo libero
e ad Alessandro che l'ha riempito

Aknowledgements

I wish to thank Prof. Armanini for his continuous supervision; Prof. Righetti for his advices and scientific support; Prof. Nikora for his interest and helpfulness, and for his useful suggestions.

Thanks to Fabio Sartori, Lorenzo Forti, Andrea Bampi and Paolo Scarfiello, the technicians who have helped me set up my laboratory work. And thanks to Eng. Andrea Salizzoni, Eng. Elisa Jeradi, Eng. Eleonora Costan Zovi, Selene Spornberger, Carlo Ongaro and Alessio Chesani for their collaboration and involvement.

Thanks very much to Alessandro for the important help with the drawings, and for his patience, encouragement and support, and for having sometimes forced me to go out to take my mind off the thesis; and to my parents and friends, who have not seen me for several weeks and have been patient! A particular thanks to my colleagues who have shared with me this path and who have been a fundamental moral support. Among them, I want to particularly thank to Francesca and Stefania, who have been dear friends.

Abstract

The vegetation is an important factor of quality of the river ecosystem, given its capability to contribute to the chemical, biological and physical quality of water. On the other hand, the presence of vegetation in riverbed modifies flow structure, flow resistance, sediment transport and morphology. Each single modification has been largely studied, but the knowledge on the mutual relationships are still limited.

This project faces a part of these still-unknown aspects by considering the case of rigid and emergent vegetation and the relationships with sediment transport, flow field, flow resistance and bed forms at small scale. The thesis is based on experimental approach coupled with theoretical analysis.

In particular, the research contributes with a rational approach (*ballistic approach*) to the formulation of sediment transport capacity of a vegetated riverbed as a function of hydrodynamic conditions, types of sediments, dimension and distribution of plants. The validity of the ballistic approach is proved by the comparison with a large number of experimental results obtained in a laboratory channel, in which the vegetation was modeled with cylindrical and rigid elements. The experimental results were carried out for different flow conditions, arrangement of cylinders and cylinder dimensions. For the tests, three different sediments were used, at different densities and grain sizes. The comparison allows the determination of some empirical parameters related with the velocity of movement of particles, characteristics of sediments and plants incumbrance.

A partially rational approach for the determination of the empirical parameters comes from the analysis of the flow field through the cylinders. The experimental data highlight bed areas in which the contribution to the sediment discharge is smaller, and bed areas in which is larger, with respect to an unvegetated riverbed at the same flow conditions.

The flow field analysis shows also the physical mechanisms which rule the formation of bed forms induced by plants. Height and length of vegetation bed forms are measured and related with the density of vegetation, with the plant diameters and with the average distance between the cylinders interaxis. In particular, the experimental data show the linearity between length of bed forms and average

distance between stems.

Finally, measurements of the drag force exerted by the cylinders to the flow were carried out by means a load cell fixed to the cylinders in staggered configuration. The measurements were done in a channel with fixed bed, both plane and with bed forms. The experimental measurements of drag show that the drag coefficient depends on the density of vegetation and on the presence of bed forms. This dependence is confirmed by comparing the indirect measurements of the drag coefficient with the measurements done with the load cell and fixed bed. The indirect measurements were done in the flume with mobile bed and sediment transport, for both the staggered and random distribution of cylinders.

The direct measurements in the different experimental setup and the comparison between direct and indirect measurements put in evidence that the vegetation bed forms give a contribution to global resistance that, in particular cases, is comparable with the contribution due to the rigid stems, demonstrating that to consider negligible their effect can be sometimes a rough approximation.

Contents

List of Figures

List of Tables

Nomenclature

Δ_D	Height of bed forms
$\kappa = 0.41$	Von Karman's constant
Λ_D	Length of bed forms
$\langle\ \rangle$	Symbol indicating spatial average
$\mathbf{B}$	Buoyancy force
$\mathbf{L}$	Lift force
$\mathbf{W}$	Weight force
μ	Water dynamic viscosity
ν	Kinematic viscosity of water
Ω_v	Density of vegetation
-	Symbol indicating time average
$\overline{u(z)}$	Time average of the velocity u at z above the bed
$\Psi = g\Delta d/u_*^2$	Einstein flow intensity parameter
ρ	Density of water
ρ_s	Density of sediments
σ	Variance of a probability distribution
τ	Shear stress
τ_0	Shear stress at the bottom of an open-channel
τ_0'	Shear stress due to grain roughness

τ_0'' Shear stress due to bed forms roughness

τ_v Shear stress due to vegetation

D Drag force

L Lift force

$\theta' = (u_*')^2/g\Delta d$ Shields mobility parameter related to grain roughness

$\theta = u_*^2/g\Delta d$ Shields parameter of mobility

$\theta_c = u_{*,c}^2/g\Delta d$ Shields critical parameter of mobility

$\{\ \}$ Symbol indicating ensemble average

B Width of the channel

C Concentration of sediments along the perpendicular of the bed river or along the water depth

C^* Grain packing density

$c_* = u_s/u_*$ Constant defining the ratio between u_s and u_*

C_D Drag coefficient

C_L Lift coefficient

$c_u = u_0/u_*$ Constant defining the ratio between u_0 and u_*

C_{Dp} Drag coefficient of plant

d Characteristic diameter of grains

D_* Reduced diameter of particles

d_c Diameter of cylinder

d_p Diameter of plants

f Darcy-Weisbach coefficient

f_v Darcy-Weisbach coefficient for vegetation

F_{bf} Drag force due to bed forms

$Fr = U/\sqrt{gh}$ Froude number

g Gravitational acceleration

h Water depth

h_{veg} Height of the vegetation

i_b Bed slope

i_E Energy gradient

k_e Characteristic size of roughness, or Nikuradse equivalent roughness

L_p Averaged distance travels by a particle

M_v Stiffness parameter of the vegetation

p Pressure

p_1 Detachment probability of a particle

Q Water discharge

q_b Bedload discharge per unit width

q_s Sediment transport discharge per unit width

q_{ss} Suspended load discharge per unit width

R'_h Hydraulic radius with respect to the grain

R_h Hydraulic radius

R_p Resistance exerted by a plant

$Re = Uh/\nu$ Bulk Reynolds number

$Re_* = du_*/\nu$ Shear Reynolds number

$Re_p = Ud_p/\nu$ Reynolds number of plants

$T = \left((u'_*)^2 - (u_{*,cr})^2\right)/(u_{*,cr})^2$ Flow stage parameter

T_p Exchange time

U x averaged component of the velocity of flow

u Value of velocity in the main direction of flow (x direction)

$u'_* = \sqrt{\tau'_0/\rho}$ Shear velocity with respect to grain roughness

$u_* = \sqrt{\tau_0/\rho}$ Shear velocity

U_0 Undisturbed flow velocity

u_0 Velocity of a particle at the beginning of motion

$u_{*,c}$ Shear velocity in condition of incipient motion

w_s Settling velocity of a sediment particle

z_b Instantaneous elevation of bed

PIV Particle Image Velocimetry technique, to analyze the flow field

Chapter 1

Introduction

1.1 The role of vegetation in water courses

In parallel to the economical development and to the population growth in Europe, the hydromorphology of European river systems has been artificially modified in the last two centuries.

In the European context, the development of hydraulic and environmental research is following the last European Directives (i.e. the Water Framework Directive and the Flood Directive) which have as objectives the definition of coherent measures aimed at improving the ecological status of river bodies, guarantying contemporarily hydraulic safety and adequate protection of human activities.

The results obtained from European Union Member States at the end of 2004 show that the departure from the natural equilibrium of water courses has caused a reduction of the quality of water ecosystems. A high proportion of the water bodies were identified as being at risk or probably at risk because of alterations to their structural characteristics (i.e. their morphological characteristics) and associated impacts on their water flow and level regimes.

In river systems, the ecological equilibrium is very sensitive to changes; vegetation, if present in beds or embankments, is able to improve at the same time the chemical, the physical and the biological characteristics of water. Vegetation might be a good instrument of protection against hydromorphological hazards (flooding, floodplain erosion, protection of river infrastructures), if correctly man-

aged.

Accordingly, vegetation in riverbeds becomes one of the most important topics to face, since the role played by plants and bushes in flood protection is still to clarify. The presence of vegetation modifies the structure of flow fields and, consequently, the relationships among water discharge, sediment transport, geometry of channel, hydrodynamics and flow resistance. These factors, if not correctly designed, might decrease, instead of increase, the human safety by increasing the hydromorphological hazard.

One of the additional risks (or advantages, if correctly managed) is the modification of sediment transport capacity in a vegetated riverbed and the consequence and the impact on river morphology, at small and large scale. Furthermore, the presence of plants, bushes or herbaceous vegetation in beds or embankments substantially increases the flow resistance, in different ways for different typologies of vegetation, and consequently changes also the water flow.

It is in this wide context that the thesis is inserted. In particular, the research focuses on the physics of sediment transport in presence of rigid and emergent vegetation, by relating the transport of sediments, the flow field and the flow resistance by using experimental data and rational approaches.

1.2 State-of-art

As has been already introduced in the preceding section (Section 1.1), given the importance of the presence of vegetation in rivers ecosystems, a huge amount of bibliography is available on these arguments, but not all its effects have been already faced with the same degree of detail.

In the earliest studies on this topic, the investigation of the role of vegetation in rivers was directed towards the interactions between plants and hydrodynamics. The analysis of the resistance due to vegetation was largely faced, in particular on the determination of the contribution of herbaceous and algal vegetation to flow resistance (Kouwen 1988), a question that is still open (Nikora 2010). In the last years several papers have tackled the problem of the resistance exerted by bushes (Järvelä 2004; Righetti and Armanini 2002) or, in general, by submerged vegetation (Baptist et al. 2007; Stephan and Gutknecht 2002).

Another fundamental aspect is represented by the influence of rigid and emergent plants on flow resistance (Ishikawa, Mizuhara, and Ashida 2000a; James et al. 2004; Kothyari, Hayashi, and Hashimoto 2010; Tanino and Nepf 2008). The relationship between turbulence and drag resistance is one of the most complex issues concerning the interactions plant-flow. Because of its complexity, the research is now moving toward a deeper analysis of the turbulence structure and diffusive transport processes through plants (Ghisalberti and Nepf 2009; Li and Shen 1973; López and García 2001; Nepf and Ghisalberti 2008; Nepf 1999; Takemura and Tanaka 2007). These studies include sediment transport processes (mostly suspended load transport), diffusion and dispersion of passive and reactive scalars and its implications for water quality problems and for transport processes in rivers. Almost all the investigations which focus on flow field and flow resistance, however, have neglected the contribution of morphological elements related with rigid vegetation in beds. The open question is whether to neglect the contribution due to bed forms is a correct assumption, since in non-vegetated beds the same assumption would be considered a rough approximation.

Although the interactions vegetation-sediment raise the interest of the researcher community, the physics of sediment entrainment and sediment transport is rarely approached. The projects in this direction are often finalized to determine the behavior of morphology of water courses at large scale (formation of meanders, dunes, bars) often by considering the presence of patterns of vegetation (Gran and Paola 2001; Perucca, Camporeale, and Ridolfi 2007; Tsujimoto 1999). On the contrary, only a few studies have focused on the determination of a method to evaluate the sediment transport in presence of rigid plants (Ashida 1972; Ishikawa, Mizuhara, and Ashida 2000b; Jordanova and James 2003; Kothyari, Hashimoto, and Hayashi 2009).

The hydraulic designers are still lacking of a rational method to determine the sediment transport rate in vegetated riverbeds. Nowadays, numerical modeling on sediment transport processes has a high level of complexity and precision. By now, a rational approach to calculate the sediment transport capacity is necessary for mathematical models treating flood hazard and morphological modifications. Generally empirical formulation are used, but it is well known that the majority of empirical studies are valid only in limited cases. In the next future, mathe-

matical models will work with rational approaches and vegetation will have to be considered in modeling and in calculation of sediment transport capacity.

1.3 Objectives and innovative aspects of the research

The thesis is formed by three big topics, in relation with the presence of rigid and emergent vegetation in riverbeds: sediment transport, flow field and drag force.

The main aim of the research is the definition of a rational method to determine the sediment transport capacity in a vegetated riverbed, by approaching the problem from an innovative and rational point of view. The rational formula is compared with experimental data. The data are obtained in a laboratory channel by modifying the distribution of stems, the density of vegetation and the characteristics of sediments.

The second objective of the research is the study of other effects due to the presence of rigid stems. First of all, the modification of the flow field through the stems and its relationship with sediment entrainments and transport. This part of the study is useful for evaluating the parameters of the rational approach on sediment transport and for defining the mechanisms of formation of vegetation bed forms.

Another experimentally faced effect is the relationship between drag force and vegetation bed forms. The vegetation bed forms and their relation with the distribution of stems are defined; afterwards the role of bed forms on flow resistance is analyzed in order to show that their contribution is not always negligible.

1.4 Thesis structure

This thesis is organized in according to the following structure:

1. Definition of the concepts of resistance in natural river systems (Chapter 2). In the Sections 2.2 and 2.3, which are the contributions to flow resistance in vegetated rivers will be described. This chapter will include also a description of theoretical and rational approaches to the topic (Sections 2.2 and 2.3). The last part will focus on the method of study of turbulence structure

through rigid plants (Section 2.4) and on the already gained knowledge.

2. In the next chapter (Chapter 3), the mechanisms related to the transport of sediments will be described: the beginning of the motion of particles (paragraph 3.1.1), the different typologies of sediment transport (bedload in Section 3.1.2, suspended load in Section 3.1.3) and the literature about these arguments.
3. In the same chapter, in the Sections 3.2, 3.3 and 3.4, the Einstein (1950) and Yalin (1977) formulae will be reported, since their approaches are at the base of the definition of the rational formulation. Finally, in the Sections 3.6 and 3.7, the procedure for the definition of the rational approach (termed *ballistic approach*) will be reported, applied to non-vegetated and vegetated riverbeds.
4. In Chapter 4, the experimental set-up and all the tests will be described; the results will be discussed in the next chapter (Chapter 5).
5. Chapter 5 will contain the results obtained from the experiments, the discussion and analysis of data. It will begin with the analyses on drag coefficient due to rigid stems on plane bed (Section 5.1). Then, the part related with the flow field through vegetation will be reported (Section 5.2). The third part of the chapter will treat the bed forms induced by the vegetation (Section 5.3) and the drag force in presence of bed forms. Finally, the experimental data for sediment transport will be compared with the ballistic approach (Section 5.4).

Chapter 2

Flow resistance in water courses

2.1 Flow resistance in open-channel flow

In a natural river, the global flow resistance is due to a sum of different factors: morphological structure of river, presence of vegetation, presence of bed forms, grain roughness, and so on. If we do not consider for now the effects due to the presence of vegetation, that will be discussed in detail in the following, among these factors the most important are the grain roughness and the stress induced by bed forms.

The flow resistance, as other flow characteristics (turbulence structures, sediment entrainments and movements, secondary flows, etc.), is particularly influenced by the presence of bed forms. Furthermore, the problem is implicit, given that the characteristics of bed forms (length, shape, structure, dimensions, stability, etc.) depend on flow structure.

In water courses different typologies of bed forms are recognizable. In the lowest regime (subcritical flow), ripples and dunes are the likeliest bed forms; increasing the velocity of flow, the bed becomes plane (transcritical flow) and then (in supercritical flow) antidunes are formed. For steep channels, steps and pools are rather common. Furthermore, not only small bed forms can affect the resistance, but also planimetric bed forms, like for instance migrating bars.

The bed shear stress is generally indicated with τ_0 and estimated with the following expression, obtainable by the balance of momentum in uniform flow

condition:

$$\tau_0 = \gamma R_h i_E \tag{2.1}$$

where $\gamma = \rho g$ is the specific weight of water, being ρ the density of water, and g the gravitational acceleration; R_h is the hydraulic radius; i_E is the energy gradient, that in uniform flow condition is equal to the bed slope.

In order to evaluate the resistance in a channel in presence of bed forms, normally the superposition of effects is considered a good approximation; according to which the global stress τ_0 can be expressed as:

$$\tau_0 = \tau_0' + \tau_0'' \tag{2.2}$$

where τ_0' is the contribution due to grain roughness, and τ_0'' is the contribution due to bed forms. Eq. (2.2) can be formulated also in terms of shear velocity:

$$(u_*)^2 = (u_*')^2 + (u_*'')^2 \tag{2.3}$$

where $u_*' = \sqrt{\tau_0'/\rho}$ is in relation with grain roughness, and $u_*'' = \sqrt{\tau_0''/\rho}$ with bed forms. If τ_0 is defined as in eq. (2.1), then

$$R_h i_E = (R_h i_E)' + (R_h i_E)'' \tag{2.4}$$

The topics related with this matter have been largely studied, since the fifties of the last century. The approaches most cited in literature are:

- the Einstein and Barbarossa's method (Einstein, Barbarossa, and Civil Engineers. Hydraulics Division 1951), to calculate the contribution of bed forms by the grain roughness. In particular, they represented U/u_*'' as a function of the Einstein flow intensity parameter (Section 3.2) $\Psi_{35}' = g\Delta d_{35}/u_*'$, related to the shear stress due to grain roughness u_*';

- the modification to Einstein and Barbarossa's method by Shen (1962), who considered also the dependence on the settling velocity of particles;

- Engelund (1966) method, in which the loss of energy due to bed forms is assimilated to a Borda energy loss. Engelund found that the Shields' param-

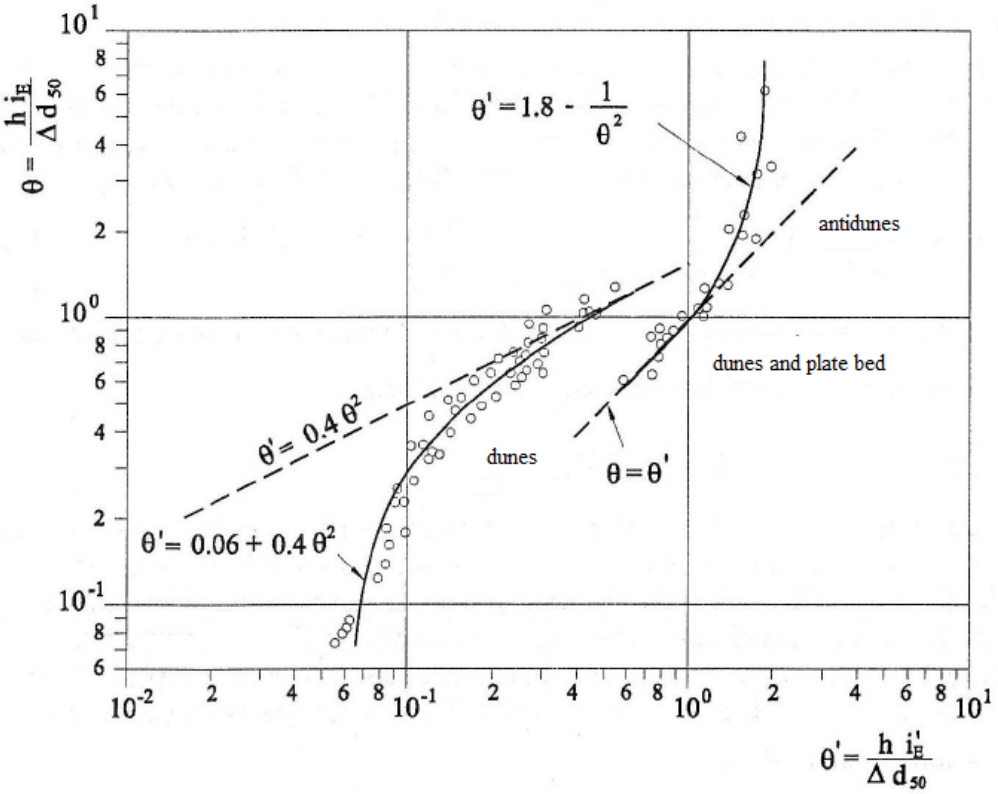

Figure 2.1: The expression for flow resistance as a function of grain roughness by Engelund (1966) (taken by Armanini (1999))

eter of mobility relative to bed forms ($\theta'' = (u''_*)^2 / g\Delta d$) (see Section 3.1.1) is a function of the grain roughness mobility parameter ($\theta' = (u'_*)^2 / g\Delta d$): $\theta'' = \text{fct}(\theta', \theta)$. Moreover, the author deduced that the global mobility parameter θ is the only variable which affects the mobility grain roughness parameter (Figure 2.1): $\theta' = \text{fct}(\theta)$;

- Van Rijn (1984) classified the bed forms as a function of the characteristic parameter of sediment $D_* = d\left(d\Delta/\nu^2\right)^{1/3}$, called by the author *reduced diameter of particles*, and $T = \left((u'_*)^2 - (u_{*,cr})^2\right)/(u_{*,cr})^2$, called by van Rijn *flow stage parameter*. d indicates the diameter of grain; $\Delta = (\rho_s - \rho)/\rho$ is the reduced relative density of the sediments, being ρ_s the density of sediment and ρ the density of water; ν is the kinematic viscosity of water. T expresses the difference between the shear stress related to grain and the shear stress $u_{*,cr}$ correspondent to the condition of incipient motion of grains (see Section 3.1.1). The results obtained by the author are represented in Figure 2.2. Van Rijn proposed the following equations to evaluate the height Δ_D and the length Λ_D of dunes as a function of water depth h, a characteristic grain diameter (d_{50}) and the flow stage parameter T:

$$\frac{\Delta_D}{h} = 0.11 \left(\frac{d_{50}}{h}\right)^{0.3} \left(1 - e^{-0.5T}\right)(25 - T) \tag{2.5}$$

$$\frac{\Delta_D}{\Lambda_D} = 0.015 \left(\frac{d_{50}}{h}\right)^{0.3} \left(1 - e^{-0.5T}\right)(25 - T) \tag{2.6}$$

Finally, van Rijn proposed a method to evaluate the equivalent roughness k_e in case of bed forms:

$$k_e = 3d_{90} + 1.1\Delta_D \left(1 - e^{-25\frac{\Delta_D}{\Lambda_D}}\right) \tag{2.7}$$

In eq. (2.7) d_{90} is, in author's opinion, the grain size to add to the dunes contribution for considering the contribution of grain roughness.

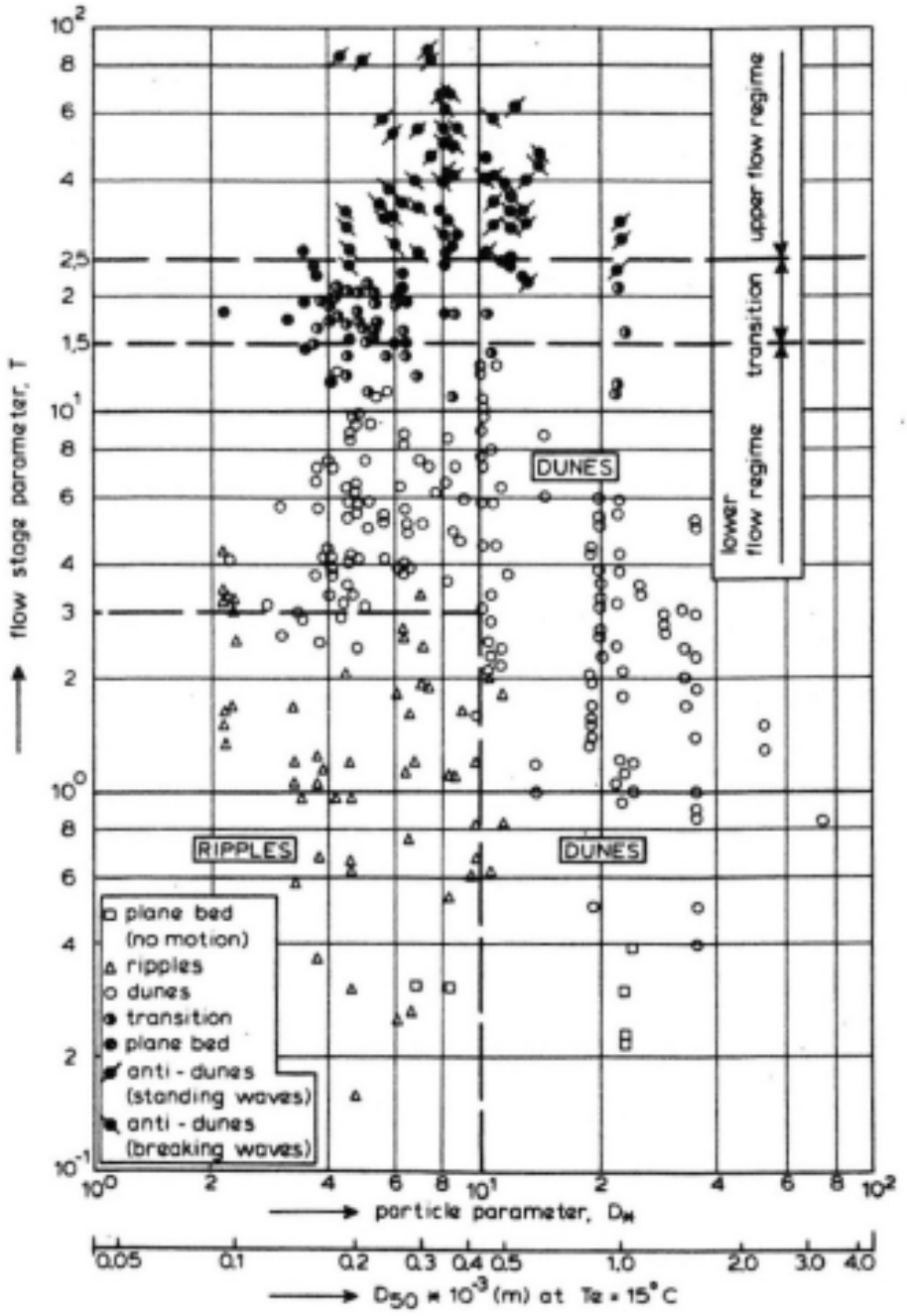

Figure 2.2: Classification of bed forms by Van Rijn (1984)

2.2 The resistance in vegetated rivers

2.2.1 State of art

In order to evaluate the effect of vegetation on global resistance, it would be necessary to consider the different typologies of vegetation and their natural characteristics, as shape and stiffness of branches and leaves, or shape and stiffness of trunk. Some investigations have approached the definition of drag considering also the presence of leaves and branches (Fa and Kouwen 1997; James et al. 2004; Järvelä 2004; Jarvela 2005; Righetti and Armanini 2002; Stone and Hung 2002; Wilson, Stoesser, and Bates 2005), but generally only for the case of submerged vegetation. Other authors have considered also the flexibility of linearly elastic stems in the value of the drag coefficient (Babovic and Keijzer 2000; Li and Xie 2011), but only by numerical modeling.

An experimental study on drag and vegetation, which considers also the natural characteristics of leaves, branches and trunk, should be carried out in a natural river or at real scale. In a laboratory channel, indeed, by working in reduced scale, the real stiffness, that is typically non-linear, is difficult to model. For this reason, most of studies addressed to the drag force on rigid vegetation prefers to model plants as cylindrical elements (Ishikawa, Sakamoto, and Mizuhara 2003; Kothyari, Hayashi, and Hashimoto 2010; Li and Shen 1973; Nepf 1999; Tanino and Nepf 2008; Wu, Shen, and Chou 1999). This is an extreme simplification of vegetation in riverbeds, but it however allows one to face some peculiar relationships between vegetation and flow, besides between vegetation and sediment transport. In particular, the cylindrical elements are useful for measuring the drag coefficient exerted by rigid plants on the flow. For this reason, this simplification will be assumed also in this research.

The drag coefficient has been evaluated also with numerical modeling of the flow field through the cylinders (Souliotis and Panagiotis 2007), by modeling rigid vegetation with cylindrical elements. At the contrary, in most numerical models of the flow field through vegetation, the value of drag coefficient is considered constant (Baptist et al. 2007), notwithstanding the definition of the drag coefficient is probably the most uncertain parameter to evaluate, as it will be analyzed in the

following.

Another common simplification for experimental and numerical approaches rises by the consideration that the bed forms present in vegetated beds have an influence that is limited to a region very close to the bed (within one stem diameter - Nepf, Sullivan, and Zavistoski (1997)). Therefore, bed forms are rarely considered in the total resistance and the scientific literature is, in this case, very limited. Our research will consider also this aspect.

2.2.2 Definition of drag force

When a body is immersed in a fluid in motion, the fluid exerts locally on the body a system of forces that can be broken down into shear stresses and pressure:

$$\mathbf{F} = \int_S \tau \hat{s} dA - \int_S p \hat{n} dA \tag{2.8}$$

In eq. (2.8) $\int_S \tau \hat{s} dA$ expresses the skin drag, and $\int_S p \hat{n} dA$ is the pressure drag.

With respect to the undisturbed flow condition, the component of the force along the main direction of the flow is generally called *resistance* (or *drag force*), while the perpendicular component (vertical component) is called *lift force*. Both the values of drag force, **D**, and lift force, **L**, are dependent on the characteristics of fluid and flow and on the geometrical characteristics of the body. The dependence on the geometry of the body is generally identified with a reference area, A, (usually the ortographic projection of the body) and with the shape of the body (shape factor).

In order to describe the physical relationships among the variables, the dimensionless drag and lift coefficients are introduced. The drag coefficient C_D is defined as:

$$C_D = \frac{D}{A\rho \frac{U_0^2}{2}} \tag{2.9}$$

where ρ is the density of fluid; U_0 is the undisturbed flow velocity. The lift coef-

ficient C_L has a similar definition:

$$C_L = \frac{L}{A_1 \rho \frac{U_0^2}{2}} \tag{2.10}$$

where A_1 is a characteristic area that can be or not be equal to A.

2.2.3 The drag coefficient for flexible and submerged vegetation

Flexible and submerged vegetation influences the flow resistance depending on the degree of submergence and on the characteristics of vegetation. This problem has been approached in different ways, since the thirties, but the most popular method for the calculation of the drag is by considering the vegetation as an additional resistance. The resistance laws are commonly expressed as

$$\frac{U}{u_*} = \sqrt{\frac{8}{f}} \tag{2.11}$$

where U is the vertically-averaged velocity, obtained by integration on the depth of the velocity profile; u_* is the shear velocity and f the Darcy-Weisbach parameter describing the roughness. In a channel, the velocity profile follows generally the logarithmic law. The drag for the vegetation is supposed to be evaluated by an analogous expression:

$$\frac{U}{u_*} = \sqrt{\frac{8}{f_v}} = A_v \ln \frac{h}{k_v} + B_v \tag{2.12}$$

In eq. (2.12) the coefficients A_v and B_v depend on the typology of vegetation and on its state; their values are tabulated in literature. The parameter k_v, which influences also the values of A_v and B_v, represents the equivalent roughness due to vegetation.

In particular, k_v can be identified with the height of the vegetation (h_{veg}) or can be expressed as a function of the flexibility of plants. This flexibility is expressed by Kouwen (1988) as a function of the stiffness parameter M_v, which implicity

contains also the spatial density of stems:

$$k_v = 0.14 h_{veg} \left(\frac{\left(\frac{M_v}{\tau_0} \right)^{0.25}}{h_{veg}} \right)^{1.59} \tag{2.13}$$

where τ_0 is the bed shear stress, and

$M_v = 319\, h_{veg}^{3.3}$ $\mathrm{N/m^2}$ for living vegetation;
$M_v = 25.4\, h_{veg}^{2.26}$ $\mathrm{N/m^2}$ for dead vegetation;
$M_v = 233\, h_{veg}^{3.125}$ $\mathrm{N/m^2}$ for vegetation in intermediate conditions.

2.3 The drag coefficient for rigid vegetation

2.3.1 The resistance of a cylinder in an indefinite flow field

In the thesis, rigid stems are modeled by circular cylindrical elements in a flume. A part of the thesis will be focused on the analysis and measurements of the drag exerted on cylinders disposed in different distributions and densities. In particular, the case of an isolated cylinder will be used as reference for comparison of drag of mutually interfering cylinders.

The drag coefficient for the infinite cylinder in an undisturbed flow depends only on the Reynolds number, and just for very high Reynolds number, also on the roughness of its surface. This is mainly due to the nature of wakes that are formed downstream the cylinder and that is dependent on the value of bulk Reynolds number, $Re = Ud_c/\nu$ (d_c diameter of the cylinder), as showed in Figure 2.3. The drag coefficient is strictly related to the wake formation and hence it is often reported as a function of Re (Figure 2.4).

A little more complex is the case of a finite cylinder, which causes a three-dimensional flow that reduces the drag coefficient with respect to the infinite one. Rather complex is the case of an array of finite cylinders in an open-channel flow, when the distances between the cylinders are sufficiently small to cause interactions between the wakes and the cylinders, modifying the drag coefficient of the single cylinder. This matter will be approached in the thesis and the results will

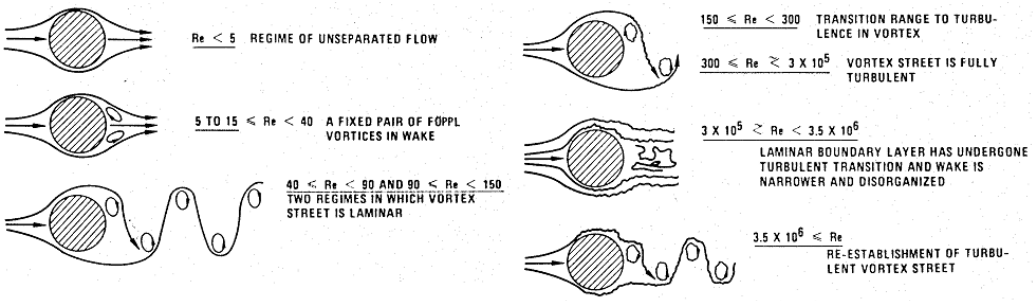

Figure 2.3: The nature of the oscillating wakes downstream an infinite cylinder is depending on $Re_c = Ud_c/\nu$ (taken by Blevins (1984)).

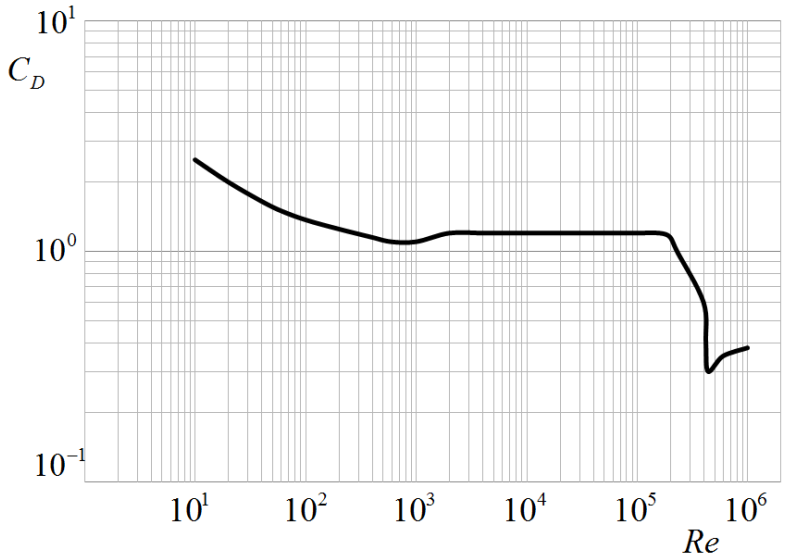

Figure 2.4: Curve representing the tendency of the drag coefficient for an isolated infinite cylinder in an indefinite flow.

be applied to the definition of the effects of rigid stems on sediment transport.

2.3.2 The case of an isolated cylinder in a free surface flow

It is useful to adopt the general definition in eq. (2.9) also for the drag exerted by rigid vegetation:

$$R_p = C_{Dp}\rho A_p \frac{U^2}{2} \tag{2.14}$$

where R_p is the total resistance exerted by a plant on the flow, C_{Dp} is the drag coefficient of the plant, A_p is the orthographic projection to flow and U is the undisturbed average velocity of flow (Figure 2.5). In this way, flow resistance is characterized by the value of drag coefficient C_{Dp}, that can change significantly with the different typologies and characteristics of vegetation.

The first step of this analysis regards the determination of the drag coefficient C_{Dp} of a cylinder in a free-surface flow. The difference with the isolated cylinder in an infinite flow field is due to the interaction with the free surface. In fact, the wake formation in this case does not affect only the flow downstream the cylinder, but affects strongly also the profile of the free surface, because of the different pressures around the cylinder. In addition, the experimental data are obtained in a laboratory channel, in which also the ratio between the width of the channel and the diameter of the cylinder might affect the values of drag.

The variables which influence the drag R_p are:

$$R_p = f_1\left(U, \rho, \mu, d_p, g, h, B\right) \tag{2.15}$$

where $U = \langle \bar{u} \rangle$ is the undisturbed average velocity of the flow, ρ and μ are the density and the viscosity of the fluid, d_p is the diameter of the plant (cylinder), g is the gravity, h is a characteristic value of the water depth, B is the width of the channel (Figure 2.5).

By using the Buckingham theorem (also known as Π theorem), the variable R_p in eq. (2.15), that is a function of 7 dimensional parameters, can be led to a

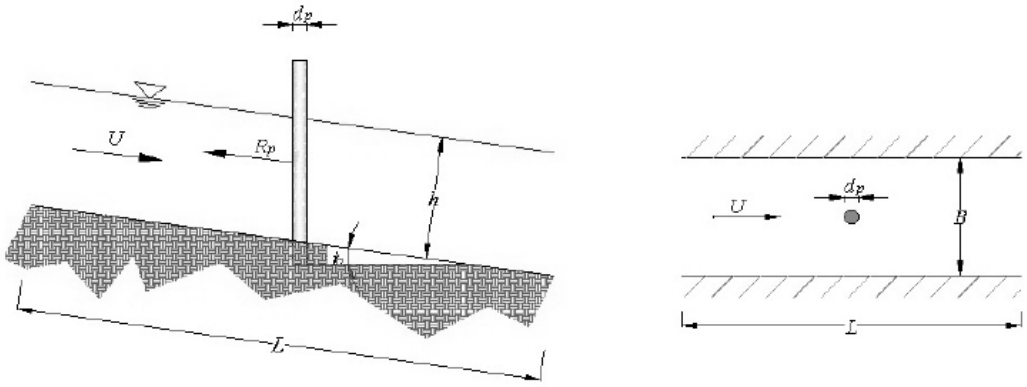

Figure 2.5: Isolated cylinder in a channel: geometrical and hydrodynamics dimensions

dimensionless variable dependent on $7 - 3 = 4$ dimensionless quantities:

$$\frac{R_p}{\rho d_p^2 U^2} = \phi_1 \left(\frac{\mu}{\rho U d_p}, \frac{g d_p}{U^2}, \frac{h}{d_p}, \frac{B}{d_p} \right) \tag{2.16}$$

The combination of two or more parameters in the ϕ_1 expression is admitted for the Buckingham theorem, but assuring the independence of the parameters. We can choose to combine the parameters in order to isolate some dimensionless parameters which are more meaningful for the study we are facing.

In this case the inverse of Reynolds number of plants, Re_p, can be identified in eq. (2.16):

$$\Pi_\mu = \frac{\mu}{\rho U d_p} = \frac{1}{Re_p}; \tag{2.17}$$

then, by combining $\Pi_g = g d_p / U^2$ and $\Pi_h = h/d_p$, the square of Froude number, Fr, can be isolated:

$$\Pi_g \Pi_h = \frac{g d_p}{U^2} \frac{h}{d_p} = \frac{g h}{U^2} = \frac{1}{Fr^2} \tag{2.18}$$

Finally, also the expression on the left side of the eq. (2.16) can be changed in order to obtain the formulation of the drag coefficient C_{Dp} ($\Pi_{R_p} = R_p / \rho d_p^2 U^2$):

$$2 \Pi_{R_p} \Pi_h^{-1} = C_{Dp} \tag{2.19}$$

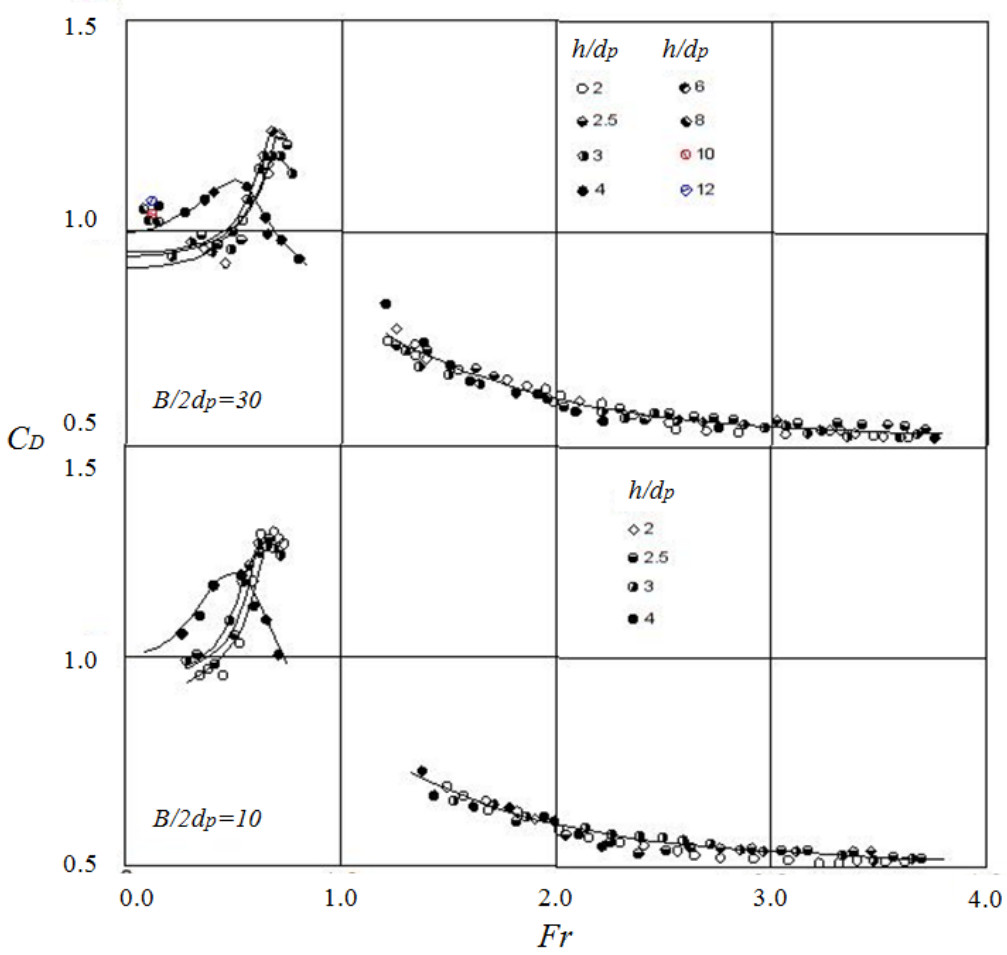

Figure 2.6: Results by Hsieh (1964) on drag coefficient as a function of the ratio $B/2d_p$ and h/d_p

So, finally, we can write:

$$C_{Dp} = \phi_2 \left(Re_p, Fr, \frac{h}{d_p}, \frac{B}{d_p} \right) \tag{2.20}$$

The dependence of the drag coefficient on the above quantities is well described by Hsieh (1964), and reported in Figures 2.6 and 2.7. In particular, the Figure 2.6 shows the behavior of the drag coefficient for $B/2d_p = 30$, in the upper graph, and $B/2d_p = 10$, for the down graph, as a function of the ratio h/d_p and of the Froude number, Fr. The curves for the drag are different for subcritical

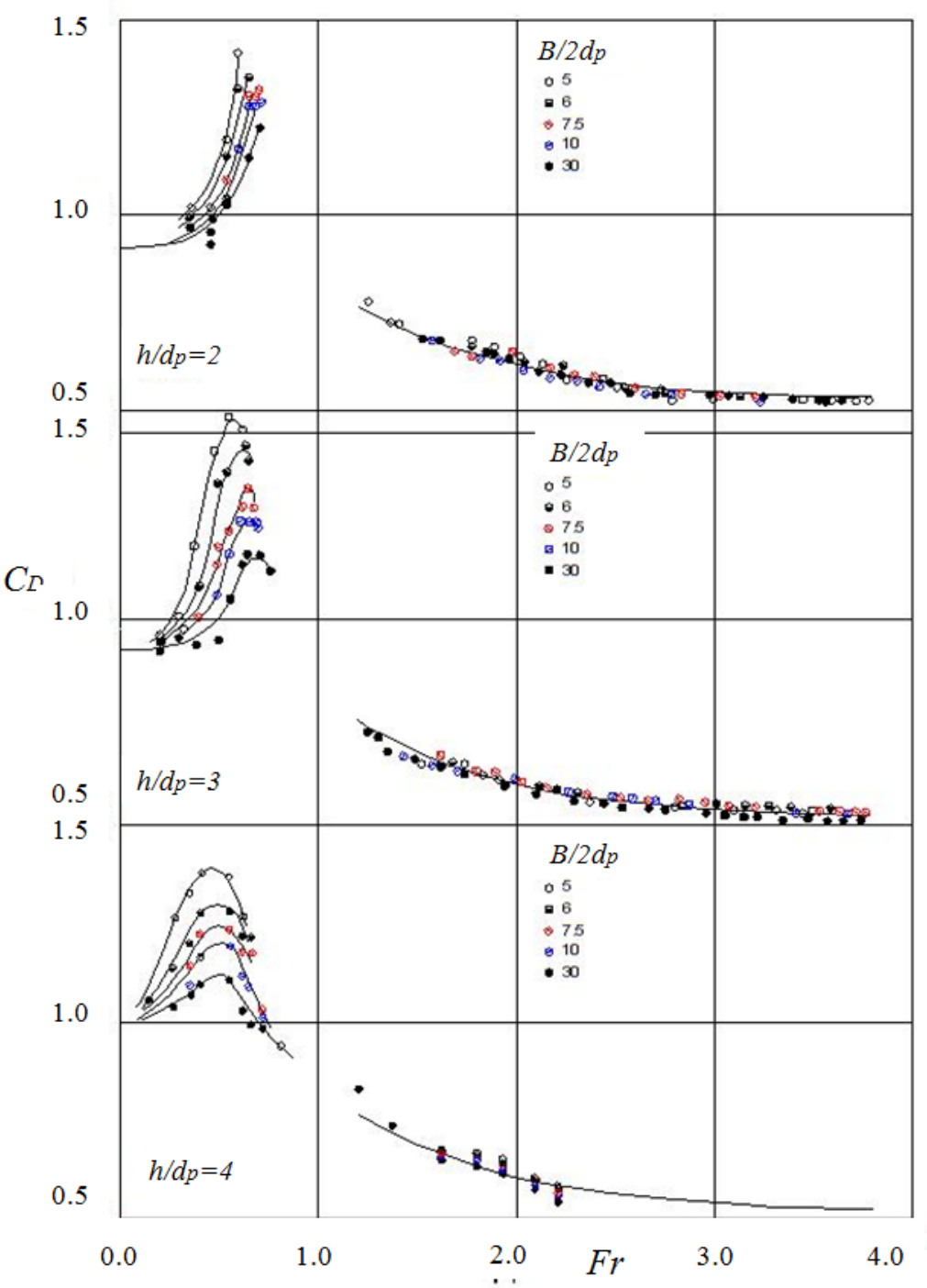

Figure 2.7: Results by Hsieh (1964) on drag coefficient as a function of the ratio $B/2d_p$ and h/d_p

and supercritical conditions: for $Fr < 1$, the values of the C_D present a peak for every ratio h/d_p represented. The lower C_D at the peak is for $h/d_p = 4$, for both the ratio $B/2d_p$. For $Fr > 1$, the curve decreases monotonically with Fr.

The three graphs in Figure 2.7 show the evolution of C_D as a function of the Froude number Fr, for three different values of the ratio h/d_p. To each value of the Froude number corresponds a different value of the narrowing ratio $B/2d_p$. In these graphs it is possible to distinguish an interesting behavior of the drag coefficient: for $Fr < 1$, the C_D increases if $B/2d_p$ decreases. Also in this case, for $Fr > 1$, the curve decreases monotonically with Fr.

The experimental analysis on the drag coefficient for an isolated cylinder will be useful for:

1. comparing the results with data in literature, in order to verify whether the effect of the width of the channel is influent;
2. choosing which is the better definition of *average velocity* to use for the analysis.

2.3.3 Approaches for determining the drag coefficient for rigid and emergent vegetation

The drag coefficient of an array of stems can be totally different with respect to the drag of an isolated stem. This is due, in principle, to the mutual interactions between cylinders and wakes. Some authors have tried to distinguish the behavior of drag, depending on the distance among elements (Carmo et al. 2011; Kothyari, Hayashi, and Hashimoto 2010; Li and Shen 1973; Tanino and Nepf 2008), and hence as a function of the mutual interaction between cylinders, in order to comprehend how to take it into account. It is generally accepted that these interactions can play a crucial role also in the sediment entrainment and transport. Qualitatively: (i) if the elements are very close, then the wake is a single one and the colony behaves as a single body (Takemura and Tanaka 2007); (ii) if the distance between the interaxes of elements with respect to the diameter of stems (Λ_p/d) is sufficiently large (up to several units), then the wakes are strongly interacting (Figure 2.8 (a)); (iii) finally, the wakes may be independent if the ratio Λ_p/d is larger than several units (Figure 2.8 (b)).

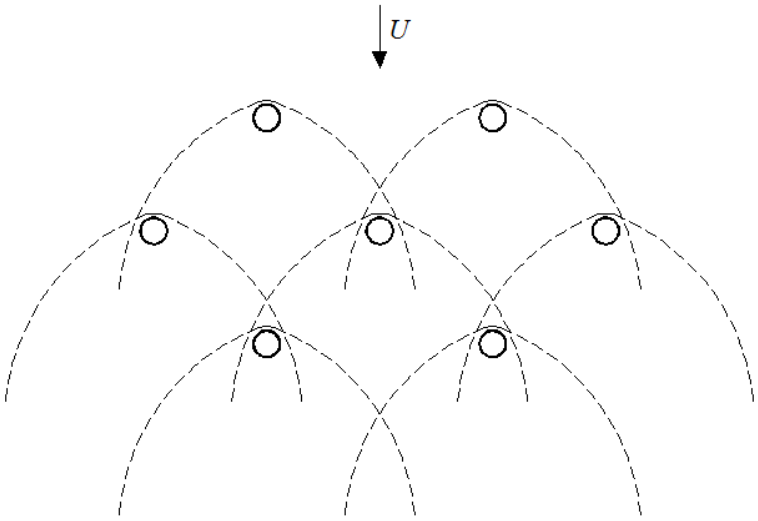

(a) interactive wakes

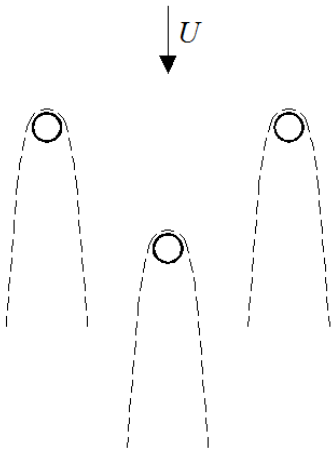

(b) independent wakes

Figure 2.8: Representation of the possible interactions of wakes in an array of stems: (a) the elements are sufficiently close for the interaction of wakes; (b) the stems are sufficiently far, to make the wakes independent of each other.

As in the case of a non-vegetated channel (see Section 2.1), also in presence of stems, the global resistance can be broken down into independent contributions: grain stress, bed forms stress and vegetation drag. Hence:

$$\tau_0 = \tau_0' + \tau_0'' + \tau_v \tag{2.21}$$

in which τ_0 is the global stress, τ_0' is the part due to the grain roughness, τ_0'' is due to the potential presence of bed forms, and τ_v is the contribution of the vegetation.

The drag resistance exerted by rigid stems is treated as if every stem were an independent element with respect to the others; that is, the total resistance due to an array of plants is considered as the sum of the drag forces due to the single plants:

$$R_p = \sum_{n=1}^{N} R_{p,j} = \sum_{n=1}^{N} C_{Dp,j} \rho A_{p,j} \frac{u^2}{2} \tag{2.22}$$

In eq. (2.22) R_p is the global drag force, which is the sum of the drag force of all the N stems considered separately; $C_{Dp,j}$ is the drag coefficient for the j stem; $A_{p,j}$ is the orthographic projection to the flow (called *cross section*); u is a characteristic velocity of flow. This kind of approach does not consider the possible mutual interaction of plants and their different behavior for different interaxes.

The non-mutual interaction of plants is not the only hypothesis that is considered in literature. Alternative hypotheses are:

- the drag coefficient is considered as a constant value, that is dependent neither on the characteristics of flow nor on stems. Moreover, generally this coefficient assumes the value of the drag coefficient of the isolated cylinder, that may be correct only in case of non-mutual interference; this approach is adopted in many numerical models;

- the characteristic velocity u is considered equal to the velocity of undisturbed flow; but in other investigations, it assumes the value of the double-averaged velocity through the stems $\langle \bar{u} \rangle$ (see Section 2.4.1).

Generally the study of resistance exerted by rigid stems is approached by modeling the stems as rigid cylinders with constant diameter. The publications which

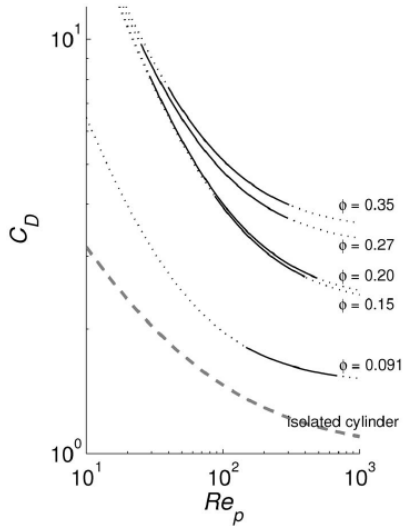

Figure 2.9: The drag coefficient as a function of the Reynolds number of plants, Re_p, and vegetation density ϕ, by Tanino and Nepf (2008)

treat the topic with this simplification are numerous (see Section 2.2.1). Among them, the most significant for this project research are:

Tanino and Nepf (2008), who considered random distribution of cylinders at different densities of stems. They obtained an expression for C_{Dp} as a function of the Reynolds number of plants ($Re_p = \langle \bar{u} \rangle d_p/\nu$) and of the density of vegetation ϕ (Figure 2.9). The expression they formulated for the drag coefficient is:

$$C_{Dp} = 2\left(\frac{\alpha_0}{Re_p} + \alpha_1\right) \tag{2.23}$$

where α_0 is a constant, but α_1 is a parameter depending on the density ϕ:

$$\alpha_1 = (0.46 \pm 0.11) + (3.8 \pm 0.5)\,\phi \tag{2.24}$$

Ishikawa, Mizuhara, and Ashida (2000b), who proposed an expression to evaluate the drag coefficient for different gradients of channel bed (i_b) and as a

function of the area occupied by trees, λ:

$$\begin{aligned} C_D &= 1.71\,\lambda^{0.11} \quad \text{when} \quad i_b = 2\% \\ C_D &= 2.45\,\lambda^{0.20} \quad \text{when} \quad i_b = 5\% \\ C_D &= 3.89\,\lambda^{0.31} \quad \text{when} \quad i_b = 10\% \end{aligned} \tag{2.25}$$

Their experimental results were obtained by measuring the drag force on cylinders which were arranged in staggered configuration in a laboratory channel.

Kothyari, Hashimoto, and Hayashi (2009), with a similar distribution of cylinders, who obtained a formula to evaluate the drag coefficient as a function of the stems Reynolds number (Re_p) and of the density of vegetation λ:

$$C_D = 1.53\left[1 + 0.45\ln\left(1 + 100\lambda\right)\right] Re_p^{-3/50} \tag{2.26}$$

In addition, the authors highlighted that in case of dense vegetation ($\lambda = 0.0885$), the dependence of the drag coefficient on the Froude number (Fr) is not negligible. In those cases, the formula to calculate the drag coefficient for the authors is:

$$C_D = 1.53\left[1 + 0.45\ln\left(1 + 100\lambda\right)\right] Re_p^{-3/50}\left(0.8 + 0.2Fr - 0.15Fr^2\right) \tag{2.27}$$

In presence of rigid vegetation at sufficiently high density and mobile bed, the stems produce particular bed forms, that in the following will be termed *vegetation bed forms*. In fact, around every stem a scour is formed, due to the effect of the vorticity alteration, which in turn determines a local increase of sediment entrainment (Figure 2.10). Downstream every stem, the entrainment capacity is reduced, and a deposition process is induced. This process reaches an equilibrium between scours and depositions, that induces the formation of bed forms. These special bed forms are not tackled in depth in scientific literature, even if they are present and visible at every test at sufficiently high density of rigid vegetation. Hence, for simplicity, the role of bed forms is generally considered a negligible contribution to flow resistance in vegetated channels, notwithstanding the same hypothesis for non-vegetated channels would be considered a rough approximation.

In this thesis, the contribution of bed forms to flow resistance in presence of rigid and emergent vegetation is analyzed in detail. We will propose a new experimental method to evaluate length and height of *vegetation bed forms*. Moreover, the drag coefficients obtained in different experimental conditions will be compared: for different densities of stems; with or without sediment transport; with or without bed forms.

2.3.4 Uniform flow condition in a vegetated channel

The concept of uniform flow condition in a vegetated channel must be better defined. In a channel with emergent plants, indeed, the water depth and the average velocity cannot be constant in each section of the domain, but both change punctually, also as a function of the distance from the plants. Hence, the uniform flow condition can be defined only by considering a control volume sufficiently large and containing a sufficiently large number of plants. The uniform flow condition in the control volume becomes an averaged concept. The water depth is the averaged values of the punctual water depths in the whole domain; and the uniform flow velocity is generally considered as double-average velocity, which will be described in detail in the following (Section 2.4).

In the channel used for the experimental data, the uniform flow conditions are verified before each measurement, by measuring the water depth all along the channel and by verifying that it is constant on average, or, alternately, that bed slope and free-surface are parallel. In mobile bed conditions, moreover, the uniform flow condition is the only possible condition for a steady regime, as will be demonstrated in Section 4.2.4.

2.3.5 Indirect determination of drag coefficient

For a theoretical approach to the global resistance in a vegetated channel, we consider a control volume (a stretch) of a natural river in which the disposition of rigid plants is random, but with a density which is uniform on average. In steady conditions, and depending on the condition of flow, the situation is something similar to what is represented in Figure 2.10 (a). In this condition, the global

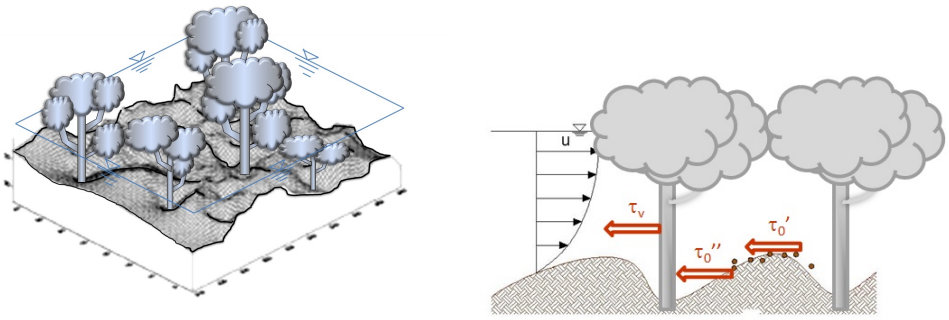

(a) 3D view (b) lateral view

Figure 2.10: Representation of a possible steady condition in a vegetated natural river.

resistance depends on the grain roughness, the bed form stress and the drag exerted by plants (Figure 2.10 (b)).

The problem can be approached by considering the balance of momentum in uniform flow conditions. In the situation depicted in Figure 2.10, the global resistance R_t in uniform flow conditions is:

$$R_t = \tau_0' A + \sum R_{p,j} + F_{bf} \tag{2.28}$$

where A is the total area, excluded the surface occupied by plants, that is the area in which the grain roughness contributes to the global resistance; $R_{p,j}$ is the resistance of a single plant (eq. 2.22); F_{bf} is the contribution due to bed forms.

The global resistance is balanced by the component of the weight of water contained in the control volume, along the main direction of flow (x-direction):

$$W_x = \tau_0' A + \sum R_{p,j} + F_{bf} \tag{2.29}$$

The term F_{bf} is totally unknown and it is often neglected; if $F_{bf} = 0$:

$$W_x = \tau_0' A + \sum R_{p,j} \tag{2.30}$$

As already said, we can consider the plants modeled as rigid cylinders, with constant diameter d_p, and a rectangular control volume, of width B (the width of the channel) and length L, containing a sufficiently large number of plants (Figure

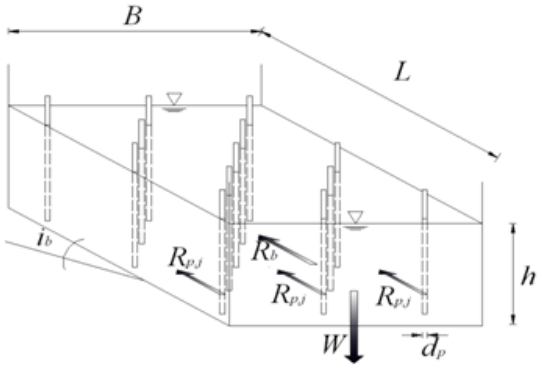

Figure 2.11: The forces in action in a vegetated river. R_b identifies the bed roughness, that is grain roughness together with bed forms stress.

2.11). In uniform flow conditions, the longitudinal component of the weight of water can be expressed by considering the volume not occupied by the stems:

$$W_x = \rho g B L h \left(1 - \Omega_v\right) i_b \tag{2.31}$$

where ρ is the density of water; g is the gravity; i_b is the bed slope; h is the water depth; Ω_v is the density of stems, that is:

$$\Omega_v = \frac{\sum_{j=1}^{N} A_{p,j}}{A_{tot}} \tag{2.32}$$

where $A_{p,j}$ is the area occupied by the single plant and A_{tot} the total base of the control volume. If the N cylinders contained in the control volume have an average diameter equal to d_p, the formulation in eq. (2.32) becomes:

$$\Omega_v = N \frac{\pi d_p^2/4}{BL} \tag{2.33}$$

In eq. (2.30), $\tau_0' A$ is the grain drag. By using the Strickler (1923) definition of the resistance:

$$\frac{U}{u_*} = \frac{k_{s,b} R_h^{1/3}}{\sqrt{g}} \tag{2.34}$$

and hence

$$\tau_0' = \rho u_*^2 = \frac{\rho U^2 \sqrt{g}}{k_{s,b} R_h^{2/3}} \tag{2.35}$$

where U is a suitable average velocity. Which is the best definition for the averaged velocity will be defined experimentally, by considering different definitions of *averaged velocity*. $k_{s,b}$ is the Gauckler-Strickler coefficient for the grain roughness; R_h is the hydraulic radius. By multiplying eq. (2.35) for the free area:

$$\tau_0' A = \rho U^2 \frac{g}{k_{s,b} R_h^{2/3}} BL\left(1 - \Omega_v\right) \tag{2.36}$$

The coefficient $k_{s,b}$ can be evaluated with the Strickler formula:

$$k_{s,b} = \frac{21.1}{d_{50}^{1/6}} \tag{2.37}$$

Finally, by considering $R_h \cong h$ and by substituting eqs. (2.31), (2.36), (2.37) and (2.22) into eq. (2.30):

$$\rho g BLh\left(1 - \Omega_v\right) i_b = \rho U^2 \frac{g}{k_{s,b}^2 R_h^{2/3}} BL\left(1 - \Omega_v\right) + \sum_{j=1}^{n_p} C_{Dp} \rho A_{r,j} \frac{U^2}{2} \tag{2.38}$$

and hence:

$$C_{Dp} = \frac{\pi}{2} \frac{1 - \Omega_v}{\Omega_v} \frac{d_p}{h} \left[\frac{ghi_b}{U^2} - \frac{g}{21.1^2} \left(\frac{d_{50}}{h} \right)^{1/3} \right] \tag{2.39}$$

In conclusion, according to the same approach of the isolated cylinder (Section 2.3.1), the parameters which influence the drag force of plants are:

$$R_p = f(u, \rho, \mu, d_p, g, h, B, \Omega_v) \tag{2.40}$$

According to the Π-theorem, the drag coefficient for a simplified situation results to be dependent only on 5 dimensionless quantities:

$$C_{Dp} = \phi\left(Re_p, Fr, \frac{h}{d_p}, \frac{B}{d_p}, \Omega_v \right) \tag{2.41}$$

where $Re_p = U d_p / \nu$ is the Reynolds number of the plants, $Fr = U/\sqrt{gh}$ is the

Froude number.

2.4 Turbulent velocity profile

The velocity profile in a turbulent channel flow can be described by different laws, also depending on the sublayer which these laws refer (inner region, buffer, viscous sublayer, etc.). The most common law is the logarithmic:

$$\frac{u(z)}{u_*} = \frac{1}{\kappa} \ln\left(\frac{u_* z}{\nu}\right) + C_1 \tag{2.42}$$

for smooth wall; or

$$\frac{u(z)}{u_*} = \frac{1}{\kappa} \ln\left(\frac{z}{k_e}\right) + C_2 \tag{2.43}$$

for rough wall, being C_1 and C_2 two constants. For both, rough and smooth wall, the formulation can be generalized as:

$$\frac{u(z)}{u_*} = \frac{1}{\kappa} \ln\left(\frac{z}{k_e}\right) + B\left(\frac{u_* k_e}{\nu}\right) \tag{2.44}$$

where B is not constant, but it is a suitable function of the roughness Reynolds number $u_* k_e/\nu$, where $u_* = \sqrt{\tau_0/\rho}$ is the shear velocity:

$$B = B\left(\frac{u_* k_e}{\nu}\right) \tag{2.45}$$

In the above equations (eq. 2.42 to 2.45): $\kappa = 0.41$ is the von Karman constant; ν is the kinematic viscosity of water; k_e is the Nikuradse's equivalent roughness, or another characteristic dimension of roughness (as example, see the van Rijn's approach for bed forms roughness in Section 2.1).

In some cases, it is possible to express the velocity profile by means of a power law:

$$\frac{u}{u_0} = \left(\frac{z}{z_0}\right)^{1/m} \tag{2.46}$$

where u_0 is the reference velocity at the coordinate z_0; the power $1/m$ is very often taken constant ($m = 6 \div 7$) (Hinze 1959; Schlichting, Gersten, and Gersten

2000), but some authors (Chen 2007) have expressed $1/m$ as a function of the flow characteristics (for instance, the shear velocity u_*).

By the integration of the velocity profile over the depth, the resistance law can be formulated as a function of the Darcy-Weisbach coefficient, f:

$$\frac{U}{u_*} = \sqrt{\frac{8}{f}} \tag{2.47}$$

where U is the depth averaged velocity.

The above expressions (eqs. 2.42 to 2.46) are generally valid for fixed bed channels in uniform flow conditions. When rivers with rigid vegetation and mobile bed are concerned, the generation of wakes downstream of the stems and bed shear are the phenomena that mainly affect the turbulent flow field. The fluid-vegetation interaction, which generates different kinds of instabilities, such as wakes and horseshoe vorteces, together with the bed effects (including both grain roughness and bed forms) concur to generate a turbulent flow which is hard to define as "uniform". The characteristics of the resulting flow depend also on the distribution of stems and on the geometry of bed forms.

In flows with strong spatial variation the application of the Double-Averaged Methodology (DAM) can be useful. During the last 30 years, this method has been developed by many authors (see e.g. Finnigan (2000) and Nikora (2010)) and applied to different kinds of environmental flows which present strong spatial variation. *Double-average* means that the velocity, defined for each point of a control volume of a fluid in motion, is first averaged in space (spatial average), and then the spatial average is averaged in time.

2.4.1 Double-Averaged Equation for turbulent open-channel flow

In order to explain the double-average from an analytical point of view, it is necessary to define the three different kinds of average which can be applied to an instantaneous and punctual velocity u:

- ensemble average:

$$\{u\,(x,t)\} = \sum_{n=1}^{\infty} u_n(x,t) \tag{2.48}$$

is the average of all the values of the velocity for all the points of the domain and for all the time period considered;

- time average:

$$\overline{u(x,t)} = \frac{1}{T}\int_{t-T/2}^{t+T/2} u(x,t')dt' \tag{2.49}$$

is the average of the velocity in one point for a time period T;

- spatial average:

$$\langle u(x,t)\rangle = \frac{1}{L}\int_{x-L/2}^{x+L/2} u(x',t)dx' \tag{2.50}$$

is the averaged velocity for an area extent of L and only one instant.

In the double-average method, every term of the fluid equations, for each point of the domain of analysis, can be broken down into two terms. By considering for instance the velocity:

$$u(t) = \langle u(t)\rangle + u'(t) \tag{2.51}$$

where $\langle u(t)\rangle$ is the spatial average, and $u'(t)$ is the fluctuating component, related with each point of the domain. The spatial average $\langle u(t)\rangle$ can be split again into two terms:

$$\langle u(t)\rangle = \bar{u}(t) + \tilde{u}(t) \tag{2.52}$$

where $\bar{u}(t)$ is the temporal average and $\tilde{u}(t)$ is the fluctuating part.

The DA equations are obtainable by applying the division of the velocity into the three terms in eqs. (2.51) and (2.52). In particular, they can be evaluated with two different methodologies:

1. by applying the spatial average to the Reynolds equations, which are already temporally averaged;
2. by applying the spatial average to the Navier-Stokes equations and then the ensemble average to the resulting equations.

Several authors (Nikora et al. 2007) sustain that the first method seems the most suitable for the fluid mechanics topics, especially because it follows the classical

approach, resulting the clearest procedure for hydraulic scientists. Anyhow, by the ergodicity hypothesis, the results by the two methods are identical.

In order to obtain the DA equations, the first step is to consider the transition from Navier-Stokes equations to Reynolds equations. The Navier-Stokes equations are:

$$\frac{\partial u_i}{\partial t} + \frac{\partial u_i u_j}{\partial x_j} = -\frac{1}{\rho}\frac{\partial p}{\partial x_i} + \nu\frac{\partial^2 u_i}{\partial x_j \partial x_j} \tag{2.53}$$

where the subscripts i and j indicate two directions of flow and p is the pressure (punctual and instantaneous). By applying the decomposition in the average and fluctuating component:

$$u_i = \langle u_i \rangle + u_i' \quad p = \langle p \rangle + p' \tag{2.54}$$

the Reynolds equations are obtained:

$$\frac{\partial \langle u_i \rangle}{\partial t} + \frac{\partial \langle u_i \rangle \langle u_j \rangle}{\partial x_j} = -\frac{1}{\rho}\frac{\partial \langle p \rangle}{\partial x_i} - \frac{\partial \langle u_i' u_j' \rangle}{\partial x_j} + \nu\frac{\partial^2 \langle u_i \rangle}{\partial x_j \partial x_j} \tag{2.55}$$

For the second step of analysis, i.e. the application of the spatial average, the results are more complex. Many authors have formulated several DA equations by using different working hypotheses (Whitaker 1999), obtaining similar but not equal formulations. Among these, the application to flow fields through vegetation is treated by several authors, among them Nikora (2004). The relative equations will be reported in the following section (Section 2.4.2).

2.4.2 Turbulent flow in a vegetated channel

Turbulence production and transport phenomena can have several sources in natural rivers. When rivers with rigid vegetation are concerned, the characteristics of the resulting flow depend on the distribution of stems, nature and geometry of bed forms, besides the obvious dependence on flow depth.

The analysis of turbulence structure through vegetation is particularly important also because the dynamics of the flow and the drag coefficient - both due to vegetation and bed roughness - are strictly related. Figure 2.12 shows schematically how the presence of a rigid stem can affect the velocity of flow. The fig-

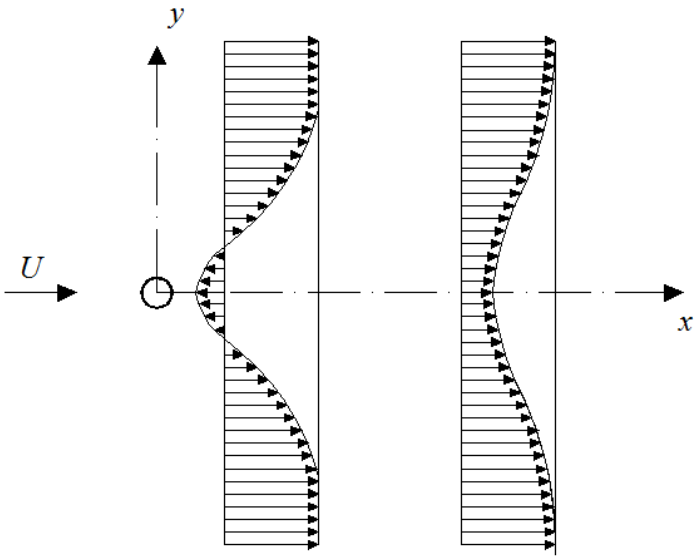

Figure 2.12: Representation of the profile of the velocity in presence of a rigid stem (of ideally cylindrical shape) for an ideal horizontal section.

ure, however, represents only the interference with the main direction of flow, neglecting the effects on the vertical direction (due mainly to bed roughness) and transversal (y) direction.

The double-averaged method through vegetation is the most used and useful method to evaluate the characteristic velocities of flow. The next equations are reported only as example of the simplest equations which can be applied to vegetated reaches:

$$\begin{cases} gi_b - \langle \dfrac{\partial \tilde{p}}{\partial x} \rangle - \dfrac{1}{\phi} \dfrac{\partial \phi \langle \tilde{u}\tilde{w} \rangle}{\partial z} = 0 \\ g + \dfrac{1}{\rho} \dfrac{\partial \langle \bar{p} \rangle}{\partial z} + \dfrac{1}{\rho} \langle \dfrac{\partial \tilde{p}}{\partial z} \rangle + \dfrac{1}{\phi} \dfrac{\partial \phi \langle \overline{w'^2} \rangle}{\partial z} = 0 \end{cases} \tag{2.56}$$

In eq. (2.56) u, v and w are the instantaneous components of velocity along the three main directions x, y and z. The brackets, overbars and tildes in the equations have the meanings already reported in Section 2.4.1. In addition, in eq. (2.56) is present the term ϕ which describes the porosity of vegetation (in the approach, applied to submerged and flexible vegetation). The eq. (2.56) has been used by several authors, among them Righetti (2008) and Righetti and Armanini (2002), and it was obtained by neglecting the viscous contributions on averages in

horizontal layer.

Implicitly in eq. (2.56) is also present the definition of the drag coefficient of vegetation, since the variations of pressure in the xy-plane are related with the drag coefficient. Despite the fact that many experimental observations show that the drag coefficient is a function of plant density and arrangement, and of flow conditions (see e.g Kothyari, Hayashi, and Hashimoto (2010), Ishikawa, Mizuhara, and Ashida (2000a) and Tanino and Nepf (2008)), usually this term is considered as a constant in many numerical models. This can be a rough approximation which can lead to inaccuracy, especially for low Reynolds number conditions.

In the present work, the spatial heterogeneities of the flow field through stems are shown and are related with the entrainment and turbulent transport of bed particles. In particular, the dispersive component of the flow field are not analyzed, but only the time averaged velocities in some representative vertical planes, and the spatial averaged components of the flow field are evaluated, with the aim to infer the implication for sediment entrainment and transport.

Chapter 3

Mechanics of sediment transport

3.1 Modalities of sediment transport

3.1.1 The beginning of particles motion

In the scientific literature there are several approaches for the description of the beginning of the motion of a particle lying on the bed of a channel, but the most popular is the Shields' theory (Shields, Ott, and Van Uchelen 1936). The Shields' theory is widely used in the specialist literature on sediment transport, and it has been revised and generalized by other authors (Coleman and Nikora 2008; Yalin 1977). The Shields' approach is based on the balance of forces acting on a particle lying on a quasi-horizontal bed. Shields assumed that the flow field in the proximity of the particle is described by a logarithmic law of velocity. The friction force $\mathbf{F}$, which is assumed to be a Colombian force, is proportional to the normal components of the forces acting on the particle (weight $\mathbf{W}$, buoyancy $\mathbf{B}$ and lift $\mathbf{L}$) (Figure 3.1). The incipient motion condition is given by the balance between friction and drag force:

$$\mathbf{D} = \tan\varphi(\mathbf{W} - \mathbf{B} - \mathbf{L}) \tag{3.1}$$

where $\mathbf{D}$ is the drag force:

$$\mathbf{D} = C_D \alpha_2 d^2 \rho \frac{u^2}{2} \tag{3.2}$$

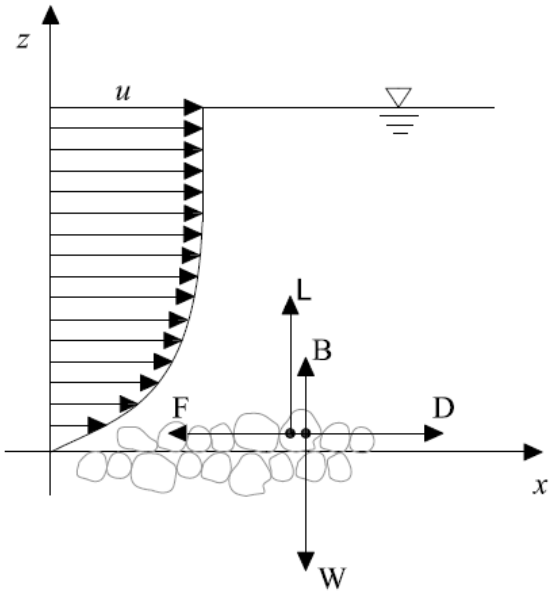

Figure 3.1: A scheme of the forces acting on a particle lying in a quasi-horizontal riverbed

and $\mathbf{L}$ is the lift force:

$$\mathbf{L} = C_L \alpha_2 d^2 \rho \frac{u^2}{2} \tag{3.3}$$

In eqs. (3.2) and (3.3) α_2 and α_3 are geometrical coefficients; d is the characteristic grain size; C_D and C_L are the drag and lift coefficients; ρ is the water density; u is the velocity in the proximity of the particle. The difference between the weight and the buoyancy is:

$$\mathbf{W} - \mathbf{B} = g(\rho_s - \rho)\alpha_3 d^3 \tag{3.4}$$

where ρ_s is the density of the sediments and g is the gravity.

By substituting eqs. (3.2), (3.3), (3.4) into eq. (3.1) we obtain:

$$C_D \alpha_2 d^2 \rho \frac{u^2}{2} = \tan\varphi \left[g(\rho_s - \rho)\alpha_3 d^3 - C_L \alpha_2 d^2 \rho \frac{u^2}{2} \right] \tag{3.5}$$

In order to specify the velocity appearing in eq. (3.5), Shields adopted the logarithmic distribution:

$$\frac{u}{u_*} = \frac{1}{\kappa} \ln \frac{z}{k_e} + B\left(\frac{k_e u_*}{\nu}\right) \tag{3.6}$$

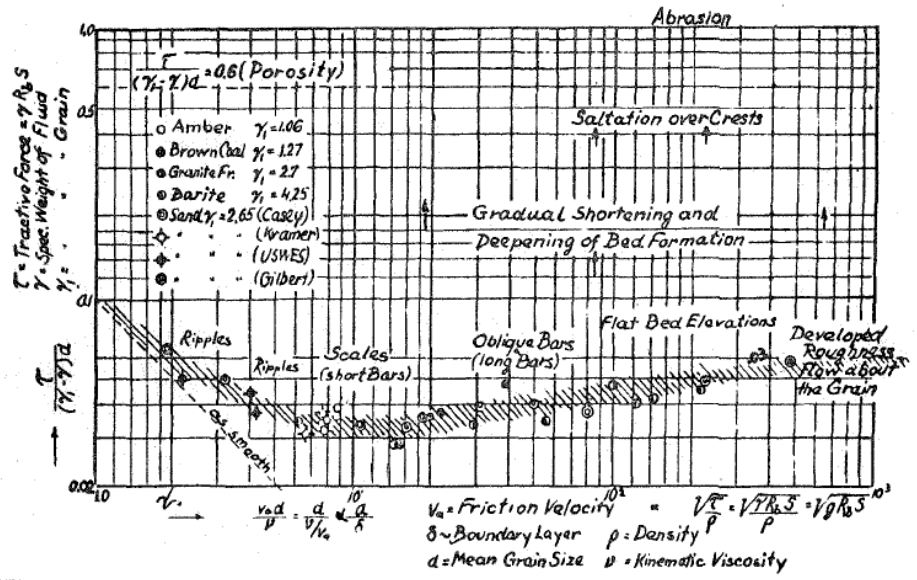

Figure 3.2: The original figure inserted by Shields (Shields, Ott, and Van Uchelen 1936) in his article on the beginning of motion

where u is the time-averaged velocity in the longitudinal direction (x direction) and z is the vertical direction; $u_* = \sqrt{\tau_0/\rho}$ is the shear velocity; k_e is a characteristic size of the roughness, and generally $k_e = \alpha_k d$; κ is the von Karman's constant; the velocity can be evaluated at a distance from the bottom proportional to the grain size: $z = \alpha_z d/2$; α_k and α_z are constants basically related to the particle geometry. Hence, from eq. (3.6):

$$u = u_* \left[\frac{1}{0.41} \ln \left(\frac{\alpha_z}{\alpha_k} \right) + B \left(\frac{d u_*}{\nu} \right) \right] \tag{3.7}$$

By substituting the eq. (3.7) into eq. (3.5), the Shields' critical parameter of mobility, θ_c, results to be only a function of du_*/ν:

$$\theta_c = \frac{u_{*,c}^2}{g \Delta d} = \text{fct} \left(\frac{d u_*}{\nu} \right) \tag{3.8}$$

The parameter of mobility is the ratio between the shear velocity, u_*, and $g\Delta d$, where $\Delta = (\rho_s - \rho)/\rho$ is the reduced relative density of sediments. The expression in eq. (3.8) means that:

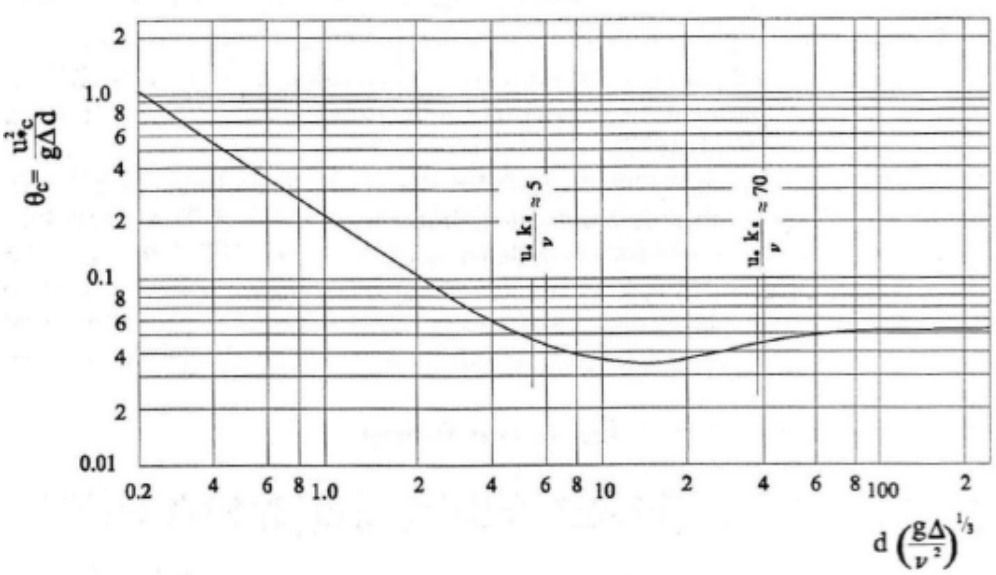

Figure 3.3: The curve by Yalin (1977) for the calculation of Shields' parameter for incipient motion

- θ is a dimensionless parameter which defines the movement of a particle for a specific flow condition;
- a critical value of θ_c describes the incipient motion of particles for a specific flow condition;
- the critical parameter of mobility θ_c depends only on the *shear Reynolds number* $Re_* = du_*/\nu$.

The curve obtained by Shields and shown in Figure 3.2 has an implicit nature, since the parameter $u_{*,c}$ is present in both the axes. Another curve, more useful, can be obtained by a combination of the shear Reynolds number and θ, so that in abscissa the dependence on $u_{*,c}$ decays: $(\theta Re_*^{-2})^{1/3} = d(d\Delta/\nu^2)^{1/3} = D_*$, where D_* is termed *reduced grain diameter*. The curve is shown in Figure 3.3 (taken from Yalin (1977)) The best formula to fit the curve is proposed by Brownlie and Brooks (1981):

$$\theta_c = 0.22D_*^{-1} + 0.06e^{-17.77D_*^{-1}} \tag{3.9}$$

Almost all the investigations on sediment transport initiation are based on the Shields theory, although it is known that the incipient motion is too complicate to

be completely described by a balance of forces acting on a particle. In fact, it is generally recognized that coherent structures, such as turbulent bursts and sweeps, are also fundamental mechanisms for causing sediment motion (Zedler and Street 2001), that are not investigated by Shields. Several researchers are still facing the problem of the incipient motion (Armanini and Gregoretti 2005; Giménez-Curto and Corniero 2009; Hardy 2005; Papanicolaou et al. 2002; Wilcock and McArdell 1993), because the questions on the matter are numerous, as described in Coleman and Nikora (2008). Among the open questions of this topic, there is also the dependence of drag and lift force on shear Reynolds number, $Re_* = u_* d/\nu$, and on the distance from the wall. Lee and Balachandar (2010), for example, have verified that the drag force on a particle increases logarithmically as the particle moves closer the wall and that the coefficient decreases as Re_* increases.

3.1.2 Bedload transport

It is common use to distinguish the sediment transport in bedload and suspended load transport. A rough distinction between the two modalities of transport can be made by considering the average displacement of grains: in bedload the single average displacement is scaled by the grain size; in suspended load, by the water depth. Several authors have established that the suspended load is possible only if the ratio between the shear velocity u_* and the terminal velocity w_s is (Hayashi and Ozaki 1980):

$$\frac{w_s}{u_*} < 0.8 \tag{3.10}$$

Other authors believe that this simple relationship is not sufficient as distinction, and they have observed that the different behaviors of sediments depend on the turbulent phenomena which are involved: bedload transport is considered as a consequence of sweep motions in the fluid (Best 1992; Drake et al. 1988), whereas turbulent bursting events may play a larger role in suspension (Cao, Zhang, and Xi 1996; Jackson 1976).

The literature on sediment transport, both for bedload and suspended load, is very wide, but almost all the methods to evaluate the sediment transport capacity are based on empirical formulation, notwithstanding the stochastic nature of sediment movements. One of the few methods based on theoretical considera-

tions is the Einstein's theory (Einstein 1950) on sediment transport, which will be extensively discussed in Section 3.2.

Many researchers deplore not only the lack of theoretical formulation, but also the lack of reliable data to test the large amount of existing empirical formulae. Moreover, several applications have demonstrated the poor precision in calculation of sediment transport capacity of the most of these formulations (Martin 2003) and some of them have observed that existing formulations give results one or two order of magnitude by the real sediment transport capacity (Ancey et al. 2006; Bravo-Espinosa, Osterkamp, and Lopes 2003). Bravo-Espinosa, Osterkamp, and Lopes (2003) verified different empirical formulation applied to field data: Bagnold, Einstein-Brown, Kalinske, Meyer-Peter and Müller, Parker, Schocklitsch, and Yalin. The authors found that not all the empirical formulations can predict the bedload transport with the same precision, and some formulations are better in agreement with field data in some specific conditions of flow, but less in other. In authors opinion, the best formula, because of its good agreement in different flow conditions, is the one proposed by Schocklitsch. This is due to the adaptability of this method, since it is expressed by a general formulation to apply to local conditions by modifying the parameters:

$$q_b = c_s i_b^{\beta} \left(q - q_{cr}\right) \tag{3.11}$$

In eq. (3.11) c_s is a coefficient related with the sediments; i_b is the slope of the bed; β is an empirical exponent; q is the water discharge per unit of width, and q_{cr} is the value of water discharge for which the sediments begin to move. The Schocklitsch formula is referable to the du Boys' theory, that is based on a purely Colombian assumption.

Among the empirical methods cited above, only the methods which will be used as comparison to the theoretical considerations are reported.

Parker's method (Parker 1990)

The Parker's formula is largely used to calculate the bedload capacity. The advantage of this formulation is that it can be applied at different conditions and it is

validated with a large amount of field and laboratory data. The expression is:

$$\Phi = G(\xi_0)0.0021\theta^{1.5} \tag{3.12}$$

where $G(\xi_0)$ is a function of the Shields parameter θ (eq. 3.8); Φ is the dimensionless sediment transport rate defined by Einstein (Einstein 1950):

$$\Phi = \frac{q_b}{d\sqrt{g\Delta d}} \tag{3.13}$$

In eq. (3.13) q_b is the bedload capacity of the river; d is the characteristic diameter of sediments transported; $\Delta = (\rho_s - \rho)/\rho$, being ρ the density of water and ρ_s the density of sediments. In eq. (3.12) $G(\xi_0)$ assumes different values depending on ξ_0, which is:

$$\xi_0 = \frac{\theta}{0.0386} \tag{3.14}$$

The values for G can be evaluated with three different expressions:

$$\begin{cases} G = \xi_0^{14.2} & \text{if} \quad \xi_0 < 1 \\ G = e^{14.2(\xi_0-1)-9.28(\xi_0-1)^2} & \text{if} \quad 1 \leq \xi_0 < 1 \\ G = 5474\left(1 - \frac{0.853}{\xi_0}\right)^{4.5} & \text{if} \quad \xi_0 > 1.591 \end{cases} \tag{3.15}$$

.

Meyer-Peter and Müller's method (Meyer-Peter and Müller 1948)

The Meyer-Peter and Müller's formula (Meyer-Peter and Müller 1948) is one of the formulae most utilized for evaluating the sediment transport capacity. It was formulated by the researchers of the Hydraulic Laboratory of Zurich and, for this, it is also called E.T.H. (Eidgenössische Technische Hochschule) formula. This formula is valid only for rivers with bed slope smaller than 2%, while for higher bed slopes, the formula tents to underestimate the real sediment transport capacity. In addition, it is particularly recommended for gravel bed rivers.

The formula can be expressed in terms of the Einstein's (Φ) and Shields' (θ) parameters:

$$\Phi = 8\left(\theta' - \theta_c\right)^{1.5} \tag{3.16}$$

The formula only considers the grain roughness, being $\theta' = (u'_*)^2/g\Delta d$ a function of the shear velocity related to grains (see Section 2.1).

Experimental formulations often are expressed by using critical thresholds to the motion of particles, like the Meyer-Peter and Müller formulation. It means that only for certain conditions of flow ($\theta > \theta_c$) is possible to have sediment transport, for other conditions the transport of grains is not present. The authors proposed a value for the critical parameter of mobility: $\theta_c = 0.047$.

Van Rijn's method (Van Rijn 1984)

Van Rijn (1984) formulated an expression for the calculation of sediment transport capacity for particle size in the range 0.2 to 2 mm:

$$q_b = \alpha w_s d \frac{T^{2.1}}{D_*^{0.3}} \tag{3.17}$$

where w_s is the settling velocity of particles, $T = \left((u'_*)^2 - (u_{*,c})^2\right)/(u_{*,c})^2$, related only with the grain shear, is called by van Rijn *flow stage parameter*; $D_* = d\left(d\Delta/\nu^2\right)^{1/3}$ is the *reduced diameter of particles*.

Also the parameter α is a function of the same parameter D_*:

$$\begin{cases} \alpha = \dfrac{0.6}{D_*} & \text{for} \quad D_* < 10 \\ \alpha = 0.06 & \text{for} \quad D_* \geq 10 \end{cases} \tag{3.18}$$

3.1.3 The suspended load

A large number of investigations have tried to find a single equation to describe the total transport, even if several authors believe that this is basically impossible, since movement in suspension follows principles which are entirely different from those which govern bedload transport (Einstein 1950; Hu and Guo 2010). Several authors affirm (Nikora and Goring 2002) that there are too many theories and a few experimental validation on suspended load. Nowadays, with better methods of investigation, especially images analysis (ADV or PIV), several new empirical approaches on suspended load are led.

The most common method to approach the suspended sediment transport is

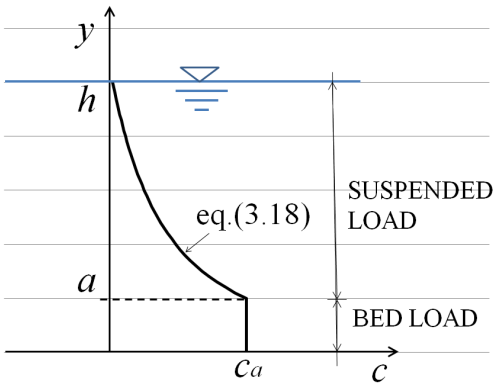

Figure 3.4: Distribution of the concentration of suspended particles according to Rouse formulation (eq. 3.19).

based on the integration of the advection/diffusion equation of suspended load in steady uniform flow conditions (Fang and Wang 2000; Lane and Kalinske 1941; Rouse 1937; Van Rijn 2007; Wu, Rodi, and Wenka 2000). Several expressions for evaluating the concentration c of the suspended sediments have been published. Among them, the Rouse's formulation:

$$c = c_a \left(\frac{h-y}{y} \frac{a}{h-a} \right)^Z \tag{3.19}$$

In eq. (3.19), c_a is the initial concentration at the level a (Figure 3.19); Z is a function of the ratio between the settling velocity, w_s of particles and the shear velocity, u_*:

$$Z = \frac{w_s}{\beta \kappa u_*} \tag{3.20}$$

where β should be larger that 1 ($\beta > 1$) and $\kappa = 0.41$ is the von Karman constant. For the evaluation of c_a, there are several expression in literature; the formula proposed by Einstein (Einstein 1950) is:

$$c_a = \frac{1}{11.6} \frac{q_b}{a u_*} \tag{3.21}$$

where q_b is the bed load transport capacity calculated with Einstein's theory (Einstein 1950). In this case, the value of a can be evaluated as a function of water depth or of the height of possible dunes. Also Van Rijn (Van Rijn 1984; Van Rijn

et al. 1993) proposed a method for calculating c_a:

$$\begin{cases} c_a = 0.015\,(1 - p_{clay})\, f_{silt} \dfrac{d_{50}}{a} \dfrac{T^{1.5}}{D_*^{0.3}} \\ \text{with} \quad c_a \leq 0.05 \quad \text{(maximum value)} \end{cases} \tag{3.22}$$

In eq. (3.22) $D_* = d_{50}\,(g\Delta/\nu^2)^{1/3}$ is the reduced particle diameter;

$$T = \frac{(u_*)'^2 - (u_{*,cr})^2}{(u_{*,cr})'^2}$$

is called by van Rijn *flow stage parameter*; $f_{silt} = d_{sand}/d_{50}$ is the silt factor, and $f_{silt} = 1$ for $d_{50} > d_{sand} = 62\ \mu\mathrm{m}$; a is a reference level in $[\mathrm{m}]$, and a is at least $0.01\ \mathrm{m}$, whereas its maximum value is equal to half of bed roughness value (typically the height of bed forms).

The suspended load discharge q_{ss} can be defined as:

$$q_{ss} = \int_a^h cu dz \tag{3.23}$$

where a is the thickness of layer interested by bedload transport; h is the water depth; c is the concentration of sediment in suspension along the vertical direction z; u is the flow velocity in x-direction. By the integration in (3.23), several authors proposed their formulation; among them Van Rijn (2007) obtained the next formula:

$$q_{ss} = 0.012 u d_{50} \left[(\theta - \theta_c)^2\right]^{2.4} D_*^{-0.6} \tag{3.24}$$

where q_{ss} is the suspended load discharge; θ is the Shields' parameter of mobility, and θ_c the parameter for the incipient motion.

The Rouse's profile is used by many authors (e.g.: Van Rijn (2007)) to build advection-diffusion models for mixing. Recent publications, however, have agreed in saying that turbulence and sediment bursting events are closely coupled but not identical, as assumed instead in some studies (Cao, Zhang, and Xi (1996) and references herein). This suggests that in theoretical considerations, the analysis of turbulent events cannot be a substitute for analysis of sediment events. Coleman (1970) showed that the sediment diffusivity in steady flow is larger (up to a factor

of 5) than the fluid momentum diffusivity and increases for increasing values of w_s/u_*.

3.2 Einstein's approach on sediment transport

Einstein's approach (Einstein 1950) is one of the few rational approaches on sediment transport. His theory allows the determination of bedload transport with a reasonable approximation, notwithstanding the formulation has some critical points that will be illustrated in the following.

In order to evaluate the bedload transport, Einstein considered a predetermined part of the bed area of a flume and marked the contained particles by coloring them (Figure 3.5). After the beginning of the motion, all marked particles were gradually eroded and replaced by others of the same type, in a certain time T_p. After the experiments, Einstein affirmed that:

1. the probability of a sediment particle to be eroded by the flow from the bed surface depends on the particle size, shape, and weight and on the flow pattern near the bed, but not on its previous history;
2. the motion of bed particles by saltation as described by Bagnold (1936) may be neglected in water, as proved by Kalinske (1942). It means that: (i) the impact of a particle on the bed surface in water does not influence the movement of the hit particles; (ii) the length of bed forms does not influence the length of the average distance traveled by the particles;
3. the particle moves if the instantaneous lift force overcomes the particle submerged weight;
4. once in motion, the probability for the particle to be redeposited is equal in all the points of the bed, if the local velocity is not large enough to remove the particle again;
5. the average distance traveled by any particle is constant and is independent of the flow condition. For the sediment grain of average sphericity this distance may be assumed to be 100 grain-diameters.

Following these hypotheses, Einstein obtained his formulation for sediment transport capacity. Firstly, he considered a channel, in steady uniform flow conditions, which was supposed to be sufficiently large to consider the flow as onedi-

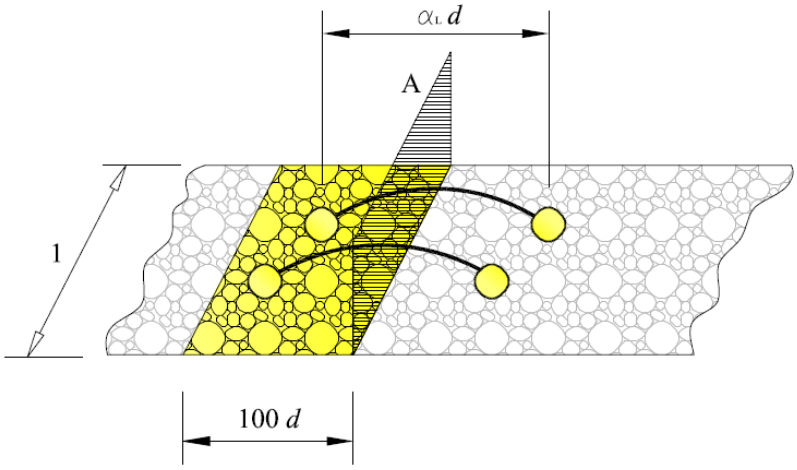

Figure 3.5: A scheme of the experiments carried out by Einstein (1950). In the figure, the marked particles are represented. The particles move through the section A, depositing after a displacement $\alpha_L d$ long.

rectional. The bedload can be determined in a base region with an area 100 grain-diameters long, composed by uniform material with constant grain size. In this condition, the characteristic diameter of grains, for calculating the bed roughness, is the d_{65}. This value is used to evaluate the friction factor:

$$\frac{\overline{u}}{u'_*} = 5.75 \log \left(3.67 \frac{R'_h \delta'}{d_{65}} \right) \tag{3.25}$$

In eq. (3.25) $\overline{u}$ is the time average of the velocity u; u_* is the shear velocity, while the u'_* is the shear velocity with respect to the grain (see Section 2.1); R'_h is the hydraulic radius with respect to the grain; and

$$\delta' = \frac{11.6\nu}{u'_*} \tag{3.26}$$

is the thickness of the laminar sublayer.

A grain can move if the lift force $\mathbf{L}$ is larger than the submerged weight, $\mathbf{W} - \mathbf{B}$ (see Section 3.1.1 and Shields, Ott, and Van Uchelen (1936)):

$$\mathbf{L} \geq \mathbf{W} - \mathbf{B} = g\left(\rho_s - \rho\right) \alpha_3 d^3 \tag{3.27}$$

where: ρ_s is the density of grains; ρ is the density of water; $\alpha_3 d^3$ is the average volume of a grain. $\mathbf{L}$ is dependent on the turbulence in the point, that is $\mathbf{L}$ is a random function of the time. By defining $L = p_L \alpha_2 d^2$, Einstein evaluated the average lift pressure $\overline{p_L}$ as:

$$\overline{p_L} = 0.178\rho\frac{u^2}{2} \tag{3.28}$$

where the velocity u must be calculated at a distance $0.35d_{35}$ from the bed. The pressure fluctuations p'_L due to turbulence ($p_L = \overline{p_L} + p'_L$) follow the normal distribution, and the standard deviation is equal to 0.364. The experiments used by Einstein to validate the assumptions are not reported in the paper (Einstein 1950).

The bedload rate q_b per unit width is the volume of particles crossing a reference section in an unit time (Figure 3.5). Each particle which crosses the area can be deposited anywhere in a distance between 0 and $100d$, which is the average displacement, or, more generally, from 0 to $\alpha_L d$ downstream the section. Hence, the total number of particles deposited per unit time in the unit of bed area is:

$$\frac{q_b}{\alpha_L d \alpha_3 d^3} \tag{3.29}$$

where $\alpha_3 d^3$ is the average volume of the single grain.

The rate of the particles eroded from the bed per unit of time is proportional to the number of particles exposed at the bed surface per unit of area and to the probability p_s of such a particle to be eroded during a second:

$$\frac{p_s}{\alpha_2 d^2} \tag{3.30}$$

Einstein changed p_s, which is the probability of detachment per second, that is equal to the number of detachments per second, with p, the absolute probability calculated in a time T_p, termed *exchange time*. So the number of particles eroded per unit area and time is:

$$\frac{p}{\alpha_2 d^2 T_p} \tag{3.31}$$

The definition of *probability during a second* which Einstein used is one of the less clear points of the theory, since the probability per second is a rather questionable

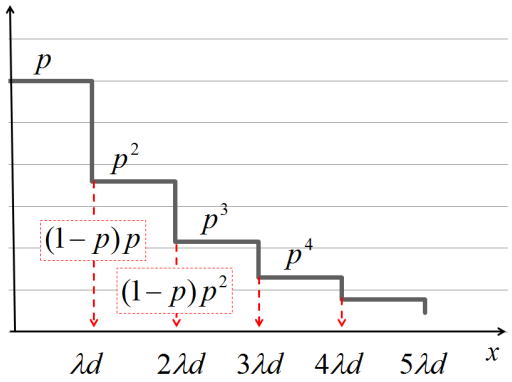

Figure 3.6: Scheme of the probability of deposition of particles for Einstein's theory.

concept.

Einstein supposed that the *exchange time* T_p may be another characteristic constant of the particles, so he assumed that this time is proportional to the time necessary for a particle to settle through a distance equal to its own size:

$$T_p = \alpha_t \frac{d}{w_s} = \alpha_t \sqrt{\frac{d}{g\Delta}} \tag{3.32}$$

where w_s is the settling velocity of a particle and $\Delta = (\rho_s - \rho)/\rho$. The number of particles eroded per unit area and time (eqs. (3.31) and (3.32)) is:

$$\frac{p}{\alpha_2 \alpha_t d^2} \sqrt{\frac{g\Delta}{d}} \tag{3.33}$$

that is equal to the number of particles crossing the section and which is deposited downstream (eq. 3.29):

$$\frac{q_b}{\alpha_L \alpha_3 d^4} = \frac{p}{\alpha_2 \alpha_t d^2} \sqrt{\frac{g\Delta}{d}} \tag{3.34}$$

Einstein defined the probability p as the fraction of the total time during which at any spot the local flow conditions cause a sufficiently large lift on the particle to remove it. Hence p can be considered also as a fraction of the bed on which at any time the lift on a particle is sufficient to cause motion.

By using this definition, the average distance $\alpha_L d$ traveled by particles can be expressed using the same probability: if p particles are traveling after have covered a distance λd, $p(1-p)$ of these particles are deposited after covering $2\lambda d$, but p^2 particles continue their travels. Of these particles, $p^2(1-p)$ particles are deposited after $3\lambda d$, and so on (Figure 3.6). Hence the total (averaged) distance traveled is:

$$\alpha_L d = \sum_{n=0}^{\infty}(1-p)p^n(n+1)\lambda d = \frac{\lambda d}{1-p} \tag{3.35}$$

By substituting eq. (3.35) into eq. (3.34):

$$\frac{q_b(1-p)}{\alpha_3 \lambda d^4} = \frac{p}{\alpha_2 \alpha_t d^2}\sqrt{\frac{g\Delta}{d}} \tag{3.36}$$

$$\frac{p}{1-p} = \frac{\alpha_2 \alpha_t}{\alpha_3 \lambda}\frac{q_b}{\sqrt{g\Delta d^3}}$$

$$\frac{p}{1-p} = A_* \Phi \tag{3.37}$$

where Φ is a dimensionless parameter representing the sediment transport rate.

The only parameter which has not been yet specified is the probability p. As already said, this probability depends on the probability of the lift force to be larger than the weight of the particle (eq. 3.27). The submerged weight of a particle is:

$$\mathbf{W} - \mathbf{B} = g(\rho_s - \rho)\alpha_3 d^3 \tag{3.38}$$

and the lift force:

$$\mathbf{L} = C_L \rho \frac{u^2}{2}\alpha_2 d^2 = \overline{L}(1+\eta) \tag{3.39}$$

where $\overline{L}$ is the averaged lift, while $\overline{L}\eta$ is the fluctuating part. The particle starts to move if the following ratio, from eq. (3.27), is smaller than 1:

$$\frac{g(\rho_s - \rho)\alpha_3 d^3}{\overline{L}(1+\eta)} < 1 \tag{3.40}$$

Einstein assumed that the value of η may be positive or negative, but in both cases the lift force is positive (Figure 3.7). This assumption is one of the weakest points in Einstein's theory. The η_{lim}, corresponding to the incipient motion, can

be evaluated by imposing the inequality in eq. (3.40), from which:

$$|(1+\eta)| > \frac{g(\rho_s-\rho)\alpha_3 d^3}{\overline{L}} = \frac{g(\rho_s-\rho)\alpha_3 d^3}{c_L \rho \frac{\overline{u}}{2}\alpha_2 d^2} \tag{3.41}$$

Einstein assumed that the velocity in $0.35d_{35}$ is proportional to d, then $\overline{u} \sim u_*$ ($\overline{u} = Ku_*$). Hence eq. (3.41) becomes:

$$|(1+\eta)| > \frac{2\alpha_3}{C_L \alpha_2 K}\frac{g\Delta d}{u_*^2} = c_\Psi \Psi \tag{3.42}$$

c_Ψ represents the shape of the particle, whereas $\Psi = g\Delta d/u_*^2$ is the *Einstein flow intensity parameter*, that is the inverse of the Shields parameter θ (Section 3.1.1).

Einstein solved the inequality in eq. (3.41) by squaring and dividing for the standard deviation η_0 of the fluctuating function η (Figure 3.7):

$$\left(\frac{1}{\eta_0} + \eta_{*,lim}\right)^2 = (B_*\Psi)^2$$

or:

$$\eta_{*,lim} = \pm B_*\Psi - \frac{1}{\eta_0} \tag{3.43}$$

where $\eta_{*,lim} = \eta_{lim}/\eta_0$; B_*, which is a constant in Einstein's approach, is defined (Hayashi and Ozaki 1980; Yalin 1977) as the parameter related to the critical condition of motion, given that it has a similar physical meaning as the dimensionless critical Shields parameter θ_{cr}. By assuming a normal distribution for η_*, we have:

$$p = 1 - \frac{1}{\sqrt{\pi}}\int_{-B_*\Psi-1/\eta_0}^{B_*\Psi-1/\eta_0} e^{-t^2}dt \tag{3.44}$$

and finally, by combination with eq. (3.37):

$$p = 1 - \frac{1}{\sqrt{\pi}}\int_{-B_*\Psi-1/\eta_0}^{B_*\Psi-1/\eta_0} e^{-t^2}dt = \frac{A_*\Phi}{1-A_*\Phi} \tag{3.45}$$

Einstein established experimentally the following constant values:

$$1/\eta_0 = 2.0 \quad A_* = 27.0 \quad B_* = 0.156 \tag{3.46}$$

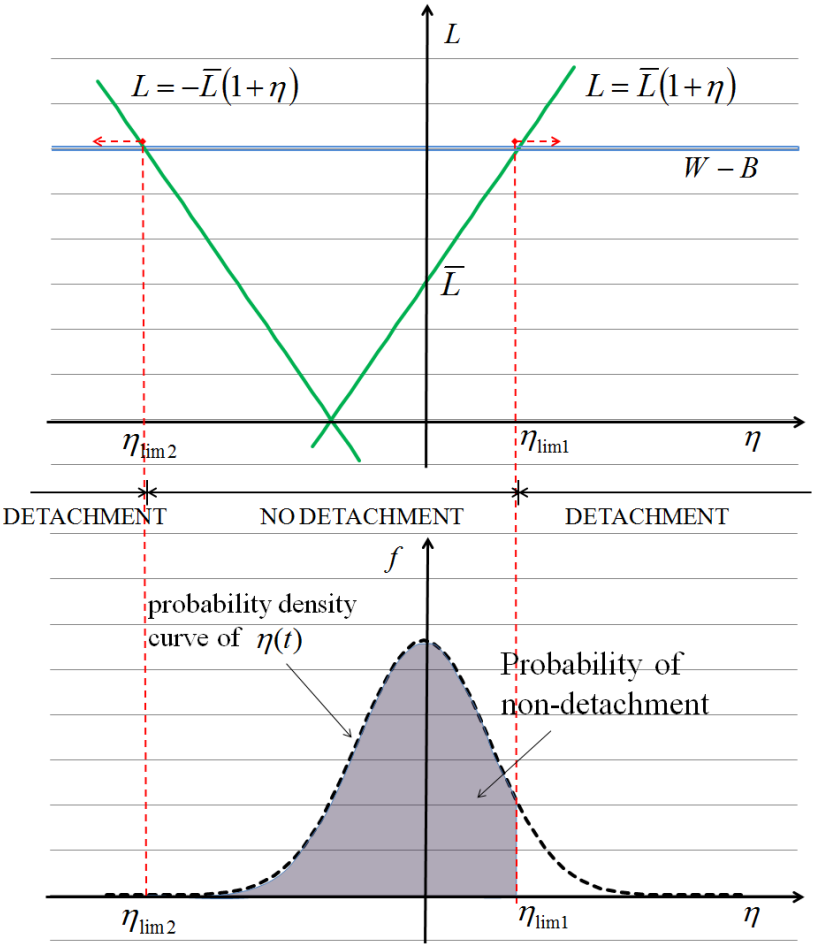

Figure 3.7: Method for the evaluation of η_{lim}, limits of the integral of the distribution probability of detachment of a particle, according to Einstein Einstein (1950).

Figure 3.8 shows the Einstein's formula (eq. 3.45) compared with the empirical Meyer Peter and Müller formula (eq. 3.16) and with a large number of experimental data. The Einstein's formula is in good agreement with the experimental data, but not for the highest values of sediment transport. In fact, by comparing the eq. (3.45) and the eq. (3.16), the Meyer Peter and Müller formula fits the data better than Einstein's formula.

For conditions of high mobility of sediments, the Shields parameter of mobility tents to infinity, $\theta \rightarrow 0$, hence the Einstein flow intensity parameter tents to zero, $\Psi \rightarrow 0$. In this condition the integral in eq. (3.45) can be expanded as a series (Yalin 1977). It is possible to show, for high values of sediment transport, that the eq. (3.45) varies following a hyperbolic law:

$$\Psi\Phi = K \tag{3.47}$$

in which K is a constant equal to 7.84. This value (Figure 3.8) seems to underestimate the real sediment transport capacity.

3.3 Revision of Einstein's theory by Yalin

Several authors have revised the Einstein's theory in order to obtain a more convincing approach, getting over the weakest points of Einstein's formulation. For example, Ancey et al. (2006) have indicated that there is a discrepancy in the statistical properties of the key variables, such as the solid discharge and the number of moving particles, between their experimental data and Einstein theory. Hayashi and Ozaki (1980) have tried to explain theoretically the Einstein's definition of the limits of integration and the definition of the average length of jump, but Yalin (1977) proposed a complete and systematic revision of the Einstein's theory.

Yalin (1977) explained the Einstein theory by considering a section A at the final of a reach of a channel nL_p long (Figure 3.9) and by defining how many grains cross the section during the time interval T_p. In Einstein's theory, p is equivalent to p_n, defined by Yalin as the probability of each grain to detach from the bottom at least n times in a period T_p, where T_p is sufficiently larger than the duration of the mean bounce; in addition, p_n is also the probability of a particle to

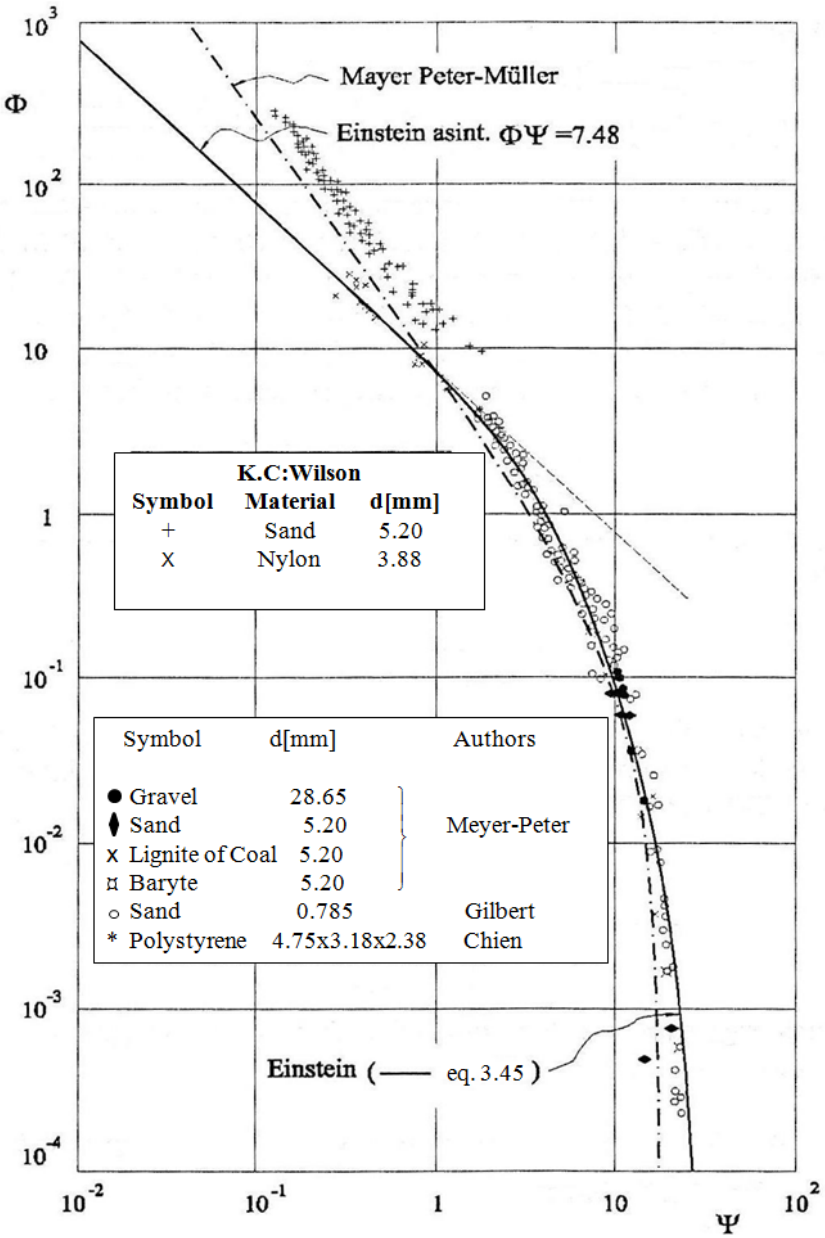

Figure 3.8: The Einstein formula (eq. 3.45) compared with experimental analysis and the Meyer Peter and Müller formula (eq. 3.16) (taken by Armanini (1999)).

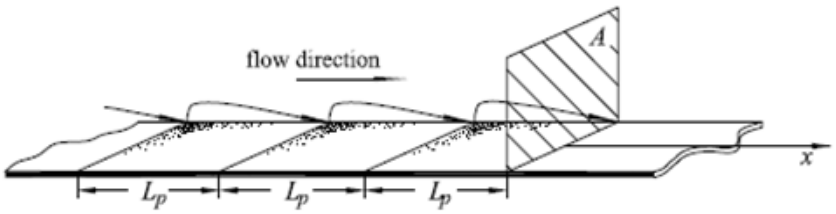

Figure 3.9: A reach of a channel with the division proposed by Yalin (1977)

cover a distance at least of nL_p. The total number of particles crossing the section A is the sum of those which have been detached at least n times and thus which will be displaced by a distance not less than nL_p:

$$\sum_{n=1}^{\infty} p_n \frac{L_p}{T_p \alpha_2 d^2} \tag{3.48}$$

By multiplying the expression in eq. (3.48) for the volume of a single grain, $V = \alpha_3 d^3$, we have the total volume of the grains passing through A per unit time, which is nothing else but the specific transport rate q_b (since the width of the section A is unitary). Thus:

$$\begin{aligned} q_b &= \alpha_3 d^3 \sum_{n=1}^{\infty} p_n \frac{L_p}{T_p \alpha_2 d^2} \\ &= \frac{\alpha_3}{\alpha_2} \frac{L_p}{T_p} d \sum_{n=1}^{\infty} p_n \end{aligned} \tag{3.49}$$

Einstein assumed L_p proportional to the grain size d:

$$L_p = \alpha_L d \tag{3.50}$$

and the period T_p (the *exchange time*) dependent only on the particle settling velocity and on its size (eq. 3.32), as explained in the previous section (Section 3.2):

$$T_p = \alpha_t \frac{d}{w_s} \tag{3.51}$$

where α_L and α_t are regarded as constants. By using for w_s a general relation:

$$w_s = \alpha_w \sqrt{g\Delta d} \tag{3.52}$$

then:

$$T_p = \alpha_t \frac{d}{\alpha_w \sqrt{g\Delta d}} \tag{3.53}$$

By substituting the definitions (3.50) and (3.53) into eq. (3.49), then:

$$\begin{aligned} q_b &= \frac{\alpha_3}{\alpha_2} \frac{\alpha_L d}{\alpha_t \dfrac{d}{\alpha_w \sqrt{g\Delta d}}} d \sum_{n=1}^{\infty} p_n \\ &= \frac{\alpha_3 \alpha_L}{\alpha_2 \alpha_t} \alpha_w d \sqrt{g\Delta d} \sum_{n=1}^{\infty} p_n \end{aligned} \tag{3.54}$$

It remains to evaluate the sum of the probabilities p_n on the right-hand side of eq. (3.54). Einstein, with his expression, considered each jump of a particle independent from the other particles. So he was able to write:

$$\sum_{n=1}^{\infty} p_n = \sum_{n=1}^{\infty} p_1^n \tag{3.55}$$

where p_1 is the probability of the occurrence of at least one detachment during T_p. Since $p_1 < 1$ is valid, the series at the right-hand side converges to the following limit:

$$\sum_{n=1}^{\infty} p_1^n = \frac{p_1}{1 - p_1} \tag{3.56}$$

By substituting eq. (3.56) into eq. (3.54):

$$\frac{q_b}{d\sqrt{g\Delta d}} = \frac{1}{A_*} \frac{p_1}{1 - p_1} \tag{3.57}$$

where

$$A_* = \frac{\alpha_2 \alpha_t}{\alpha_3 \alpha_L \alpha_w} \tag{3.58}$$

For the dimensionless term at left-hand side of the eq. (3.57), Einstein adopted the symbol Φ, which was called by Yalin *Einstein flow intensity parameter*, that

is:

$$\Phi = \frac{q_b}{d\sqrt{g\Delta d}} \tag{3.59}$$

and

$$\Phi = \frac{1}{A_*}\frac{p_1}{1-p_1} \tag{3.60}$$

and thus:

$$p_1 = \frac{A_*\Phi}{1+A_*\Phi} \tag{3.61}$$

In order to evaluate the probability function of "at least one detachment", we can consider that a particle can be detached only if the punctual lift force is larger than the submerged weight (as in the Einstein's approach):

$$p_1 = f\left(\frac{\mathbf{L}}{\mathbf{W}-\mathbf{B}}\right) = f\left(\frac{C_L\alpha_1 d^2\rho u^2}{g\left(\rho_s-\rho\right)\alpha_3 d^3}\right) \tag{3.62}$$

According to the Shields theory on the incipient motion of a particle, the eq. (3.62) is reduced to:

$$p_1 = f\left(\theta\right) = f\left(\frac{1}{\Psi}\right) \tag{3.63}$$

where θ is the Shields parameter of mobility, that is the inverse of the *Einstein flow intensity parameter*, $\Psi = g\Delta d/u_*^2$.

The lift force $\mathbf{L}$ is a function of time and assumes random values, given that it is a function of the turbulence structure of the flow. It can be divided in a time average component, $\overline{\mathbf{L}}$, and on a fluctuating component, $\mathbf{L}'$:

$$\mathbf{L} = \overline{\mathbf{L}} + \mathbf{L}'$$

and

$$r = \frac{\mathbf{L}}{\overline{\mathbf{L}}} \tag{3.64}$$

where r defined by Yalin is equal to $1+\eta$ by Einstein (eq. 3.39). Einstein assumed that the dimensionless lift force $r = 1+\eta$ should have a Gaussian distribution of probability:

$$f\left(r\right) = \frac{1}{\sigma\sqrt{2\pi}}\exp^{-\frac{(r-1)^2}{2\sigma^2}} \tag{3.65}$$

where σ is the variance of the distribution.

We can define a threshold for the detachment of the particle by the definition of r (eq. 3.64), by knowing that the detachment is possible only if the lift force is at least equal to the submerged weight. Hence, the threshold a is:

$$a = \frac{\mathbf{W} - \mathbf{B}}{\overline{\mathbf{L}}} \tag{3.66}$$

and with respect to r, the detachment is possible only if $r > a$. Accordingly, the "non-detachment" probability is:

$$P_0 = 1 - p_1 = \int_{-\infty}^{a-1} f\left(r\right) dr \tag{3.67}$$

From eq. (3.67), the detachment probability is:

$$p_1 = 1 - \frac{1}{\sigma\sqrt{2\pi}} \int_{-\infty}^{a-1} \exp^{-\frac{(r-1)^2}{2\sigma^2}} dr \tag{3.68}$$

Furthermore, the above integral was not used as it stands, but as:

$$p_1 = 1 - \frac{1}{\sigma\sqrt{2\pi}} \int_{-(a+1)}^{a-1} \exp^{-\frac{(r-1)^2}{2\sigma^2}} dr \tag{3.69}$$

The limits of the integral in eq. (3.69) mean that the detachment is possible if $|\mathbf{L}| > \mathbf{W} - \mathbf{B}$, instead of simply $\mathbf{L} > \mathbf{W} - \mathbf{B}$. By using the considerations above and by changing the variable, the eq. (3.69) becomes:

$$p_1 = 1 - \frac{1}{\sqrt{\pi}} \int_{-\frac{(a+1)}{\sqrt{2}\sigma}}^{\frac{(a-1)}{\sqrt{2}\sigma}} e^{-\xi^2} d\xi \tag{3.70}$$

where $\xi = (r-1) \,/\, \left(\sqrt{2}\sigma\right)$.

By considering the limits of the integral:

$$-\frac{(a+1)}{\sqrt{2}\sigma} = -\left(\frac{\Psi}{\sqrt{2}\sigma} + \frac{1}{\sqrt{2}}\right)\alpha_\Psi = -\left(B_*\Psi + \frac{1}{\eta_0}\right) \tag{3.71}$$

$$\frac{(a-1)}{\sqrt{2}\sigma} = \left(\frac{\Psi}{\sqrt{2}\sigma} - \frac{1}{\sqrt{2}}\right)\alpha_\Psi = B_*\Psi - \frac{1}{\eta_0} \tag{3.72}$$

Yalin recalibrated the Einstein's parameters (eq. 3.46) in:

$$1/\eta_0 = 2.0 \quad A_* = 43.50 \quad B_* = 0.143 \tag{3.73}$$

And finally the Einstein's final expression was obtained through the Yalin's analysis:

$$\frac{A_*\Phi}{1+A_*\Phi} = 1 - \frac{1}{\sqrt{\pi}} \int_{-\left(B_*\Psi+\frac{1}{\eta_0}\right)}^{B_*\Psi-\frac{1}{\eta_0}} e^{-\xi^2} d\xi \tag{3.74}$$

or better:

$$\Phi = \frac{1}{A_*} \left(\frac{1}{\frac{1}{\sqrt{\pi}} \int_{-\left(B_*\Psi+\frac{1}{\eta_0}\right)}^{B_*\Psi-\frac{1}{\eta_0}} e^{-\xi^2} d\xi} - 1 \right) \tag{3.75}$$

It is important to remind that Einstein did not consider the drag due to bed forms, but only the roughness of grains.

3.4 The Yalin's formulation

Starting from the Einstein's theory, Yalin (1977) formulated a different rational approach which overcame the weakness points of the Einstein's theory. The points examined by Yalin are the following:

- in Einstein's theory, the dimensionless length of the averaged jump is treated as a constant quantity ($\alpha_L = L_p/d = 100$). Yalin asserted (also supported by other authors, among them Hayashi and Ozaki (1980)) that neither experimental evidence nor theoretical explanation support the validity of this statement. On the contrary, he reported some measurements which indicate that the dimensionless jump length varies as a function of Ψ^{-1}. In particular, for Ψ sufficiently small, α_L appears to increase linearly with Ψ^{-1};

- with regard to the period T_p, the author affirmed that it must be proportional to the shear velocity u_*, and not only to the settling velocity w_s. Therefore, he assumed that T_p must be measured in terms of the averaged period of turbulent fluctuation, t_*. He obtained $t_* = \alpha_* e_s/u_*$, where e_s is the height

of the sand roughness and α_* is a function of the shear Reynolds number, $Re_* = u_* d/\nu$. Yalin defined:

$$T_p = N t_* \tag{3.76}$$

where N is the number of periods of fluid fluctuation which form T_p. By substituting the definition of t_*:

$$T_p = N \alpha_*(Re_*) \frac{d}{u_*} \tag{3.77}$$

Hence, the Einstein's proportional factor α_t is not a constant but a certain function of shear Reynolds number, $\alpha_*(Re_*)$;

- as a consequence, the parameters A_*, B_* and η_0, which Einstein defined as:

$$A_* = \frac{\alpha_2 \alpha_t}{\alpha_3 \alpha_L \alpha_w}$$

and

$$-\frac{(a+1)}{\sqrt{2}\sigma} = -\left(\frac{\Psi}{\sqrt{2}\sigma} + \frac{1}{\sqrt{2}}\right)\alpha_\Psi = -\left(B_*\Psi + \frac{1}{\eta_0}\right)$$

cannot be constants, but they must be functions of the shear Reynolds number, of the mobility parameter and of the diameter of grains;

- the most important point introduced by Yalin regards the hypothesis on the expression for the probability adopted by Einstein. In particular the hypothesis:

$$\sum_{n=1}^{\infty} p_n = \sum_{n=1}^{\infty} p_1^n$$

is valid only if the probability p_n is referred to nT_p intervals, but in Einstein's idea p_n is the probability of (*only*) n detachments in the same interval T_p (as p_1 is referred to *only* one jump). Yalin solved the matter by considering that the probability for a particle of the occurrence of *at least* n jumps

during the time T_p can be expressed as:

$$p_n = \sum_{i=n}^{\infty} p_i$$

and hence:

$$\sum_{n=1}^{\infty} p_n = \sum_{n=1}^{\infty} \sum_{i=n}^{\infty} p_i = \sum_{n=1}^{\infty} n P_n.$$

where P_n is the probability of the occurrence of *only* n jumps in the period T_p. By assuming that the probability P_* of the occurrence of one detachment in one fluctuation is very small, while the number of fluctuations contained in the time T_p is very large, the probability P_n can be given by the Poisson formula:

$$P_n = \frac{\lambda^n}{n!} e^{-\lambda}$$

where

$$\lambda = N P_*$$

The final result is:

$$\sum_{n=1}^{\infty} p_n = N \int_{a-1}^{\infty} f(r') dr' \tag{3.78}$$

with

$$a = B_* \Psi \eta_0$$

Yalin obtained a new formulation for Einstein's theory, starting from the eq. (3.49), which is herein reported:

$$q_b = \frac{\alpha_3}{\alpha_2} \frac{L_p}{T_p} d \sum_{n=1}^{\infty} p_n \tag{3.79}$$

and the eqs. (3.77) and (3.78). By substituting, the author obtained:

$$A_{*1} \Phi = \frac{1}{\Psi^{3/2}} \int_{a-1}^{\infty} f(r') dr' \tag{3.80}$$

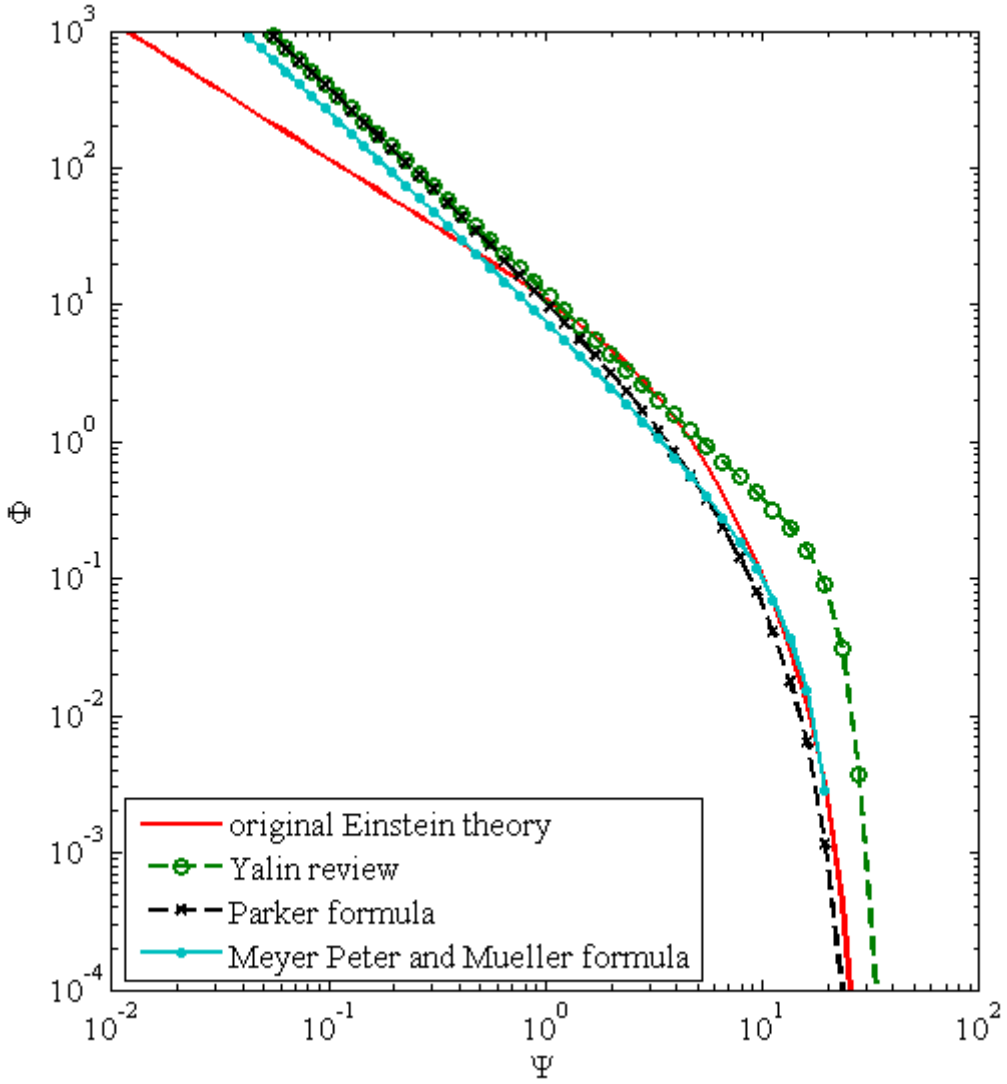

Figure 3.10: Comparison among Yalin's revision (eq. 3.83), Einstein's formula (eq. 3.75), Parker's empirical method (eq. 3.12) and Meyer Peter and Müller's formula (eq. 3.16).

where

$$A_{*1} = \frac{\alpha_1 \alpha_*}{\alpha_L} \tag{3.81}$$

Hence:

$$A_{*1}\Phi = \frac{1}{\Psi^{3/2}\sqrt{\pi}} \int_{B_*\Psi - 1/\eta_0}^{\infty} e^{-\xi^2} d\xi \tag{3.82}$$

which can also be expressed as

$$A_{*1}\Phi = \frac{1}{\Psi^{3/2}} \left(1 - \frac{1}{\sqrt{\pi}} \int_{-\infty}^{B_*\Psi - 1/\eta_0} e^{-\xi^2} d\xi \right) \tag{3.83}$$

Yalin evaluated also the values of the constants:

$$\eta_0 = 0.290 \quad A_{*1}^{-1} = 12.10 \quad B_* = 0.1667 \tag{3.84}$$

Figure 3.10 shows the comparison among Yalin's revision (eq. 3.83), Einstein's formula (eq. 3.75), Parker's empirical formula (eq. 3.12) and Meyer Peter and Müller's formula (eq. 3.16). From the Figure 3.10, for the highest values of sediment transport, Yalin's revision is in better agreement with respect to the Einstein's formula to the Parker and Meyer Peter and Müller formulas, but it is in worst agreement at the smallest values of sediment transport. The better agreement of the Yalin formulation at the highest values of sediment transport is due to the new definition of the characteristic velocity of the phenomenon. Einstein defined separately T_p (eqs. 3.51 and 3.53), the exchange time, and L_p (eq. 3.50), the average distance travel by a particle in a jump. In this way, the ratio L_p/T_p, that can be interpreted as a characteristic velocity for the sediment transport, results:

$$\frac{L_p}{T_p} = \frac{\alpha_L d}{\alpha_t \dfrac{d}{w_s}} \tag{3.85}$$

Hence:

$$\frac{L_p}{T_p} \sim w_s \tag{3.86}$$

For conditions of high mobility, it is not expected that the phenomenon "moves" only with the settling velocity of particles. It is more reasonable to assume that the

velocity scale of the phenomenon has to depend also on the turbulent fluctuations of the flow (Armanini 1999; Armanini, Cavedon, and Righetti 2010). Yalin, by defining the exchange time as a function of the fluid fluctuation (eq. 3.77), solved this inconsistency.

3.5 A first revision of the Einstein's theory

In Yalin's revision (Section 3.3), the probability of each particle to cross a vertical section (A in Figure 3.9) is expressed by a staircase function (eq. 3.35). This probability can be rendered more rational by revising the function as a monotonically decreasing probability function. From eqs. (3.49) and (3.55):

$$q_b = \frac{\alpha_3}{\alpha_2}\frac{L_p}{T_p} d \sum_{n=1}^{\infty} p_1^n \tag{3.87}$$

If we assume a continuous function for the probability, the sum has to be substituted by the integral (Figure 3.11):

$$\sum_{n=1}^{\infty} p_1^n = \int_0^{\infty} p_1^{\frac{x}{L_p}+\frac{1}{2}} d\left(\frac{x}{L_p}\right) = -\frac{p_1^{1/2}}{\ln(p_1)}$$

Hence:

$$\sum_{n=1}^{\infty} p_1^n = \frac{p_1^{1/2}}{\ln(1/p_1)} \tag{3.88}$$

and, by substituting the eq. (3.88) into eq. (3.87):

$$q_b = \frac{\alpha_3}{\alpha_2}\frac{L_p}{T_p} d \frac{p_1^{1/2}}{\ln(1/p_1)} \tag{3.89}$$

The Einstein's definitions of L_p and T_p leads to:

$$\frac{L_p}{T_p} = \frac{\alpha_L d}{\alpha_t \frac{d}{w_s}} = \frac{\alpha_L}{\alpha_t} w_s \tag{3.90}$$

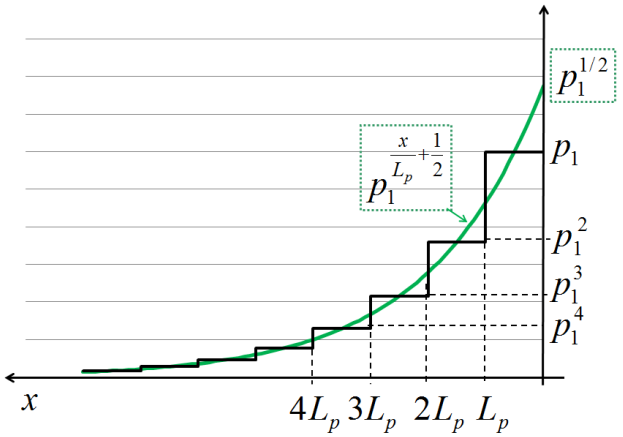

Figure 3.11: Extension of the Einstein's probability of crossing a vertical section in $x = 0$. The figure shows the staircase function by Einstein compared with the proposed continuous function.

Hence:

$$q_b = \frac{\alpha_3 \alpha_L \alpha_w}{\alpha_2 \alpha_t} d\sqrt{g\Delta d} \frac{p_1^{1/2}}{\ln(1/p_1)}$$

$$\Phi = \frac{q_b}{d\sqrt{g\Delta d}} = \frac{1}{A_*} \frac{p_1^{1/2}}{\ln(1/p_1)} \tag{3.91}$$

For the definition of the probability p_1 of detachment of each particle, we can use the same Gaussian distribution of Einstein, with the same limits of the integral. In this hypothesis p_1 is:

$$p_1 = 1 - \frac{1}{\sqrt{\pi}} \int_{\eta_{*,inf}}^{\eta_{*,sup}} e^{-t^2} dt \tag{3.92}$$

In conclusion, the extension of Einstein's probability function leads to the next set of equations:

$$\begin{cases} \Phi = \dfrac{q_b}{d\sqrt{g\Delta d}} = \dfrac{1}{A_*} \dfrac{p_1^{0.5}}{\ln(1/p_1)} \\ p_1 = 1 - \frac{1}{\sqrt{\pi}} \int_{\eta_{*,inf}}^{\eta_{*,sup}} e^{-t^2} dt \\ \eta_{*,inf} = -(B_* \Psi + 2) \\ \eta_{*,sup} = (B_* \Psi - 2) \end{cases} \tag{3.93}$$

In eqs. (3.93) p_1, $\eta_{*,inf}$ and $\eta_{*,sup}$ have the same definitions as in Einstein's theory,

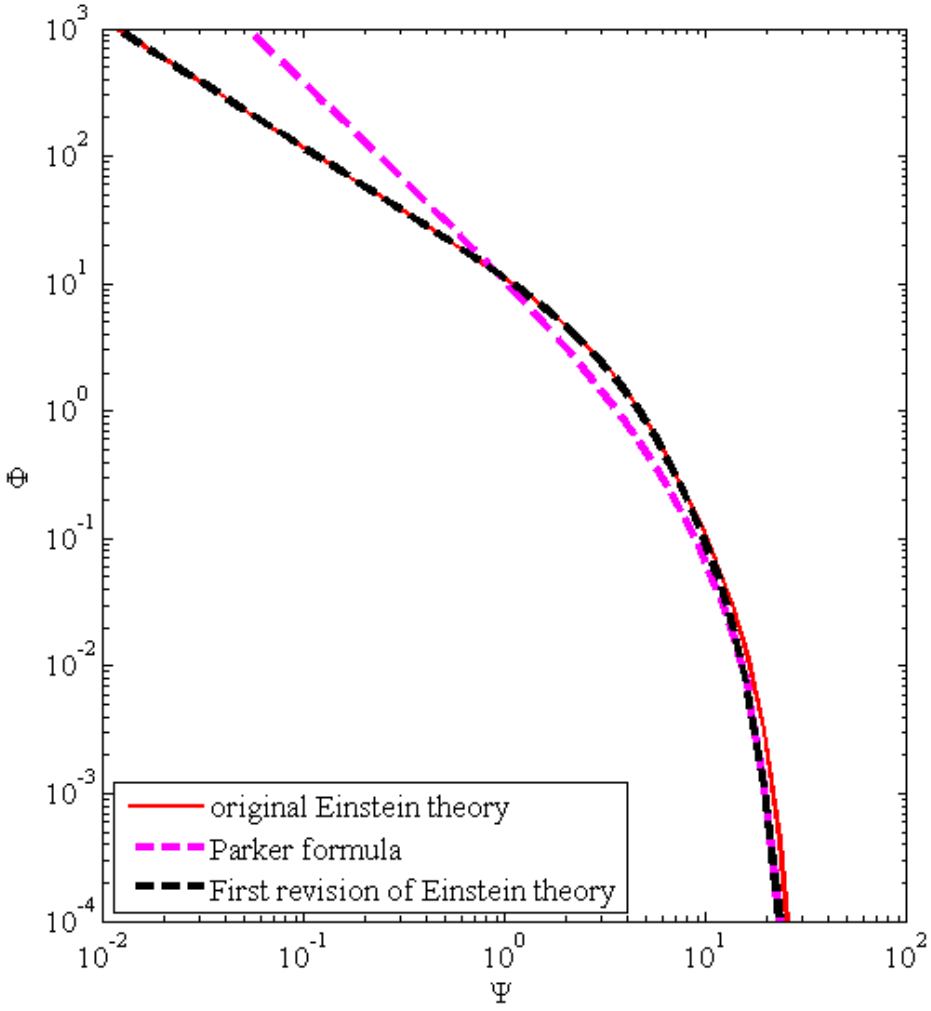

Figure 3.12: Results obtained with the first revision of Einstein theory (eq. 3.93) and comparison with Einstein original formula (eq. 3.75) and Parker formula (eq. 3.12)

but the empirical constants A_* and B_* might be recalibrated by comparing the expression in eq. (3.93) with other experimental data and with other formulations: Einstein's (eq. 3.75), Parker's (eq. 3.12) and Meyer-Peter and Müller's (eq. 3.16) formulas. Actually, this first adjustment is not sufficient to allow a better approximation to Parker or Meyer Peter and Müller formulas (Figure 3.12), because the slope of Einstein's curve for $\Psi \to 0$ does not change.

The Figure 3.12 shows the curve calculated by using the same parameters and the Einstein's limit of integration: $A_* = 27$, $\eta_{*,inf} = -(B_*\Psi + 2)$, $\eta_{*,sup} = (B_*\Psi - 2)$ and $B_* = 0.156$. The curve corresponding to the Einstein's original theory in Figure 3.12 is not fully visible because it is substantially coincident with the revisited formula.

3.6 The ballistic approach

The Einstein's theory is a milestone among the stochastic approaches on sediment transport capacity. Many authors (Ancey et al. 2006; Hayashi and Ozaki 1980; Yalin 1977) have tried to explain or revise Einstein's approach, by analyzing the hypotheses and the weakest points of the theory. The approach described in this section is inspired by Einstein's theory and the final formula is similar to Einstein's and Yalin's equations. In this formulation, however, the weakness points of Einstein theory are overcome.

The solid discharge is defined as the volume of particles crossing a vertical section. The infinitesimal sediment discharge dq_s is due to all the grains arriving from an infinitesimal element dx in an unit time, where dx is located at a distance x from a section A (Figure 3.13). Hence:

$$dq_s = u_s \alpha_2 d \frac{dx}{\alpha_2 d} P \tag{3.94}$$

where u_s is the normal component of the particle velocity the instant it crosses the section A (Figure 3.13); $\alpha_2 d$ is the averaged surface of particles (in an onedimensional point of view); dx is the infinitesimal element at the coordinate x; P represents the probability that the particle, detached by the lift force and leaving from dx, reaches the section A. In fact, not all the particles which leave dx cross

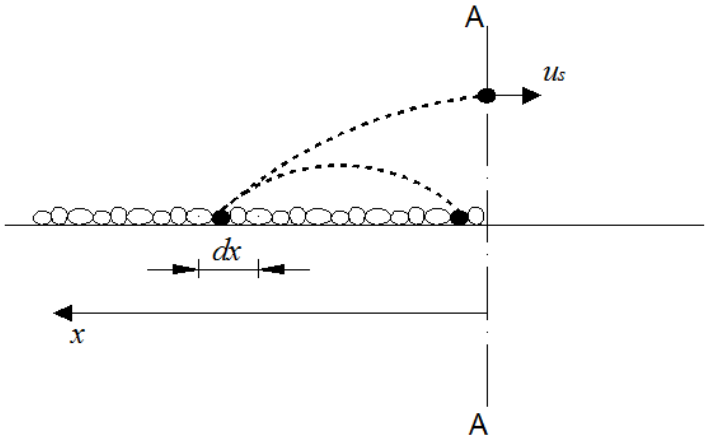

Figure 3.13: A particle crossing the section A of the channel. u_s is the normal component to the section of the particle velocity in the instant it crosses the section A.

the section, but only the part of particles which makes a jump longer than the distance between A and x. In mathematical terms, the particle crosses the section A only if $0 < x < \bar{x}$, where $\bar{x}$ is the jump length (Figure 3.14). In eq. (3.94), the ratio $dx/\alpha_2 d$ expresses the number of particles (onedimensionally) contained in the element dx. Eq. (3.94) can be simplified:

$$dq_s = u_s P dx \tag{3.95}$$

The distance covered by a particle in a jump can be expressed with the equation for the range of a projectile (Figure 3.14):

$$\bar{x} = \sin(2\alpha)\frac{u_0^2}{g} \tag{3.96}$$

where u_0 is the velocity of the particle at the beginning of motion, and:

$$\sin(2\alpha) = 2\frac{C_L}{C_D}$$

with C_L and C_D the lift and drag coefficients, at the instant of detachment.

Close to the wall, the initial velocity for the particle can be considered proportional to the shear velocity u_* (Einstein 1950; Shields, Ott, and Van Uchelen

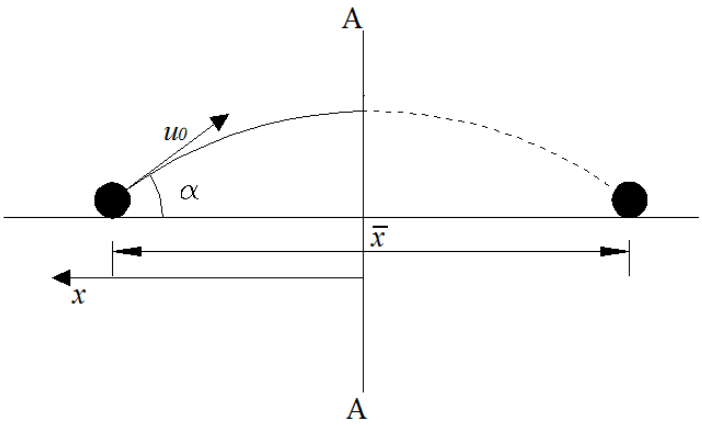

Figure 3.14: Detachment of a grain and the range it travels.

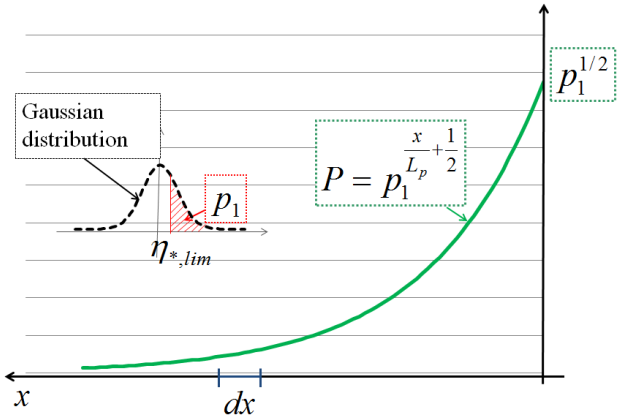

Figure 3.15: Schematic image of the distribution of probability which a particle has to reach the section A from the area dx, x distant from A.

1936; Van Rijn 1984): $u_0 = c_u u_*$; and hence the eq. (3.96) becomes:

$$\bar{x} = K\frac{u_*^2}{g} \tag{3.97}$$

with

$$K = 2\frac{C_L}{C_D}c_u^2 \tag{3.98}$$

The probability P is between 0 and 1 and can be defined by using the first Einstein's revision that we have proposed (eq. 3.88), by substituting the discrete

constant L_p (Figure 3.15) with the continuous variable $\bar{x}$:

$$P = p_1^{\frac{x}{\bar{x}}+\frac{1}{2}} \tag{3.99}$$

By substituting eq. (3.97) into eq. (3.99):

$$P = p_1^{\frac{xg}{Ku_*^2}+\frac{1}{2}} \tag{3.100}$$

In eq. (3.100), the function p_1 is the probability of each particle to be detached. Therefore, the probability $p_1^{1/2}$ is the maximum probability to cross the section A, and it is correspondent to the particle that stands in $x = 0$. By increasing the distance from the section A, the probability P decreases (Figure 3.15).

The probability of detachment p_1 can be calculated with the integral of the Gaussian distribution:

$$p_1 = \frac{1}{\sqrt{\pi}} \int_{\eta_{*,lim}}^{\infty} e^{-t^2} dt \tag{3.101}$$

This hypothesis is generally accepted, although several investigations show that it is not always verified (Hu and Guo 2010; Kuhnle and Southard 1988) and some authors prefer to use other probability distributions (Ancey et al. 2006; Yalin 1977).

The lower limit of the integral in eq. (3.101) expresses the condition of the incipient motion and can be determined as in Einstein's theory. Figure 3.16 shows the scheme for the evaluation of $\eta_{*,lim}$, by considering the Gaussian distribution of probability for $\eta(t)$.

The probability function p_1, written as in eq. (3.101), is independent of the position x of the particles. Hence, by substituting eq. (3.100) into eq. (3.95), it results:

$$dq_s = u_s p_1^{\frac{xg}{Ku_*^2}+\frac{1}{2}} dx \tag{3.102}$$

For calculating the total sediment transport, q_s, the differential equation in (3.102) must be integrated from 0 to ∞:

$$q_s = \int_0^{\infty} u_s p_1^{\frac{xg}{Ku_*^2}+\frac{1}{2}} dx$$

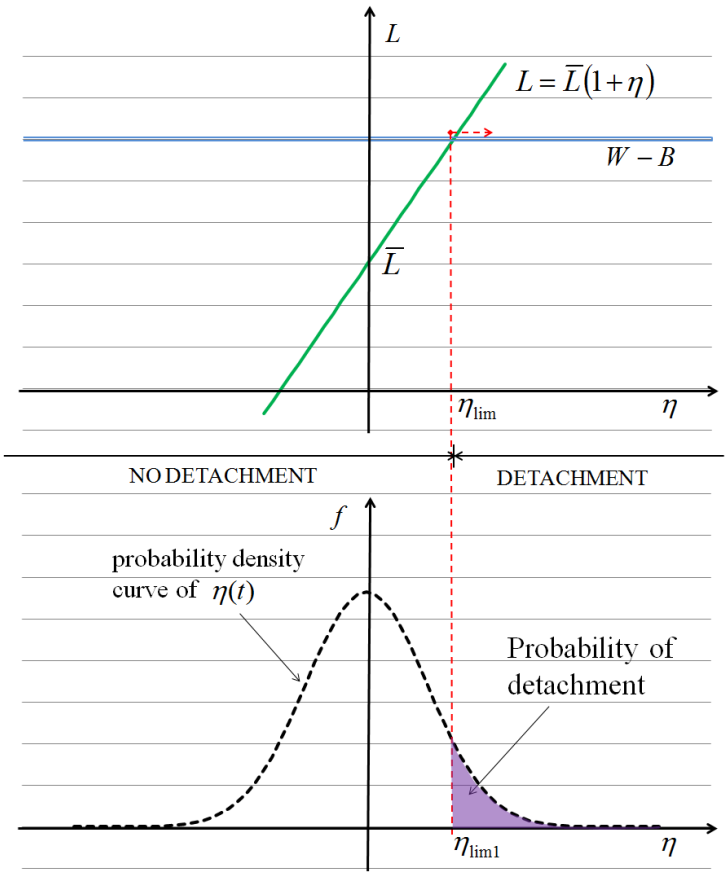

Figure 3.16: Method of evaluation of η_{lim}, which is referred to the minimum condition for the particle detachment.

and, by solving the above integral, we obtain:

$$q_s = u_s \frac{K u_*^2}{g} \frac{p_1^{1/2}}{\ln(1/p_1)} \tag{3.103}$$

In order to express the eq. (3.103) as a function of the Einstein's parameters, both the left hand and the right hand of the equation must be divided for $d\sqrt{g\Delta d}$:

$$\frac{q_s}{d\sqrt{g\Delta d}} = \frac{u_s}{d\sqrt{g\Delta d}} K \frac{u_*^2}{g\Delta d} \Delta d \frac{p_1^{1/2}}{\ln(1/p_1)}$$

and hence:

$$\frac{q_s}{d\sqrt{g\Delta d}} = \frac{u_s}{\sqrt{g\Delta d}} K \frac{u_*^2}{g\Delta d} \Delta \frac{p_1^{1/2}}{\ln(1/p_1)} \tag{3.104}$$

We can simply consider $u_s \propto u_*$ and assume that this hypothesis does not modify the approach; thus:

$$\Phi = K\Delta \frac{c_* u_*}{\sqrt{g\Delta d}} \frac{u_*^2}{g\Delta d} \frac{p_1^{1/2}}{\ln(1/p_1)}$$

By using the Einstein parameter, $\Psi = g\Delta d/u_*^2$, then:

$$\Phi = K c_* \Delta \Psi^{-3/2} \frac{p_1^{1/2}}{\ln(1/p_1)} \tag{3.105}$$

With this formulation it is not possible to render the equation independent by the sediment characteristics (Δ at the right hand of eq. (3.105)).

It is interesting to note that the power of the parameter Ψ ($\Psi^{-3/2}$) in the right hand of eq. (3.105) is the same obtained by Yalin (eq. 3.83).

3.6.1 Comparison with empirical formulation

The eq. (3.105) is the final expression obtained with the ballistic approach, where the probability p_1 is the integral of a Gaussian distribution (eq. 3.101). Moreover, the lower limit of integration, that corresponds to the limit for the detachment of

a particle, is evaluated by using the Einstein approach. The final formulation is:

$$\begin{cases} \Phi = K c_* \Delta \Psi^{-3/2} \dfrac{p_1^{0.5}}{\ln(1/p_1)} \\ p_1 = \frac{1}{\sqrt{\pi}} \int_{B_* \Psi - 2}^{\infty} e^{-t^2} dt \end{cases} \tag{3.106}$$

It remains to define the parameters K and c_*, which appear in eq. (3.105) (and eq. 3.106):

- K is a function of the ratio between drag and lift force, multiplied by a parameter, c_u, which defines the velocity of the particle when it is detached:

$$K = 2 \frac{C_L}{C_D} c_u^2 \tag{3.107}$$

  The logarithmic law is usually adopted for the turbulent velocity:

$$u_0 = u_* 5.75 \log\left(30.2 \frac{z}{d}\right) \tag{3.108}$$

  If the particle, at the moment of detachment, moves with the flow, then $z \simeq d/2$ and $c_u \simeq 6.8$. It is reasonable, however, to suppose that the velocity of the particle is lower than the velocity of flow;

- the ratio C_L/C_D might be defined as a function of the flow characteristic, but in this investigation it is considered as a constant value. On the contrary, for Lee and Balachandar (2010), the ratio should depend on the shear Reynolds number $Re_* = u_* d/\nu$; the limits for C_D and C_L are:

  - for the lowest values of Re_*, $C_D \approx 200$ and $C_L \approx 1$;
  - for the highest values, $C_D \approx 3$ and $C_L \approx 0.5$.

  Hence, the ratio should be between 0.015 and 4.

- c_* is the linear correlation parameter between the velocity of the particle crossing the section and the velocity of the flow: $u_s = c_* u_*$, where $c_* u_* = c'_u u(z)$, with $u(z)$ the velocity at the z depth and $c'_u = u_s/u(z)$; reasonably, $c'_u < 1$.

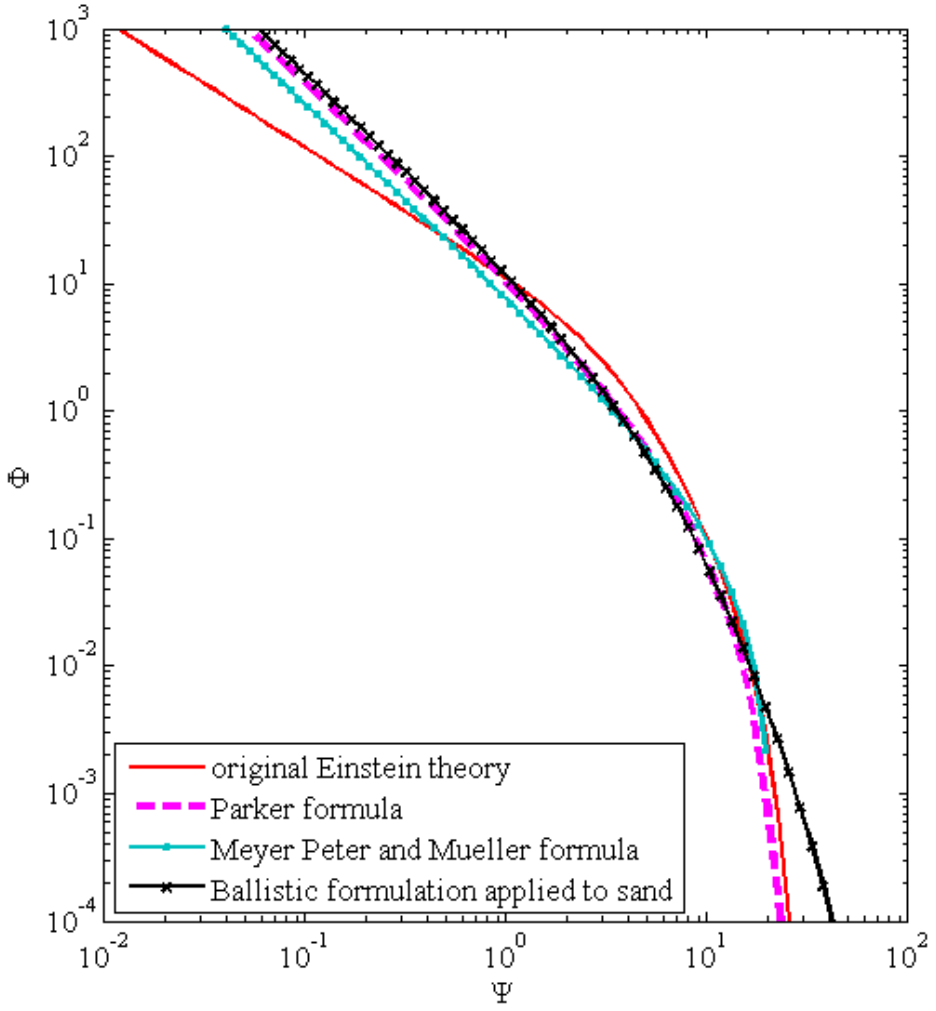

Figure 3.17: Application of ballistic approach (eq. 3.106) and comparison with Einstein original theory (eq. 3.75), Parker formula (eq. 3.12) and Meyer Peter and Müller formula (eq. 3.16)

The final expression in eq. (3.106) is an explicit function also of the property of sediments. Hence, in order to compare the expression with empirical formulations, it is necessary to consider the same materials for which the empirical formulations are valid. As first application of the method, we consider a material with relative density $\Delta = 1.65$, that is a typical value for silicates.

In Figure 3.17, the curve relating to the ballistic approach is obtained by calibrating the constants on the Parker formula, relatively to the sand characteristics. The calibration gives:

$$\text{if } \Delta = 1.65 \;\Rightarrow\; Kc_* = 0.02 \quad \text{and } B_* = 0.05 \tag{3.109}$$

The Parker curve is barely visible in Figure 3.17, because it is nearly coincident with the ballistic theory. Figure 3.17 shows that the ballistic approach is in better agreement with empirical formulations with respect the original Einstein formulation.

We can also analyze the calibrated constants in eq. (3.109). We can assume a particle velocity about $1/10$ of the local flow velocity, at the instant of detachment ($c_u \approx 0.7$), and $1/10$ at the instant of crossing the section ($c_* \approx 0.8$). Having evaluated that the best solution is for:

$$Kc_* = 2\frac{C_L}{C_D}c_u^2 c_* = 0.02$$

from eq. (3.98):

$$\frac{C_L}{C_D} = 0.025$$

that is in the range of the results by Lee and Balachandar (2010). We can affirm that the second value in eq. (3.109) seems to be reasonable. As far as concerns the calibrated value for B_*, as in Einstein's theory, there is not a physical meaning of the parameter and hence its validity can not be tested with data in literature.

3.7 Sediment transport in vegetated rivers

3.7.1 State of art

The thesis research is focalized on the role that vegetation plays relatively to the sediment movements, by studying the matter at small scale and from an onedimensional point of view. On the contrary, most of the published research have faced the relationship between morphology at large scale and vegetation (Gran and Paola 2001; Perucca, Camporeale, and Ridolfi 2007; Tsujimoto 1999; Wu et al. 2005). In other investigations, more than grain movements through vegetation, the transport of passive scalars is tackled, not influenced by gravity, like contaminants, nutrients and pollutants (Shucksmith, Boxall, and Guymer 2010; White and Nepf 2003), rather than grain sediments. Also vertical mixing is a topic studied (e.g.: for emergent vegetation, Elliot (2000)).

Only a few of studies focus on sediment transport and bed morphology. Moreover, most of the authors who face the problem of sediment transport and vegetation simply express the sediment transport capacity as proportional to the difference between equivalent total bottom shear stress τ_0 and critical value of shear stress τ_c: $q_b \propto (\tau_0 - \tau_c)^{\alpha}$, where α is an empirical exponent (Ashida 1972; Jordanova and James 2003; Kothyari, Hashimoto, and Hayashi 2009; Li and Shen 1973). Sometimes this kind of formulas use the shear stress due to grain roughness, and hence the Shields parameter θ' instead of the total shear and the θ, as in Ishikawa, Sakamoto, and Mizuhara (2003). Some examples are reported in Table 3.1.

Table 3.1: Summary of some examples of formulae for calculating the sediment transport capacity in vegetated channels

References	Empirical formula
Ashida (1972)	$\Phi = 17\theta^{1.5}\left(1-\frac{\theta_c}{\theta}\right)\left[1-\left(\frac{\theta_c}{\theta}\right)^{0.5}\right]$
Jordanova and James (2003)	$q_b = 0.017\left(\tau-\tau_c\right)^{1.05}$
Ishikawa, Sakamoto, and Mizuhara (2003)	$\Phi = 8\left(\theta'-\theta_c\right)^{2.5}$
Kothyari, Hashimoto, and Hayashi (2009)	$\Phi = 5.37\theta_c^{3/2}\left(1-\theta_c/\theta\right)$

Also investigations on suspended load through rigid plants are present in literature, and they are generally based on the integration of the diffusion/advection equations by using more or less sophisticated models (Furukawa, Wolanski, and Mueller 1997) and often $k - \varepsilon$ models (López and García 1998; Nakagawa, Tsujimoto, and Shimizu 1992).

Despite the numerous publications, there is however a lack of rational investigation on sediment transport capacity. In order to overcome the lack of theories on this topic, we have tried to extend the ballistic model described in section 3.6 to vegetated riverbeds, in presence of rigid vegetation.

3.7.2 The ballistic approach for vegetated riverbeds

In order to apply the ballistic approach to a vegetated reach, we need to retrace the method described for a non-vegetated reach (Section 3.6) from the first passages. In this last case, we assumed (eq. 3.94):

$$dq_s = u_s \alpha_2 d \frac{dx}{\alpha_2 d} P \tag{3.110}$$

where $dx/\alpha_2 d$ was the number of grains contained in an elemental streak dx of the channel.

In a vegetated reach, a part of the total area is occupied by plants (Figure 3.18). In order to determine how many grains are contained in an elemental streak of the vegetated reach, we can consider the incumbrance of the stems present in the elementary area dx. The density Ω_v of vegetation is defined as the area occupied by plants over the total area of the reach:

$$\Omega_v = \frac{\sum_{1=1}^{N_p} \frac{\pi d_{p,j}^2}{4}}{1L} \tag{3.111}$$

where N_p is the number of plants contained in the reach; $d_{p,j}$ is the average diameter of each plant; L is the length of the reach, and 1 is the width. Therefore, in an infinitesimal surface $dA = 1dx$:

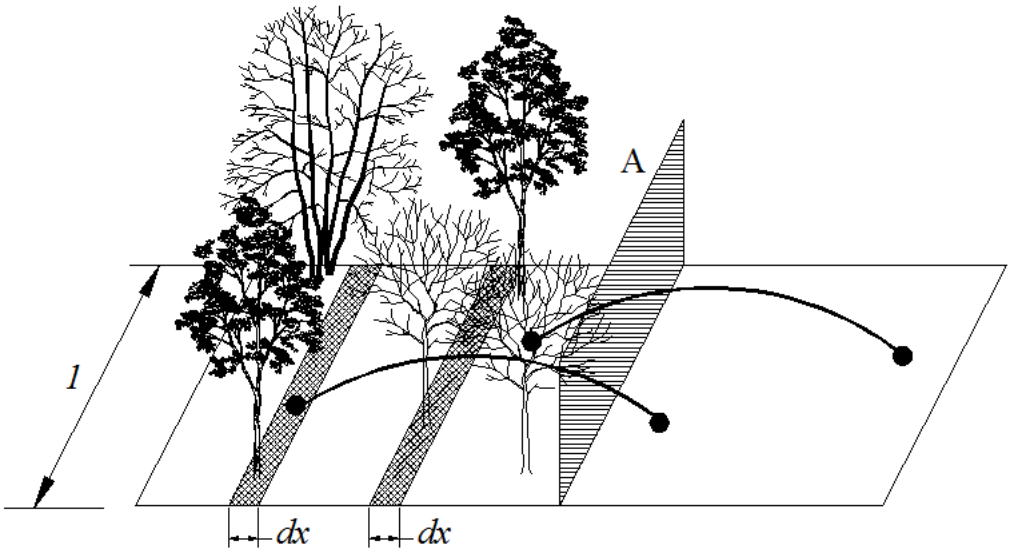

Figure 3.18: A reach of a vegetated channel

- the surface occupied by the plants is:

$$dA_p = \Omega_v dx$$

- the free area (the area free for the movement of particles) is therefore:

$$dA_{free} = dx - \Omega_v dx = dx(1 - \Omega_v)$$

The eq. (3.94) can be reformulated for vegetated beds:

$$dq_s = u_s \alpha_2 d \frac{dx(1-\Omega_v)}{\alpha_2 d} P = u_s P (1-\Omega_v) dx \tag{3.112}$$

By following the same procedure presented in Section 3.6 for non-vegetated beds, the final equations become:

$$\begin{cases} \Phi = K c_* \Delta (1-\Omega_v) \Psi^{-3/2} \dfrac{p_1^{0.5}}{\ln(1/p_1)} \\ p_1 = \frac{1}{\sqrt{\pi}} \int_{B_* \Psi - 2}^{\infty} e^{-t^2} dt \end{cases} \tag{3.113}$$

The result in eq. (3.113), which seems very similar to the result for non-vegetated beds, must be carefully analyzed. There are two important effects due to rigid stems that must be considered: the first one is a direct effect on sediment transport discharge at large scale; the second one is the effect at small scale. As far as concerns the first one, the presence of stems increases the global resistance. The main consequence is the increase of the water depth and a decrease of the bed slope, which entails a decrease of the shear stress at the bottom, τ_0'. This is the cause of the reduction of the sediment discharge in vegetated beds.

The second point to consider is how the presence of vegetation influences the sediment transport at small scale. In a vegetated bed at steady condition, the sediment discharge at each vertical section is average constant, but actually there are small areas where the displacements of sediments are larger, and areas where the exchange of sediments is very small (Figure 3.19). In particular, in parts of the bed close to plants, the grain has less tendency to the detachment, or the grain is detached, but not transported downstream (Cavedon, Righetti, and Armanini 2012). This effect was experimentally verified by means of the PIV analysis and it is reported in Section 5.2. At the contrary, there are some zones where, induced by the increase of the flow velocity around the stems, the particle jumps are larger than the average jump, and the velocity of movement is larger. In addition, secondary currents induced by the stems (like horseshoe vortices) contribute to the slowing down of the average longitudinal component of the particle velocity.

All the effects related with the movement of particles at large and small scale affect the average velocity of the particles in vegetated beds, both at the instant of the detachment, and at the instant of crossing the section A. Therefore these effects modify the definition of the parameters K and c_* (in eq. 3.113), which describe the velocities, with respect to the parameters used for non-vegetated beds (eq. 3.109). These parameters, however, will be obtained by the comparison with the experimental results and will be analyzed in a critical point of view by using their definition. We can remember that (eqs. 3.97 and 3.98):

$$\bar{x} = K\frac{u_*^2}{g} = 2\frac{C_L}{C_D}\frac{u_0^2}{g}$$

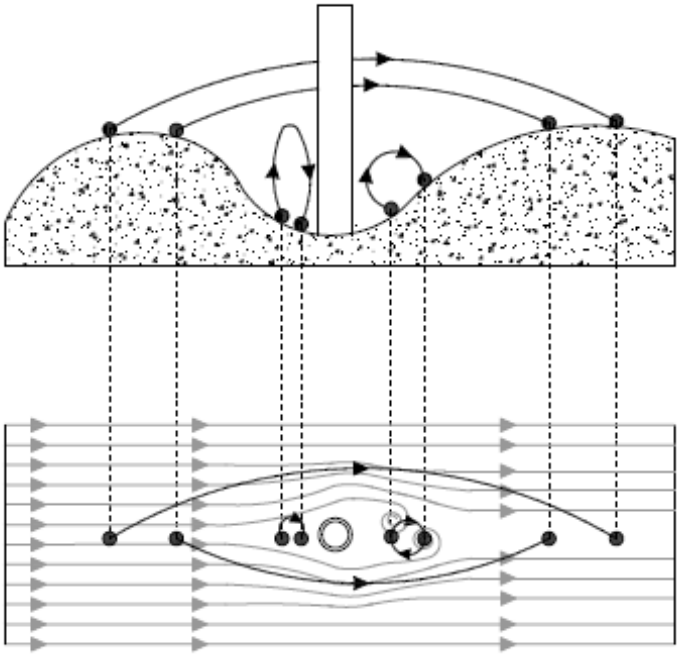

Figure 3.19: Different behaviors of the particles detached.

and hence:

$$K = 2\frac{C_L}{C_D}\left(\frac{u_0}{u_*}\right)^2$$

Whereas, regarding c_*:

$$c_* = \frac{u_s}{u_*}$$

Since the shear velocity u_* is contained in the Einstein flow intensity parameter Ψ, it is convenient to consider a modification of the definition of Ψ, rather than modify both parameters K and c_*. In this way all the effects related to the modifications of the flow field can be included in a single parameter. The new flow intensity parameter is called Ψ_v, and it is supposed to be a function of Ψ, defined by Einstein, and of the incumbrance of the stems:

1. on the bed, that can be expressed by a function of Ω_v;
2. during the movement of the particle, that can be described by the ratio between the water depth and the average diameter of stems h/d_p.

We have experimentally verified that the most reasonable definition for Ψ_v is:

$$\Psi_v = \Psi f_v(\Omega_v, h/d_p) \tag{3.114}$$

where the function f_v should assume the following form:

$$f_v = 1 + c\,\Omega_v \left(\frac{h}{d_p}\right)^{\alpha} \tag{3.115}$$

In eq. (3.115), c and α are two empirical constants to be calibrated by fitting the experimental data. The eq. (3.115):

- for $\Omega_v = 0$, $\Psi_v = \Psi$, the ballistic formula is equal to the case of non-vegetated stretches;

- for d_p increasing and h constant (or viceversa), the value of Ψ_v increases, and hence the mobility of sediment decreases.

In Section 5.4.3 the experimental data obtained in the laboratory channel will be compared with the ballistic approach and all the parameters will be analyzed and calibrated.

Chapter 4

Laboratory set up and data collection

4.1 The laboratory channel

The experiments are carried out in a laboratory channel in the Laboratory of Hydraulics of the University of Trento. The channel is $18\ \mathrm{m}$ long and $1\ \mathrm{m}$ wide. The channel is divided into two parts in the longitudinal direction (Figure 4.1). The left partition is used for experiments with conditions of mobile bed, and hence sediment transport. The right partition is used for tests carried out in condition of fixed bed.

The left partition has a constant width of $0.5\ \mathrm{m}$, while in the right partition the width of the channel can change depending on the kind of tests and on experimental conditions: the width can be $B = 0.3\ \mathrm{m}$, $0.4\ \mathrm{m}$ and $0.5\ \mathrm{m}$.

The slope of the channel can be changed from the horizontal plane to a value (in percentage) of about $i_b = 10\%$. This range of values allows a large range of flow conditions, very useful for obtaining a wide distribution of results. The point of rotation of the channel is located downstream of the reach used for measurements, and the channel is raised by two hydraulic pistons located upstream. By means of the pistons, the channel slope can be evaluated electronically. This method is quite accurate, but for some test conditions its precision is not sufficient. In those cases, the slope of the channel is obtained by measuring the elevation of

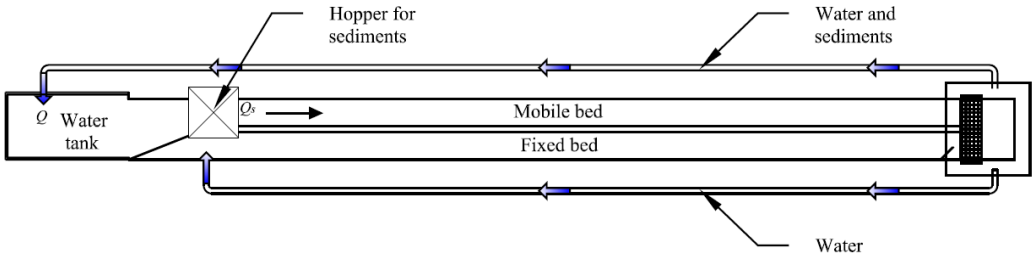

Figure 4.1: Planimetric view of the laboratory channel and all its component parts.

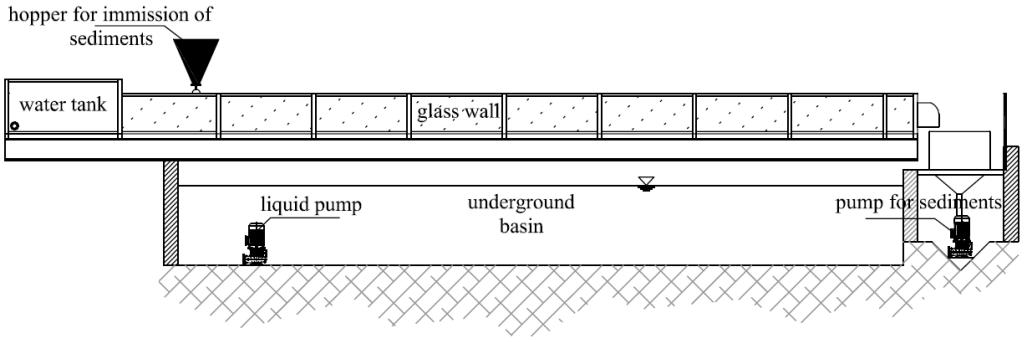

Figure 4.2: Perspective view of the laboratory channel and all its component parts.

the channel by means of an optical level every 50 cm along the x-direction of the channel. The optical level is able to evaluate the elevation of a point with a precision of 0.1 mm.

The channel (Figures 4.1 and 4.2) is composed by a tank for the incoming water flow, the stretch of the channel for the experiments and the stretch for the outlet. It is usual to have a water tank before of the channel, because the incoming water has a great kinetic energy which, in the tank, becomes potential energy. In this way the inlet flow is less disturbed and the stretch necessary for stabilizing the flow conditions is smaller. The water tank is connected only with the left partition of the channel (Figure 4.1), because it is used only for mobile bed tests. For the tests with fixed bed, the stabilization is obtained through other methods, for example by breaking the eddies of the inlet flow by a thin filter or grate.

The channel for the measurements is 15 m long. The lateral walls are of glass (0.7 m high) sustained by a structure made of steel, while the central wall, that divided the channel, is made of plastic. All the walls can be considered as smooth.

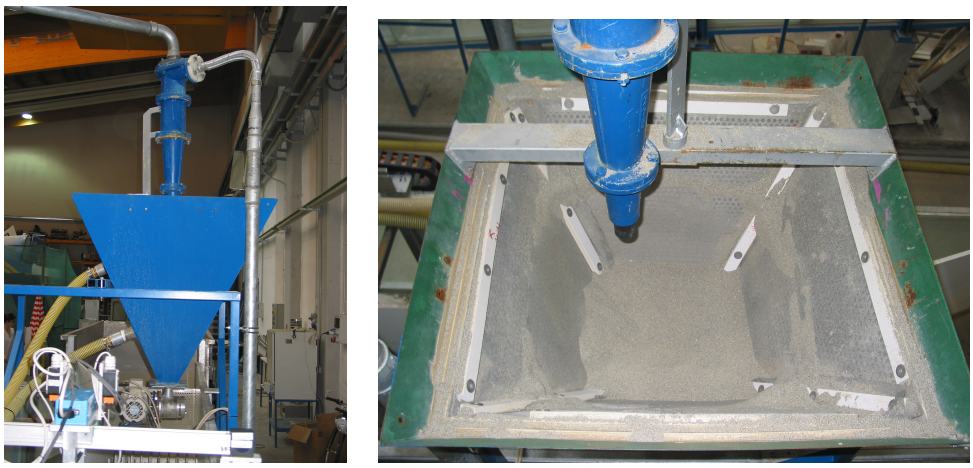

(a) lateral view (b) above view

Figure 4.3: Photo of the hooper: (a) lateral view; (b) view from above: sand can be seen into the hooper.

The outlet is made for directing the flow in another tank placed at a lower level than the point of discharge (Figure 4.2).

The channel works as a close circuit. Water is pulled in the water tank, and then it goes to the channel and to the outlet tank. In case of sediments, the water which reaches the downstream tank is mixed with the sediments. In this tank, the sediments settle, while the surplus of water goes to an underground basin, which contains up to $15\ \mathrm{m}^3$ of water. For this reason, the experimental set up needs two pumps: the first for water and sediments, the second only for water (Figure 4.2). In addition, by using two pumps, a large range of water rates can be used, increasing the possible flow conditions for the tests. If the tests are carried out in fixed bed, the two pumps work only with water.

The liquid pump carries the water to the upstream tank, while for sediments the possible paths are: if the sediment transport rate is sufficiently small, sediments and water are mixed and go together to the water tank; but, if the sediment transport rate is too high for being transportable by water through the pipes, then the sediment ratio goes to a hooper (Figure 4.3), which is located upstream the channel (Figures 4.1 and 4.2). The hooper collects the sediments and divides the rest of water. Then the sediments are released gradually to the channel. This method has the advantage to allow the regulation of sediment transport during the

Figure 4.4: The electromagnetic flowmeter.

test, which makes faster the achievement of steady conditions.

In each test performed, the choice of water discharge and (in case) sediment discharge is done a priori. The water discharge is controlled by a gate valve and measured by an electromagnetic flowmeter connected to the inlet pipe (Fig. 4.4), that has a maximum error in measurement of $0.5\%Q$, where Q is the water discharge. The sediment transport is determined by collecting for a certain time the sediment which arrives downstream the channel and by measuring the mass of the sediment collected. The collection time depends on the sediment transport rate. By knowing the density of the material, the volume can be easily calculated and hence the sediment transport rate is evaluated.

4.2 Experiments with sediment transport

This section is focused on the description of the experiments carried out in the left part of the channel, i.e. in the case of tests with mobile bed. The main purpose of these tests is the determination of the sediment discharge for different densities and distributions of rigid stems in the channel. The data will be compared with the ballistic theory described in Sections 3.6 and 3.7.2.

For the mobile bed conditions, the bottom of the channel is covered by a layer of loose sediments, which has a thick at least $5\ \mathrm{cm}$, representing the mobile bed.

Table 4.1: Chemical and mineralogical composition of sands used for experiments with sediment transport

Chemical analysis:			
Silica (S_iO_2)	83.3%	Magnesium (MgO)	1.5%
Iron (Fe_2O_2)	2.1%	Sodium(Na_2O)	2.0%
Aluminium (Al_2O3)	6.6%	Potassium (K_2O)	2.1%
Calcium (CaO)	1.2%		

Mineralogical analysis:			
Quartz	61.8%	Granitoid rocks	16.5%
Feldspar	12.7%	Other minerals (traces)	9.0%

4.2.1 Property of sediments

In the experiments, three different materials are used as sediment: two sands and one plastic material.

The two sands have the same mineralogical composition, tabulated in Table 4.1, but different grain sizes. The measurement of particle size were led through mechanical vibratory sieving of a sample of dried material. From the grading curve, the characteristics size of grain diameters can be calculated. Their values are:

- sand called *V15*: $d_{50} = 0.0005$ m; $d_{90} = 0.00067$ m;
- sand called *V17F*: $d_{50} = 0.00145$ m; $d_{90} = 0.00158$ m;
- plastic material: $d_{50} = 0.00055$ m; $d_{90} = 0.00070$ m.

The density of the sands, which is $\rho_s = 2591$ kg/m^3, was calculated by means of the pycnometer. The density of the plastic material, due to the reduced value, was evaluated by means of the hydrostatic balance; the density is $\rho_s = 1050$ kg/m^3.

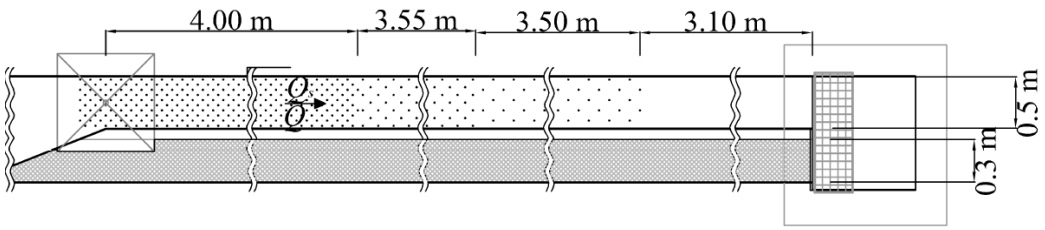

Figure 4.5: Planimetric view of the channel for the staggered distribution of cylinders.

4.2.2 Staggered distributions of cylinders

In the laboratory channel, the presence of rigid stems is modeled with circular cylindrical elements fixed at the bottom of the channel, rigid and always emergent. The distribution of the cylinders can be geometrical (*staggered distribution*) or random (*random distribution*).

In staggered configuration, the total length of the flume was partitioned into four zones in series (Figure 4.5), each of which has the elements at different concentration. The downstream final reach of the flume is free of plants, in order to have also the undisturbed flow for each condition. Each reach of the partition is long at least $3.1\ \mathrm{m}$, that is sufficient to obtain uniform flow conditions for each density of vegetation, given that it is necessary to exclude from the measure zone a short extent, across to the interfaces between different densities of vegetation (maximum length of adaptation: $2 \sim 3$ times the water depth). It is easy to prove (by the Exner equation) that the steady condition in tests with mobile bed and sediment transport always corresponds to the uniform flow condition (Section 4.2.4).

"Staggered distribution of cylinders" means that the arrangement of the cylinders is squared (Figure 4.6). In this condition, the different densities of vegetation are obtained with different distances between cylinders and different diameters of cylinders. In particular, in the *dense* distribution, the distance between two cylinders is $10\ \mathrm{cm}$; in the *intermediate* distribution, they are $15\ \mathrm{cm}$ distant; while in the *sparse* distribution, $20\ \mathrm{cm}$ distant (see Figure 4.6).

The distributions of plants are described by two parameters: the density of vegetation and the average diameter of stems. In both staggered and random con-

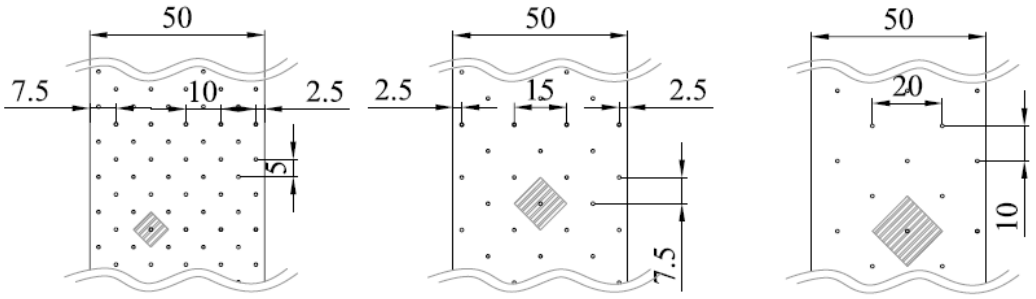

Figure 4.6: The three different staggered configurations. The sizes are given in $[\mathrm{cm}]$.

figurations, the density of plants, Ω_v, is determined by the following equation:

$$\Omega_v = \frac{A_p}{A_{tot}} = n_p \frac{\pi d_p^2}{4} \tag{4.1}$$

where A_p is the area occupied by the plants over the total area considered A_{tot}; n_p is the number of cylinders contained in A_{tot}; d_p is the average diameter of the cylinders.

In the staggered distribution, a first set of tests were carried out with the sand V15 and with all the cylinders having the same diameter equal to $1\ \mathrm{cm}$. In a second series of tests the plastic material was used. A part of these tests was performed with cylinders $1\ \mathrm{cm}$ in diameter, and a part with cylinders $3\ \mathrm{cm}$ in diameter. The results are summarized in Section 4.2.5.

4.2.3 Random distributions of cylinders

The random distributions used in the flume were generated by the software MatLab and its function `rand`. Actually, in order to maintain the random configurations comparable with the tests performed in staggered configurations, some limits at the randomness have been imposed:

- the minimum distance between the axes of adjacent cylinders has been fixed ($6\ \mathrm{cm}$ for *sparse* configuration; $3.5\ \mathrm{cm}$ for *dense* configuration) in order to generate a distribution sufficiently uniform on the whole interested area, for avoiding overlap of cylinders or areas too extended without plants, that

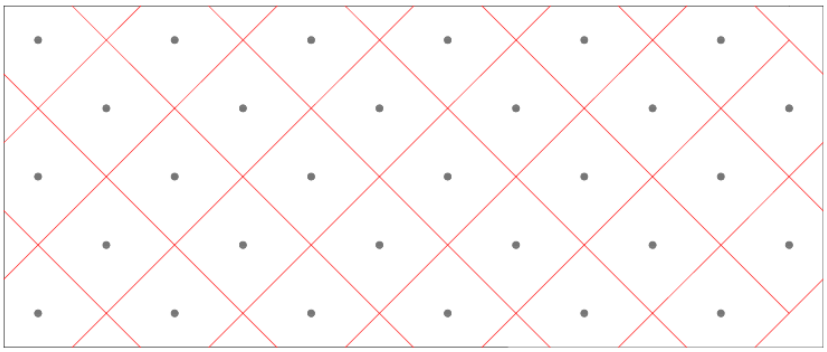

(a) staggered configuration

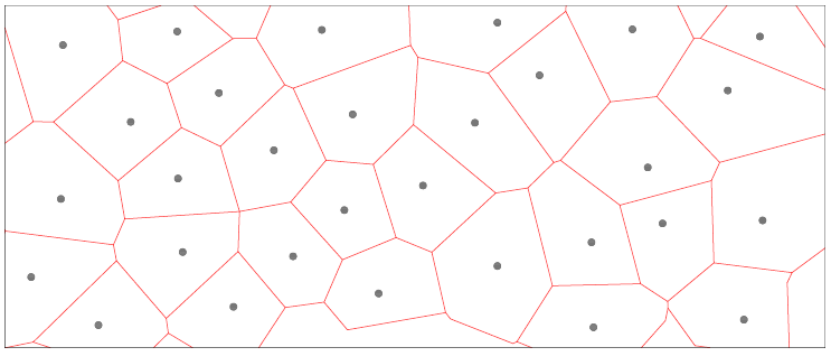

(b) random configuration

Figure 4.7: Representation of areas of influence, calculated with Voronoi diagrams, for each cylinder in (a) staggered distribution and (b) random distribution. The two distributions have the same density of stems.

Table 4.2: Data obtained by the analysis of the areas of influence of the cylinder. (a) for staggered *sparse* configuration; (b) for random *sparse* configuration.

	(a) staggered	(b) random
Averaged area of influence	183.33 cm^2	188.16 cm^2
Variance area of influence	0 cm^2	1661.88 cm^2
Density of vegetation Ω_v	0.0039	0.0039

Table 4.3: Data obtained by the analysis of the areas of influence of the cylinders: (a) for staggered *dense* configuration; (b) for random *dense* configuration.

	(a) staggered	(b) random
Averaged area of influence	47.73 cm^2	48.51 cm^2
Variance area of influence	0 cm^2	99.85 cm^2
Density of vegetation Ω_v	0.0157	0.0157

could compromise the final results;

- the area of influence of each cylinder was calculated, because the standard deviation of all the areas is an accurate and quantitative method to evaluate the spatial distribution of cylinders. Moreover, it allows the comparison with the staggered distribution;

- in order to verify that the sediment transport is not a function of the distribution, but only a function of the density of plants, for some tests it was imposed that the density of cylinders is the same used for some tests in staggered configurations.

The areas of influence of the cylinders were calculated with a program written in Fortran language, which defined the Voronoi diagrams. The results obtained for *dense* configuration are represented, as example, in Figure 4.7 (a), for staggered distribution, and Figure 4.7 (b), for random distribution. The calculated standard deviations of the values of the areas of influence for random configurations are sufficiently small to consider the results satisfying (see Tables 4.2 and 4.3).

In the case of random distribution of cylinders, the length necessary for adaptation between a configuration and the next one is larger, because of the non-uniformity of the distribution. In order to have the reach long enough to obtain

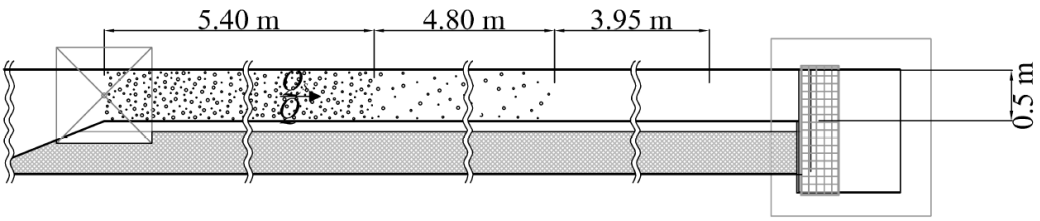

Figure 4.8: Planimetric view of the channel for the random distribution of cylinders.

uniform flow conditions, in these tests the channel was divided not in four, but in three zones: the first upstream (*dense* configuration) is 5.4 m long, the second zone (*sparse* configuration) is 4.8 m long and the rest of the channel is without plants (Figure 4.8).

The tests in random configuration are carried out with two different distributions of cylinder diameters:

1. constant diameter of cylinders, equal to $d_p = 1$ cm;
2. different size diameters: $1/3$ of the total number of cylinders with $d_p = 1$ cm, $1/3$ with $d_p = 1.9$ cm and $1/3$ with $d_p = 3$ cm.

4.2.4 Rational verification of uniform flow condition

Frequently in hydraulics research, the first problem in experimental setup is the achievement of uniform flow condition in a flume. It will be proved with some rational considerations that this aim is not a problem in condition of steady flow and for mobile bed.

We can consider a prismatic channel (rectangular, as in the tests) and a certain quantity of sediments that are moved by the water flow. In this conditions, the longitudinal direction is the main direction of flow, because, given the geometry of the channel, secondary flows can be neglected. Therefore, the total mass conservation is expressed by an only equation in the x direction:

$$\frac{\partial h}{\partial t} + \frac{\partial}{\partial x}(Uh) + \frac{\partial z_b}{\partial t} = 0 \tag{4.2}$$

where h is the water depth, U is the velocity component in x direction, and z_b

is the instantaneous elevation of bed. All the quantities have to be considered as *double-averaged quantities* (see Section 2.4.1).

Together with the total mass conservation, the sediment mass conservation (Exner equation) can be written as:

$$\frac{\partial}{\partial t}(Ch) + \frac{\partial q_s}{\partial x} + C^* \frac{\partial z_b}{\partial t} = 0 \tag{4.3}$$

in which C is the concentration of sediments along the water depth; q_s is the sediment transport rate per unit width; C^* is the grain packing density.

In the hypothesis of steady flows, all the time derivatives are zero ($\partial/\partial t = 0$), so the equations become:

$$\begin{cases} U\dfrac{\partial h}{\partial x} + h\dfrac{\partial U}{\partial x} = 0 \\ \dfrac{\partial q_s}{\partial x} = 0 \end{cases} \tag{4.4}$$

In accordance with other researchers (López and García 1998; Van Rijn 1984), the variables that affect the sediment transport rate in vegetated rivers are the same variables that govern the phenomenon in open channel flows, plus the variables that characterize the plant properties:

$$q_s = f(u_*,\ h,\ g,\ \mu,\ \rho,\ (\rho_s - \rho),\ d,\ d_p,\ \Omega_v,\ h_p,\ \epsilon) \tag{4.5}$$

where u_* is the shear velocity; g is the gravitational acceleration; μ is the flow dynamic viscosity of water; ρ is the density of water and ρ_s the density of sediments; d is a characteristic diameter of grains; d_p is the diameter of plants; Ω_v is the density of vegetation; h_p represents the height of plants, and, lastly, ϵ is the flexibility of stems.

In this research, we are considering averaged velocities. Hence, it is more useful to replace the shear velocity with the averaged velocity in the x direction, U. Moreover in the tests constant grain sizes are used; the plants along the channel have constant diameters and densities, they are emergent and completely rigid. Hence, finally, the only parameters that could change along the x directions are the velocity and the water depth. From the second equation of the system in eq.

(4.4):

$$q_s = q_s(U,h) \quad \Rightarrow \quad \frac{\partial q_s}{\partial x} = \frac{\partial q_s}{\partial U}\frac{\partial U}{\partial x} + \frac{\partial q_s}{\partial h}\frac{\partial h}{\partial x} = 0 \tag{4.6}$$

And for the system:

$$\begin{cases} \dfrac{\partial h}{\partial x} = -\dfrac{h}{U}\dfrac{\partial U}{\partial x} \\ \dfrac{\partial q_s}{\partial U}\dfrac{\partial U}{\partial x} + \dfrac{\partial q_s}{\partial h}\dfrac{\partial h}{\partial x} = 0 \end{cases} \tag{4.7}$$

from which:

$$\begin{aligned} &\frac{\partial q_s}{\partial U}\frac{\partial U}{\partial x} - \frac{\partial q_s}{\partial h}\frac{h}{U}\frac{\partial U}{\partial x} = 0 \\ &\left(\frac{\partial q_s}{\partial U} - \frac{h}{U}\frac{\partial q_s}{\partial h}\right)\frac{\partial U}{\partial x} = 0 \end{aligned} \tag{4.8}$$

The only physically possible solution for eq. (4.8) is for $\partial U/\partial x = 0$, that is the equation for defining uniform flow conditions.

The analytical results are even then verified by the experimental results (see Section 4.2.5).

4.2.5 Summary of test conditions

Both for random and staggered configuration, both with sand and plastic material, when a test is started, water and sediment discharges are chosen a priori. During the performance of a test, that can be brief (minimum 5 hours) or very long ($5-6$ days), sediments are collected every $2-4$ hours. When test is approaching to steady conditions, the sediment transport becomes constant in time. With the same frequency, the measure of the elevation of free surface and of bed is checked; the measure for checking is done every $30-50$ cm for the whole length of the channel. After sediment transport reaches regime condition, also free surface and bed elevations become constant in a short time. Since that moment, all the necessary measurements are done.

For comparing the data with the sediment transport theory (Sections 3.6 and 3.7.2), we need the values of sediment discharge, water depth and bed slope. The considered value of sediment discharge is the average of the sediment discharges measured since the instant the sediment discharge has been stable in time. For water depth and bed slope, the measurements are as accurate as possible, given

that the final results are very sensitive to their errors. For all the configurations and for the whole length of the channel, the bed and the free surface elevations are measured by using a pointer gauge, which has a precision of $0.1\ \mathrm{mm}$. The pointer gauge is mounted above the flume on a trolley moving along rails. The measurements are taken every $5\ \mathrm{cm}$. In some cases, normally for the tests performed using the plastic materials, the results are confirmed by measurements taken by means of piezometers fixed to the flume, because the low values of bed slopes - also less than 0.01% in some cases - can be affected by large errors.

Given the presence of bed forms, which make difficult the direct analysis of bed elevations, the bed slopes are obtained by fitting the data of free surface with the method of least squares and by comparing the result with the data of bed elevations. The water depth is the averaged difference between free surface and bed elevation. Bed slope and water depth change for each partition of the channel, relative to the different vegetation densities.

All together, more than 100 data are obtained; the characteristics and differences of the tests are summarized in Table 4.4.

4.3 Measurements of drag force

The value of the drag coefficient of cylinders immersed in a water flow can be evaluated directly by measuring the force exerted by the flow on one or more cylinders; or indirectly, by considering the balance of momentum in a control volume of the channel. The aim of this part of the research is the determination of the drag coefficients of cylinders and the comparison between drag coefficients obtained through direct measurements and indirect measurements.

The measurements of resistance are carried out in the right part of the channel, without sediment transport. The uniform flow conditions are obtained using an inclinable bulkhead anchored to the channel downstream. The flow is subcritical, hence by choosing the angle of the bulkhead, the downstream water depth can be changed until the conditions are uniform for a sufficiently large reach of the channel.

The resistance exerted by cylinders on flow is obtained by measuring with a load cell the force exerted by flow on cylinders.

Table 4.4: Summarized of the experimental conditions: d_{50} is the characteristic grain size; ρ_s is the density of sediments; $\overline{d_p}$ is the average diameter of plants; $\overline{\Lambda_p}$ is the (average) interaxis between adjacent stems in the longitudinal direction; Ω_v is the density of stems in the reach.

Configuration	Material of sediments	d_{50} [mm]	ρ_s [kg/m^3]	$\overline{d_p}$	$\overline{\Lambda_p}$	Ω_v
Staggered distribution	Sand V15	0.50	2590	constant: 1 cm	10 cm	0.0157
					15 cm	0.0073
					20 cm	0.0039
	Plastic	0.55	1050	constant: 1 cm	10 cm	0.0157
					15 cm	0.0073
					20 cm	0.0039
				constant: 3 cm	10 cm	0.1414
					15 cm	0.0660
					20 cm	0.0353
Random distribution	Sand V15	0.5	2590	constant: 1 cm	10 cm	0.0157
					20 cm	0.0039
				variable: 1.9 cm	10 cm	0.0608
					20 cm	0.0152
	Sand V17F	1.45	2590	variable: 1.9 cm	10 cm	0.0608
					20cm	0.0152

4.3.1 Direct measurements for an isolated cylinder

The main objectives of these measurements are:

1. to define the influence of walls and of boundary layer;
2. to focalize the actual influence of narrowing of flow field caused by the presence of cylinder;
3. to determine which is the error that can be made by using different definitions of averaged velocity.

Relatively to the last point, the velocities considered and compared are:

a) the averaged velocity calculated by means of the continuity equation:

$$U = \frac{Q}{A} \tag{4.9}$$

in which U is the averaged velocity, Q is the water discharge and A is the water section;

b) the velocity U_1 calculated with the integration of velocity profile obtained by means of the Ultrasound Velocity Profiler (AVP):

$$U_1 = \int_0^h \overline{u(z)} dz \tag{4.10}$$

where h is the water depth, $\overline{u(z)}$ is the time-averaged velocity along vertical direction.

The value of resistance exerted by the cylinder on the flow, which is measured with a load cell fixed to the cylinder, allows the determination of the drag coefficient, which is calculated with the two different definitions of velocity (eqs. 4.9 and 4.10) and then compared with the case of infinite cylinder in an undisturbed indefinite flow.

The set up of the channel

The channel for the measurements is $30.8\ \mathrm{cm}$ wide and $12\ \mathrm{m}$ long. On the bottom, sand grains are glued in order to reproduce the same grain roughness of the tests with sediment transport. The sand utilized has constant diameter: $d_{50} = 1.4\ \mathrm{mm}$ and $d_{90} = 1.8\ \mathrm{mm}$.

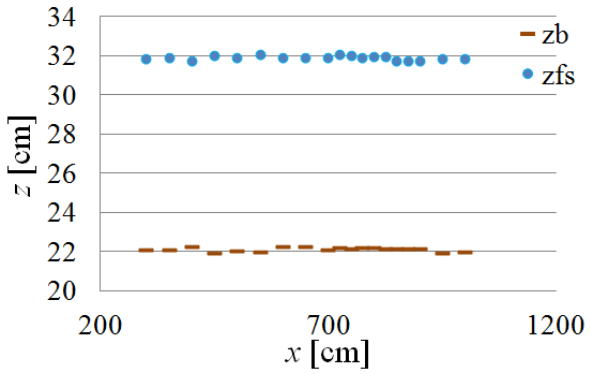

Figure 4.9: Example of measurements of free surface and bed elevation obtained by means of the pointer gauge.

During the test, and in condition of uniform flow, the water depth is measured, by means of the pointer gauge, at least every 50 cm, but the measurements are thickened close to the x-coordinate of the cylinder position (Figure 4.9).

Ultrasound Velocity Profiler

The velocity measurements are carried out by means of the Ultrasound Velocity Profiles, called DOP2000 (Figure 4.10). The velocity profiles are obtained by using the Doppler effect, for which an acoustic wave, which is intercepted and diffused by particles in motion, varies its frequency proportionally to particle velocity. In particular, the used probe (Figure 4.10 (b)) produces an ultrasonic field at the frequency of 4 MHz. For improving the quality of registered data, water is inseminated with hollow microspheres in glass, in order to guarantee a sufficiently large number of particles in motion with the flow.

This technique permits to register in real time the velocity profile along the direction of probe. The instrument can be used only in flow fields predominately unidirectional.

The velocity profiles are measured for different sections of the channel, from $x = 3$ m to $x = 10$ m, every 25 cm (Figure 4.11). This allows to verify the uniformity of flow along the channel and in which sections the uniform flow conditions are attained. In addition, with the profiles in uniform flow conditions, the double average velocity can be obtained (see Section 2.4.1).

(a) software and hardware for Dop2000 (b) probe of Dop2000

Figure 4.10: Photo of the instruments for the measurements of velocity in the channel: (a) hardware and software for acquiring the data; (b) the probe positioned for the measurements.

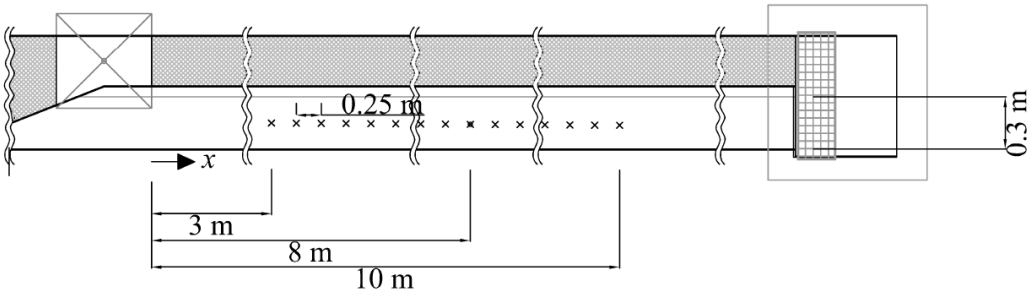

Figure 4.11: Points of measure of velocity along the channel, indicated by the crosses, and position of the cylinder, indicated by a small circle at $x = 10$ m.

The load cell

In order to measure the force exerted by water flow on the cylinder, a single point load cell (Figure 4.12 (a))- called PW4MC3, produced by HBM - is fixed to the cylinder. The load cell has a maximum capacity of 3 kg and a method of compensation of off center loads.

As every mechanical instrument, load cells have some instrumental limitations. The choice of the kind of load cell is made after to have analyzed the conditions of measure related with the instrumental limitations. First of all, the load cell must allow the measurement of the minimum forces exerted on the cylinder, which were estimated round about 10 g. Secondly, notwithstanding the capacity

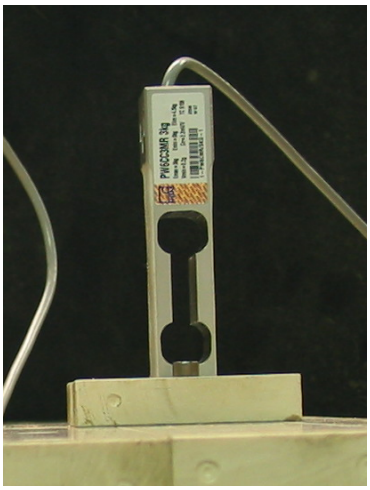

(a) photo of the load cell

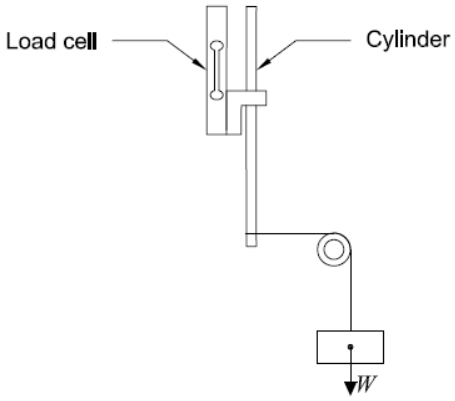

(b) Load cell calibration

Figure 4.12: (a) Photo of the load cell; (b) representation of the experimental setup for the calibration of the load cell.

to compensate the off center loads, the instrument has a limit value for eccentricity of applied load, calculated from the center of cell. The maximum eccentricity, value indicated by the technical documentation, is $300\ \mathrm{mm}$. It means that the load must be applied at a maximum distance of $15\ \mathrm{cm}$ from the center of the cell. This maximum distance becomes a limit on the water depth which can be present in the channel during the test (Figure 4.15). In order to assure that the measurements are correct, the limit on water depth is fixed in $10\ \mathrm{cm}$.

Load cells give the values of forces in $[\mathrm{mV/V}]$. In order to have results in $[\mathrm{N}]$, it is necessary to do previously a calibration. The calibration was done by means of an experimental setup composed by a system of small pulleys arranged so that the load is horizontal and perfectly perpendicular to the cell (Figure 4.12 (b)). For the calibration, given the estimated loads applied during tests, weights from $0.1\ \mathrm{g}$ to $40\ \mathrm{g}$ were applied. The values obtained are plotted in Figure 4.13. Moreover, in order to test the precision of the instrument with the minimum forces applied, the curve of calibration was compared with a second calibration (Figure 4.14), obtained with weights from $10\ \mathrm{g}$ to $300\ \mathrm{g}$, that is a load range more typical of the kind of instrument used. In the graph in Figure 4.13 also the intervals of confidence are reported, which are not visible because too small.

By knowing the equation of the linear regression, obtained with the method of

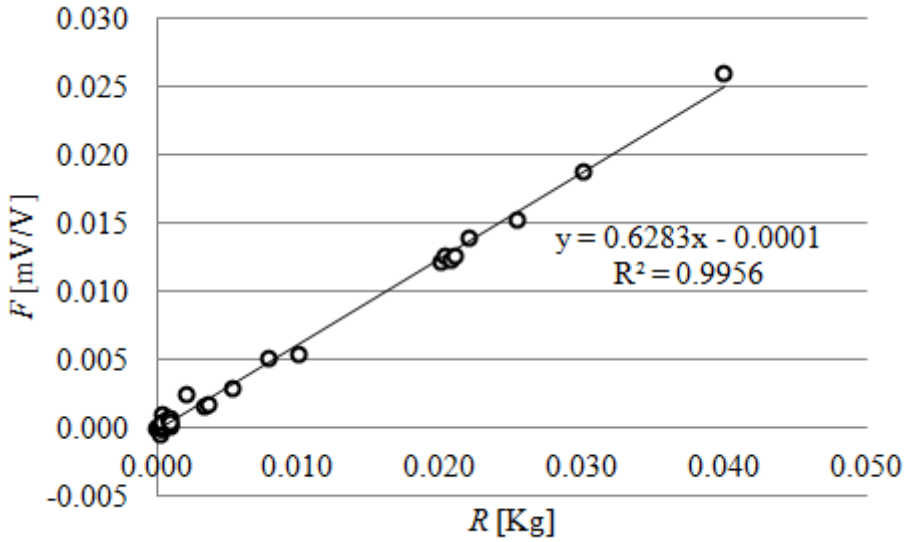

Figure 4.13: Calibration curve for the load cell, obtained by means of weights from 0.1 g to 40 g. In the figure, also the equation of the linear fitting curve calculated with least square method is represented.

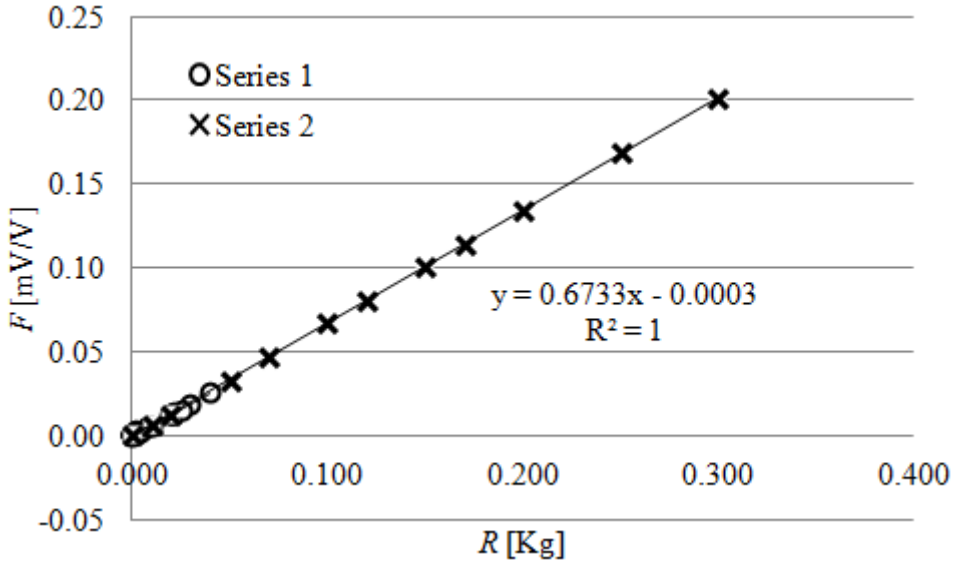

Figure 4.14: Calibration curves for the load cell, obtained by means of weights from 0.1 g to 40 g, for series 1, and weights from 10 g to 300 g, for series 2. In the figure, also the equation of the fitting curve for series 2, calculated with least square method, is represented.

Table 4.5: Parameters of the calibration curves.

range of weights	a [kg/(mV/V)]	b [kg]
$10 - 300$g	1.502	-0.000105
$0 - 40$g	1.586	0.000107

least square applied to the experimental data, the forces can be evaluated in $[\mathrm{kg}]$ as:

$$R = aF + b \tag{4.11}$$

in which R is the total force calculated in $[\mathrm{kg}]$, a is the slope of the calibration curve ($[\mathrm{kg}/(\mathrm{mV}/\mathrm{V})]$), F is the force measured ($[\mathrm{mV}/\mathrm{V}]$) and b is the y-intercept ($[\mathrm{kg}]$). The values for both the calibration curves are reported in Table 4.5.

For the calculation of forces, only the calibration curve for the range $0 - 40$ g is used, given that the differences between the two curves are not significant and that the loads measured in channel are of the same order of magnitude.

The measurements of forces

When the cylinder-load cell system is submerged in the water flow, the cylinder is perpendicular to the bottom of the channel (Figure 4.15), which is parallel to the predominant direction of the flow. In this condition the cell does not measure only the force exerted by the flow, but also the component of the weight in the x direction, since the channel has a slope equal to the slope necessary for reaching uniform flow condition. Hence, in order to calculate correctly the drag coefficient C_{Dp}, it is necessary to subtract the contribution of the submerged weight from the first measurements (Figure 4.15). The measurements of forces are obtainable with two experimental phases: firstly, the measurements are carried out in dynamic conditions (uniform flow condition); secondly, with the same condition of water depth, static conditions can be obtained by regulating the bulkhead downstream and by stopping the water flow (Figure 4.16).

Dynamic measurements are performed by immersing as much as possible the cylinder into the water, but not touching the bottom of the channel. The measurements are taken where the flow conditions are uniform - previously verified with

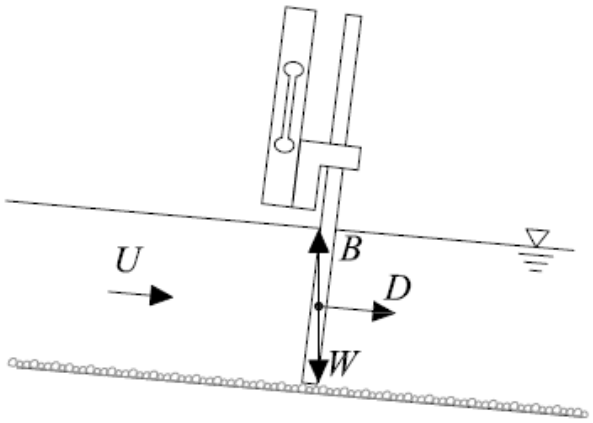

Figure 4.15: The set up of the cell during the measurements, and representation of the forces acting on the cylinder.

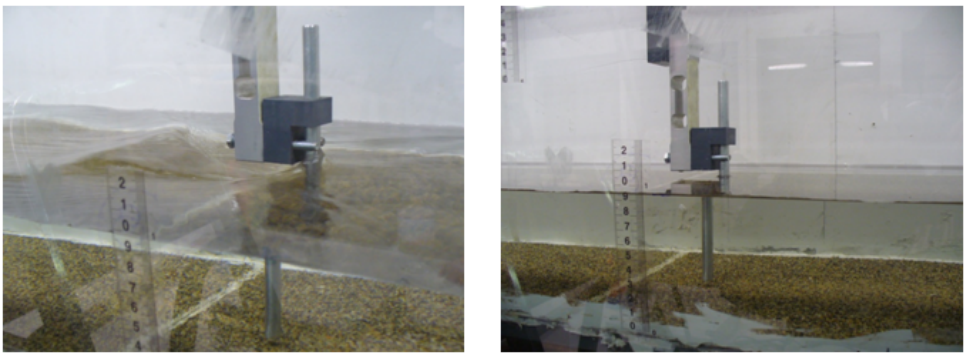

(a) dynamic condition (b) static condition

Figure 4.16: The two phases for measurements with load cell: (a) in dynamic condition of flow; (b) in static condition of flow

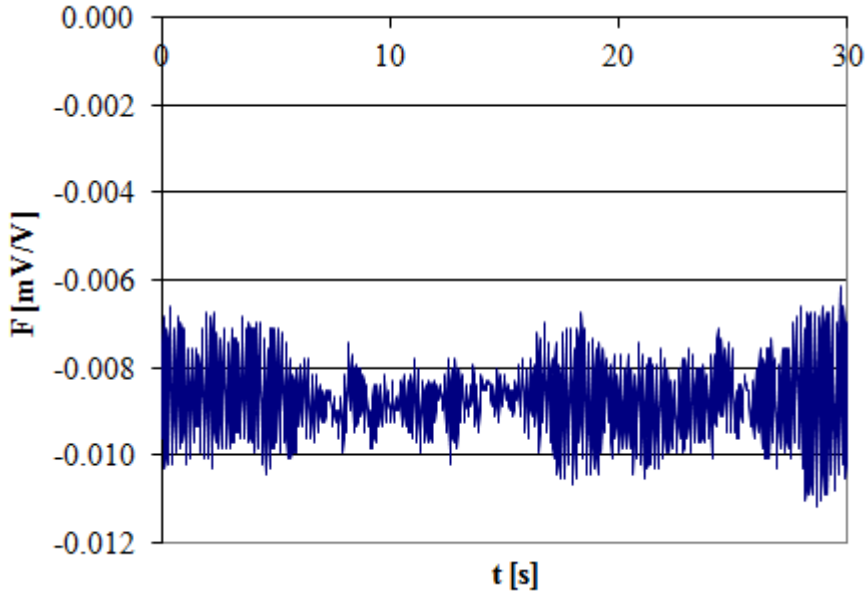

Figure 4.17: Example of the oscillating signal obtained with the load cell.

the velocity measurements. For static measurements, the cylinder position and the setup configuration are not changed, but the flow is slowed down by reducing the water flow as much as possible (until about $Q = 0.5\,\mathrm{l/s}$, which can be considered a negligible contribution to the force) and by maintaining the same water depth.

Generally, the signals registered with load cells are not constant, but they have an oscillating nature (Figure 4.17). The oscillations are due to two main causes: to the electronics nature of the instrument and to the oscillating nature of turbulent flow. The turbulent oscillations are the most important contribution to the signal oscillations.

Given that we are interested in the double-averaged quantity, the results are evaluated by averaging the output signals. However, the data analysis is made also calculating the errors of measure, which allow to determine the confidence of the oscillating nature of signals.

The result of each test is obtained evaluating the measured average force, $\overline{F}$, that is the difference between the average dynamic force, $\overline{F_{dyn}}$, and the average static force, $\overline{F_{stat}}$:

$$\overline{F} = \overline{F_{dyn}} - \overline{F_{stat}}. \tag{4.12}$$

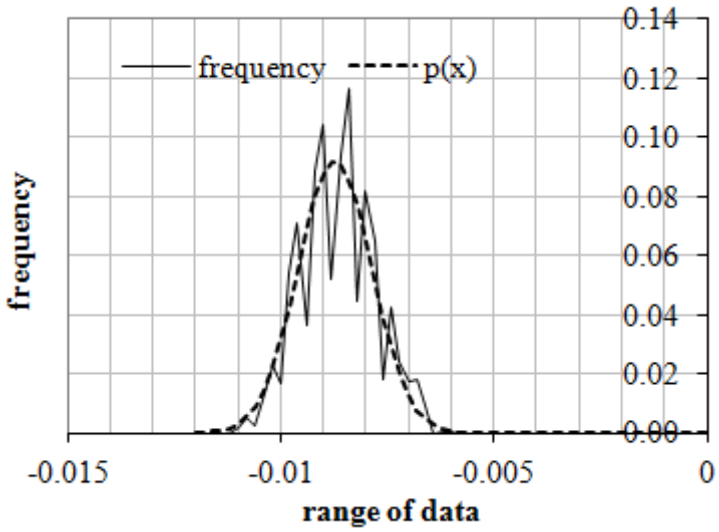

Figure 4.18: Example of the determination of Gaussian distribution of data, obtained for signal in Figure 4.17.

By using the calibration curve (Figure 4.13 and values in Table 4.5):

$$R_c = (a\overline{F} + b)g \tag{4.13}$$

where the resistance of cylinder, R_c, is expressed in [N], being g the gravity. Finally, the drag coefficient C_{Dp} can be calculated with the formula described in the Section 2.3.2:

$$C_D = \frac{R_c}{\rho A_c \frac{U^2}{2}} \tag{4.14}$$

where A_c is the cross section of the cylinder, that is $A_c = d_c h$, with d_c the diameter of cylinder and h the averaged water depth.

The evaluation of errors

For this kind of measurements, the evaluation of the uncertainties can be very useful for determining the reliability of the results. For this purpose, the theory of errors, as described in Doebelin (1990), is used. In this section, how the data are analyzed and how the interval of confidence is evaluated will be briefly described.

The errors committed in the determination of resistance (R_c) are due to two contributions: (i) instrumental errors due to problems of rumors, naturally presents in electronics signals and that can not be deleted; (ii) errors due to the calibration model. In the first case, the errors can be evaluated by determining the Gaussian distribution of signal (Figure 4.18). The normal distribution of data registered is characterized by the next equation:

$$p(x) = \frac{1}{\sqrt{2\pi}\sigma} \exp\left[-\frac{(x-\mu)^2}{2\sigma^2}\right] \tag{4.15}$$

where μ is the average of the sample of N data (of forces) $x = \{x_1, x_2, \ldots, x_N\}$, and it is defined as:

$$\mu = \frac{1}{N}\sum_{i=1}^{N} x_i \tag{4.16}$$

whereas σ is the standard deviation of the same sample, and it is defined as:

$$\sigma = \sqrt{\frac{1}{N-1}\sum_{i=1}^{N}(x_i-\mu)^2} \tag{4.17}$$

The value of force, considered also the uncertainty, is:

$$\overline{F} = \mu \pm k\sigma \tag{4.18}$$

where k is a confidence factor, definable with the statistical Student's t-distribution. For our measurements, having a number of data approximately near to infinity, if $k = 1.96$, then the probability that each datum is into the interval defined by $\overline{F}$ is equal to 95%.

The general equation for a curve of calibration is:

$$\hat{y}(x) = a_0 + a_1 x + a_2 x^2 \tag{4.19}$$

The coefficients in eq. (4.19) can be calculated by minimizing the mean square

error χ^2, defined as:

$$\chi^2 = \sum_{i=1}^{N} \left[y_i - \left(a_0 + a_1 x_i + a_2 x_i^2 \right) \right]^2 \tag{4.20}$$

that is the sum of the square of differences between experimental result y_i and the value obtained with the calibration curve. In terms of matrices:

$$\begin{pmatrix} N & \sum x_i & \sum x_i^2 \\ \sum x_i & \sum x_i^2 & \sum x_i^3 \\ \sum x_i^2 & \sum x_i^3 & \sum x_i^4 \end{pmatrix} \begin{pmatrix} a_0 \\ a_1 \\ a_2 \end{pmatrix} = \begin{pmatrix} \sum y_i \\ \sum y_i x_i \\ \sum y_i x_i^2 \end{pmatrix} \tag{4.21}$$

$$\mathbf{A}\vec{a} = \vec{b} \quad \rightarrow \vec{a} = \mathbf{A}^{-1}\vec{b} \tag{4.22}$$

It is normally termed *residual variance* of the approximation, the value calculated as:

$$\sigma^2 = \frac{\chi^2}{N - n_c} \tag{4.23}$$

in which n_c is the number of coefficients of the fitting curve. The errors of the same coefficients can be evaluated as:

$$\sigma^2_{a_{i-1}} = A^{-1}_{ii}\sigma^2 \tag{4.24}$$

Hence, by considering a generic expression for the curve calibration:

$$\hat{y}(x) = a_0 + a_1 x \tag{4.25}$$

From eqs. (4.19) to (4.23), the errors can be expressed as:

$$s_(a_0)^2 = \frac{\sigma^2}{N} \quad \text{and} \quad s_(a_1)^2 = \frac{\sigma^2}{\sum x_i^2} \tag{4.26}$$

and the coefficients are:

$$\tilde{a_0} = a_0 \pm s_(a_0) \quad \text{and} \quad \tilde{a_1} = a_1 \pm s_(a_1) \tag{4.27}$$

The final error can be determined by composing the errors of the force mea-

surements with the errors due to the calibration. By considering a generic function z of several variables $z = f(x, y, \ldots)$, the propagated error is determinable with the next differential law:

$$\sigma_z^2 = \left(\frac{\partial f}{\partial x}\right)^2 \sigma_x^2 + \left(\frac{\partial f}{\partial y}\right)^2 \sigma_y^2 + \ldots \tag{4.28}$$

Applied to our case (eqs. 4.12 and 4.13) :

$$\overline{F} = \overline{F_{dyn}} - \overline{F_{stat}} \quad \rightarrow \quad s_F = \sqrt{s_{F_{dyn}}^2 + s_{F_{stat}}^2} \tag{4.29}$$

$$R_c = (a\overline{F} + b)g \quad \rightarrow \quad s_{R_c} = \sqrt{\overline{F}^2 s_{a_1}^2 + a_1^2 s_F^2 + s_{a_0}^2} \tag{4.30}$$

After the evaluation of the error s_{R_c}, the error on the evaluation of drag coefficient can be determined. By defining the drag coefficient as in eq. (4.14), not only the force measurement is source of errors, but also the measurements of water depth h and velocities U and U_1.

The errors of U depend on the errors in measurements of water discharge and water depth, by considering that $U = Q/(Bh)$, where B is the width of the channel. Water depth and water discharge can be treated as statistical variables, thus their averaged values m_Q and m_h can be determined as:

$$m_Q = \frac{1}{N_Q} \sum_{i=1}^{N_Q} Q_i \tag{4.31}$$

and

$$m_h = \frac{1}{N_h} \sum_{i=1}^{N_h} h_i \tag{4.32}$$

where N_Q and N_h are, respectively, the number of data collected for water discharge and water depth. As far as concern the variances of water discharge s_Q and water depth s_h:

$$s_Q = \sqrt{\frac{1}{N_Q - 1} \sum_{i=1}^{N_Q} (Q_i - m_Q)^2} \tag{4.33}$$

and

$$s_h = \sqrt{\frac{1}{N_h - 1} \sum_{i=1}^{N_h} (h_i - m_h)^2} \tag{4.34}$$

Finally, the values of water discharge and water depth are:

$$Q = m_Q \pm k s_Q \tag{4.35}$$

$$h = m_h \pm k s_h \tag{4.36}$$

with k confidence factor determinable with the Student's t-distribution as a function of the number of data collected.

From the eq. (4.14) and by considering the variables that are measured during a test, the drag coefficient can be expressed as:

$$C_D = \frac{2 R_c B^2 h}{\rho Q^2 d_c} \tag{4.37}$$

Hence, from eq. (4.28) the final error is:

$$\begin{cases} s_{C_D}^2 = \left(\dfrac{\partial C_D}{\partial R_c}\right)^2 s_{R_c}^2 + \left(\dfrac{\partial C_D}{\partial Q}\right)^2 s_Q^2 + \left(\dfrac{\partial C_D}{\partial h}\right)^2 s_h^2 \\ \dfrac{\partial C_D}{\partial R_c} = \dfrac{2 B^2 h}{\rho Q^2 d_c} \\ \dfrac{\partial C_D}{\partial Q} = -\dfrac{4 R_c B^2 h}{\rho Q^3 d_c} \\ \dfrac{\partial C_D}{\partial h} = \dfrac{2 R_c B^2}{\rho Q^2 d_c} \end{cases} \tag{4.38}$$

From the eq. (4.38):

$$\frac{s_{C_D}^2}{C_D^2} = \frac{s_{R_c}^2}{R_c^2} + \frac{4 s_Q^2}{Q^2} + \frac{s_h^2}{h^2} \tag{4.39}$$

For the definition of the average velocity U_1 in eq. (4.10), the evaluation of the errors is different. The errors of the average velocity are due to:

1. the evaluation of the time-averaged velocity for each z. The error must be

determined by considering the definition of temporal average:

$$\mu_{u_1} = \frac{1}{n_t} \sum_{i=1}^{n_t} u(t, z) \tag{4.40}$$

where n_t is the number of instants of measure, $u(t, z)$ is the instantaneous velocity for the point at z. The variance is:

$$\sigma_{u_1} = \sqrt{\frac{1}{n_t - 1} \sum_{i=1}^{n_t} \left(u(t, z) - \mu_{u_1}\right)^2} \tag{4.41}$$

Hence, the time-averaged velocity with its error is:

$$\overline{u_1(z)} = \mu_{u_1} \pm k_1 \sigma_{u_1} \tag{4.42}$$

In eq. (4.42) k_1 is the constant determinable with the Student's t-distribution for an infinite number of data.

2. the average of the profile:

$$U_1 = \frac{1}{n_z} \sum_{i=1}^{n_z} \mu_{u_1} \pm (k_1 \sigma_{u_1} + k_2 \sigma_{U_1}) \tag{4.43}$$

where σ_{U_1} is the variance for the spatial averaged velocity and k_2 is another Student's t, evaluated for the number n_z of measurement points along the water depth.

The error for U_1 is $s_{U_1} = k_1 \sigma_{u_1} + k_2 \sigma_{U_1}$. By using the theory of propagation (eq. 4.28) and the errors for the water depth (eq. 4.34) and for the force (eq. 4.30), the final error for the drag coefficient is:

$$\frac{s^2_{C_{D1}}}{C^2_{D1}} = \frac{s^2_{R_c}}{R^2_c} + \frac{s^2_{U_1}}{U^2_1} + \frac{s^2_h}{h^2} \tag{4.44}$$

At this point, all the terms necessary to determine the relative errors have been defined.

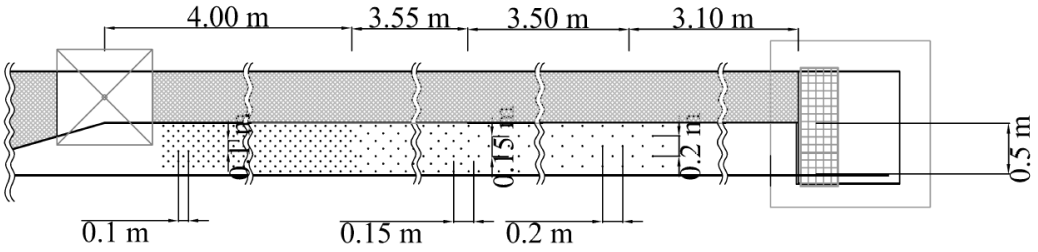

Figure 4.19: Planimetric view of the channel for measurements of drag force in staggered configuration.

4.3.2 Direct measurements for a staggered distribution of cylinders

For these measurements, the staggered distributions and the kind of the utilized cylinders are the same of the experiments with sediment transport, which have been already described in this chapter at Section 4.2.2. In this way, it is possible to compare the results obtained with these tests and with the tests related with sediment transport.

The laboratory channel

As in the precedent paragraph (Section 4.3.1), the tests are carried out in the part of channel with fixed bed, but the channel is $50\ \mathrm{cm}$ wide (Figure 4.19).

For these tests, the three configurations with different densities of plants are arranged in series. Hence, in order to obtain uniform flow conditions, the bottom of the flume assumes a particular arrangement: the bottom was lifted where the stem densities changed. As already explained in Section 4.2.4, in the mobile bed tests at the interface between the plant distributions, the bed raises for a narrow stretch, due to the reduction of the flow resistance. In the tests with mobile bed, the step was measured and the averaged raising was calculated. The bottom raising in the fixed bed has been created after analyzed the measurements done in the tests with mobile bed. The obtained results are represented in Figure 4.20.

Also in this setup, grain sediments were glued to the bed in order to render the bed roughness comparable to the grain roughness in the tests with mobile bed.

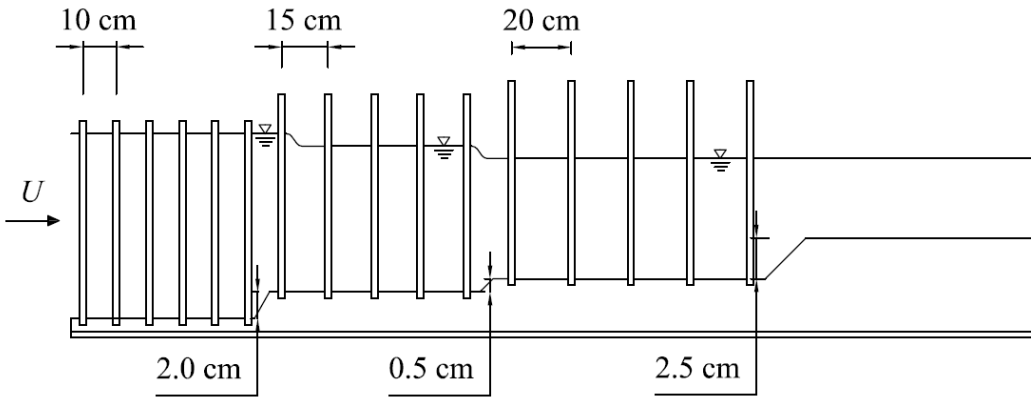

Figure 4.20: For obtaining uniform flow condition in each partition at fixed bed, the bottom of the channel is lifted as in the scheme depicted.

Table 4.6: Technical characteristics of the load cells.

name of load cell	PW4M	PW2C
load cell position	sparse configuration	intermediate and dense configuration
maximum capacity	3 kg	7.2 kg
minimum loaded	0.5 g	0.5 g
max. platform size	300 mm	380 mm

The measurement of forces

For the measurements, three different load cells are contemporarily used, each of them for a different density of vegetation. The technical characteristics of the cells are (Table 4.6): in the dense and intermediate configurations, the used load cells have a maximum load of 7.2 kg, whereas the cell used in sparse configuration is the same of the tests described in Section 4.3.1, with maximum load of 3 kg. The calibration of the cells was done as described for the smallest cell in Section 4.3.1, and the results are reported in Figures 4.21 and 4.22; the values of the slopes and intercepts of calibration curves are reported in Table 4.7.

The load cells were fixed to the channel and to two rows of cylinders with the system shows in Figure 4.23. The number of cylinders fixed to every load cell changes depending on the density of stems: $N_p = 10$ cylinders for the dense configuration, $N_p = 7$ for the intermediate configuration and $N_p = 5$ for the

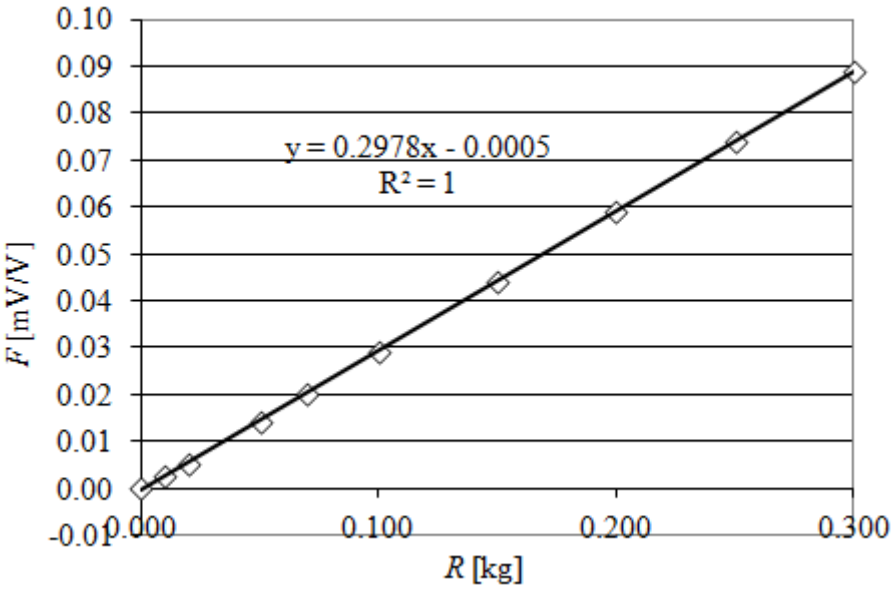

Figure 4.21: Calibration curve for the load cell used for measurements in dense distribution of stems

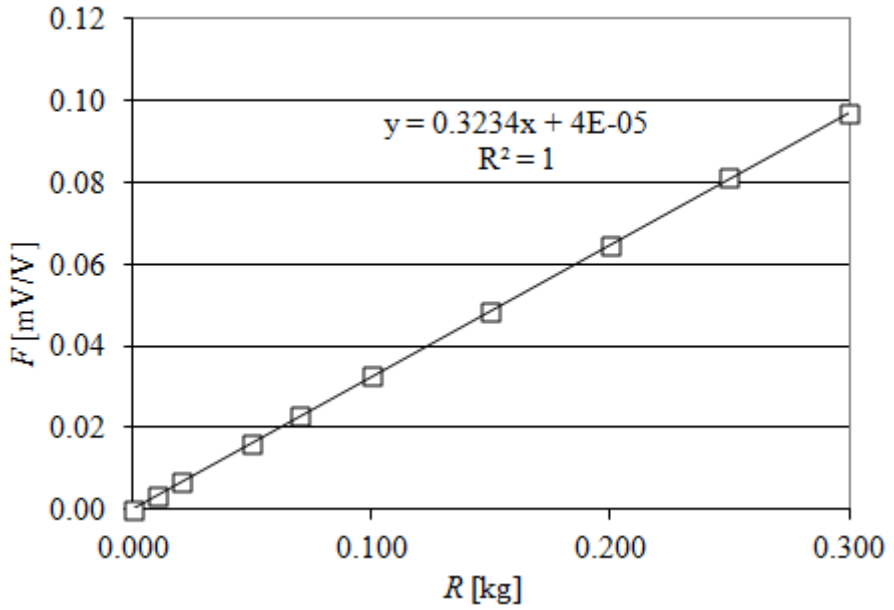

Figure 4.22: Calibration curve for the load cell used for measurements in intermediate distribution of stems

Table 4.7: Parameters of the calibration curves.

position of load cell	range of weights	a [kg/(mV/V)]	b [kg]
sparse configuration	$10 - 300$ g	1.502	-0.000105
intermediate configuration	$10 - 300$ g	3.092	0.000123
dense configuration	$10 - 300$ g	3.358	0.001650

sparse configuration. The cells are at least 1.5 m distant from the beginning of the relative configuration, that is a sufficient space to obtain uniform flow conditions. Each reach is considered in uniform flow condition if the measured water depth, obtained by means of the pointer gauge, along the reach is uniform, as defined in Section 2.3.4.

A system for micromovement allows to the cylinders, fixed to cell, the vertical movements. In this way the cylinders can be immersed as much as possible, maintaining, as in the case of the isolated cylinder (Section 4.3.1), a minimum distance from the bed (Figure 4.23).

The acquisition of data is done at a frequency of 50 data per second and a sufficiently large time of acquisition, in order to have a number of data sufficient to obtain the stabilization of the cumulative average of data and cumulative average of the data variance.

The results are obtained by substraction of static measurements from dynamic measurements (see section 4.3.1) and also the uncertainties of measurements are calculated. Finally, the drag coefficient C_{Dp} is determined by considering the equation for calculating the drag. In addition, the drag of the plants is the sum of the drag of each plant. Hence, for this experimental setup:

$$C_{Dp} = \frac{R_p}{N_p \rho h d_p \dfrac{U^2}{2}} \tag{4.45}$$

where R_p is the resistance obtained by measurements, N_p is the number of stems fixed to the load cell, d_p is the diameter of stems. The averaged velocity U, in this case, can be evaluated considering also the presence of cylinders which reduces

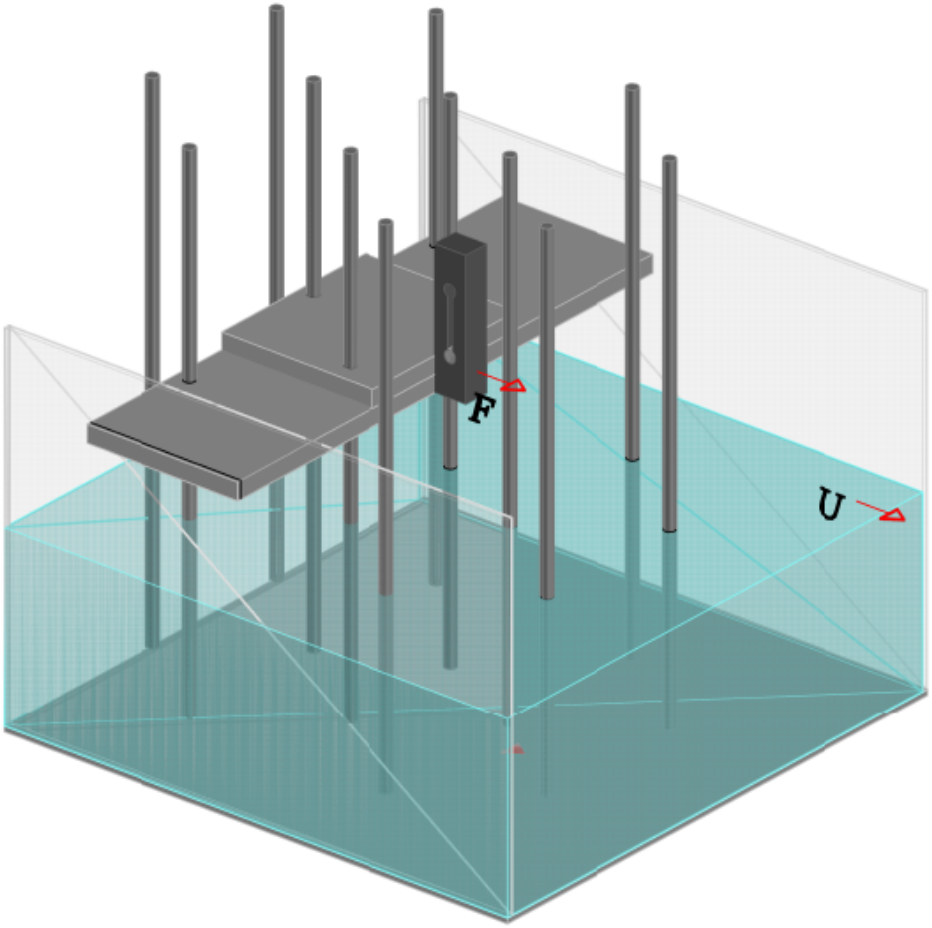

(a) 3D view

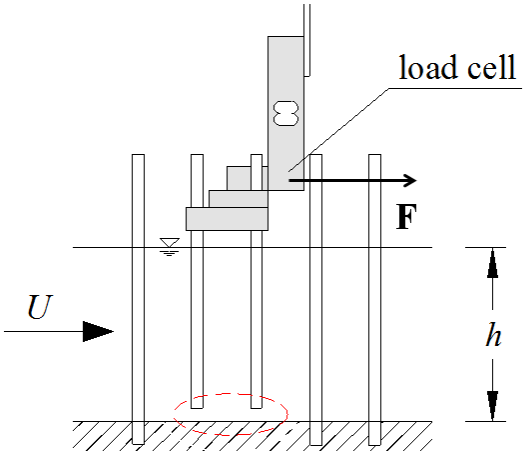

(b) section

Figure 4.23: Image of the set up of the load cell fixed to the cylinders

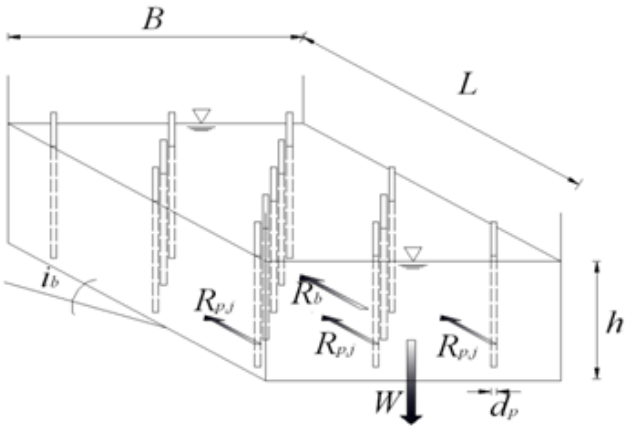

Figure 4.24: The forces in action in a vegetated riverbed. R_b identifies the bed roughness, that is grain roughness together with bed forms stress.

the free section for the flow. Hence the velocity U is defined:

$$U = \frac{Q}{B(1-\Omega_v)h} \tag{4.46}$$

where Ω_v is the density of vegetation, that is:

$$\Omega_v = \frac{n_p \pi d_p^2}{4} \tag{4.47}$$

with n_p number of plants per meter square.

4.3.3 Indirect measurements of drag coefficient

The main aim of the study on resistance is the comparison between the drag coefficient obtained with the direct measurements, described up to now, and the drag coefficient calculated through the balance of momentum applied to the channel in mobile bed conditions and sediment transport.

By considering a control volume containing a sufficiently large number of cylinders (Figure 4.24), the balance of momentum in the channel, in uniform flow condition and by neglecting the contribute of bed forms, gives the expression in

eq. (2.39) (Section 2.3.5):

$$C_{Dp} = \frac{\pi}{2}\frac{1-\Omega_v}{\Omega_v}\frac{d_p}{h}\left[\frac{ghi_b}{U^2} - \frac{g}{21.1^2}\left(\frac{d_{50}}{h}\right)^{1/3}\right] \tag{4.48}$$

All the variables in eq. (4.48) are evaluated during the tests related with sediment transport (see Section 4.2). Hence the tests in sediment transport conditions allow also the comparison of drag coefficients for direct and indirect measurements.

4.4 Measurements of flow field

In order to express the relationships between the presence of vegetation and the movement of grains, it is fundamental to understand how plants modify the hydrodynamics of flow field. The study of these relationships has been one of the main object of this part of the project.

In order to evaluate the velocity field through the cylinders, the Particle Image Velocimetry (PIV) technique is used. This experimental method is widely used in fluid dynamics because it gives simultaneous and detailed information on turbulent fields.

4.4.1 The PIV Technique

The PIV technique born in the eighties following the studies of Prandtl (Prandtl 1935) and his experiments with illuminated particles in motion with a viscous fluid. Since then, the PIV has been used in order to map instantaneous velocities fields (Adrian 1991). First advantage of the PIV technique is that it gives detailed and high-resolution information on the vectors of velocity in the whole domain of investigation with an only test, while the methods known until then had needed a large number of experiments (Raffel and Kost 1998).

Nowadays, this technique is often preferred to other methods of investigation in many fields of research, from fluid-dynamic to mechanical engineering. It was used to study air flow and water flow around objects, airfoils and other physical models (Adrian 1991; Stanislas, Kompenhans, and Westerweel 2000). Since

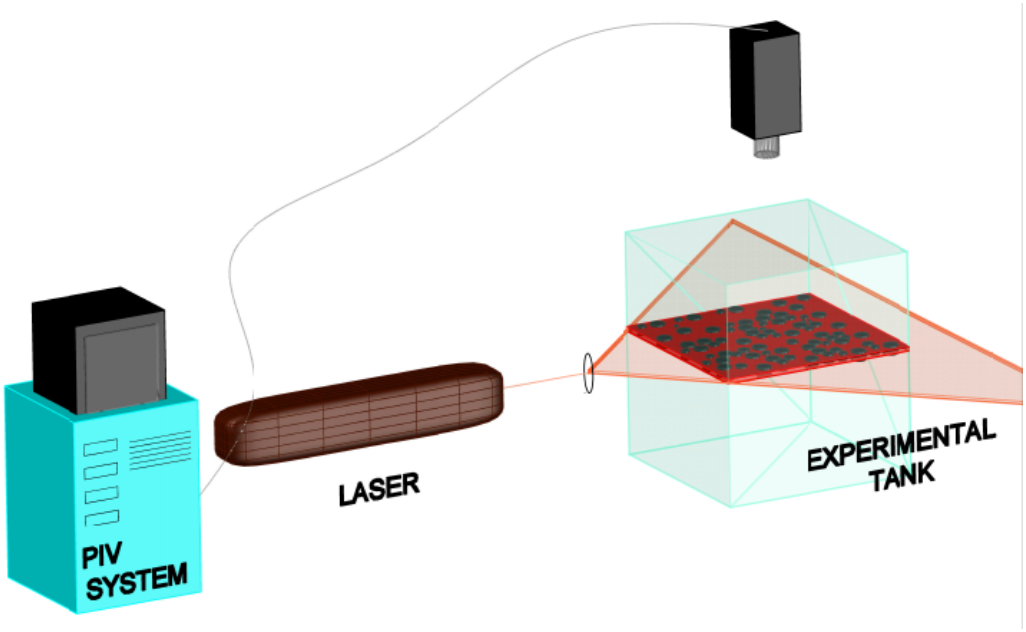

Figure 4.25: Schematic representation of PIV experimental set up

nineties, PIV technique has been also applied to biological and biogenic research (e.g: Stamhuis and Videler (1995) and Zirbel, Veron, and Latz (2000)).

Principle of PIV

The PIV technique, as the Particle Tracking Velocimetry (PTV) and the Particle Streak Velocimetry (PSV), is a *full field* method of measurement of velocities. These three methods are based on acquisition and elaboration of images of a fluid in motion, which is seeded by particles that are visible if illuminated by a strong light (pulsating or continue).

The so called PIV 2D could be defined as a mapping of average displacements of a group of particles in motion with a fluid. The mapping can be obtained by correlating an image with the next one. The images are taken at a very high frequency of acquisition.

The PIV method needs: a fluid in motion, a light source and, generally, particles for seeding the fluid. The used light must create a perfect and thin light sheet. Normally, a laser is the best choice, because its light is sufficiently strong.

In Figure 4.25, the experimental setup for PIV method is schematically repre-

sented:

1. the fluid is seeded with particles which can move together with the fluid;
2. a light sheet illuminates, thanks to a laser beam, a rectangular zone into channel (domain of measure);
3. a high-speed camera takes photographs for a certain period at high frequency of acquisition.

The seeded particles must have a density comparable to the density of water, because it is assumed that the velocity of each particle is equal to the velocity of flow.

The velocity field is obtained by elaborating each couple of the taken images: a small area (*interrogation area*) of the first image is compared with a larger area, which contains the interrogation area, of the second image. The particle velocity is calculated by using the statistical method of the cross-correlation, better described in Section 4.4.4.

For calculating the particle displacements, it is assumed that the particles move uniformly, so that the behavior of each particle can be described with a single vector for each couple of images used in the analysis. The same analysis is done for all the interrogation areas until to complete the whole domain and obtain the map of the instantaneous velocities (for each couple of images).

Characteristics of PIV technique

In the following, advantages and disadvantages of the PIV technique are briefly described:

1. it is a *full field* technique: the PIV permits to acquire images, and hence information, of an extended surface;
2. the PIV has an optimal spatial resolution, but the post-processing is quite elaborate; on the contrary, other methods allow to obtain results almost in real time;
3. indirect measurements of velocity: the PIV technique does not measure the velocity of fluid, but it actually measures the velocity of particles in motion with fluid;
4. non intrusive measurements: the PIV technique does not need probes or

other instruments to insert into fluid, because it works with optical proceeding. This characteristics is important for high velocity flows, turbulent flows and boundary layers;

5. PIV 2D is used for determining two components of velocity. Nevertheless, some innovative methods based on PIV 2D allow the determination of the third component using two cameras in the same time and some oleographic techniques.

4.4.2 The instruments used for the PIV

While in the previous section (Section 4.4.1) the characteristics and instruments for PIV technique are reported, in this section the experimental setup used for the research will be described.

Set up of the channel

In PIV tests, the right part of the channel is used with only one configuration of stems. In fact, since elaboration is very long, only the staggered intermediate configuration is used for measurements. The channel is as wide as in the case of sediment transport ($50\ \mathrm{cm}$) and the measurements are carried out in the center of the channel ($x = 8\ \mathrm{m}$ from upstream). The diameter of cylinders is $1\ \mathrm{cm}$ and the considered density of cylinders is $\Omega_v = 0.0073$. In order to render the grain roughness, sediments are pasted on the bottom. The pasted material is the plastic material used for tests with sediment transport, which has grain size $d_{50} = 0.55\ \mathrm{mm}$.

The water flow is recirculated in a close circuit and it is measured by the electromagnetic flowmeter. The uniform flow conditions are obtained with the bulkhead at downstream of the flume.

Methods of illumination

As already explained, in the PIV measurements both the initial position and the final position of particles must be registered. In order to obtain reliable results, we need a correct illumination. The illumination system:

- must have a sufficient light to allow the registration of the light reflected by particles. The smaller particles are, the better they follow the fluid, but the light they need is stronger;

- the light must be brilliant and stable;

- position and dimension of light sheet must be easily definable and measurable.

Laser beams are with no doubts the best method for illuminating the domain for PIV measurements. The most commonly used kind of laser is the Nd:Yag, that can be used in mode of pulsed or continuous light. In the project, the continuous modality is preferred to the pulsing modality. The Nd:Yag is a solid state laser: the active medium is a crystal; laser beam is generated by ions Nd^{3+} (neodymium) incorporated in crystals YAG (Yttrium-Aluminium-Granatum). The energy released by a pulse is from 10 to 400 mJ in a period of $5 \div 10$ ns.

The camera

The two high-speed cameras used for measuring the flow field are the FASTCAM X 1024 PCI by PHOTRON. They utilize a super light sensitive 10-bit CMOS sensor, 17 micron square pixels large. The CMOS (Complementary Metal Oxide Semiconductor) sensors are, together with the CCD (Charge-Coupled Device) sensors, the best technology for taking high-speed photos. Both CCD sensors and CMOS sensors capture the light in a grid formed by pixels, but they are different in the production and for the method of elaboration of images. With respect to the CCD sensors, the CMOS sensors have a higher speed in images processing, reducing the elaboration time.

The cameras are able to take 1000 frames per second at the maximum resolution of 1024 x 1024 pixel, but reducing the resolution, the maximum velocity is 109500 fps. The averaged velocity of the flow considered for the tests is about 14 cm/s. Hence, it is chosen to work with the maximum resolution and an acquisition velocity of 250 fps, which is sufficient to evaluate the cross correlation between particles in motion.

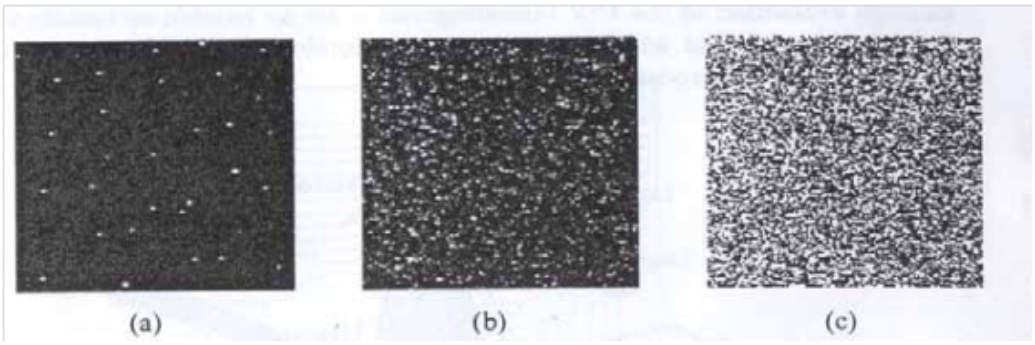

Figure 4.26: Examples of different concentration of seeded particles in the fluid: (a) *Low density*: particles can be recognized and correlated, but the data analyzed do not allow a complete mapping of the domain; (b) *mean density*: particles can be recognized and correlated; (c) *high density*: particles cannot be correlated and sometimes not even discernible.

The particles for seeding

For seeding the flow, it was chosen to use particles of sieved cedar pollen. The grain size used in the experiments is smaller than $256\ \mu\mathrm{m}$. The seeding is done sufficiently upstream the zone of measurements, introducing into the flow the particles already mixed with water. An important variable for correct measurements is just the optimal concentration of particles (Figure 4.26): too low concentration means that there are not a sufficient number of particles to obtain a complete mapping of velocities in domain; too high concentration, and the post-processing program does not recognize the particles and the displacements.

4.4.3 The set up for the measurements

Before to proceed with measurements, it is necessary to obtain the optimal configuration for the tests. For the mapping of horizontal planes, the light sheet must be perfectly parallel to the bottom. For the vertical mapping, the laser must be arranged in order to have the light sheet perpendicular to the bottom and orientated with the x-axis, coincident with the main flow direction. A non perfect alignment of the light sheet adds significant errors to the results.

Thanks to the symmetrical distribution of cylinders, all the flow field is described with the 12 vertical planes in Figure 5.34. In addition, a single test for the

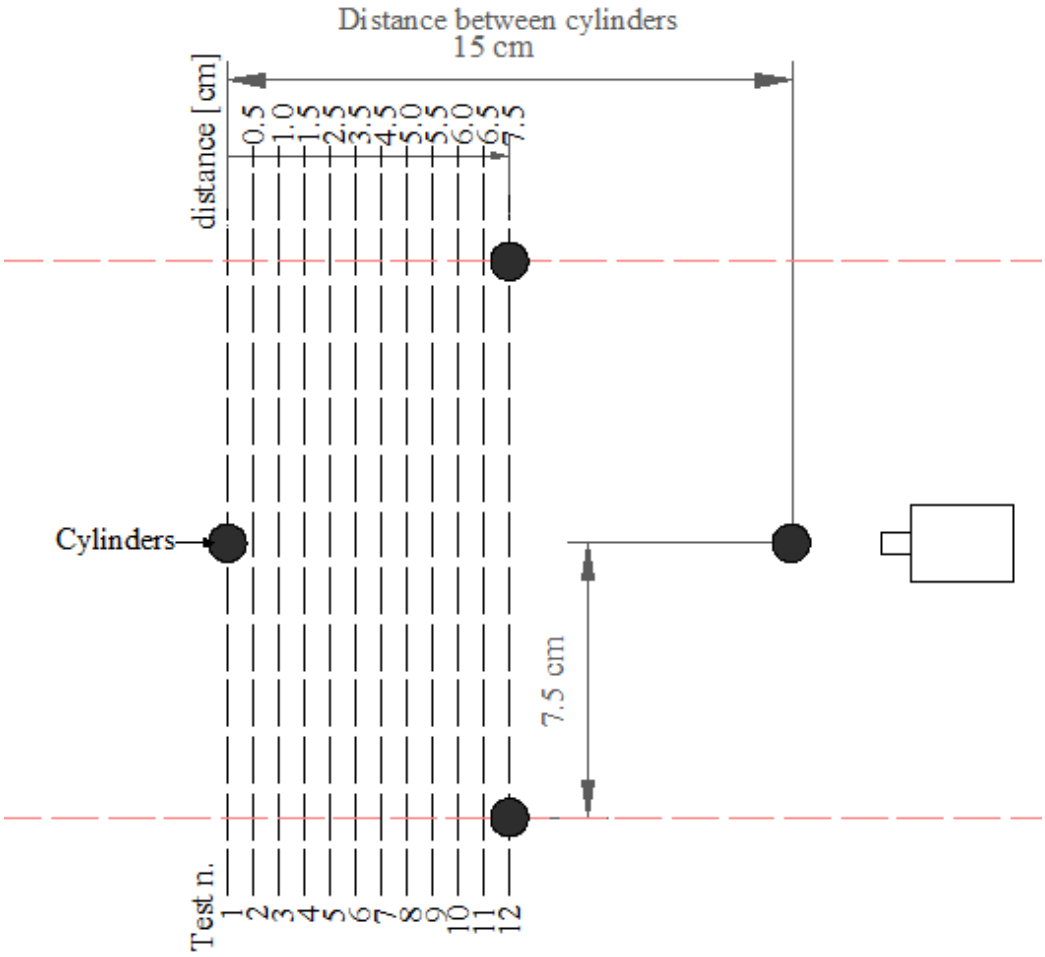

Figure 4.27: The 12 vertical planes of measurements among the cylinders.

horizontal plane at $1/4$ of the water depth from the bottom was carried out. This test is useful to see the wake downstream a cylinder.

The flow is extremely turbulent and hence the free surface is oscillating. In order to avoid the oscillation, which might give problems of reflection of the light, a thin prism in plexiglass is posed in correspondence to the free surface (Figure 4.28). CClearly the prism affects the region of the flow field closer to the free surface (about $1/5$ of the water depth), which hence will be discarded.

The two cameras are used in the same instant. For the horizontal plane, they are located above the channel. For the vertical planes, they are located close to the lateral wall and they are not parallel (Figure 4.29). This position allows to

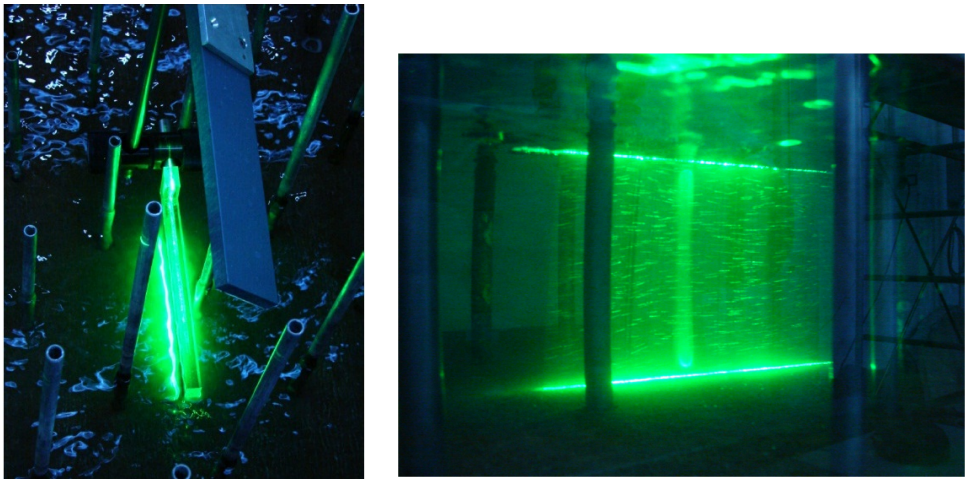

(a) (b)

Figure 4.28: Photo representing the light sheet which forms the vertical layer (plane) for measurement; in the photo (a) is shown also the prism of plexiglass used to smooth the free surface, in order to avoid possible reflections of laser light.

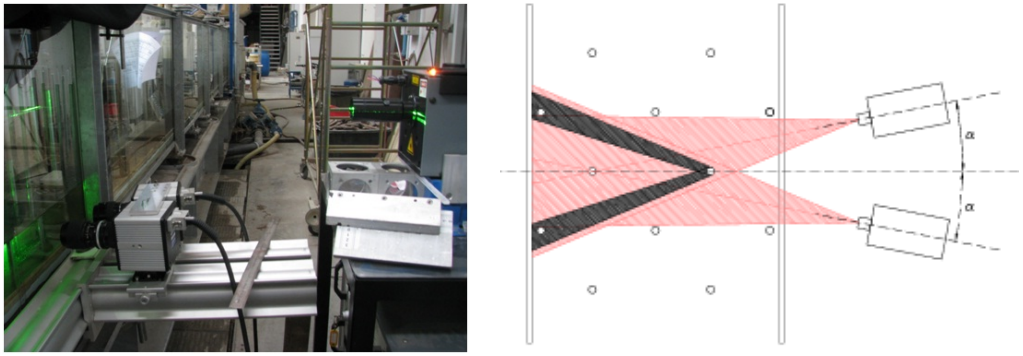

(a) (b)

Figure 4.29: In the photo (a) the two cameras in the position for acquisition of the images for tests; in the drawing (b) is shown which is the position and the angle of cameras for the best acquisition.

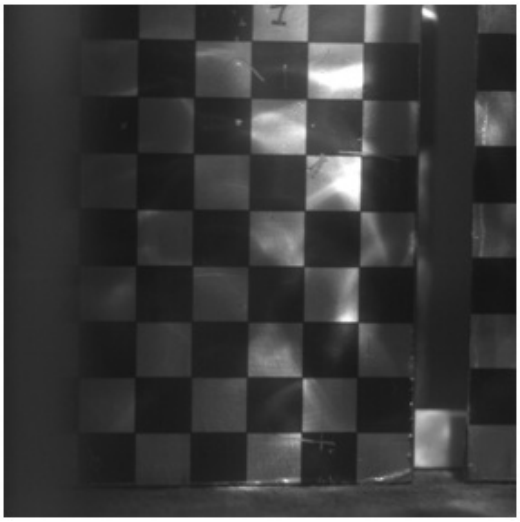

Figure 4.30: Photo of the target immersed in the flow. The target is used for the calibration, rectification and focus of images.

extend the visible field for the cameras, limiting the effect of obscuration due to the presence of cylinders in front of the light plane. If the laser ray is perfectly aligned, then the cameras can be crooked with respect the perpendicular to the light sheet, because during the pre-processing, all the effects of deformation of images are adjusted. The rectification is done using a target (see Figure 4.30), which is used also for the calibration of the images. The acquisition of the target image has several functions:

- it makes easier the focus;
- it allows to understand which is the domain that will be analyzed, and to change it if need be;
- the target image quantifies the necessary rectification for correcting the images for the post-processing (Section 4.4.4);
- it gives the calibration value, that is the number of pixels per centimeter $[(\mathrm{pxl}/\mathrm{cm})]$ in the reality.

Clearly, before each test the target must be removed for starting with the seeding of particles and the actual measurements.

4.4.4 Process for PIV results

In this Section, we will present the whole process which is necessary to obtain the field velocities in the analysis domain. After the images acquisition, the longest part of the PIV technique is the data processing. Data processing has been performed by means of a commercial software (Flow Manager Dantec®) and by means of post-processing routines written in MatLab®. Before of PIV processing, images have been rectified in order to avoid the distortion due to non orthogonal acquisition.

The acquisition of images

The images are taken with the program Photron Fastcam Viewer, which allows to set up the cameras (shutter and frequency of acquisition). For each plane of measure, 5000 images are registered and the acquisition is done at least 3 times, in order to have a number sufficiently large of images to process.

The pre-processing program

The pre-processing program is necessary in order to improve the quality of images to use in the subsequent program, which calculates the cross-correlation among the particles. In particular the pre-processing program:

1. cancels from the image what it is not particles or fluid;
2. treats and rectifies the images.

The first step is done to come closer to the ideal situation for elaboration of images, which is to have white particles that move on a black background. The images registered with the cameras, notwithstanding the use of the best technical solution, have imprecision on colors due to the presence of zones of reflection, not homogeneity in the illumination, reflection on the lens. The Matlab®subroutine uploads all the images and calculates the minimum values, which correspond to what is not particles in motion. Then it subtracts the common part from all the images and saves the new images (see Figures 4.31).

The second step of the pre-processing program is the analysis of the angle of deviation and deformation of images. The deformation of an image is quantified by comparing the target image with a regular grid (Figure 4.32), built with a

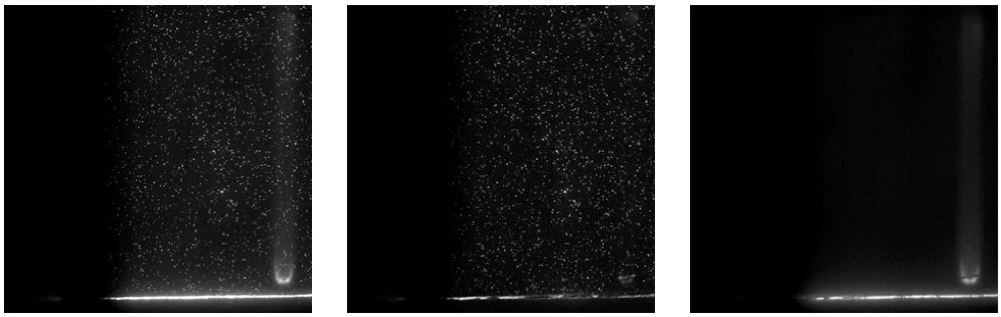

(a) original photo (b) managed photo (c) the minimum subtracted

Figure 4.31: In the photos: (a) the original image to analyze; (b) the photo after the subtraction of the minimum; (c) the minimum calculated by the MatLab®codex.

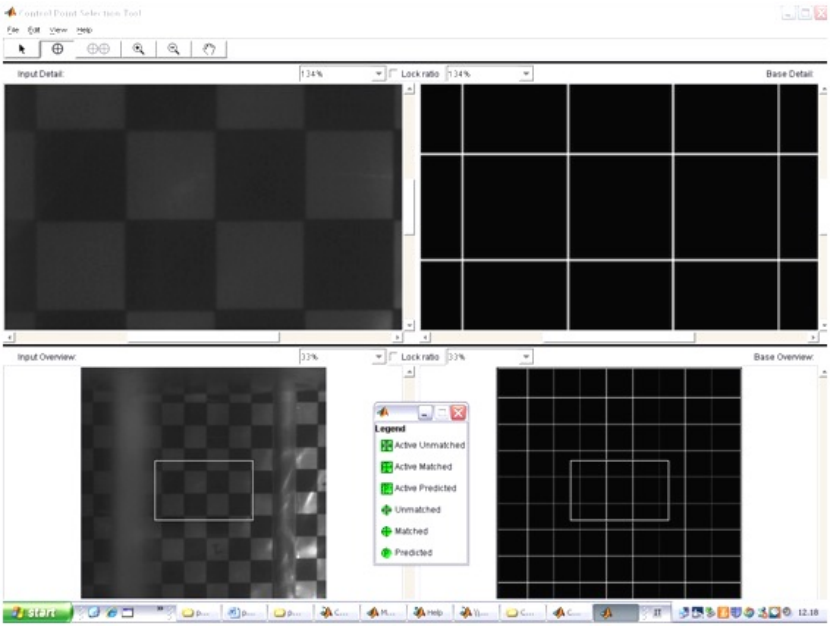

Figure 4.32: The MatLab®interface for rectification of images: at the left side, the target image; at the right side, the regular grid used as comparison for the rectification.

CAD program. The images are then rectified by applying a mathematical model generally used for the analysis of orthophotos.

The results of this pre-process are perfectly flat (and not deformed) images, which represent the seeded particles with a good precision.

The program Flow-Manager

The Flow Manager®is a program by Dantec, furnished together with the laser. This program allows the elaboration of the images in output from the pre-process program. In particular, the Flow Manager®allows several elaborations for evaluating: cross-correlation, the validity of results, the possible use of filters, derivatives. Several instruments are available for the elaborations of images: masking, chains of analysis, statistics, elaboration of images.

For obtaining the results, it was chosen to use Flow Manager®only for the cross-correlation, while the statistical analysis is made in a post-processing program written in MatLab®language.

Before the cross-correlation, the whole sample of images must be masked. The masking allows to eliminate some parts where the cross-correlation should not be done, for instance where the light is not sufficient to illuminate correctly the particles; or where the presence of a cylinder darkens a part of the image. The target image helps the determination of zones for masking (see Figure 4.33).

The cross-correlation

In order to determine the position of a particle, the Flow Manager®analyzes the density of illumination of each point of the image using the function called ”point spread”. By considering that the density of a light coming from a pinhole camera is characterized by a Gaussian distribution, similarly the point spread function considers that the light density for small particles follows a Gaussian distribution $\tau(x)$ in coordinates x and y. In this way, the Flow Manager®can recognize the position of each particle in the domain.

By using a convolution equation, the function $\tau(x)$ can be centered on a single

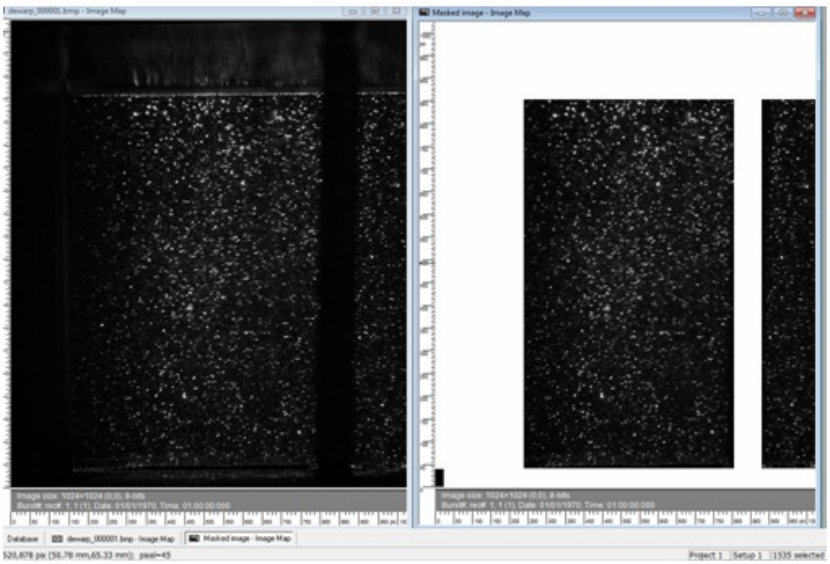

Figure 4.33: The same image before and after the masking

particle localized in a point with coordinates x_i:

$$\tau(x - x_i) = \tau(x) * \delta(x - x_i) \tag{4.49}$$

where $\delta(x - x_i)$ is the Dirac delta function.

By assuming that the particles in the fluid are small, the intensity function I for an image containing a number N of particles can be expressed as:

$$I(x, \Gamma) = \tau(x) * \sum_{i=1}^{N} V_0(X_i)\delta(x - x_i) \tag{4.50}$$

where x is the position of the image plane; Γ is the distribution of particles in the instant t; $V_0(X_i)$ is a function which expressed the light energy transferred from the object plane (X) to the correspondent image plane (x) (Figure 4.34).

Actually, the intensity of light of a particle depends on several parameters (e.g: reflection properties, particle position and optical properties). For making it easier, these factors are considered constant, but some variable weights are introduced as a function of the particle position X_i:

$$V_0(X) = W_0(X, Z)I_0(Z) \tag{4.51}$$

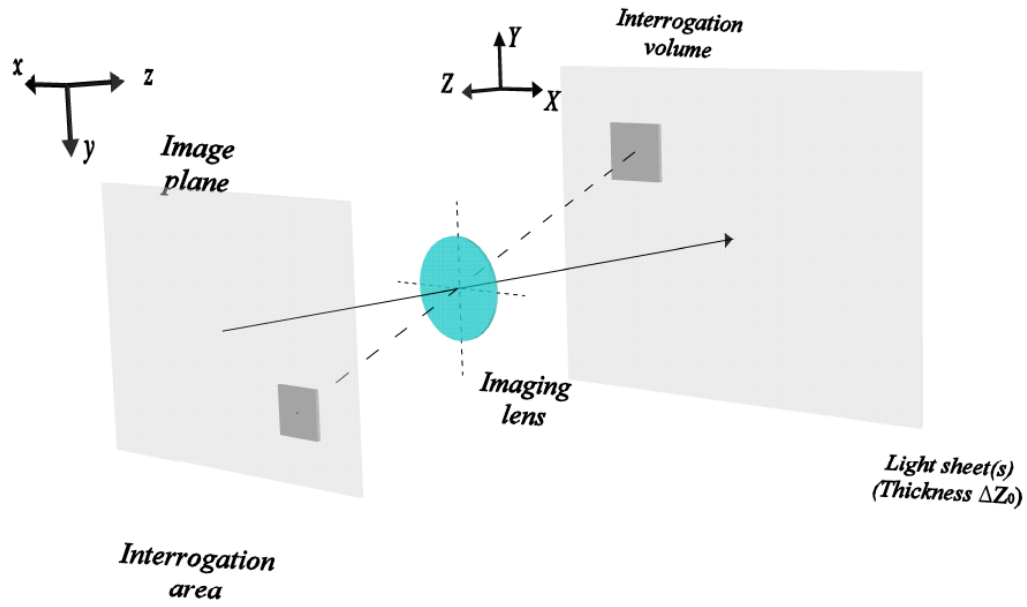

Figure 4.34: Scheme of coordinates in cross-correlation

in which $I_0(Z)$ represents the intensity of the light sheet of laser beam in the direction Z, where Z is the axis between the light sheet and the interrogation area; $W_0(X,Y)$ is the weight function which considers the parameters influencing the light intensity.

The light intensity distribution is typically Gaussian:

$$I_0(Z) = I_Z \exp\left(-8\frac{(Z-Z_0)^2}{\Delta Z_0^2}\right) \tag{4.52}$$

where ΔZ_0 is the thickness of light sheet and I_Z is the maximum intensity of light sheet. Also the weight function $W_0(X,Y)$ can be considered as Gaussian or, for some types of laser, as a constant.

Knowing that $\tau(x) * \delta(x - x_i) = \tau(x - x_i)$, the eq. (4.50) becomes:

$$I(x,\Gamma) = \sum_{i=1}^{N} V_0(X_i)\tau(x - x_i) \tag{4.53}$$

In the signal theory, the cross-correlation is the calculation of the similitude of two signals as a function of a time displacement applied to one of them. We can

suppose that all the particles, into the interrogation area, move of a constant vector D; if at the instant t they are in the position (X_i, Y_i, Z_i), at the instant $t + \Delta t$ they are in the position:

$$X_i' = X_i + D = \begin{pmatrix} X_i + D_x \\ Y_i + D_y \\ Z_i + D_z \end{pmatrix} \tag{4.54}$$

From eq. (4.53):

$$I'(x, \Gamma) = \sum_{i=1}^{N} V_0'(X_j + D)\tau(x - x_j - D) \tag{4.55}$$

The space averaged intensity function μ_I is defined as:

$$\mu_I = \overline{I(x, \Gamma)} = \frac{1}{a_I} \int_{a_I} I(x, \Gamma) dx \tag{4.56}$$

where a_I is the interrogation area. By substituting the eq. (4.53) into eq. (4.56):

$$\mu_I = \frac{1}{a_I} \sum_{i=1}^{N} V_0(X_i) \int_{a_I} \tau(x - x_i) dx \tag{4.57}$$

From which, analogously, the cross-correlation function:

$$R(s, \Gamma, D) = \frac{1}{a_I} \sum_{i,j=1}^{N} V_0(X_i) V_0(X_j) \int_{a_I} \tau(x - x_j)\tau(x - x_j + s - d) dx \tag{4.58}$$

where s is the vector of separation in the correlation plan; $R(s, \Gamma, D)$ is the function which allows the correlation between the intensity of a point in (x, y) in the image layer, with the intensity of a point of coordinates $(x' + s_x - d_x, y' + s_y - d_y)$ in the same layer. Following the approach proposed by Adrian (Adrian 1991):

$$R(s, \Gamma, D) = R_C(s, \Gamma, D) + R_F(s, \Gamma, D) + R_D(s, \Gamma, D) \tag{4.59}$$

where $R_D(s, \Gamma, D)$ represents the correlation between the same particles in the first and in the second exposition (i.e. $i = j$); $R_C(s, \Gamma, D)$ is the convolution of averaged intensity I; $R_F(s, \Gamma, D)$ considers the fluctuation due to rumors. In

particular:

$$R_D(s,\Gamma,D) = R_\tau(s-d)\sum_{i=1}^{N} V_0(X_i)V_0(X_i+D) \tag{4.60}$$

The maximum peak value corresponds to $s-d$. The peak displacement $R_D(s,\Gamma,D)$ from the center of the interrogation area is the averaged particles displacement in the same area. Hence, by knowing the time interval, the u and v velocity components can be determined.

The validation methods

In order to evaluate the instantaneous velocities, in the PIV technique all the information are registered in the same instant. It means that in some parts of the measurement domain some information could be not significant in that instant. Nevertheless, the vectorial maps give the results (called *oulier*) also where the results are not significant. It is necessary to apply some validation methods in order to recognize and eliminate the outliers. The Flow Manager allows to operate automatically and it associates a status at every controlled vector; the status can be "ok", "rejected", "outside" or "substituted".

By analyzing the experimental results, two methods of validation were chosen, and the data which are not considered as "ok" will be eliminated and not considered in the statistical analyses. These two methods, that are applied in the order below, are:

1. *peak validation method*: it is a method for the validation of single vectors;
2. *moving average method*: it considers the whole field or a subregion of the map.

The *peak validation method* rejects or accepts individually the displacement vectors depending on the height of the cross-correlation peak in the plane where they were measured. We can consider a cross-correlation function:

$$\Phi_{fg}(m,n) = \sum_{k=-s/2}^{+s/2}\sum_{l=-s/2}^{+s/2} f(k,l) * g(k+m,l+m) \tag{4.61}$$

where s is the side of interrogation area, (m,n) is the displacement vector and

f and g are light-intensity functions. The function Φ quantifies the accuracy by comparing the calculated displacements with the average displacement in the interrogation area. The function Φ increases with the number of particles that moves with (m, n).

On the contrary, the function termed *rumor function* assumes a value larger depending on the number of correlations that are not effectuated. The rumor function quantifies the particles which go into the interrogation area, or which go out.

Into an interrogation area, the *peak validation method* considers the highest peak, the signal peak, while the smaller peaks are considered as rumors. It is necessary to choose a value for the parameter k_1, which defines the minimum value for considering a smaller peak as rumor:

$$\frac{\text{highest peak}}{\text{smaller peak}} > k_1 \tag{4.62}$$

It was tested that a good value for k_1, for a mean concentration of seeding, is $k_1 = 1.2$. If the concentration is lower, k_1 should be lower than 1.2.

The second method of validation, the *moving average method*, assures the continuity of the velocity field. The hypothesis which supports this method is that the velocity field must change with continuity. So, if a vector is too much different with respect the neighbors, it is considered an "outlier". After considered a vector $v(x, y)$, the algorithm calculates the averaged vector of velocity for all the vectors in the area with center in (x, y). If this area is m x n large, then the averaged velocity is:

$$\overline{v_m}(x, y) = \frac{1}{m * n} \sum_{i=x-\frac{m-1}{2}}^{x+\frac{m-1}{2}} \sum_{j=y-\frac{n-1}{2}}^{y+\frac{n-1}{2}} \bar{v}(i, j) \tag{4.63}$$

and m and n odd integers.

By comparison between $\bar{v}(x, y)$ and $\overline{v_m}(x, y)$, the vector v is rejected if $|\bar{v}(x, y) - \overline{v_m}(x, y)| > k_2$. k_2 is a tolerance, not constant, but it can be evaluated as:

$$k_2 = \alpha \, \text{MAX} \, |\bar{v}(x, y) - \overline{v_m}(x, y)| \tag{4.64}$$

where α is termed *acceptance factor* and $0 < \alpha < 1$. The limit cases are for:

Table 4.8: The experimental parameters for the validation of data

parameter	value
k_1	1.2
Averaged area (m x n)	3 x 3
Acceptance factor α	0.1
Number of iterations	3
Options	Don't substitute rejected vectors; don't validate parameter

- $\alpha = 0$: all the vectors are rejected;

- $\alpha = 1$: all the vectors are accepted.

The acceptance factor is not a physical parameter. Generally, a good choice for its value is between 0.01 and 0.1.

The *moving average method* is an iterative method. If the number of iterations increases, the result improves but the execution time increases. In Table 4.8 are summarized the parameters chosen for the analysis.

The output files

After the operations of cross-correlation and data validation, the data obtained are exported in output files. For every time step (frame), an output data file is saved. Each file contains a table of data: 12 columns and a number of rows equal to the number of the analyzed points. In the columns the saved information is:

column 1 x-position of the interrogation area: the domain of analysis is divided into interrogation areas. Each interrogation area has its identification number (divided in x and y position) that is written in the first column;

column 2 y-position of the interrogation area;

column 3 x-coordinate of the barycenter of the interrogation area (in [pixel]) x_i;

column 4 y-coordinate of the barycenter of the interrogation area (in [pixel]) y_i;

column 5 x-coordinate of the barycenter of the interrogation area (in [cm]);

column 6 y-coordinate of the barycenter of the interrogation area (in [cm]);

column 7 horizontal velocity component calculated in [pixel/frame] u_i;

column 8 vertical velocity component calculated in [pixel/frame] v_i;

column 9 horizontal velocity component calculated in [m/s];
column 10 vertical velocity component calculated in [m/s];
column 11 magnitude of velocity in [m/s];
column 12 status: if 0, the vector is confirmed; if 1, the vector is rejected.

The output files are elaborated by the post-processing program.

Data elaboration and post-processing program

The elaboration of data obtained with the Flow Manager analysis is done using a codex written in MatLab language. In this codex, the data from the input files (which are the output files in the precedent step of analysis - and paragraph) are elaborated for calculating:

- horizontal averaged component of velocity:

$$\bar{u} = \frac{1}{n_u} \sum_{i=1}^{n_p} u_i \tag{4.65}$$

  where n_p is the total number of instants, while n_u is the number of instants ($n_u \leq n_p$) in which the status is equal to 0, that is the vectors that were not rejected. For the rejected vectors, the values of velocity components are substituted by the string 'NaN' ('Not a Number');

- vertical averaged component of velocity:

$$\bar{v} = \frac{1}{n_v} \sum_{i=1}^{n_p} v_i \tag{4.66}$$

  where n_p is the total number of instants, while n_v is the number of instants ($n_v \leq n_p$) in which the status is equal to 0, that is the vectors that are not rejected. For the rejected vectors, the values of velocity components are substituted by the string 'NaN';

- tangential shear stress:

$$\overline{u'u'} = \frac{1}{n_{uu}} \sum_{i=1}^{n_p} u'_i u'_i \tag{4.67}$$

where n_{uu} is the number of instants considered as valid; and $u'_i = u_i - \bar{u}$;

- normal shear stress:

$$\overline{v'v'} = \frac{1}{n_{vv}} \sum_{i=1}^{n_p} v'_i v'_i \tag{4.68}$$

where n_{vv} is the number of instants considered as valid; and $v'_i = v_i - \bar{v}$;

- Reynolds shear stress:

$$\overline{u'v'} = \frac{1}{n_{uv}} \sum_{i=1}^{n_p} u'_i v'_i \tag{4.69}$$

Chapter 5

Analysis of the results and discussion

5.1 The drag coefficient

5.1.1 Drag coefficient of the isolated cylinder

The evaluation of the drag coefficient of an isolated cylinder will be done with reference to the following aspect:

- comparison of the obtained drag coefficient with the drag coefficient for an infinite cylinder;
- comparison of the drag coefficient calculated with different definitions of the double average velocity of the flow;
- effect of the the narrowing of the flow.

The tests were carried out in the same laboratory channel described in Section 4.3.1. The uniform flow condition, for each test, was verified before the measurement of drag force by means of the Ultrasound Velocity Profiler (UVP), termed *DOP2000*. The flow was considered uniform if the velocity profile was constant upstream and downstream the measurement section, for a sufficiently large extension.

The cylinder was placed at the longitudinal coordinate $x = 8\ \mathrm{m}$ and, transversally, in the center of the channel at $y = 0.15\ \mathrm{m}$, raised from the bottom of approximately $2\ \mathrm{mm}$ (see Section 4.3.1). The load cell was fixed on the emergent part of the cylinder. The load cell measured the total force that the flow exerted on the cylinder.

The value of the water depth was obtained by means of a moving pointer gauge. The elevations of bed and free surface were taken along the direction of the flow for all the length of the channel (the values were taken from the section with coordinate $x = 3\ \mathrm{m}$ to $x = 7\ \mathrm{m}$ every $0.5\ \mathrm{m}$; from $x = 7\ \mathrm{m}$ to $x = 9\ \mathrm{m}$ every $0.25\ \mathrm{m}$; from $x = 9\ \mathrm{m}$ to $x = 10\ \mathrm{m}$ every $0.5\ \mathrm{m}$) and in the center of channel ($y = 0.15\ \mathrm{m}$).

From the dimensional analysis (Section 2.3.2), the relationship between the drag coefficient C_{Dp} and the dimensionless quantities of flow is:

$$C_{Dp} = \phi_2 \left(Re_p, Fr, \frac{h}{d_p}, \frac{B}{d_p} \right) \tag{5.1}$$

where $Re_p = U d_p/\nu$ is the Reynolds number related to the cylinder; $Fr = U/\sqrt{gh}$ is the Froude number; h/d_p is the ratio between the water depth and the diameter of the cylinder; B/d_p (the ratio between the width of the channel and d_p) expresses the narrowing of the flow. One problem is represented by the fact that in this case, but still more in a vegetated reach, the definitions of the average velocity and of the average water depth are not obvious. In order to obtain more generality in the comparison among the different configurations, we calculated the velocity with two different methods: (i) averaged velocity by considering the flow rate:

$$U = \frac{Q}{Bh} \tag{5.2}$$

and (ii) by considering the profile of the velocity measured by means of the Dop2000:

$$\tilde{u} = \int_0^h \overline{u(z)} dz \tag{5.3}$$

In eqs. (5.2) and (5.3) h is the water depth, $\overline{u(z)}$ the values of the time averaged velocity along vertical direction.

In the tests on the isolated cylinder, with the measurement of the drag force R_p, obtainable as described in Section 4.3.1, two different values of C_{Dp} can be compared:

$$C_{Dp} = \frac{R_p}{\rho h d_p \frac{U^2}{2}} \tag{5.4}$$

and

$$C_{Dp,1} = \frac{R_p}{\rho h d_p \frac{\tilde{u}^2}{2}} \tag{5.5}$$

In order to calculate the average velocity according to eq. (5.3), it is necessary to measure the velocity distribution along the depth. The velocity profiles were calculated by registering the instantaneous velocity profiles for a period sufficient long. We have been able to ascertain that it was necessary to register at least 10000 time instants for having the convergence of data to the average velocity. The result was obtained by verifying, for a large number of data, in which instant both the cumulative average velocity and the cumulative variance converged. An example of the convergence with 10000 data is reported in Figure 5.1.

The velocity profiles were obtained all along the channel at every $25\ \mathrm{cm}$ (Figure 5.2), but Figure 5.3 reports only the obtained profiles at every $50\ \mathrm{cm}$, for clarity. The profiles in the figure were obtained by dividing the fluctuating part of the velocity $u(z) - \tilde{u}$ for the average velocity $\tilde{u}$ (eq. 5.3):$(u(z) - \tilde{u})/\tilde{u}$. In the figure also the ratio between the spatial velocity $\tilde{u}$ and the double-averaged velocity $\langle\overline{u}\rangle$ is reported in the top part of the plot, for each profile in the x-direction. The double-averaged velocity $\langle\overline{u}\rangle$ is the average of all the velocities measured along the channel. The ratio $\tilde{u}/\langle\overline{u}\rangle$ in the graph does not show a tendency towards a constant value. The tendency can be seen by comparing directly the profiles, as in Figure 5.4. In this figure, the profiles for $x = 4.5\ \mathrm{m}$ and $x = 5.0\ \mathrm{m}$ show that the flow is far from the uniform flow conditions; the stabilized conditions are verified since the profile at $x = 6.5\ \mathrm{m}$. For the following analyses, the double-averaged velocity is calculated by averaging the velocity profiles between $x = 7\ \mathrm{m}$ and $x = 9\ \mathrm{m}$, i.e where the flow is verified to be uniform.

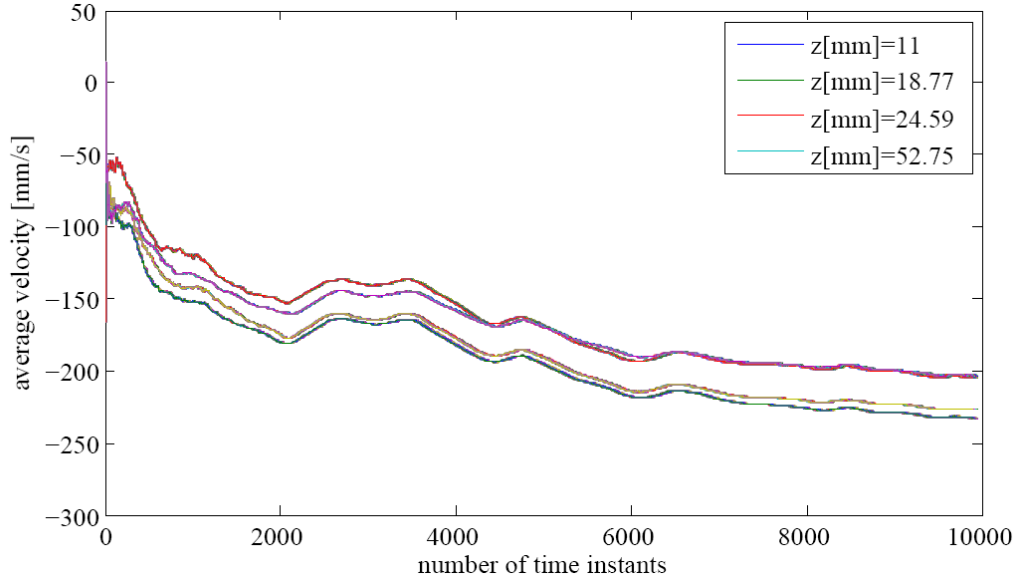

(a) cumulative averaged velocity

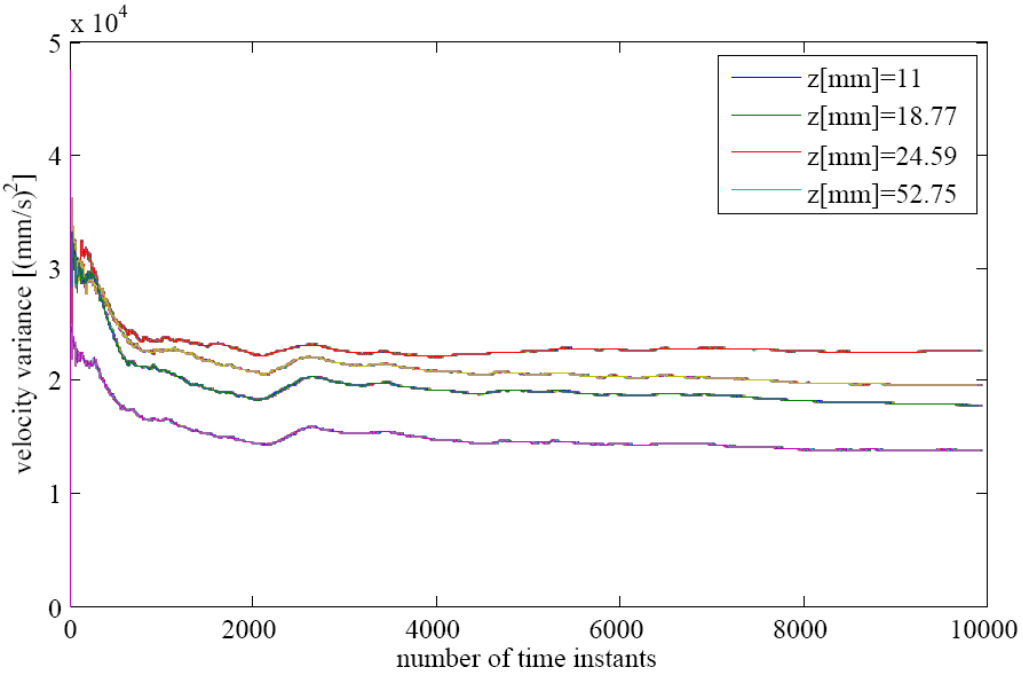

(b) cumulative variance

Figure 5.1: Example of the (a) cumulative averaged velocity and (b) cumulative variance for four different points along the water depth

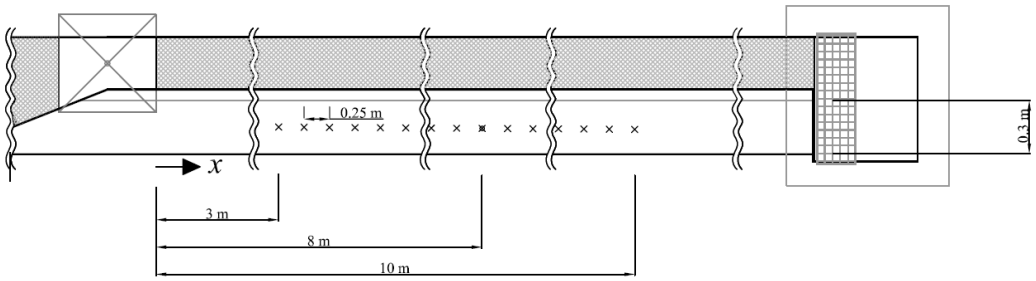

Figure 5.2: The channel for the measurement of drag force for an isolated cylinder. The cylinder is placed in the point represented with the small circle ($x = 8$ m); the small crosses indicate the points of measurements of velocity with the DOP2000.

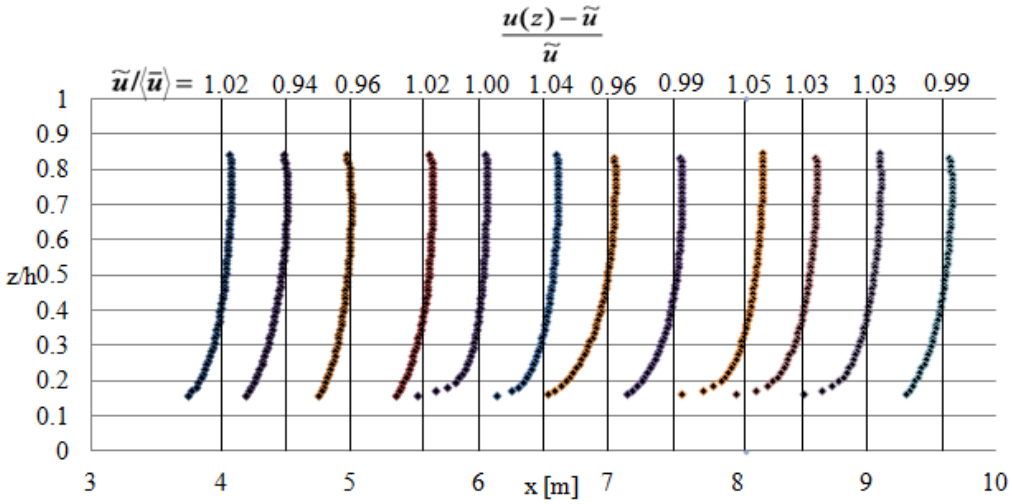

Figure 5.3: Example of the velocity profiles measured for all the length of the channel with the DOP2000

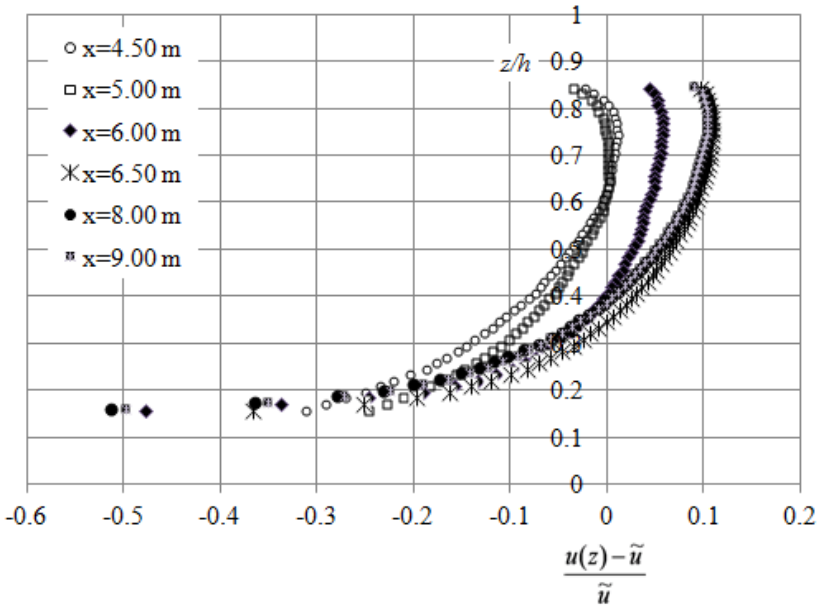

Figure 5.4: Comparison among velocity profiles for different x, and verification of uniform flow conditions

Comparison of the drag coefficients evaluated with the two different definitions of double-averaged velocity

Figure 5.5 shows the drag coefficients obtained with the measurements and calculated with the two different definitions of the velocity (eqs. (5.4) and (5.5)), as a function of the plant Reynolds number $Re_p = Ud_p/\nu$ (or $Re_p = \tilde{u}d_p/\nu$). The data are compared also with the graph of the drag coefficient for the infinite cylinder. The results, that are zoomed in the Figure 5.6, put in evidence that:

- the two definitions of the drag coefficient give results that are in good agreement, and both are very close to the curve for the infinite cylinder;

- the plant Reynolds number in the tests are between 1850 and 6450. In this range, the wake downstream the cylinder is completely turbulent and the drag coefficient assumes a constant value. For our test, the average measured value is 1.24, which is nearly coincident with the value 1.2 reported for the isolated cylinder. The difference may depend on the effects due to the free surface and the grain roughness;

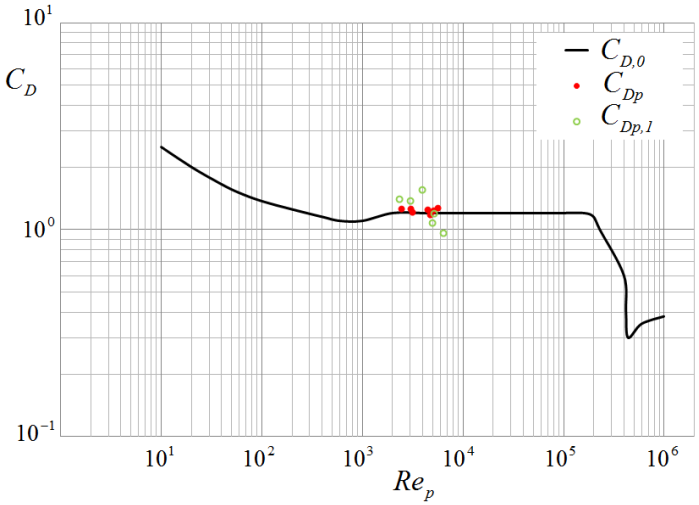

Figure 5.5: Comparison among the drag coefficient for the infinite cylinder, the drag coefficient evaluated with the velocity $U = Q/Bh$ and the drag coefficient evaluated with the averaged velocity $\tilde{u}$ obtained by the velocity profile.

- the drag coefficient obtained from eqs. (5.3) and (5.5) has a larger spread, mainly due to the method of measurement. In fact, the UPV is an excellent method to evaluate the velocity profiles in a natural channel, but at laboratory scale its precision is very often not enough. This is mainly due to the dependence of the results on the parameters setting for the instrument: angle of probe, sound velocity in the water, limits for the rumors, and others;

- the confidence interval for C_{Dp} and C_{Dp1} are equally extended. It means that the determination of the velocity with the profiler does not increase the precision of measurements. This result does not conflict with what affirmed in the last point. The errors related with the setting of the parameters are instrumental errors, that can not be quantified. On the other hand, the large number of data registered for the velocity contributes to reduce the total error.

In conclusion, there is not a real advantage to use the profiler for the determination of the drag coefficient. For this reason, in the following of the research, the evaluation of the drag coefficient is made by considering the depth averaged velocity calculated with the water discharge and water depth.

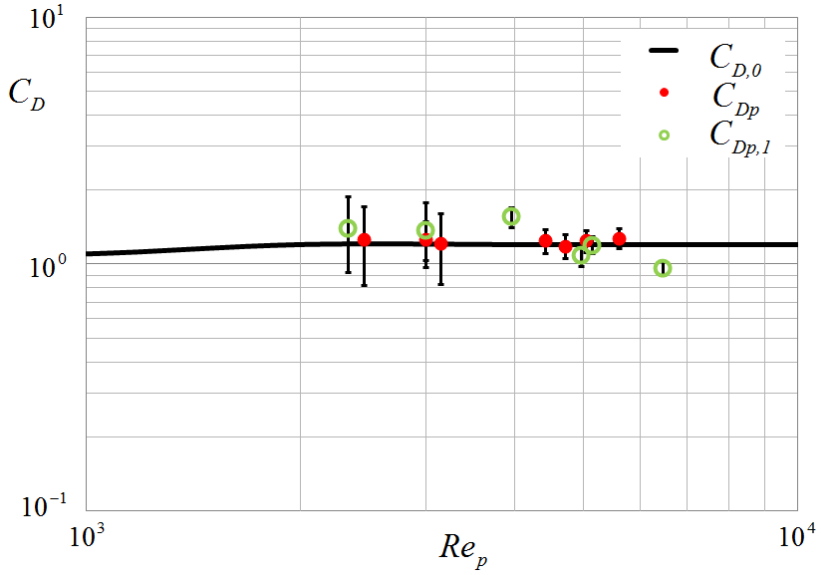

Figure 5.6: Zoom of the Figure 5.5 on the comparison among the drag coefficient for the infinite cylinder, the drag coefficient evaluated with the velocity $U = Q/Bh$ and the drag coefficient evaluated with the averaged velocity $\tilde{u}$ obtained by the velocity profile.

Dependence on the width of the channel

A cylinder in a channel produces a narrowing of the flow. The free surface profile depends on the narrowing and on the Froude number, as described by Marchi and Rubatta (1981). Depending on Fr and b/B, in proximity to the narrow, the water depth can remain larger than the critical depth or can be lower than the critical depth. In the second case, downstream the narrow, a hydraulic jump is formed. The Marchi's curve (Figure 5.7) is described by the following equation, in which $b = B - d_p$, where $B = 0.308$ is the width of the channel:

$$\frac{b}{B} = \left(\frac{3}{2}\right)^{3/2} \frac{Fr}{\left(1 + \frac{Fr^2}{2}\right)^{3/2}} \tag{5.6}$$

Figure 5.7 shows the Marchi's curve corresponding to eq. (5.6), which separates the two situations: for the values over the curve the profile is the first one, without jump; for the values under the curve, the jump will be formed. This effect is

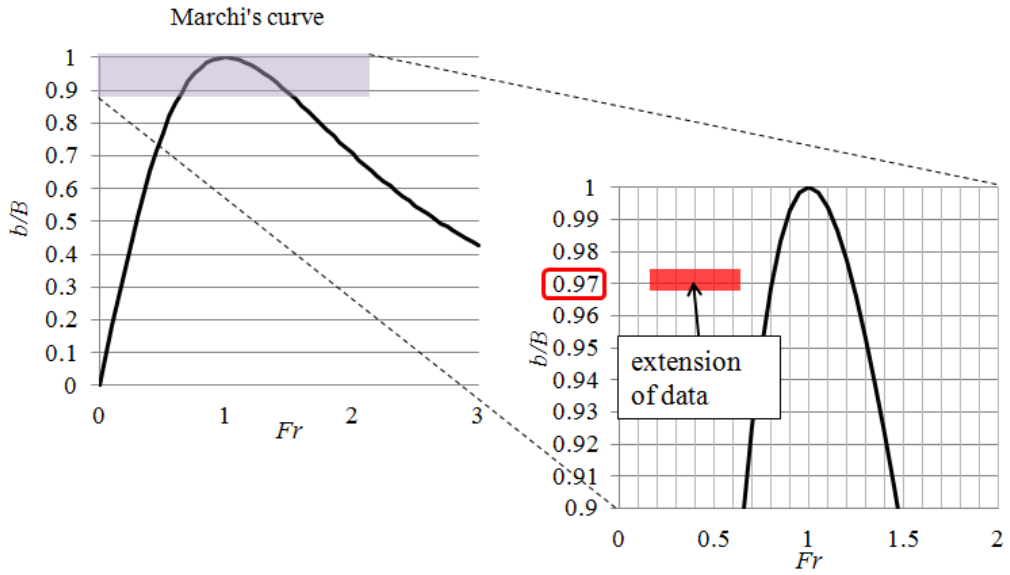

Figure 5.7: Range of values of the obtained data, and comparison with the Marchi's curve.

the reason of the different tendency of the drag coefficient for different Froude numbers (Section 2.3.2 and Hsieh (1964)).

Our tests are carried out for Froude numbers comparable to the Froude numbers in natural rivers. The range of Froude numbers adopted in the experiments (red rectangle in Figure 5.7) corresponds to the Froude number values smaller than 0.65. The free surface profiles did not present hydraulic jumps downstream the cylinder.

It remains to verify that, also with this hypothesis, in any case the narrowing does not affect the drag coefficient. From Figure 5.8, the drag coefficient seems to be independent of the ratio B/h and hence to be independent of the narrowing of the flow for the range of data considered.

5.1.2 Direct measurements of drag coefficient

These series of experiments, extensively treated in Section 4.3.2, have as main aim the measurements of the drag coefficient of the cylinders in the staggered configuration and fixed bed. The diameters of the stems were constant and equal

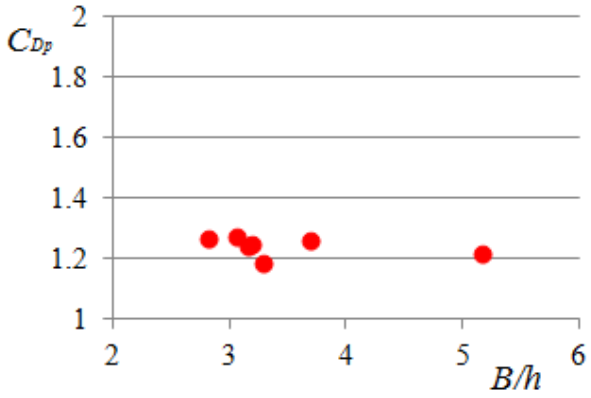

Figure 5.8: Representation of the drag coefficient as a function of the ratio between the channel width and the water depth.

to 1 cm, in a first series, and 3 cm, in a second one. The 6 different densities of vegetation were obtained with different distances between the cylinders interaxes. The channel was divided into the four partitions.

The values of water depth, free surface and bed elevations were measured together with the liquid discharges. In the Section 5.1.4, the obtained results will be compared with the drag coefficient calculated for mobile bed tests in the same configurations of cylinders.

From dimensional analysis, we have:

$$C_{Dp} = \phi_2 \left(Re_p, Fr, \frac{h}{d_p}, \Omega_v \right) \tag{5.7}$$

in which, respect to the case of the isolated cylinder (eq. 5.1), there is a new parameter, Ω_v, representing the density of vegetation. B is considered to be not influent for which it was already verified for the isolated cylinder (Section 5.1.1).

In a channel, Reynolds number and Froude number are in strictly correlation. When one of the measured quantities is changed, for instance the water depth, Re_p and Fr change contemporarily. To obtain experimental conditions in which one parameter is fixed and the other changes, it would be necessary to change the fluid properties. It would be redundant to present the results as a function of both the parameters. The data will be represented only as a function of the Reynolds

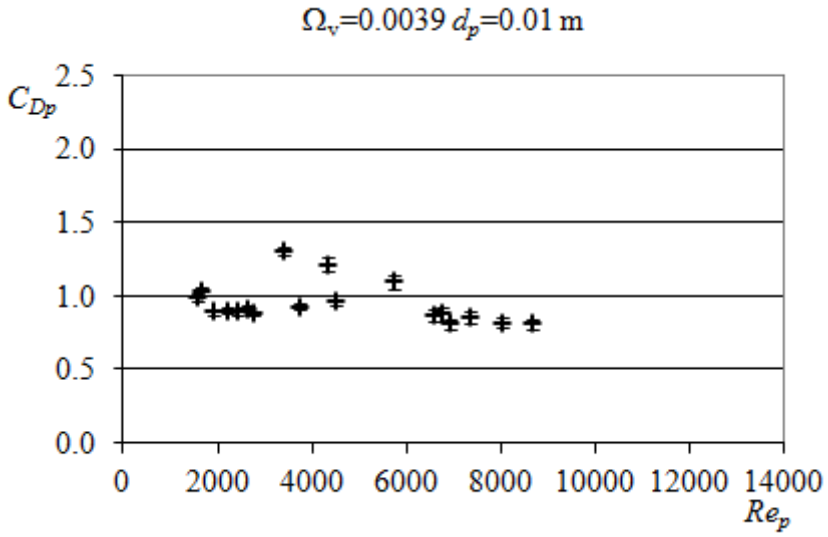

Figure 5.9: The measured drag coefficients for the staggered distribution of cylinders and $\Omega_v = 0.0039$.

number and of the stems density, Ω_v.

We would have expected that the drag coefficient depends in the same way on the relative dimension of the stems h/d_p, but in our experiments we did not find any effect of h/d_p, probably because the range of variation of this parameter was not wide enough, caused by the instrumental limitations.

In Figures from 5.9 to 5.14 (Armanini, Cavedon, and Righetti 2010), the measured C_{Dp} are plotted as a function of Re_p for different values of the plant density Ω_v. As emerges from the figures, the drag coefficient depends on the Reynolds number only for the lowest values of Re_p; if $Re_p > 6000 \sim 8000$, the drag coefficient becomes independent of Re_p. In the following, the asymptotic value will be indicated by $C_{Dp,\infty}$.

In Figures from 5.9 to 5.14, also the confidence interval of each value is reported. It represents the uncertainties in the measurements due to the combination of instrumental and systematic errors. In the direct measurements the uncertainties are mainly due to the combination of the instrumental errors and of the errors related to (small) fluctuations of the cylinders induced by the turbulence. It can be concluded that the uncertainties are acceptable and the measurements are rather

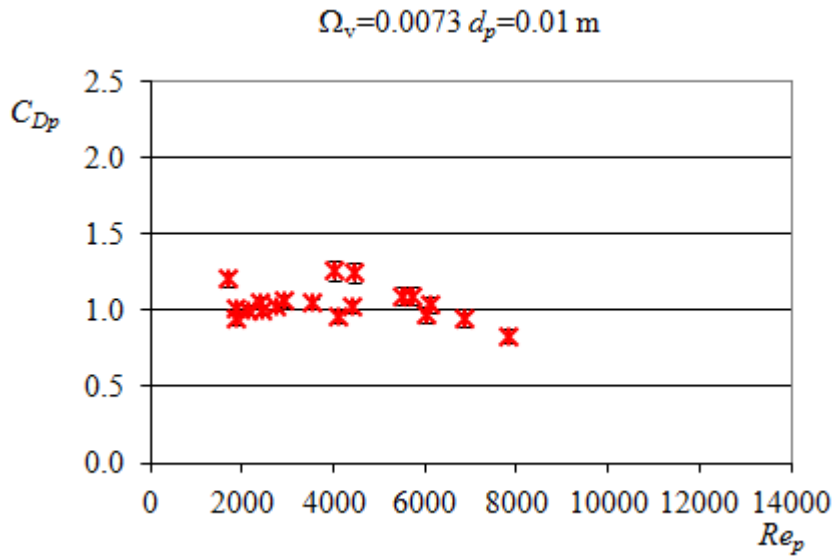

Figure 5.10: The measured drag coefficients for the staggered distribution of cylinders and $\Omega_v = 0.0073$.

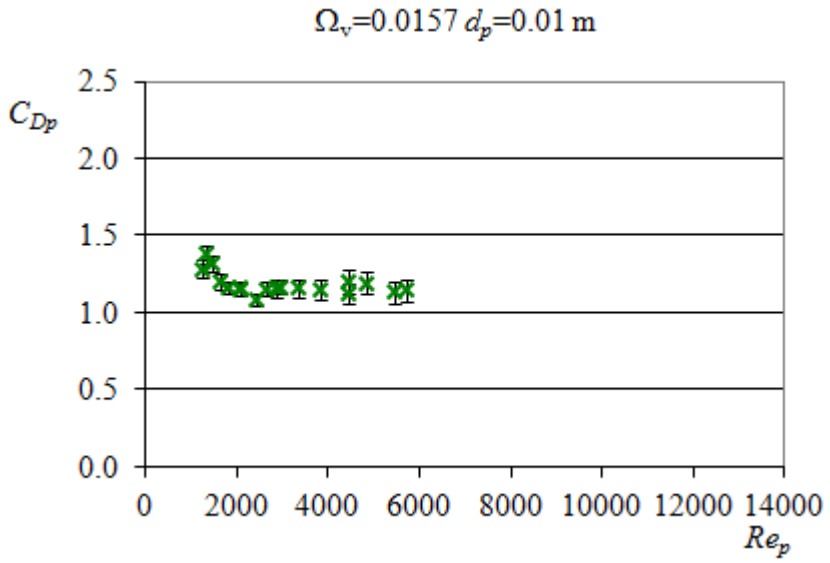

Figure 5.11: The measured drag coefficients for the staggered distribution of cylinders and $\Omega_v = 0.0157$.

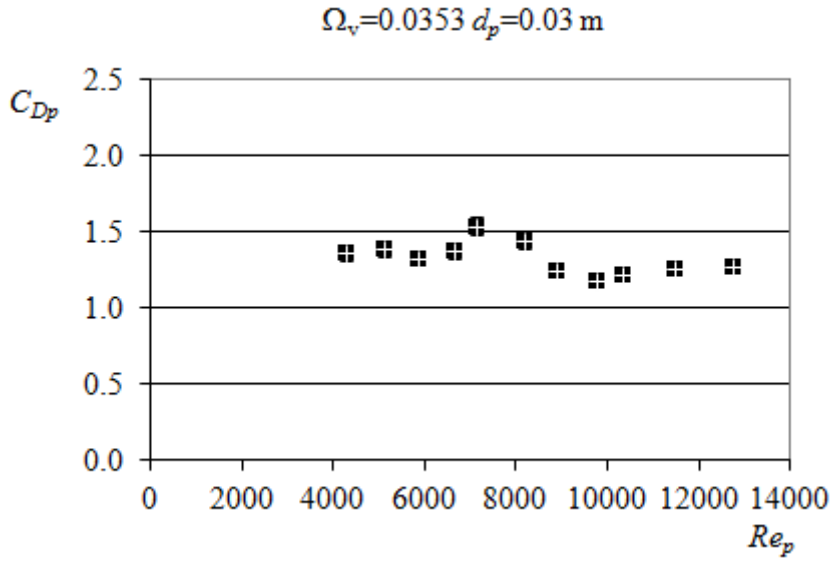

Figure 5.12: The measured drag coefficients for the staggered distribution of cylinders and $\Omega_v = 0.0353$.

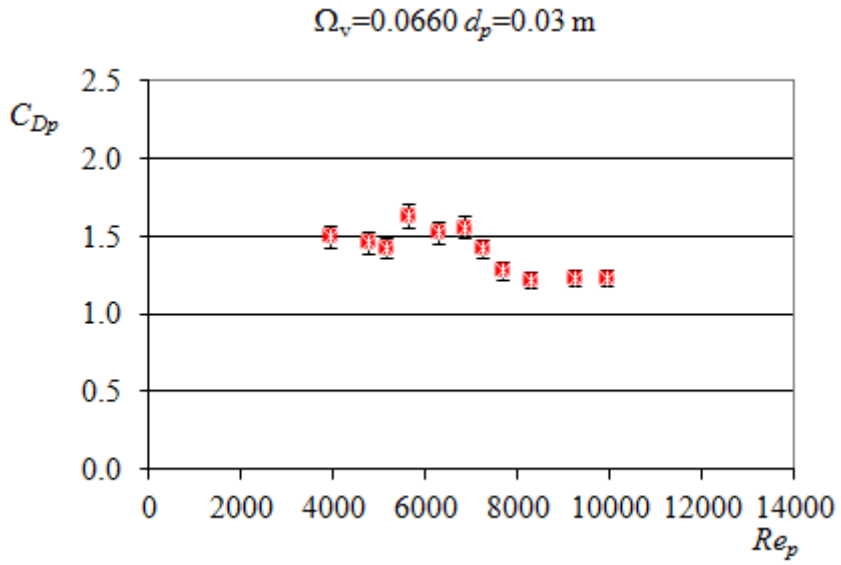

Figure 5.13: The measured drag coefficients for the staggered distribution of cylinders and $\Omega_v = 0.0660$.

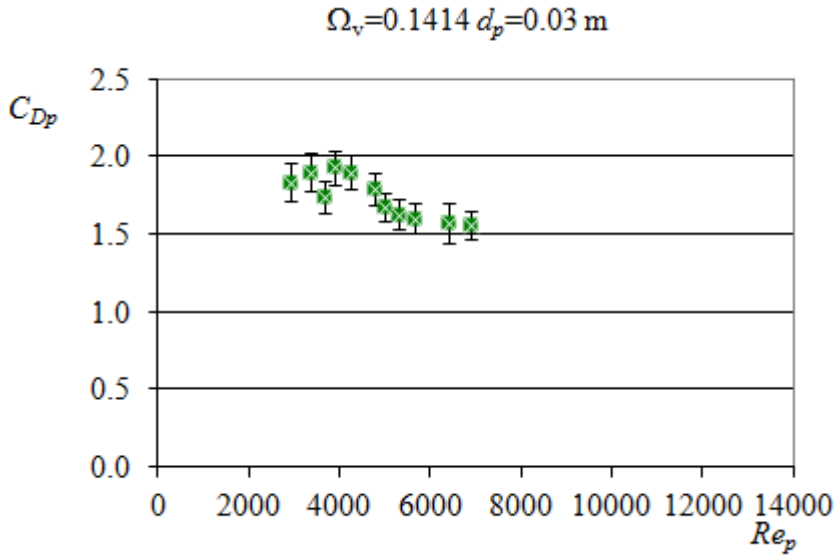

Figure 5.14: The measured drag coefficients for the staggered distribution of cylinders and $\Omega_v = 0.1414$.

precise.

Figures from 5.9 to 5.14 and Figure 5.15 show that the drag coefficient depends primarily on the density of vegetation. In particular, C_{Dp} tends to increase with the density of vegetation, as it was expected, especially for the lowest Reynolds numbers.

Figure 5.16 shows that the asymptotic value of the drag coefficient depends on the density of vegetation. In particular, the asymptotic drag coefficient increases with the increase of the density of plants. We propose also an empirical relationship to fit the experimental data:

$$C_{Dp,\infty} = 0.8 \left[1 + 0.75 \left(\frac{\Omega_v}{0.1 + \Omega_v} \right)^{0.5} \right] \tag{5.8}$$

In Figure 5.17, the experimental ratio between C_{Dp} and $C_{Dp,\infty}$ is, finally, reported. The points are relatively dispersed. Notwithstanding the dispersion of the experimental data in the figure, it emerges that at minor Reynolds numbers the relative drag coefficient is bigger for the smaller plants density, and that for

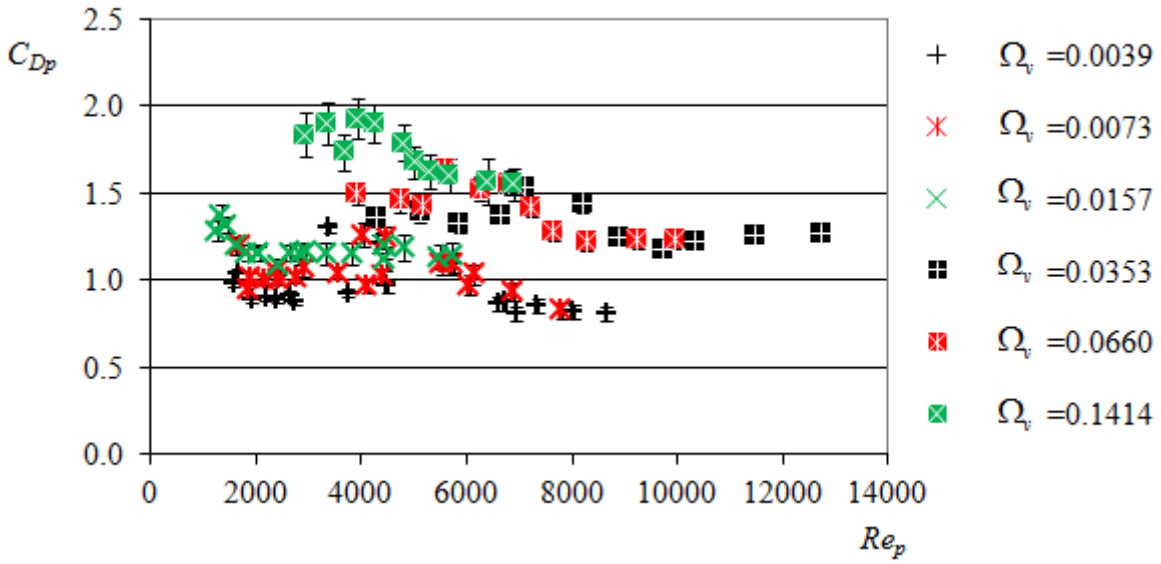

Figure 5.15: Representation of all the drag coefficients measured for different densities of vegetation.

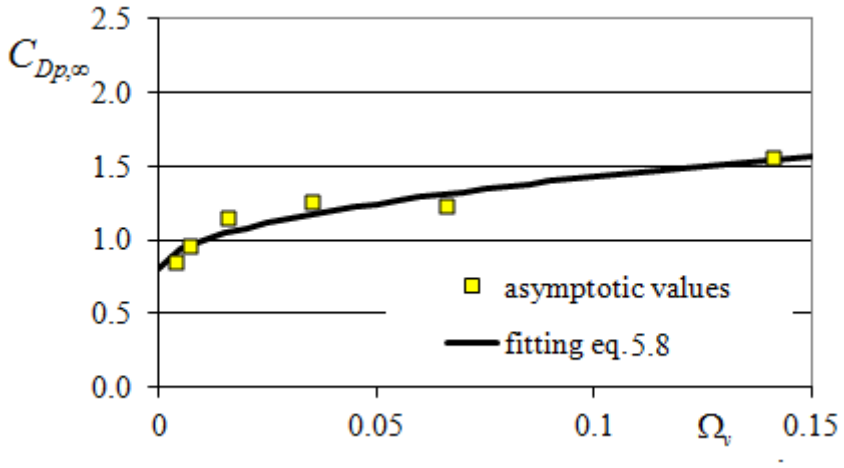

Figure 5.16: Representation of the asymptotic values of the drag coefficient compared with the empirical formulation (eq. 5.8).

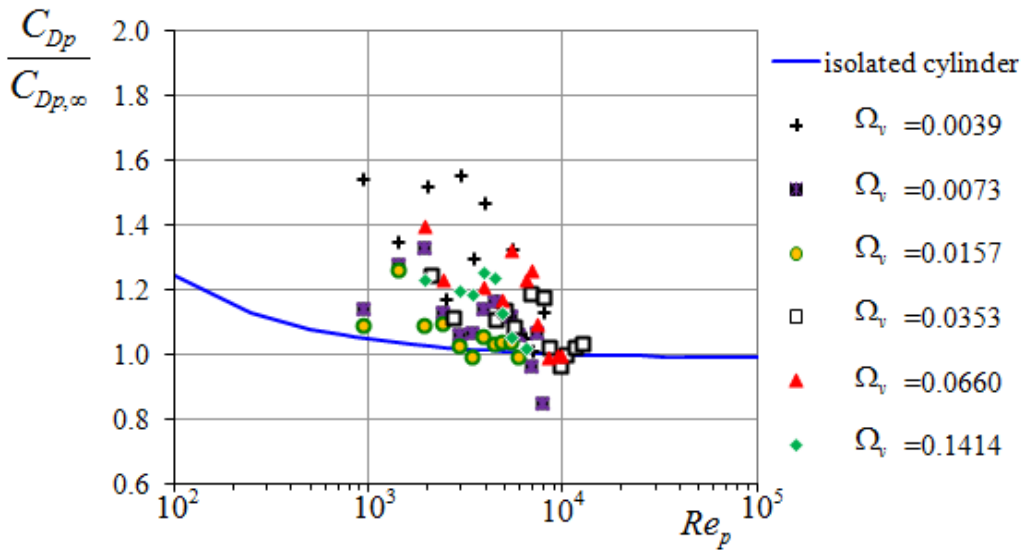

Figure 5.17: The ratio between the drag coefficients and the infinity drag coefficients versus plant Reynolds number, for each density of vegetation. The continuous (blue) line represents the behavior of an isolated cylinder.

the array of cylinders the effect of Reynolds number on $C_{Dp}/C_{Dp,\infty}$ is prolonged even for larger Reynolds numbers with respect to the isolated cylinder, as already observed by other authors (Poggi et al. 2004; Righetti 2008). This behavior will be correlated in Section 5.2 with the shape of the wake downstream the cylinder.

Comparison with literature data

In Figures from 5.18 to 5.23, the comparison between our results on drag coefficient, and the formula proposed by Tanino and Nepf (2008) are shown. In the figures, the two curves represented by broken lines are obtained with eqs. (2.23) and (2.24), herein reported:

$$C_{Dp} = 2\left(\frac{\alpha_0}{Re_p} + \alpha_1\right) \tag{5.9}$$

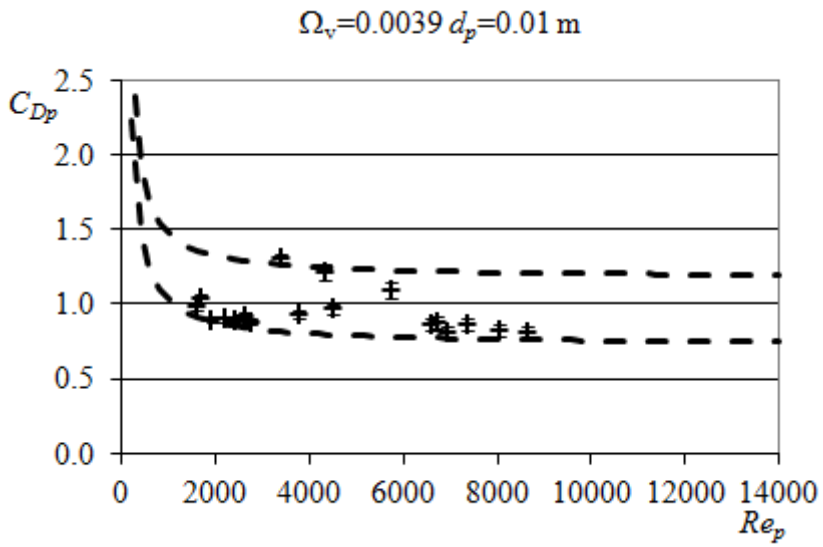

Figure 5.18: The comparison between the drag coefficient for a staggered distribution of cylinders ($\Omega_v = 0.0039$) and the formula in eqs. 5.9 and 5.10, by Tanino and Nepf (2008).

Table 5.1: Values for α_0 used in the eq. (5.9) for the best fitting of the experimental data.

Ω_v	0.0039	0.0073	0.0157	0.0353	0.0660	0.1414
α_0	150	200	250	350	350	350

where α_0 is a parameter calibrated on the experimental data, but α_1 is a parameter depending on the density Ω_v:

$$\alpha_1 = (0.46 \pm 0.11) + (3.8 \pm 0.5)\,\Omega_v \tag{5.10}$$

For fitting our experimental data the parameter α_0 does not results to be a constant, but it increases with the vegetation density. The results of the best fitting are reported in Table 5.1. The Figures from 5.18 to 5.22 show a good agreement with the proposed formula, but for the highest density, that is for $\Omega_v = 0.1414$, the data are smaller than the curves (Figure 5.23).

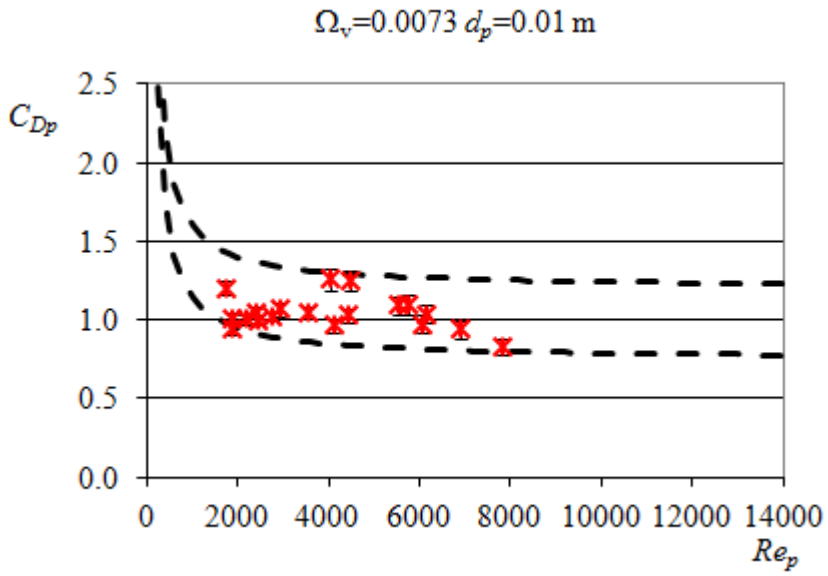

Figure 5.19: Comparison between the drag coefficient for a staggered distribution of cylinders ($\Omega_v = 0.0073$) and the formula in eqs. 5.9 and 5.10, by Tanino and Nepf (2008).

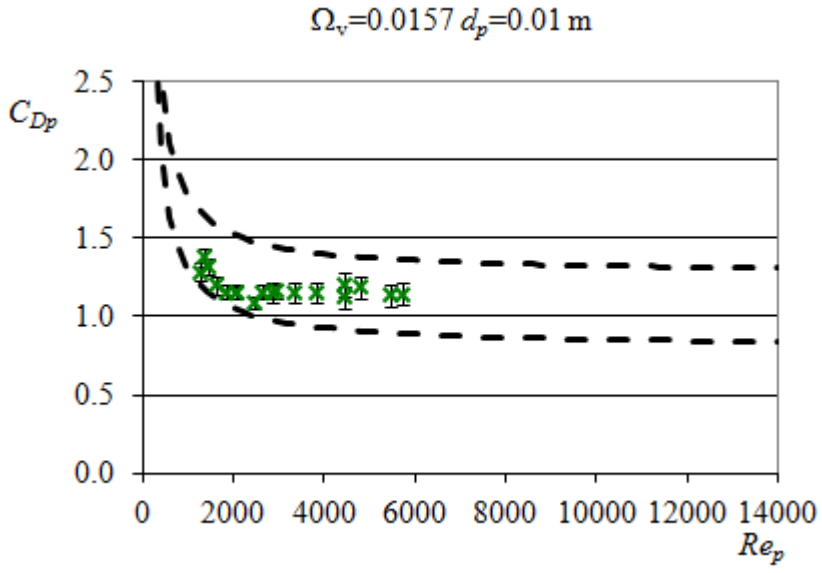

Figure 5.20: Comparison between the drag coefficient for a staggered distribution of cylinders ($\Omega_v = 0.0157$) and the formula in eqs. 5.9 and 5.10, by Tanino and Nepf (2008).

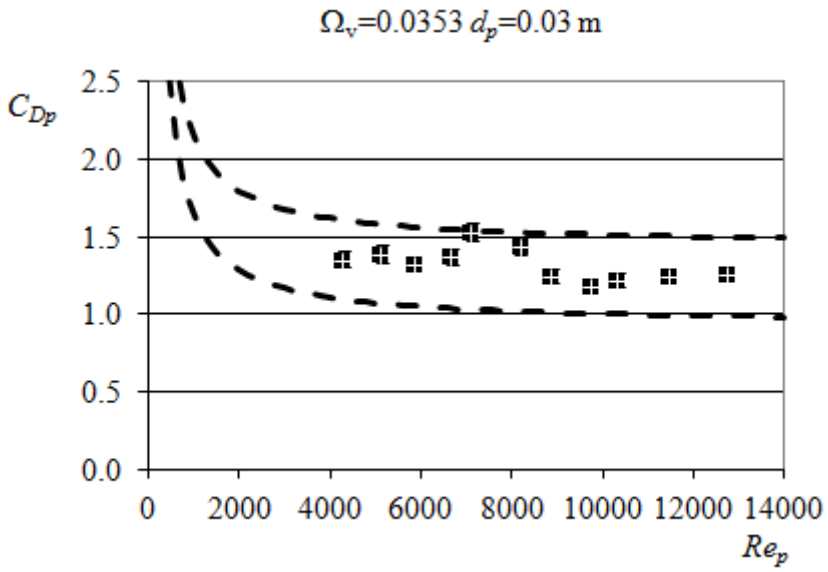

Figure 5.21: Comparison between the drag coefficient for a staggered distribution of cylinders ($\Omega_v = 0.0353$) and the formula in eqs. 5.9 and 5.10, by Tanino and Nepf (2008).

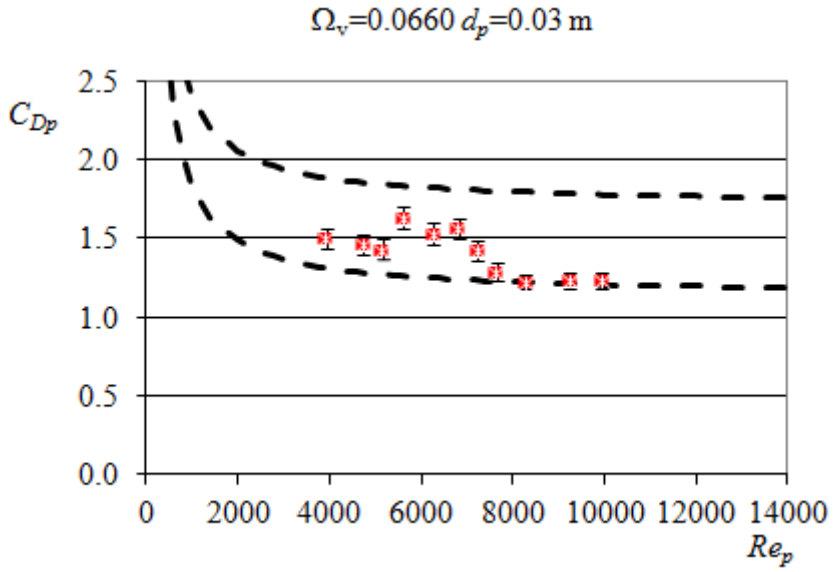

Figure 5.22: Comparison between the drag coefficient for a staggered distribution of cylinders ($\Omega_v = 0.0660$) and the formula in eqs. 5.9 and 5.10, by Tanino and Nepf (2008).

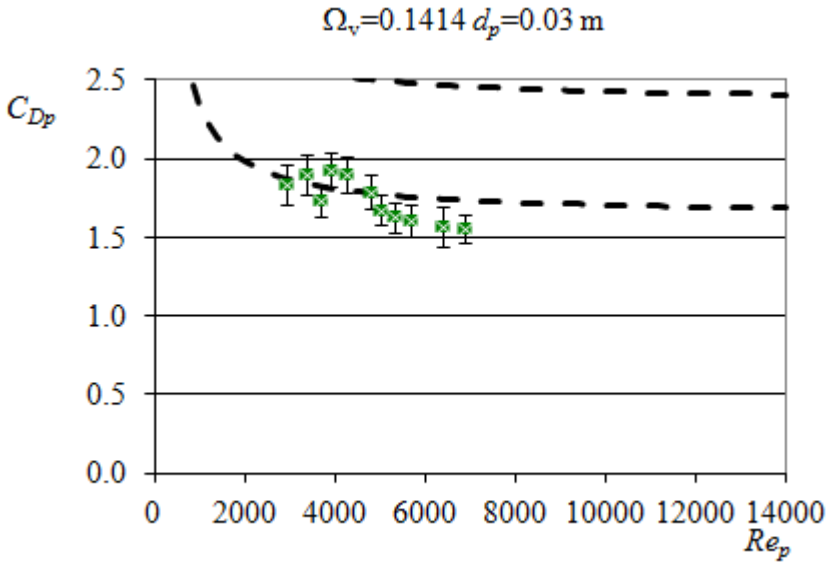

Figure 5.23: Comparison between the drag coefficient for a staggered distribution of cylinders ($\Omega_v = 0.1414$) and the formula in eqs. 5.9 and 5.10, by Tanino and Nepf (2008).

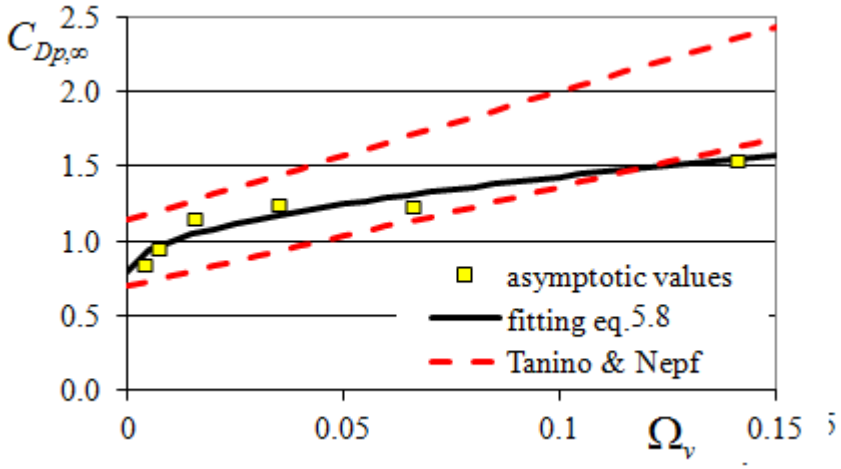

Figure 5.24: Comparison among the experimental asymptotic data, the eq. (5.8) and the eqs. 5.11 and 5.10.

According to eq. (5.9), the asymptotic value for $Re_p \to \infty$ is:

$$C_{Dp,\infty} = 2\alpha_1 \tag{5.11}$$

where α_1 is given by eq. (5.10). The comparison among eq. (5.11), the experimental values and the eq. (5.8) is represented in Figure 5.24. The comparison shows that the Tanino and Nepf formula becomes a linear function of the density of vegetation for $Re_p \to \infty$, but our experimental data put in evidence the non-linear relationship between $C_{Dp,\infty}$ and Ω_v. In addition, for $\Omega_v = 0.1414$ the data is out from the range of validity of Tanino and Nepf formula, as in the precedent analysis for finite values of Re_p (Figure 5.23).

5.1.3 Indirect measurements of the drag coefficient

From the momentum balance in a rectangular channel, by neglecting the contribution due to bed forms, the drag coefficient can be determined indirectly with the formula obtained in Section 2.3.5:

$$C_{Dp} = \frac{\pi}{2}\frac{1-\Omega_v}{\Omega_v}\frac{d_p}{h}\left[\frac{ghi_b}{U^2} - \frac{g}{21.1^2}\left(\frac{d_{50}}{h}\right)^{1/3}\right] \tag{5.12}$$

Eq. (5.12) allows the indirect calculation of the C_{Dp} for the different experimental configurations with mobile bed and in presence of sediment transport (Section 4.2). The quantities in eq. (5.12) were measured (density of vegetation Ω_v, averaged plant diameter d_p, water depth h, bed slope i_b, grain roughness d_{50}) or evaluated (average velocity U). Moreover, the drag coefficient for rigid stems should depend on:

$$C_{Dp} = \phi\left(Re_p, Fr, \frac{h}{d_p}, \frac{B}{d_p}, \Omega_v\right) \tag{5.13}$$

as deduced by the dimensional analysis in the same section. In eq. (5.13) $Re_p = Ud_p/\nu$, $Fr = U/\sqrt{gh}$, B is the width of the channel. Hereafter, the dependence on h/d_p and B/d_p will not be considered, because the limited instrumental conditions obtainable in the channel do not allow to appreciate the dependence on these quantities.

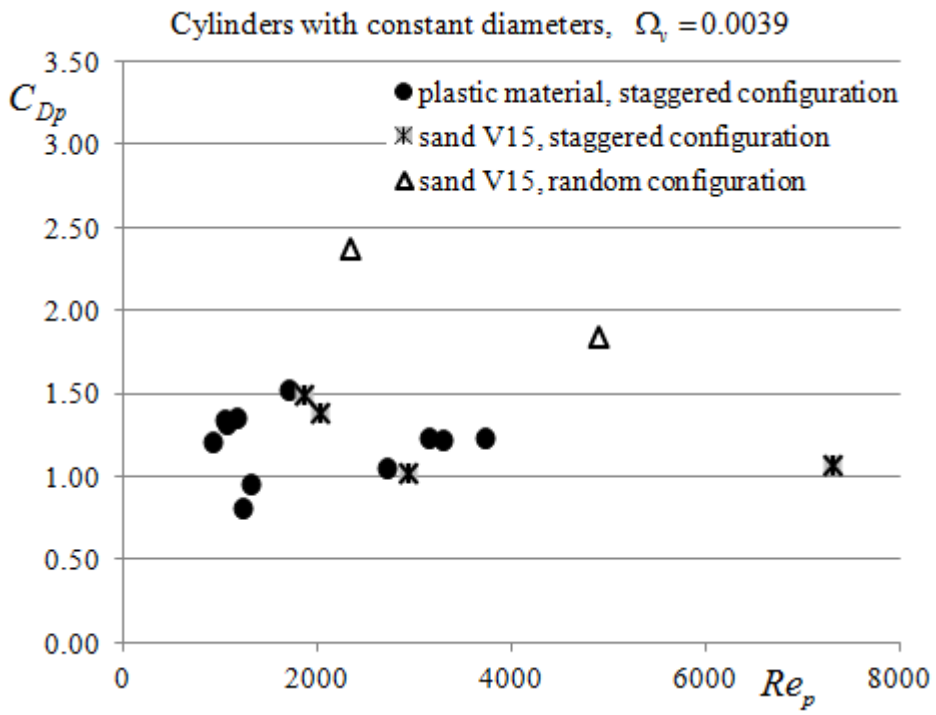

Figure 5.25: Comparison among the drag coefficients obtained with the indirect method for different configurations and $\Omega_v = 0.0039$.

The Figures 5.25, 5.26 and 5.27 represent the indirect drag coefficient evaluated for staggered and random distribution of cylinders. Each figure represents the data with the same density of vegetation (Figures 5.25 and 5.26) or density of vegetation very similar (Figure 5.27). This last figure, in particular, allows the comparison among the staggered distribution, the random distribution but constant stem diameters, and random distribution and variable stem diameters.

The first figure (Figure 5.25) is for the data obtained with a vegetation density $\Omega_v = 0.0039$. The tests, in this configuration, were carried out with two different sediment materials: the plastic material and the sand V15. The results induce to assume that the drag coefficient does not depend on the sediment density (the two materials have the same grain size). On the contrary, the same figure shows that the indirect drag coefficient depends on the distribution of stems: the random distribution produces a drag coefficient larger (even more than two times greater) than the staggered distribution. Moreover, the data are rather spread. These two

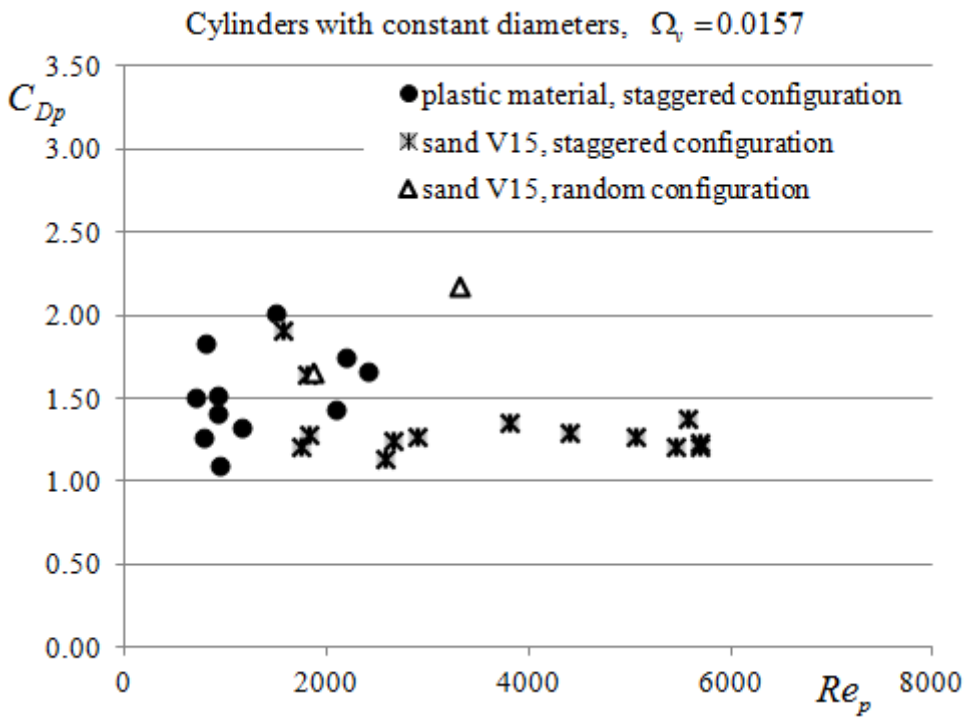

Figure 5.26: Comparison among the drag coefficients obtained with the indirect method for different configurations and $\Omega_v = 0.0157$.

last effects are due, in our opinion, to the effect of the bed forms, that has been neglected in the evaluation of the indirect drag coefficient. The bed forms related to the presence of vegetation will be treated in Section 5.3.

Figure 5.26 shows the indirect C_{Dp} for staggered and random distribution, for sand and plastic material, as a function of Re_p for $\Omega_v = 0.0157$. As for $\Omega_v = 0.0039$, also in this case the data are spread and the comparison between plastic and sand, for staggered distribution, does not show substantial differences. Whereas, as far as concerns the drag for staggered and random distribution of stems, in this case the tendency to be larger in random distribution is only partially confirmed. Probably, the data obtained are insufficient for defining a clear tendency.

In the Figure 5.27, the data already reported in Figure 5.26 are compared also with a similar density of stems, but obtained with 3 different stem sizes in random configuration. The results show that with increasing the randomness, that

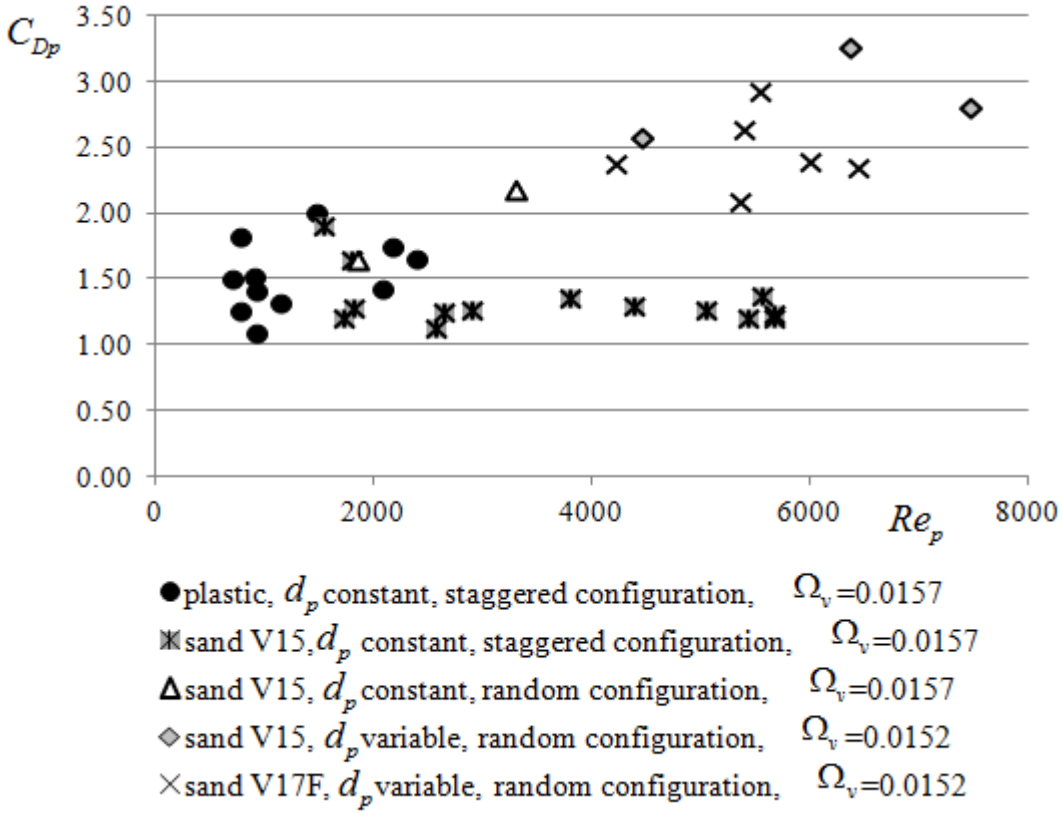

Figure 5.27: Comparison among the drag coefficients obtained with staggered and random distribution of cylinders.

is by adding also the variability on the cylinder diameters, the drag coefficients further increase. The C_{Dp} evaluated for random configuration and variable cylinder diameters are up to three times larger than the drag coefficients in staggered distribution. This behavior seems to confirm that the bed forms have an important role in the total flow resistance. In fact, we will experimentally verify that the bed forms are bigger for variable stem diameters (Section 5.3.2); this effect might be the cause of the increase of the drag coefficient, which contains also the drag exerted by bed forms.

In addition, the drag coefficients seem to be not influenced by the grain size. In fact, the results obtained for the sand V17F, that has got a size three times larger than the sand V15, are overlapped with the results for the sand V15. This

is probably due to the fact that, in presence of rigid stems, the grain roughness is basically negligible.

In Figure 5.27, although the spread of data, a peculiar behavior of the drag coefficient can be distinguished: for staggered distribution of stems, the drag tends to become constant for $Re_p > 3000$, tendency already observed for the direct measurements of drag (Section 5.1.4). For random distribution, at the contrary, the drag coefficient increases with Re_p increasing. This behavior is very difficult to explain with the classical approaches.

The same data have not been represented as a function of Fr, since the test conditions are always for $Fr < 1$, where the dependence of C_{Dp} on Froude number and Reynolds number is the same.

5.1.4 Comparison between direct and indirect measurements of drag coefficient

Figures from 5.28 to 5.33 show the drag coefficient obtained with the direct measurements (Section 5.1.4) of the drag force on the cylinders, and the indirect measurements of the drag coefficient for mobile bed conditions (Section 5.1.3). The data are those in staggered distribution, and different vegetation densities. We have verified, and reported in the precedent section (Section 5.1.3), that the drag coefficient for random distribution is actually not comparable. The data are represented as a function of Re_p and Ω_v.

As emerges from Figures from 5.28 to 5.33, the drag coefficients evaluated with the two methods are nearly coincident, although the indirect measurements are more spread at low Reynolds numbers. In these cases, the spreading of data and the distance from the direct measurements, in our opinion, is due to the hypothesis that bed forms resistance is negligible with respect the drag exerted by stems. In fact, at low Reynolds numbers, generally bed forms are present in the between the stems (as will be analyzed in the Section 5.3), while the eq. (5.12) was obtained neglecting the bed forms contribution.

In the Figures from 5.28 to 5.33, also the confidence interval of each value is reported. The confidence interval quantifies the uncertainties in the measurements due to the combination of instrumental and systematic errors (Section 4.3). As

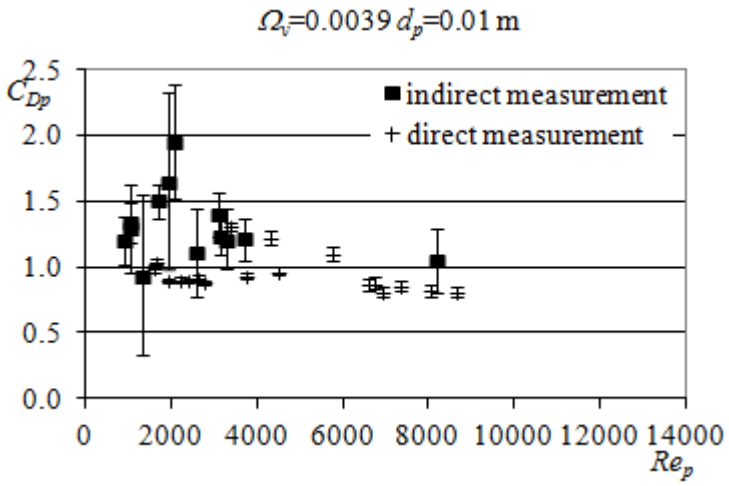

Figure 5.28: Comparison between the direct and indirect measurements of drag coefficient for $\Omega_v = 0.0039$.

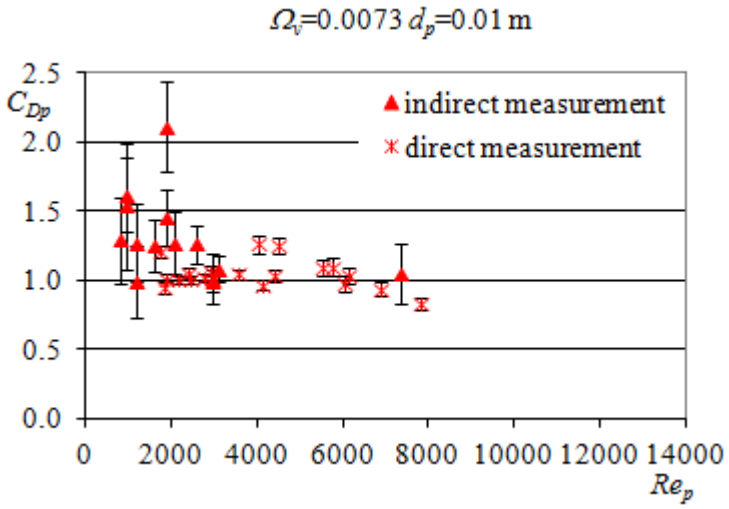

Figure 5.29: Comparison between the direct and indirect measurements of drag coefficient for $\Omega_v = 0.0073$.

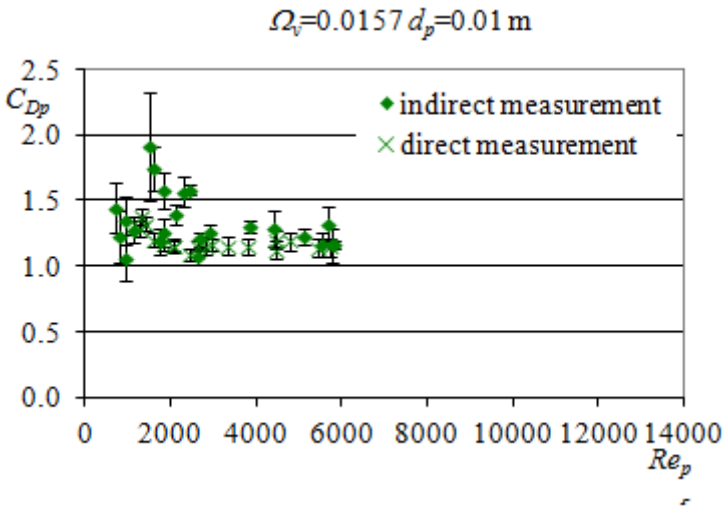

Figure 5.30: Comparison between the direct and indirect measurements of drag coefficient for $\Omega_v = 0.0157$.

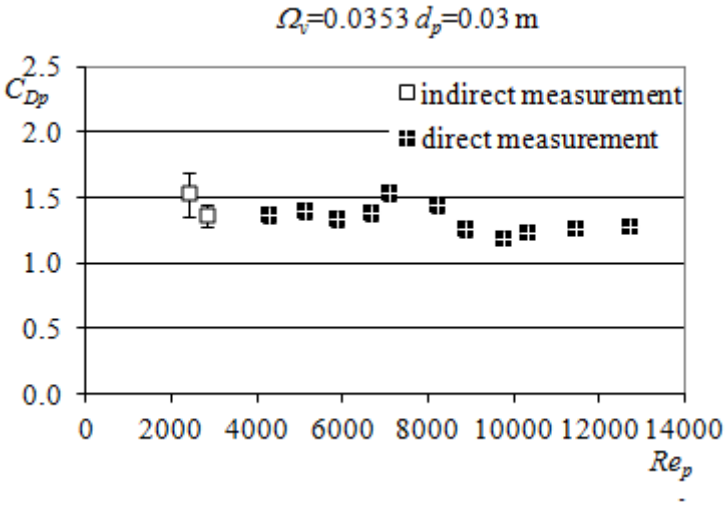

Figure 5.31: Comparison between the direct and indirect measurements of drag coefficient for $\Omega_v = 0.0353$.

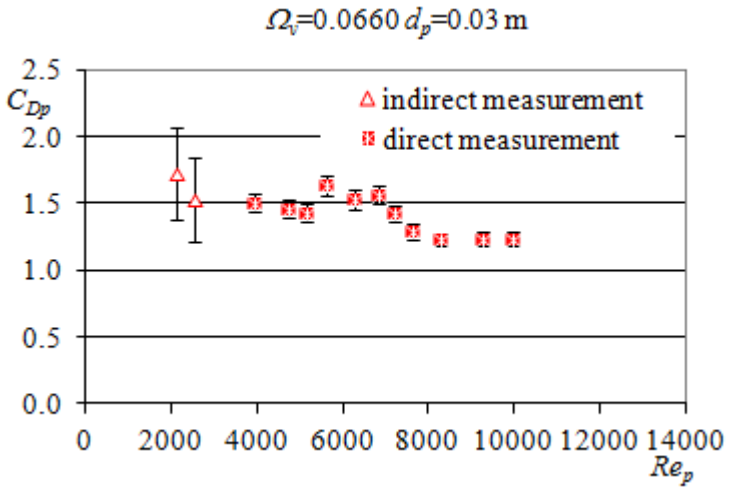

Figure 5.32: Comparison between the direct and indirect measurements of drag coefficient for $\Omega_v = 0.0660$.

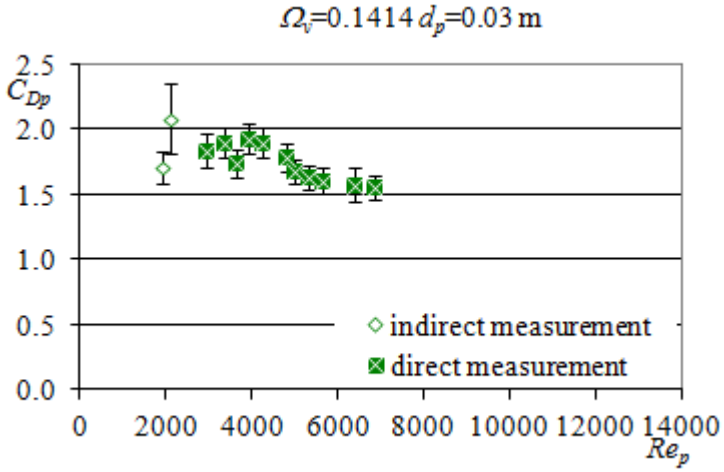

Figure 5.33: Comparison between the direct and indirect measurements of drag coefficient for $\Omega_v = 0.1414$.

already said, in the direct measurements the uncertainties are caused by the instrumental errors and by the errors related to (small) vibrations of the cylinders. In the indirect measurements, the instrumental errors (pointer gauge and flowmeter) are combined with the uncertainties related to the calculation of the water depth and of the slope. In the direct measurements the uncertainties are smaller than in the case of indirect measurements. This difference is due mainly to two reasons. Firstly because the errors considered in the indirect measurements are, to a great extent, larger. In particular in the indirect measurements the errors exerting the major influence on the results are the ones associated with slopes and water depths. Whereas, in the direct measurements the large number of acquired data, for the measurements of the forces, reduces the total error. Moreover, the measurements of bed slope and water depth are less affected by errors, because at fixed bed, bed and free surface elevations are easier to measure.

The second important cause of the larger errors in indirect measurements is due to the method of calculation, i.e. to the propagation of errors; in the direct measurements the total error of the drag coefficient is given by the combination of a lower number of errors, just because the direct evaluation.

Moreover, the errors at low Reynolds number are larger, both in the indirect and direct procedures. This effect is mainly due to the error in the slope measure, which increases significantly when the slope decreases and consequently also when the Reynolds number decreases. To some extent, however, the errors in this range of Reynolds numbers is not important in a natural context, where usually the Reynolds numbers do not assume the smaller values considered in the data.

On the other hand, by considering the indirect measurements and their confidence interval, we can see that the direct points are, in most cases, located into the confidence interval. It means, in a certain extent, that to consider as negligible the contribution due to bed forms may be a correct approximation.

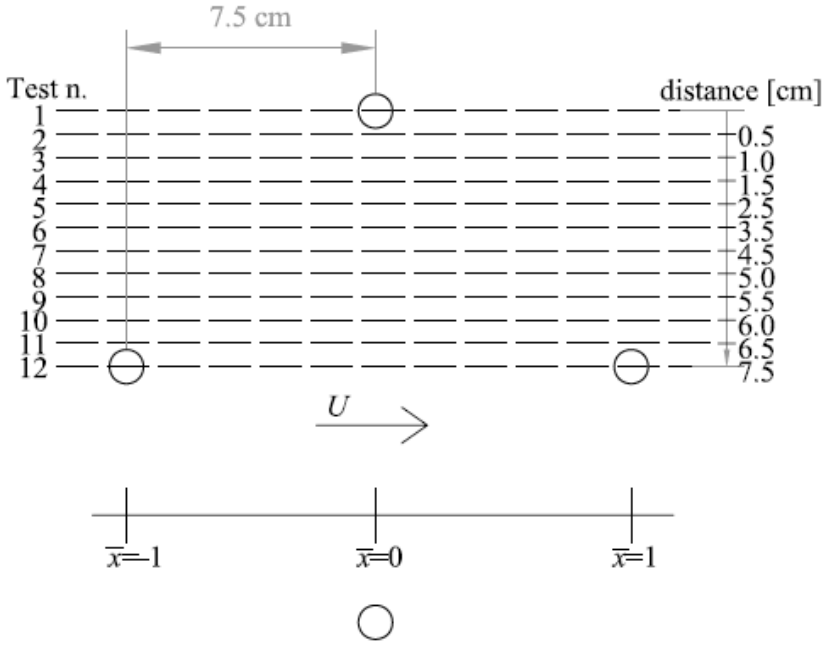

Figure 5.34: Drawing of the 12 planes of measurement among the cylinders.

5.2 Interactions between flow field and sediment transport

The measurement of the velocity field through the cylinders was carried out in the staggered distribution of cylinders with constant diameter $d_p = 1$ cm and vegetation density $\Omega_v = 0.0073$. The measurements were done in 12 vertical planes (Figure 5.34) and in a horizontal plane located at a distance $z/h = 0.25$ from the bottom, as described in Section 4.4. The main aim of the PIV measurements is the determination of the effects of flow field on the sediment entrainments and displacements.

The double averaged velocity, which was calculated with the PIV results, for the considered control volume was: $\langle \bar{u} \rangle = 0.139$ m/s in the x direction, and $\langle \bar{v} \rangle = 0.0002$ m/s, that is about 0, in the vertical direction. Hereafter, not all the mapping results are reported, but only the most significant cases.

In Figure 5.35 is depicted the instantaneous flow in the horizontal plane. It is possible to observe the typical oscillating wake behind the central cylinder. This wake is modified by the presence of the other cylinders of the array and appears

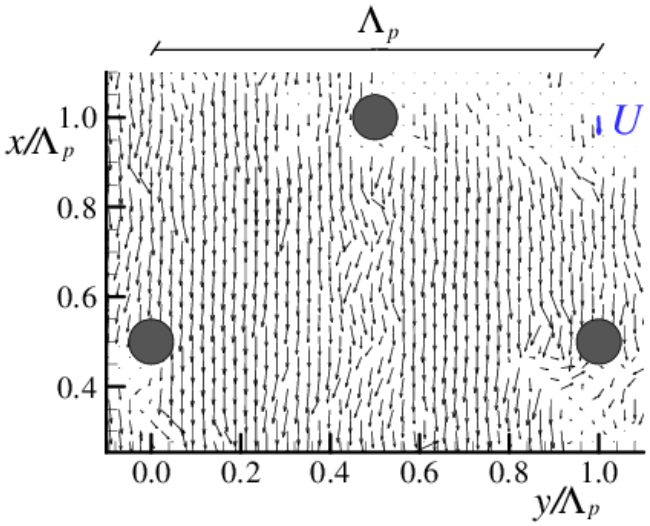

Figure 5.35: Distribution of the instantaneous velocity vectors (the scale is in the picture) in the horizontal plane at $z/h = 0.25$.

to be more confined and more regular than the wake around an isolated cylinder. This difference may explain the tendency of the drag coefficient, shown in Figure 5.17, to reach the asymptotic value for larger values of Re_p with respect to the isolated cylinder. According to Poggi et al. (2004), in fact, the sheltering exerted by the other cylinders prolongs the effect of Reynolds number on C_{Dp} even for larger Reynolds numbers.

In the following figures, the dimensionless coordinates are those represented in Figure 5.34. The horizontal axis represents the dimensionless distance between cylinders, x/Λ_p, and it is simply indicated by $\overline{x}$. $\overline{x} = 0$ is the coordinate correspondent to the centered cylinder; $\overline{x} = -1$ and $\overline{x} = 1$ are, respectively, the upstream staggered cylinder and the downstream staggered cylinder. The vertical direction is represented as z/h, where h is the water depth, and it is indicated by $\overline{z}$. Due to the presence of the transparent plate on the surface, we have not considered valid the data located above $z/h > 0.75$.

In the next figures (Figures from 5.36 to 5.42), the time averaged velocity, $\bar{u}$, is represented for the first vertical plane (test 1) and the sixth vertical plane (test 6). The velocities are represented in a dimensionless form, i.e. compared with the double-averaged velocity $\bar{u}/\sqrt{\langle\bar{u}\rangle^2 + \langle\bar{v}\rangle^2}$ and $\bar{v}/\sqrt{\langle\bar{u}\rangle^2 + \langle\bar{v}\rangle^2}$. In the legend of

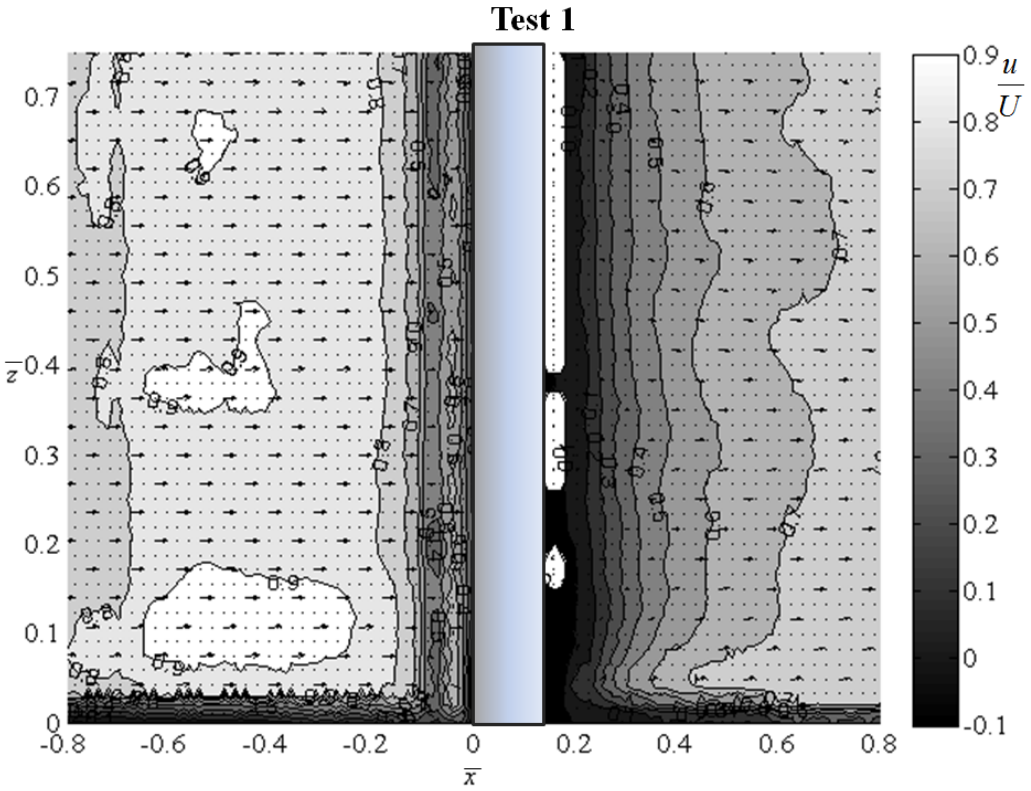

Figure 5.36: Time averaged velocity for the test 1.

the figures, the symbol U is the module of the double averaged quantities, that is $U = \sqrt{\langle\bar{u}\rangle^2 + \langle\bar{v}\rangle^2}$, and $u = \sqrt{\bar{u}^2 + \bar{v}^2}$.

In the Figure 5.36 is shown the results of the test 1, in the vertical plane containing the axis of the cylinder (Figure 5.34). The velocity distribution tends to decrease rapidly, as one approaches the cylinder. In the region immediately downstream the cylinder ($\overline{x} < 0.2$), a zone with negative longitudinal velocity is present, as a result of the recirculation that occurs in the separation zone (Figure 5.37). Going further downstream, out of the separation zone, the longitudinal velocity assumes positive values. This behavior is more or less present all along the flow depth. In this section, the velocity does never reach the uniformity, and the maximum value is located upstream the cylinder ($u/U = 0.9$), while the whole region downstream is strongly affected by its presence.

Figure 5.38 shows the vertical distribution of the velocity components in the plane of the test 1 and the differences obtainable by averaging the values of $\bar{v}$ for

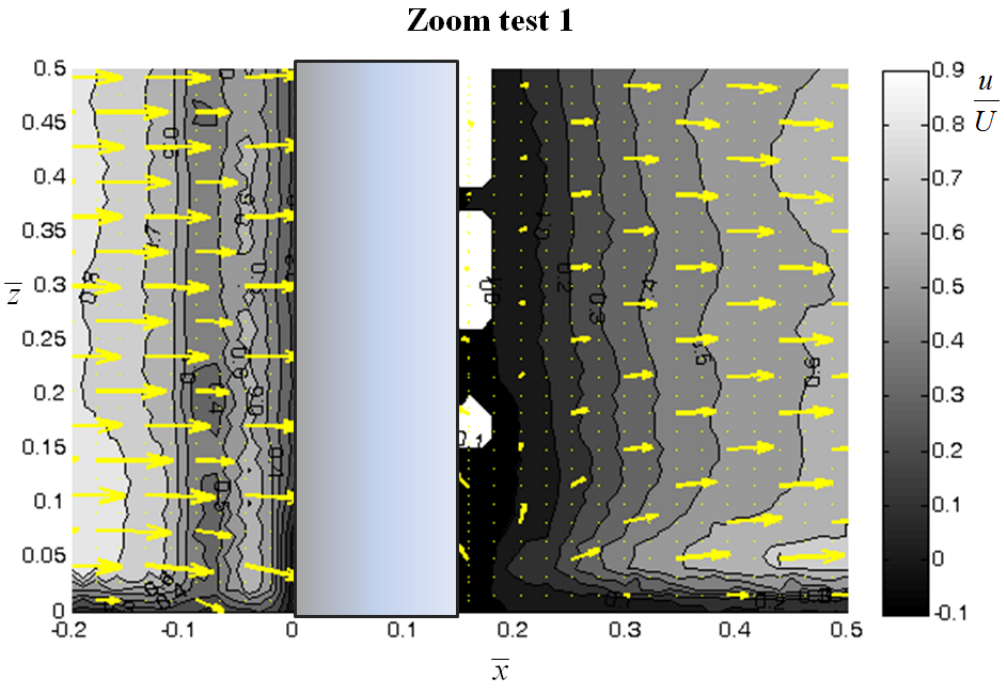

Figure 5.37: Time averaged velocity for a small area of the test 1.

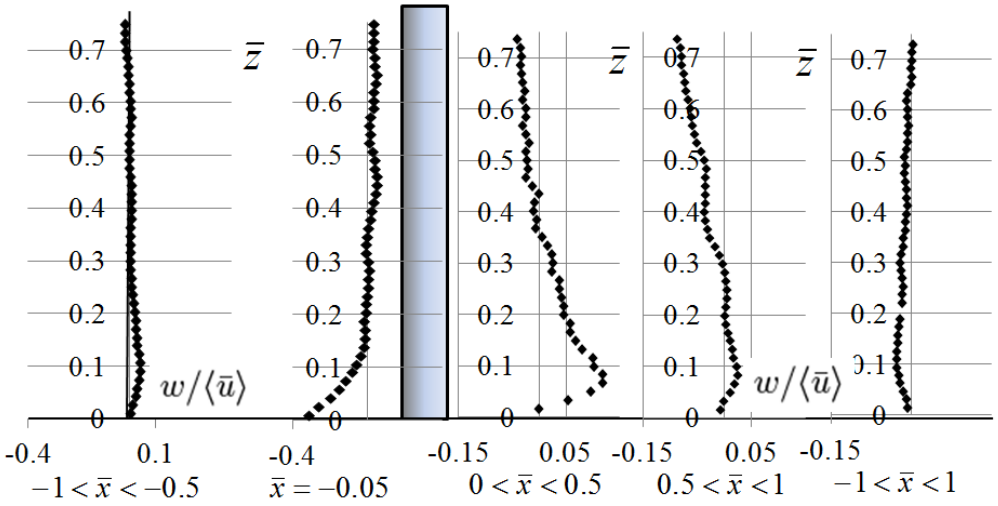

Figure 5.38: Vertical component of the time and spatial averaged velocity of test 1. In the figure, five profiles of velocity are shown: 3 profiles are the velocity averages for intervals of data in the x; 1 is the punctual profile for a x coordinate close to the cylinder ($x = -0.05$); the last one is the averaged profile for all the test 1.

five different ranges of $\overline{x}$. It is particularly interesting (Figures 5.37 and 5.38) the tendency of the flow, upstream the cylinder and close to the bottom, to be downward oriented. This feature of the flow field is well known and deeply discussed by Kirkil, Constantinescu, Ettema, et al. (2008), at least for the case of an isolated cylinder. In that zone the vertical component of the instantaneous velocities is always oriented toward the bed. It is also known that in this region a significant scour is present in case of mobile bed.

Figure 5.39 shows how the profiles of Reynolds stresses ($\overline{u'w'}/u_*^2$) change frequently their signs, in test 1, proceeding from downstream to upstream the cylinder and at different distances. In particular, five different profiles are shown: two averaged profiles of the Reynolds stresses for a range of data far from the cylinder, both downstream and upstream ($-1 < x/\Lambda_p < -0.5$ upstream, and $0.5 < x/\Lambda_p < 1$ downstream); two vertical profiles very close to the cylinder ($x/\Lambda_p = -0.05$ upstream, and $x/\Lambda_p = 0.05$ downstream); the last one is the averaged profile for all the domain ($-1 < x/\Lambda_p < 1$). In all the cases, the Reynolds stress profiles are very different from the traditional triangular profiles. Therefore, the effect of the presence of the cylinder is not quenched before having reached the next cylinder, by confirming the mutual interaction between two cylinders. In other words, the recirculating zone which develops downstream a cylinder affects the flow field upstream the following cylinder. Hence, a boundary layer-like flow field cannot develop in the planes in line with the cylinders, like the plane of Test 1 and Test 12 (see Figure 5.34).

Figure 5.39 shows that immediately upstream the cylinder, in Test 1 (see Figure 5.34), the local Reynolds stresses assume negative values but not particularly high in module; here the longitudinal component of the averaged velocity (Figure 5.38) is very small, due to the formation of a stagnation point on the upstream face of the cylinder. All these consideration allow one to infer that the recirculating region just downstream the cylinder, characterized by evident erosion phenomena, actively participate to the sediment detachment but not to the sediment transport. The erosion processes which take place are particularly significant (see e.g. Ettema, Nakato, and Muste (2008)) but seems to be poorly related to the local values of the Reynolds stresses $u'w'$, therefore in this area the scouring can be hardly be related to a shear mechanism.

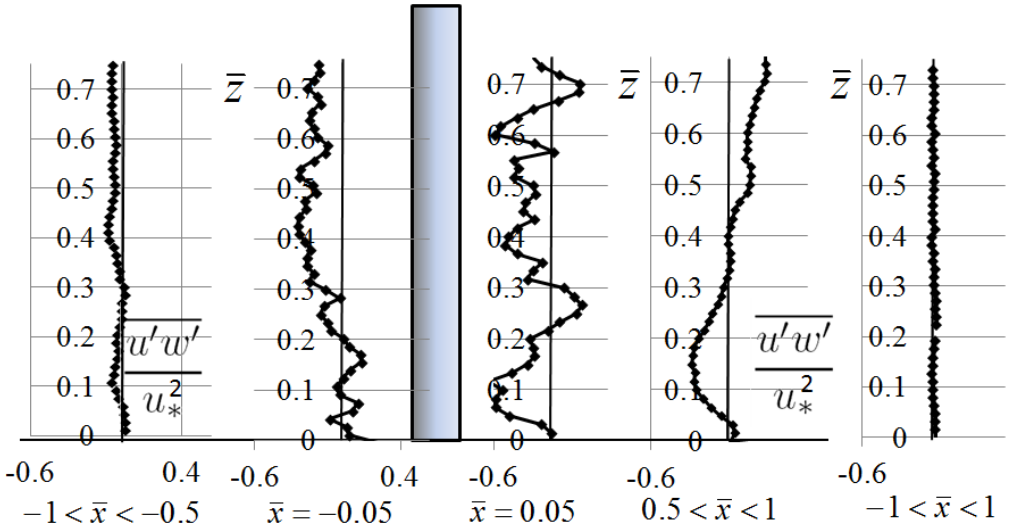

Figure 5.39: Profiles of averaged Reynolds stresses for 3 different x ranges of test 1, and 2 punctual profiles ($x = -0.05$ and $x = 0.05$).

The profile closest to the cylinder, represented in Figure 5.39, confirms what already said for the vertical component of velocity, since upstream the cylinder $\overline{u'w'} > 0$. Positive values of Reynolds stresses mean that the shear stress at the bed ($\tau = -\rho\overline{u'w'}$) is directed upstream, and this is due to the transversal axis vortex that takes place at the bottom (Kirkil, Constantinescu, Ettema, et al. 2008). An erosion is present, but it does not contribute to the sediment discharge, since the sediments are continuously eroded and reposited inside the hole.

The same remarks can be done as far as concerns the behavior of the flow downstream the cylinder. The vertical components (Figures 5.37 and 5.38) are positive, i.e. directed upward. This corresponds to a decrease of the module of Reynolds stresses close to the cylinder (Figure 5.39), which however maintains a negative value. This means that there is an area close to the cylinder in which the shear stress are directed upstream and hence it does not actively participate to the sediment transport, but it rather behaves as a sink for sediment. Indeed it can be argued that sediment particles are displaced to be "entrapped" in the recirculating zone. In the whole region downstream the cylinder and close to the bed, however, the tendency of the Reynolds stresses is to assume positive values. Instead, they can be positive or negative along the depth, but by averaging for all the domain

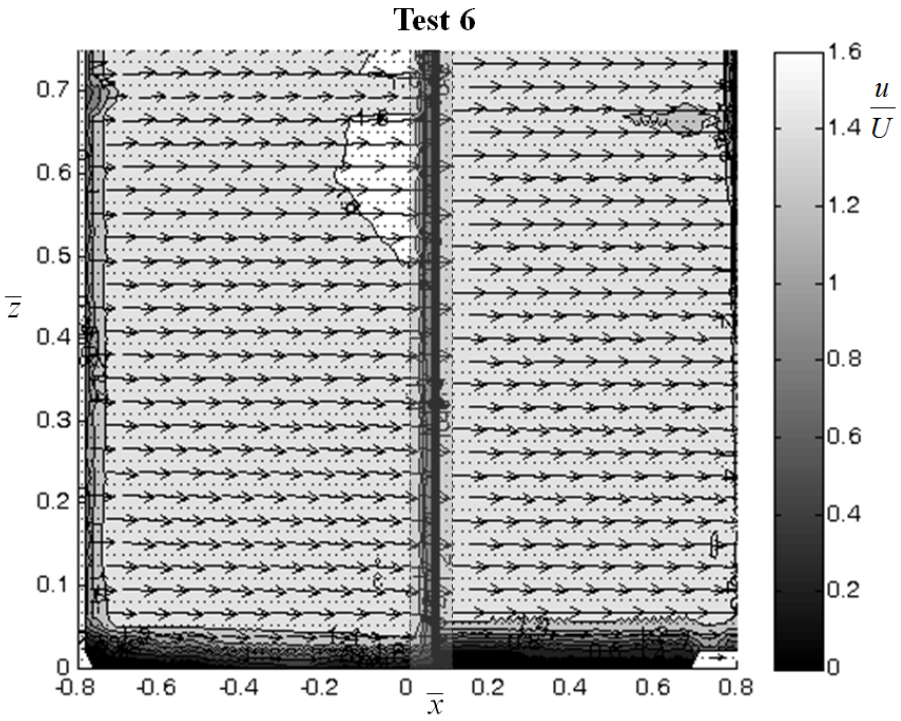

Figure 5.40: Time averaged velocity for the test 6. The central darkest band is caused by errors due to the superposition of the upstream and downstream images which form the global domain.

(last profile in Figure 5.39, for $-1 < x < 1$) they assume very small values.

The behavior is totally different if, instead of the test 1, we consider a section sufficiently distant from the cylinder, such as in the test 6 (Figures 5.40 and 5.41). It is clear that the flow becomes uniform, both for the horizontal and vertical components of velocity. Relatively to the Reynolds stresses represented in Figure 5.42, the first two profiles ($-1 < x < -0.5$ and $-0.5 < x < 0$) have the classical triangular trend close to the bottom. The last profile ($-1 < x < -0.5$) has a different behavior at the bottom: the Reynolds stresses go to zero, and this could be due to the effect of the wake of the closest upstream cylinder.

Finally, concerning the changes of the averaged velocity, the averaged velocity is smaller for the test closer to the cylinder: in the test 1 (the plane containing the cylinder) $\langle\sqrt{\bar{u}^2+\bar{v}^2}\rangle_1/\sqrt{\langle\bar{u}\rangle^2+\langle\bar{v}\rangle^2} = 0.8$ that is much smaller than the averaged velocity in the test 6, where the behavior is totally uniform (Figure 5.40),

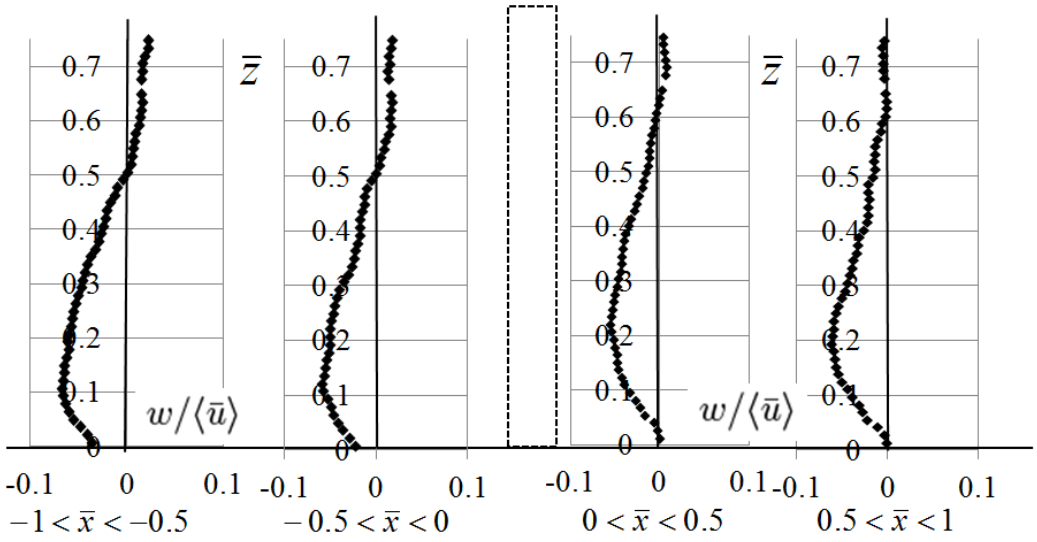

Figure 5.41: Vertical component of the time and spatial averaged velocity of test 6, for 4 different x ranges of measurements.

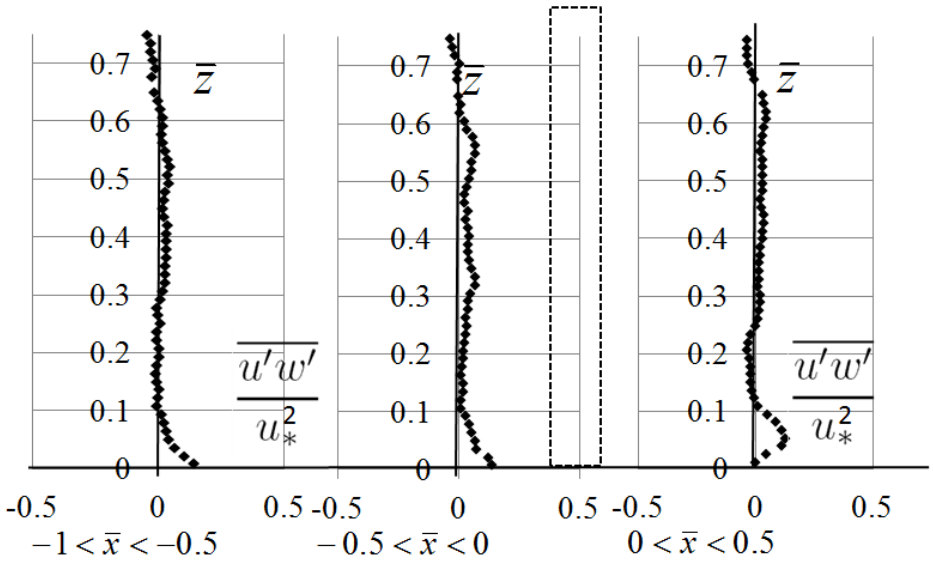

Figure 5.42: Averaged Reynolds stress for test 6, for 3 different x ranges of measurements.

and the ratio of the velocities results $\langle\sqrt{\bar{u}^2+\bar{v}^2}\,\rangle_6/\sqrt{\langle\bar{u}\rangle^2+\langle\bar{v}\rangle^2}=1.34$. From the Figures 5.38, 5.39 and 5.42, it is evident that, in this case, this spatial average, represented by the last profile of each figure, is not sufficient to describe the spatial variation of the flow characteristics. For this reason we decided to analyze the different profiles.

For summarizing, the PIV analysis has put in evidence that there is an area of the bed where the velocity at the bottom results upstream directed, and hence where the sediments are entrained towards upstream and do not contribute to the sediment discharge, unless they reach a sufficient height to be transported by the flow. This height is as smaller as the sediment is far from the cylinder.

The results demonstrate that the double-averaged velocity is not always and completely descriptive of the behavior of the whole domain of the flow, in particular if the flow field is related with the sediment transport.

Concluding, the mechanisms of sediment transport in vegetated rivers are different by the mechanisms of transport in unvegetated rivers, because different mechanisms of entrainment and transport have to be considered. In particular, sediment transport is not everywhere in correlation with local values of shear stress at the bottom, as usually assumed in spatially homogeneous flows. The present analysis shows that there are zones of active particle erosion but negligible transport downstream and zones of transport. All these aspects should be properly taken into account if modifications of existing sediment transport formulas or new formulation for sediment transport capacity in vegetated rivers are proposed.

5.3 The vegetation bed forms

5.3.1 Description of the experimental approach

We have already punctuated that the vegetation modifies the structure of flow fields and, consequently, the relationships among water discharge, hydrodynamics, flow resistance and river morphology. The analysis of these effects is the main objective of the thesis. In this regard, one of the most intriguing aspects is to achieve how vegetation modifies the morphology of rivers at small and large scale. As far as concerns the morphology at large scale, the observations more interest-

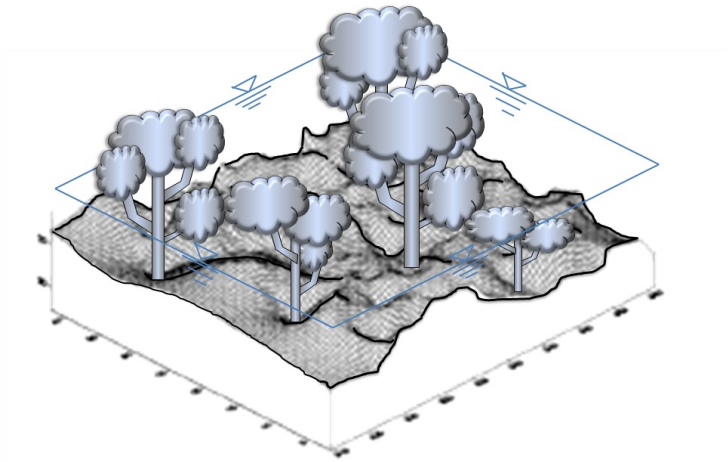

Figure 5.43: Example of a possible configuration of the vegetated bed in a reach of the laboratory channel

ing regard the effects on planimetric forms and their interactions with patterns of vegetation. For the small scale, the most significant aspect is the relationship between the modification of the nature of bed forms and the effects on resistance, that is the objective of this part of experimentation.

In presence of rigid vegetation at sufficiently high density, the stems produce particular bed forms, that in the following will be termed *vegetation bed forms* (Figure 5.43). The mechanisms for the bed forms formation are related with the secondary currents and horseshoe vorteces, as already described in Section 2.3.3. These mechanisms are partially visible by the PIV results (Section 5.2).

In order to analyze the influence of vegetation density and distribution on bed forms, measurements of length and height of vegetation bed forms were carried out for each test, after having reached the steady condition. In order to obtain precise values of bed form length and height, the survey of the bed elevation was thickened up to $0.5 \sim 2$ cm around a certain number of bed forms.

In steady conditions all the parameters which influence the flow and bed regime are determined by the solid and liquid discharge, provided that sediment characteristics are not modified. Hence, the height of vegetation bed forms,Δ_{vf}, depends

on the parameters related with the flow and with the sediments properties:

$$\Delta_{vf} = f_1(q, q_s, \rho, \rho_s, \mu, g, d_s, \Lambda_p, d_p) \tag{5.14}$$

In eq. (5.14) q and q_s are the liquid and sediment discharge respectively; ρ and ρ_s are the density of water and of sediments; μ is the viscosity of water; g is the gravity; d_s is the characteristic grain size; Λ_p is the averaged distance among stems and d_p is the average stems diameter. According to the Buckingham theorem, eq. (5.14) can be reduced to the following relationship in dimensionless parameters:

$$\frac{\Delta_{vf}}{d_p} = \varphi_1(\frac{q_s}{q}, \frac{\rho_s}{\rho}, \frac{q\rho}{\mu}, \frac{q}{d_p\sqrt{gd_p}}, \frac{\Lambda_p}{d_p}, \frac{d_p}{d_s}) \tag{5.15}$$

where $q\rho/\mu$ represents the Reynolds number, and $q/d_p\sqrt{gd_p}$ the Froude number. For the length of dunes, Λ_{vf}, the formulation is analogous:

$$\frac{\Lambda_{vf}}{d_p} = \varphi_2(\frac{q_s}{q}, \frac{\rho_s}{\rho}, \frac{q\rho}{\mu}, \frac{gd_p^3}{q^2}, \frac{\Lambda_p}{d_p}, \frac{d_p}{d_s}) \tag{5.16}$$

The experimental investigation is addressed to understand the mutual influence of the above parameters.

5.3.2 Length and height of vegetation bed forms

5.3.3 Data analysis for staggered distribution of stems

In staggered distribution of stems, the length of the vegetation forms is strictly and clearly correlated with the distance between the stems. In Figure 5.44 the ratio between the measured length of vegetation forms, Λ_{vf}, and the averaged distance between cylinders, Λ_p (in the longitudinal direction), is represented as a function of the ratio q_s/q. The results shown in the Figure 5.44 are plotted by regrouping the points by different densities of stems, where the value of the density is indicated by the symbol Ω_v, which is defined as the area occupied by plants over the total considered area (eq. 4.1). Figure 5.44 shows that the length of the bed forms is not influenced by the density of vegetation, given that the same length of the forms corresponds to different densities. To better specify, both for

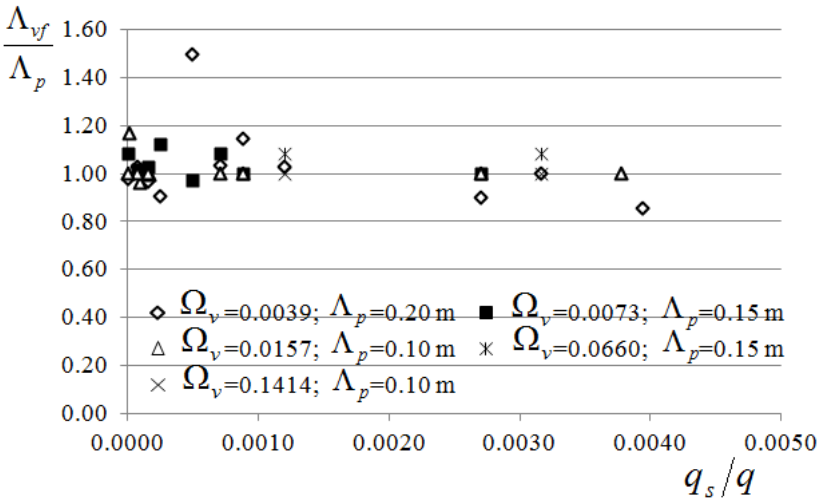

Figure 5.44: Length of bed forms in staggered configuration of cylinders for different densities of stems

$\Omega_v = 0.0157$ and $\Omega_v = 0.1414$, that have the same distance between cylinders ($\Lambda_p = 10$ cm), the ratio Λ_{vf}/Λ_p is equal to 1. The same thing occurs for the densities $\Omega_v = 0.0073$ and $\Omega_v = 0.0660$ ($\Lambda_p = 15$ cm), and $\Lambda_{vf}/\Lambda_p = 1$.

On the contrary in the sparse configuration ($\Lambda_p = 0.20$ m, $\Omega_v = 0.0039$) the distance between the stems depends also on the flow characteristics (q_s/q). In this case, the distance between the stems is probably too large to inhibit the formation of natural dunes and their downstream migration.

Figure 5.45 shows that bed forms height is of the same order of magnitude of the natural dunes measured in the non-vegetated reach of the flume (the last partition, see Section 4.2).

In the Figure 5.45, the data show a dependence of the height of bed forms by the concentration of sediment (q_s/q). For $q_s/q > 0.05\%$ the ratio Λ_{vf}/d_s tends to decrease. This trend is not surprising, because when q_s/q starts to increase above a certain value, the flow tends to the critical condition and the bed tends to become plane, that is the height of the dunes tends to be reduced.

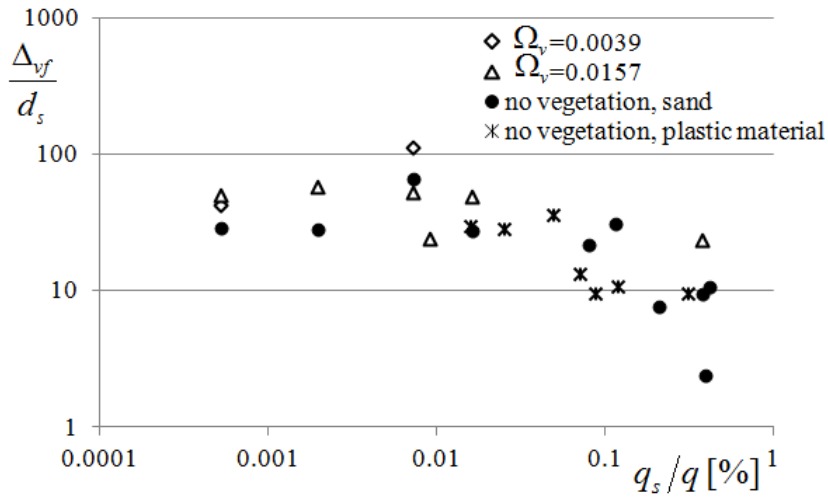

Figure 5.45: Height of vegetation bed forms in staggered configuration of cylinders for different densities of stems, compared with the height of dunes in the non-vegetated reach of the channel.

5.3.4 Data analysis for random distribution of stems

For random distribution of stems, the bed forms are very irregular. Length and height of each individual form is significantly different (Figures 5.46 and 5.47).

Figures 5.48 and 5.49 show that the length of vegetation bed forms depends linearly on the distance between cylinders. The ratio Λ_{vf}/Λ_p is nearly equal to 1 (as for staggered distribution), for the cases of constant diameter, and about 1.4 for the variable diameters of cylinders. A possible explanation of this difference is that the vegetation bed forms are more influenced by the cylinders with the largest diameters. The averaged distance, in this case, is probably not a significant parameter.

The experimental results have put in evidence that, for a sufficiently high density of stems, the length of vegetation bed forms is not influenced by the vegetation density, but only by the distance between the plants. On the contrary, the height of the forms seems to be not dependent on the vegetation densities, but it could be more probably related with the characteristics of the flow field and with the sediment properties.

For sparse distribution of stems, the vegetation bed forms are much more similar to the natural dunes in non-vegetated beds. The length of these bed forms

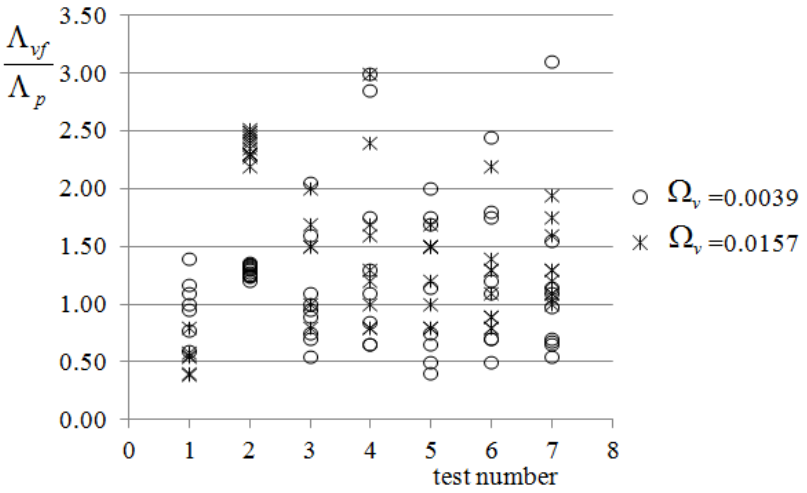

Figure 5.46: Measured length over the averaged distance between cylinders for each test.

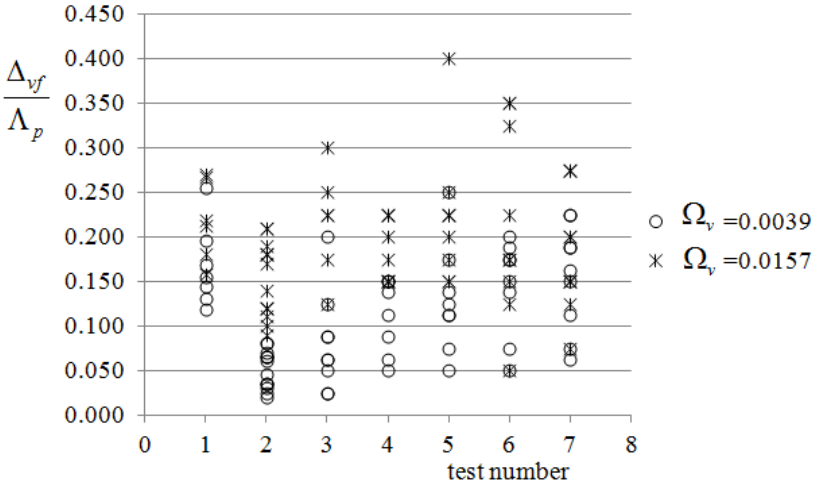

Figure 5.47: Measured height over the averaged distance between cylinders for each test.

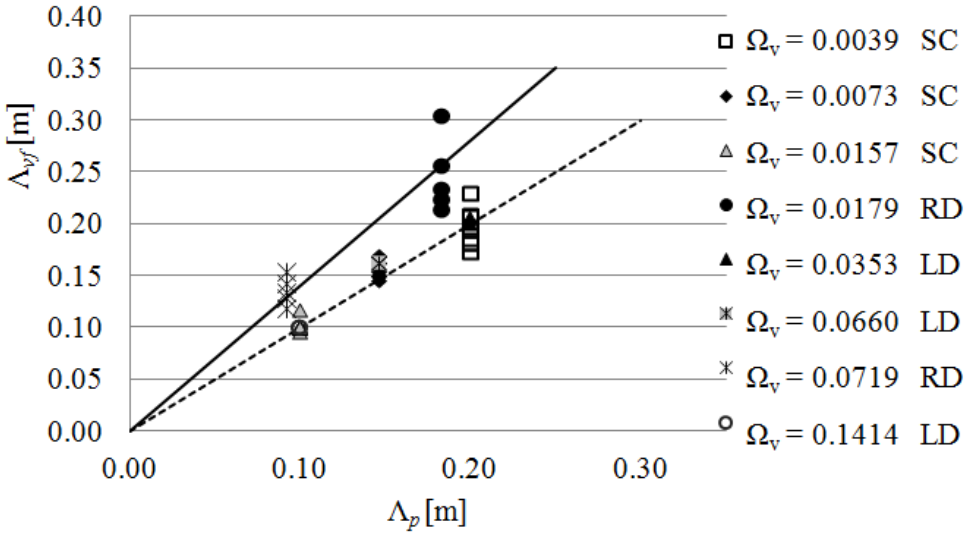

Figure 5.48: Comparison between the measured averaged length of bed forms and the averaged distance among stems. In the representation, it is indicated with SC the tests carry out with constant Small Cylinder ($d_p = 0.01$ m); with LD, the tests with constant Large Cylinder ($d_p = 0.03$ m); with RD, the tests with random diameters of cylinders ($d_p = 0.01$, 0.019 and 0.03 m).

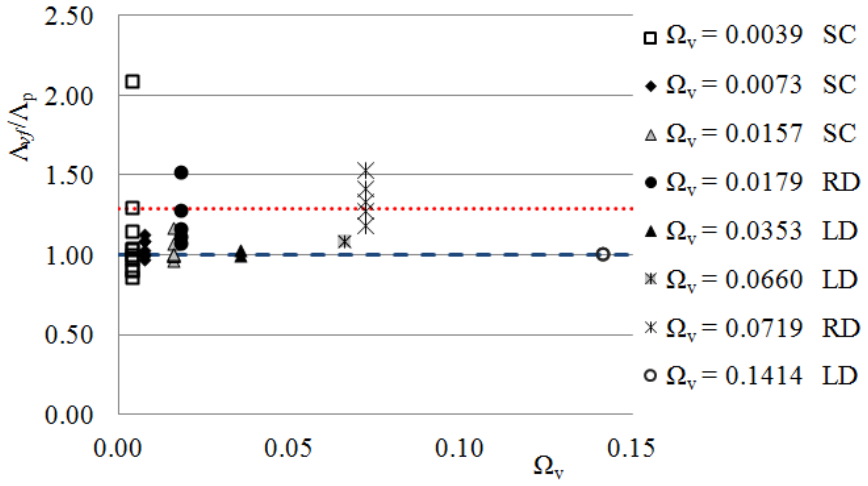

Figure 5.49: Measured averaged lengths of bed forms divided for distribution of stems. In the representation, it is indicated with SC the tests carry out with constant Small Cylinder ($d_p = 0.01$ m); with LD, the tests with constant Large Cylinder ($d_p = 0.03$ m); with RD, the tests with random diameters of cylinders ($d_p = 0.01$, 0.019 and 0.03 m).

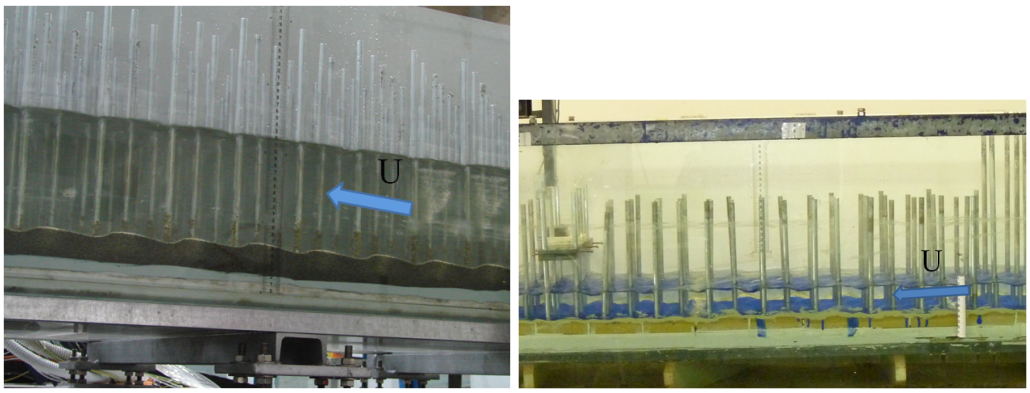

(a) mobile bed (b) modeled bed

Figure 5.50: The (a) vegetation bed forms formed in case of staggered configuration are reproduced (b) in plastic material for the measurements of drag force.

results to be less influenced by the distance between cylinders. In fact, in some tests it is evident as both kinds of bed forms (vegetation forms and natural dunes) are contemporarily present, and they interact mutually and overlap.

In some tests and for small vegetation density, when the incipient motion condition is approaching, the bed forms migrate downstream as the dunes, notwithstanding the presence of vegetation. At the contrary, when the density is relatively high, the presence of the stems inhibits every migration.

5.3.5 The contribution of bed forms to global resistance

The modeled bed forms

With the measurements of the height and length of bed forms in staggered configuration, a model of the bed forms in plastic rigid material was made (Figure 5.50). The length of channel covered by the model was $4\ \mathrm{m}$, the width of the channel was $0.3\ \mathrm{m}$, the density of stems was equal to 0.0157 and the distribution of stems was staggered (Figure 5.51). The length of the reach was sufficient for reaching uniform flow condition. In this experimental setup, the load cell was fixed to two rows of cylinders and the drag force was measured for different flow conditions (Figure 5.51 (c)).

The bed slope was obtained as in the precedent experiments. The water depth was measured not for one transversal coordinates, but, given the asymmetric bed,

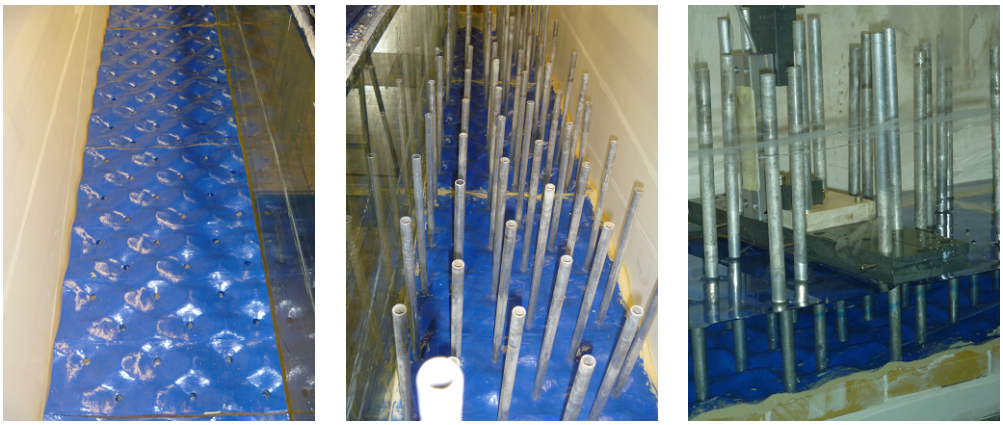

(a) without cylinders (b) with cylinders (c) the load cell

Figure 5.51: A reach of the channel with the modeled bed forms, (a) before the fixing of cylinders and (b) after the fixing of cylinders. (c) The load cell fixed to the cylinders for the measurements of drag force.

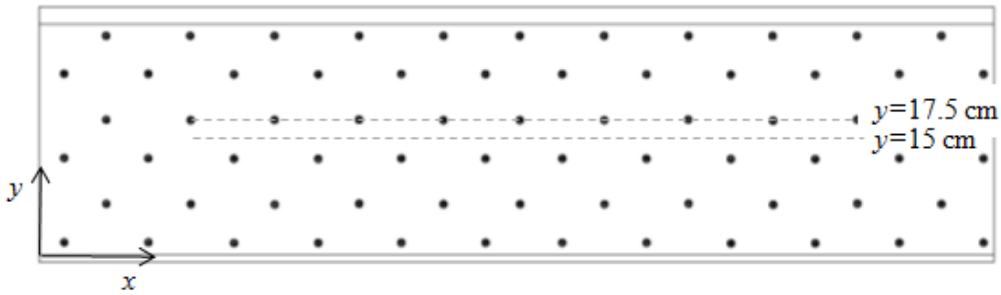

Figure 5.52: y coordinates of measurements of water depth.

it was measured for two different y: $y = 15$ cm, coincident with the center of the channel, and $y = 17.5$ cm, coincident with a row of cylinders (Figure 5.52). In the x direction, the data were collected every 2 cm. In accordance with the definition of uniform flow in a vegetated channel, given in Section 2.3.4, the water depth was the averaged of water depth measured along the channel.

The comparison between drag coefficient with bed forms and plane bed

Figure 5.53 shows the comparison between the drag coefficients obtained with plane bed (and already reported in Section 5.1.4) and the drag coefficients ob-

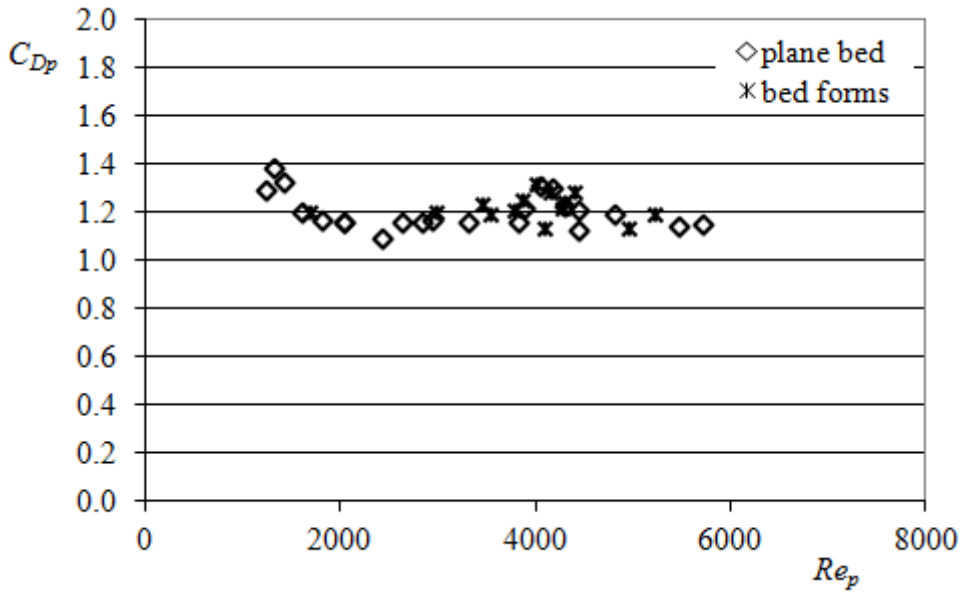

Figure 5.53: Comparison of drag coefficient between plane bed and modeled bed forms.

tained in the case of bed forms. The drag coefficients in the two conditions are comparable, but the drag coefficient with bed forms, for the same $Re_p = Ud_p/\nu$, is generally larger than the drag coefficient in plane bed.

The tendency is more evident in the following figure (Figure 5.54), where for the same ranges of Reynolds number the drag coefficients in plane bed and with bed forms are compared. In the figure the straight line is the bisector; since almost all of the points are in the down part of the bisector division, it can be reaffirmed the above assumption, i.e. $C_{Dp,plane}$ is generally smaller than $C_{Dp,bed\,forms}$.

Moreover, the ratio between $C_{Dp,bed\,forms}/C_{Dp,plane}$ seems larger for the smaller values of C_{Dp}. This means that when the drag exerted by stems is smaller, then the effect due to bed forms is more evident.

In order to evaluate which is the real contribution due to bed forms, some tests were carried out without stems. In uniform flow conditions, the resistance law can be evaluated as:

$$\frac{U}{u_*} = \sqrt{\frac{8}{f}} \tag{5.17}$$

In the tests without stems, the only contribution to the global shear resistance is

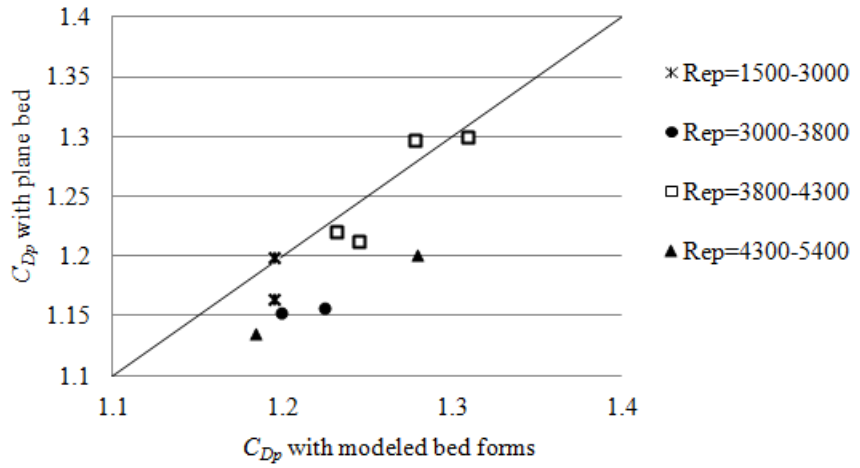

Figure 5.54: Comparison of drag coefficient between plane bed and modeled bed forms for ranges of Re_p.

due to the bed forms, then eq. (5.17) becomes:

$$\frac{U}{u''_*} = \sqrt{\frac{8}{f''}} \tag{5.18}$$

By substituting $u''_* = \sqrt{ghi_b}$, f'' can be evaluated. In Figure 5.55 is represented f'' as a function of the averaged velocity $U = Q/B$. In Figure 5.55 is represented also the curve of interpolation, that has the following equation:

$$f'' = 0.0712U^{-1.298} \tag{5.19}$$

With the direct measurements of the bed forms roughness, the direct value of the bed forms drag R_{bf} can be obtained for a control volume of width B and length L:

$$R_{bf} = \tau''_0 BL \tag{5.20}$$

The equivalent shear stress due to the bed forms is $\tau''_0 = \rho ghi_b$.

These values can be compared with the R_{bf} evaluated through the balance of momentum (Section 2.3.5):

$$W_x = \tau'_0 BL + \sum R_{p,j} + R_{bf} \tag{5.21}$$

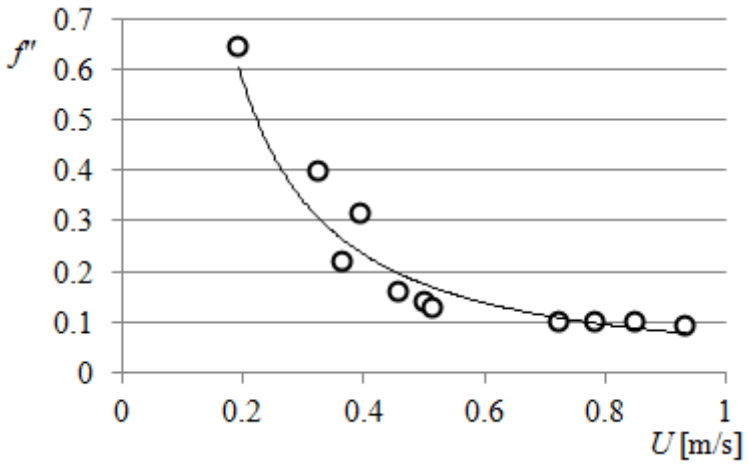

Figure 5.55: Evaluation of the Darcy-Weisbach coefficient for the bed forms as a function of the averaged velocity U.

In this case, the grain roughness is negligible, because no sediment is present. Hence:

$$R_{bf} = W_x - \sum R_{p,j} \tag{5.22}$$

and, by substituting the measured quantities:

$$R_{bf} = \rho g h i_b B L \left(1 - \Omega_v\right) - \sum_{i=1}^{N_p} C_{Dp,j} \rho A_{r,j} \frac{U^2}{2} \tag{5.23}$$

where N_p is the number of stems contained in the surface BL extend.

By dividing by BL, given the experimental configuration, from eq. (5.23) the bed forms shear stress is:

$$\tau_0'' = \frac{R_{bf}}{BL} = \rho g h i_b \left(1 - \Omega_v\right) - \sum_{i=1}^{n_p} C_{Dp,j} \rho A_{r,j} \frac{U^2}{2} \tag{5.24}$$

where $n_p = N_p/BL$ is the number of stems per meter square. In conclusion, by measuring the drag coefficient $C_{Dp,j}$, the water depth h and the bed slope i_b, the indirect value of equivalent shear stress, τ_0'', can be evaluated for different flow conditions. The indirect measurements can be compared with the direct measurements obtained without stems (eq. 5.20).

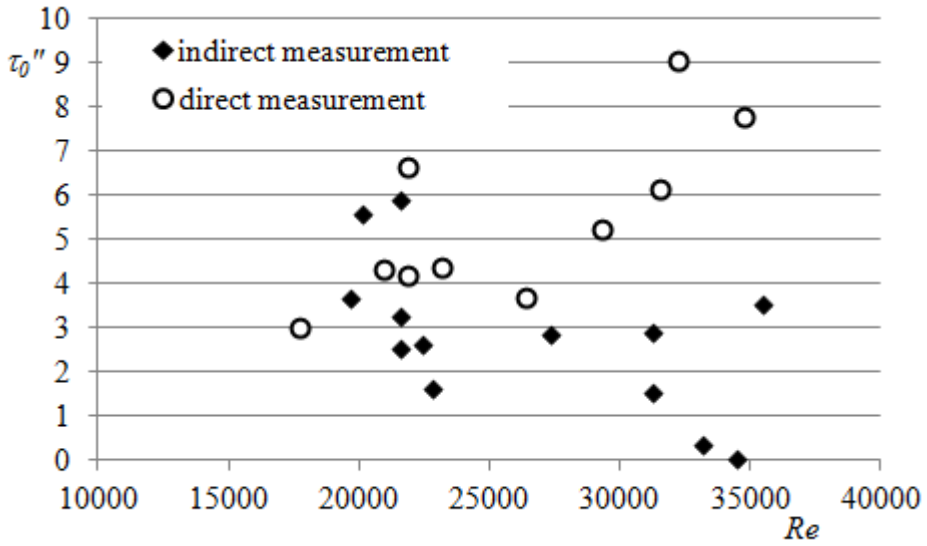

Figure 5.56: Comparison between the equivalent shear stress measured directly and indirectly as a function of the Reynolds number $Re = Uh/\nu$.

In Figure 5.56 the τ_0'' obtained indirectly and directly are compared as a function of the Reynolds number $Re = Uh/\nu$. The indirect results clearly show that the bed forms roughness is generally not negligible in vegetated beds. On the contrary, the indirect values are totally comparable with the direct measurements. This means that the bed forms contribution is important in vegetated beds as in non-vegetated beds.

In Figure 5.56, the points of direct and indirect measurements are overlapped for $Re < 25000$; for $Re > 25000$ the indirect measurements are always smaller than the direct measurements. This means that for the highest values of Re, the drag exerted by the bed forms is larger when the stems are not present, that is consistent with what already observed by other authors (Nepf, Sullivan, and Zavistoski 1997). For $Re < 25000$ this assumption is, however, no more valid and the bed forms contribution is the same as in non-vegetated beds.

The comparison between direct and indirect measurements is shown in the Figure 5.57 as a function of the Froude number Fr. The considerations for this case are similar to what already said for the Figure 5.56. For $Fr < 0.5$, the indirect values are basically larger than the direct one; for $Fr > 0.5$ the data are

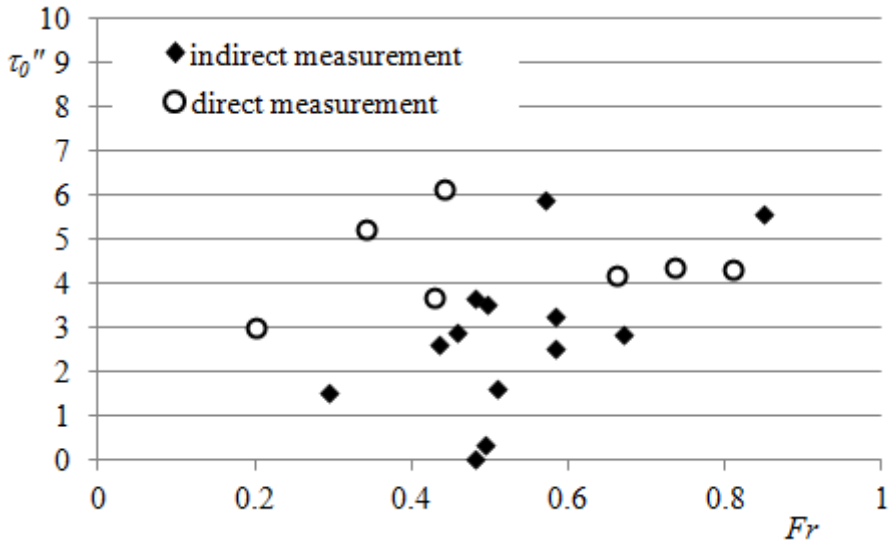

Figure 5.57: Comparison between the drag coefficient measured directly and indirectly as a function of the Froude number.

overlapped. This means that the bed forms roughness in vegetated beds is smaller if the Froude number is smaller, while for $Fr > 0.5$, the bed forms roughness is totally comparable with the bed forms roughness in unvegetated beds. Also in this case, it is clear that the resistance due to bed forms is not negligible.

In last figure (Figure 5.58) the equivalent shear stress is shown as a function of a possible relative bed roughness h/Δ_{vf}, where h is the water depth and Δ_{vf} is the height of bed forms. It is necessary to premise that water depth and bed forms height are, in our tests, of the same order of magnitude. This means that the results are limited and not generalizable. For the values of the tests in Figure 5.58, the results highlight that the tendency for the equivalent shear stress is to decrease with the increase of the water depth. The direct and indirect measurements are totally overlapped.

The influence of the water depth on the drag coefficient

These experiments were done in order to understand which part of the cylinder, above or below the height of the bed forms, affect more the drag resistance. For this purpose, the cylinders were cut at the level of the top of bed forms, as in

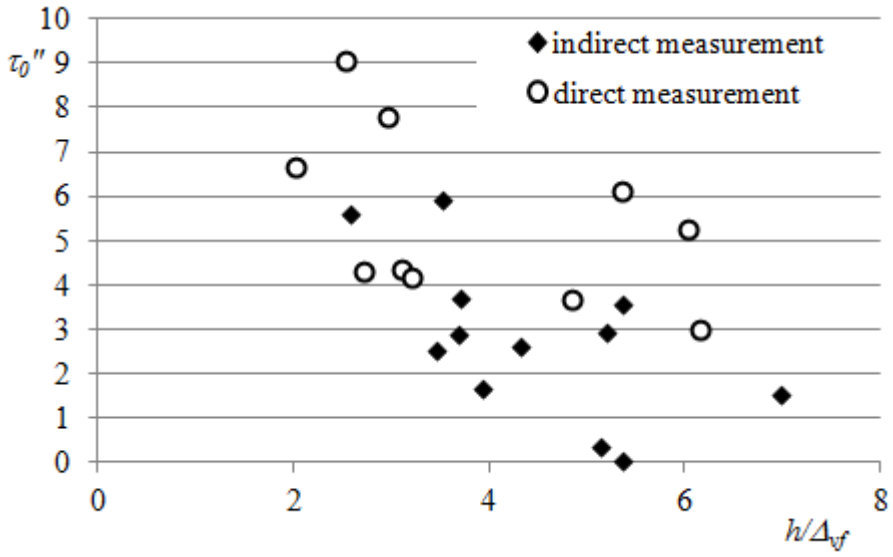

Figure 5.58: Comparison between the drag coefficient measured directly and indirectly as a function of the relative roughness due to bed forms h/Δ_{vf}.

Figure 5.59. Consequently, the load cell, fixed at the cut cylinders, measured the resistance only of the upper part of the cylinder.

We are expected that the under part of the cylinder does not contribute to the global resistance, because of the recirculating currents inside the bed forms. In this case, the evaluation of the drag coefficient can be made by using the general expression:

$$C_{Dp} = \frac{R_p}{N_p \rho \frac{U^2}{2} d_p h} \tag{5.25}$$

where h is the averaged water depth. The drag coefficients calculated according to the eq. (5.25) are shown in Figure 5.60. The drag coefficients of the cut cylinders are clearly smaller than that of the non-cut cylinders. This means that in the calculation of the resistance the averaged water depth has to be considered instead of the total water depth close to the cylinder.

The drag coefficient, by considering only the over part of the cylinders (Figure 5.61), is:

$$C_{Dp} = \frac{R_p}{N_p \rho \frac{U^2}{2} d_p h_u} \tag{5.26}$$

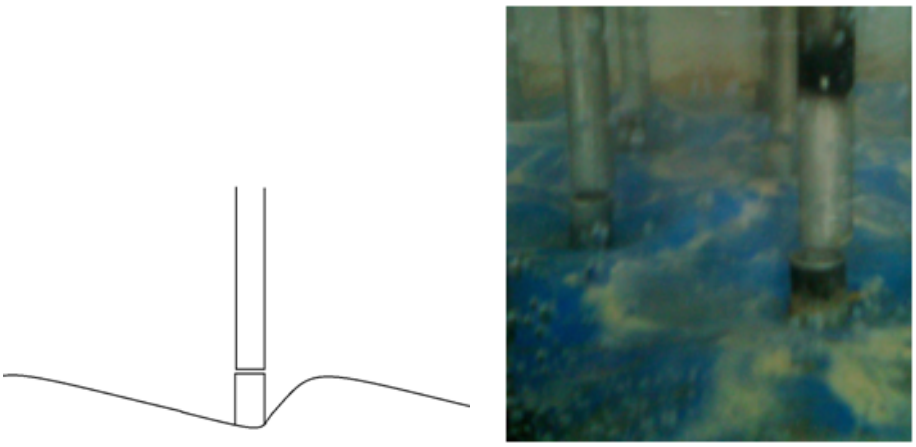

(a) (b)

Figure 5.59: The cylinders are cut at the height of dunes.

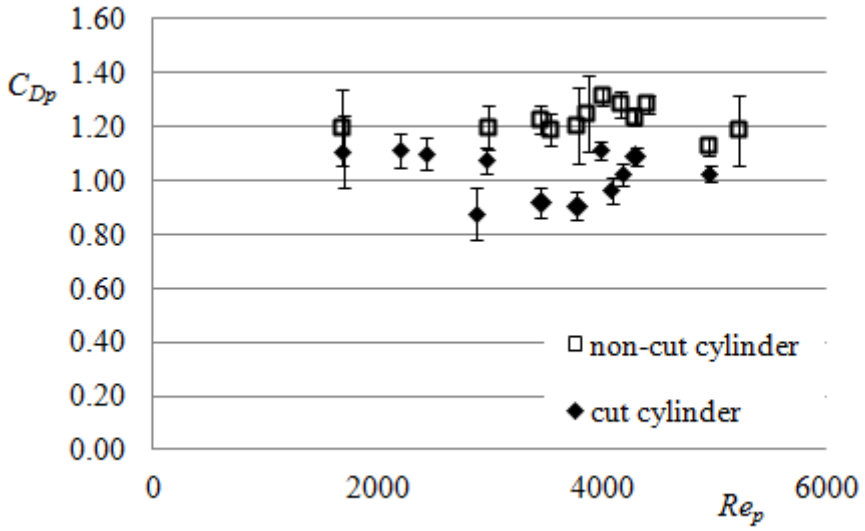

Figure 5.60: Comparison between the drag coefficient measured for non-cut and cut cylinders as a function of Re_p (eq. 5.25).

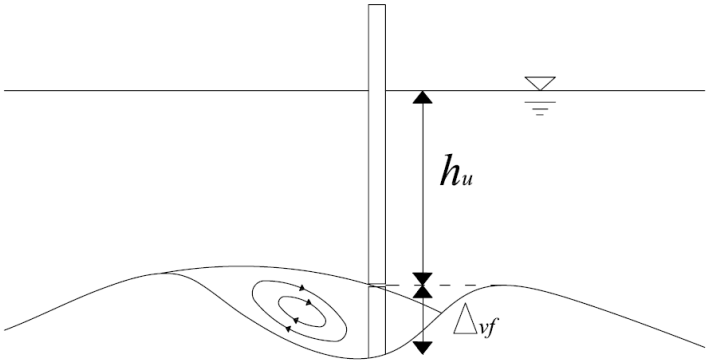

Figure 5.61: Definition of the water depth h_u.

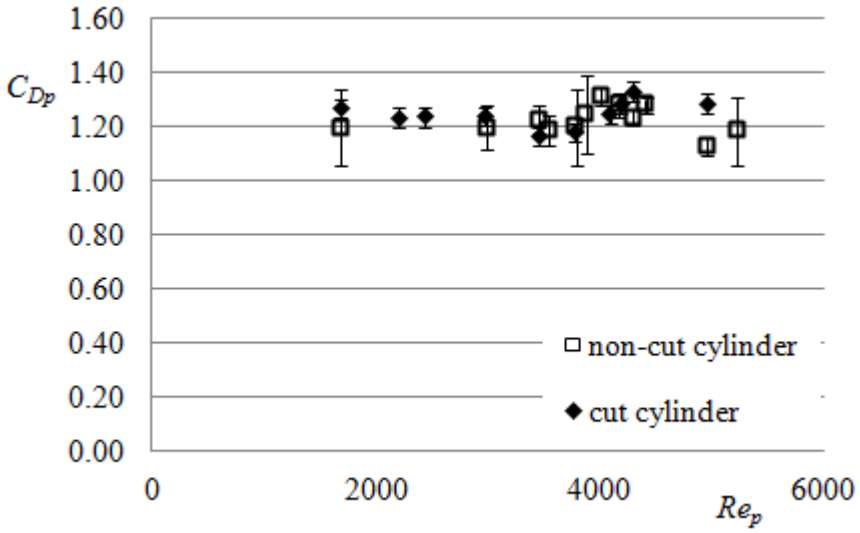

Figure 5.62: Comparison between the drag coefficient measured for non-cut and cut cylinders as a function of Re_p, with the adjustment of the definition of water depth (eq. 5.26).

The results are shown in Figure 5.62: the drag coefficients for cut and non-cut cylinders are, in this case, nearly coincident. It means that the contribution of the part of cylinders which is below the crests of bed form height is comparable to the contribution of the part of cylinder above the crests.

In conclusion, the different experimental results described in this chapter lead to affirm that the bed forms are not always negligible in calculation of the global resistance. At the contrary, our experiments demonstrate that:

- the presence of the bed forms affect directly the value of the drag coefficient of the cylinders;
- the contribution of bed forms on the global flow resistance is not always negligible. On the contrary, their contribution is comparable with the contribution of the cylinders.

5.4 The ballistic formulation compared with experimental data

5.4.1 A brief summary on the ballistic formulation

In this paragraph the final formulation of the ballistic approach, which is completely described in Section 3.6, is briefly reported.

The final formulation is:

$$\begin{cases} \Phi = K c_* \Delta \Psi^{-3/2} \dfrac{p_1^{0.5}}{\ln\left(1/p_1\right)} \\ p_1 = \frac{1}{\sqrt{\pi}} \int_{B_* \Psi - 2}^{\infty} e^{-t^2} dt \end{cases} \tag{5.27}$$

where Φ is the dimensionless sediment transport capacity according to Einstein (Einstein 1950):

$$\Phi = \frac{q_s}{d\sqrt{g\Delta d}} \tag{5.28}$$

in which q_s is the sediment discharge per unit width; d is a characteristic grain size; g is the gravity; $\Delta = (\rho_s - \rho)/\rho$ is the relative reduced density of sediment.

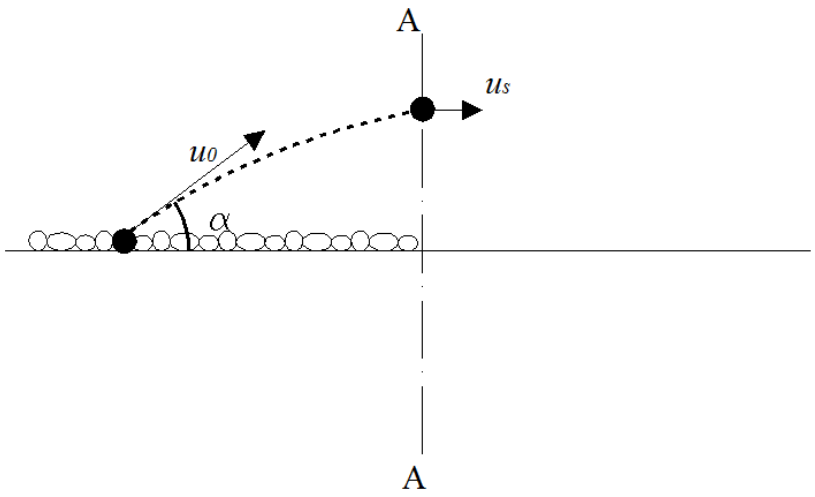

Figure 5.63: The particle is detached with a velocity u_0 and crosses the section A with a velocity u_s.

Ψ is the Einstein flow intensity parameter:

$$\Psi = \frac{g\Delta d}{u_*^2} \tag{5.29}$$

that is the inverse of the Shields parameter $\theta = 1/\Psi$; and u_* is the shear velocity. In eq. (5.27), p_1 expresses the probability that a particle has to be eroded and it is evaluated by the integral of a Gaussian distribution. The lower limit of the integral is related to the incipient motion, and it depends on the Einstein flow intensity parameter Ψ and on an empirical parameter B_*.

In eq. (5.27) two parameters are present: K and c_*. The first was expressed in Section 3.6 as:

$$K = 2\frac{C_L}{C_D}c_u^2$$

where C_L/C_D is the ratio between the lift and drag coefficient at the instant of the detachment of particles; c_u is the ratio between the velocity u_0 of the particle at the same instant (Figure 5.63), and the shear velocity: $c_u = u_0/u_*$. If the velocity of the particle u_0 was equal to the velocity of the flow, then $c_u \approx 6.8$. This value is obtained by calculating (with a log law) the velocity at half grain diameter from the bed. Whereas, if it is supposed that the particle moves with a velocity n times

lower, then $c_u \simeq 6.8/n$.

In eq. (5.27), the second parameter to be determined is c_*. c_* represents the ratio between the velocity of the particle when crosses the reference section A (Figure 5.63) and the shear velocity: $c_* = u_s/u_*$. Also in this case, if the particle moved with the flow, then the value of c_* would be at least about 8.5, value that can be obtained by applying the log law at a distance from the bed equal to the grain diameter. It is reasonable, however, to assume that the particle moves with a lower velocity, and hence $c_* < 8.5$.

5.4.2 Experimental data for the non-vegetated reach

The experimental data relevant for the non vegetated bed were obtained in the reach of the channel without stems (the last partition of the channel) (Section 4.2 and Section 4.2.5). In the experiments we used three different materials for sediment transport: two silicates (*V15* and *V17F*) and one plastic material, which has a density much lower (Section 4.2.1). Two different kinds of transport correspond to the three materials: the sands are characterized by bedload moving by saltation and rolling; the plastic material, at the contrary, moves partially as suspended load. This is equivalent to say that the length of jumps for the sands is comparable with the grain size, whereas the displacement of plastic material is scaled by water depth. The different behavior gives different results, that are shown in the following sections.

The Einstein's parameters Φ and Ψ, corresponding to the experimental data, are calculated by using the measurements of the sediment discharge, q_s, the water depth, h, and the bed slope, i_b. The calculation of the Einstein's parameters is immediate (eqs. (5.28) and (5.29)), since:

- u_* for inserting in the definition of Ψ (eq. 5.29) is evaluated as:

$$u_* = \sqrt{gR_h i_b} \tag{5.30}$$

R_h, which is the hydraulic radius, in the channel is:

$$R_h = \frac{Bh}{B + 2h} \tag{5.31}$$

where B is the width of the channel ($B = 0.5$ m). Being B sufficiently larger than h, there is not necessity to adjust the hydraulic radius for considering the different wall roughness (for example, by considering the Einstein-Horton approach).

- For the dimensionless sediment transport rate (eq. 5.28) the data are obtained with the measurements at regime conditions.

On the contrary to what Einstein assumed, by calculating the shear velocity as in eq. (5.30), the parameter of mobility Ψ is relative to the global resistance and not only to the resistance due to the grain roughness. The global bed shear stress is compound by the grain roughness and the bed form roughness (Section 2.1). The results obtained are represented in the next sections.

Experimental data with silicate sediments

The sands used in the experiments had a relative reduced density equal to $\Delta = 1.59$, that is a density somewhat lower than the density considered in the application in Section 3.6. Notwithstanding this difference, the parameters used in that application are suitable also for the two sands used in the experiments. In Figure 5.64 the data are obtained by adopting the following parameters:

$$\Delta = 1.59 \quad B_* = 0.05 \quad K = 0.025 \quad c_* = 0.8 \tag{5.32}$$

We have already demonstrated (Section 3.6) that with the above parameters (eq. 5.32), the ratio C_L/C_D is equal to 0.025 and that this value is similar to that obtained by Lee and Balachandar (2010).

Figure 5.64 shows that the ballistic approach matches reasonably well the experimental data. The ballistic approach is clearly in a better agreement than the Einstein's formulation (eq. 3.75) and it is nearly coincident with Parker's method (eq. 3.12).

Experimental data with plastic sediments

Not all the material relevant to the plastic sediment is transported as bedload, but due to their reduced density ($\Delta = 0.05$), a certain fraction is transported in sus-

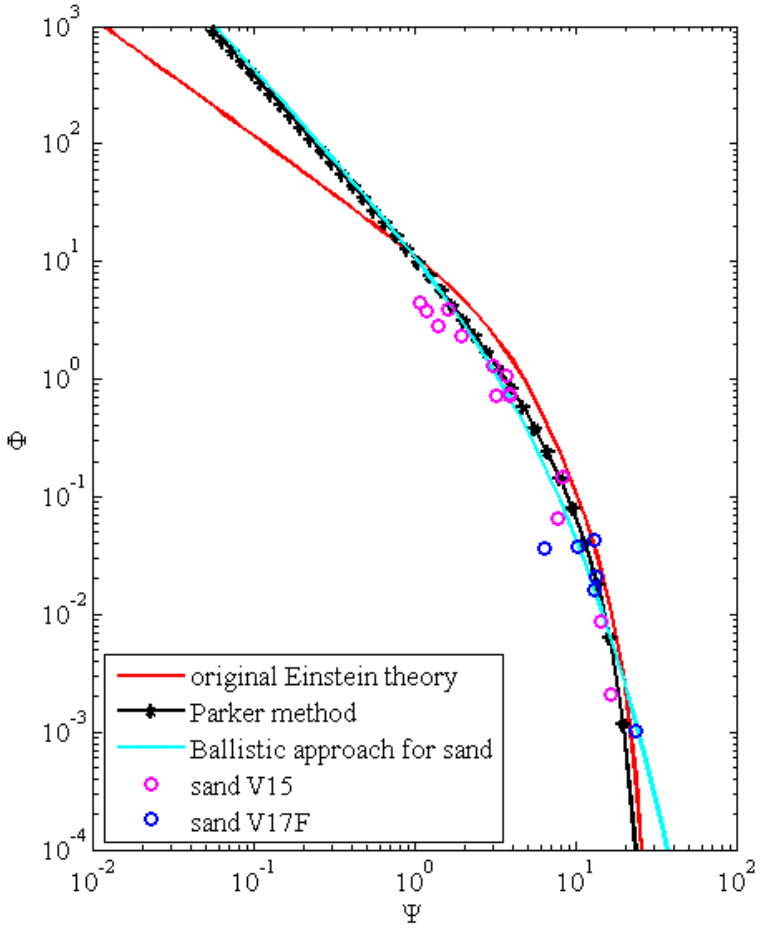

Figure 5.64: Comparison among the ballistic approach (eq. 5.27 and eq. 5.32), the experimental data obtained in the channel with the sands, Einstein original formula (eq. 3.75) and Parker formula (eq. 3.12).

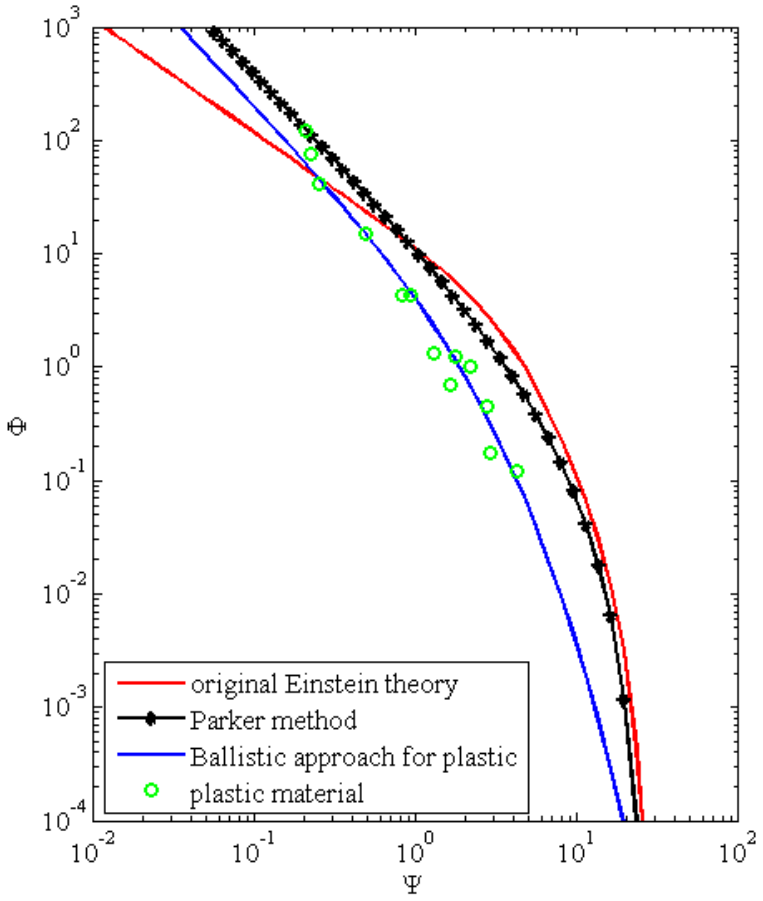

Figure 5.65: Comparison among the ballistic approach (eq. 5.27 and eq. 5.33), the experimental data obtained in the channel with the plastic material, Einstein original formula (eq. 3.75) and Parker formula (eq. 3.12).

pension. In order to evaluate the parameters in this situation, we have considered that the velocity of the particles in suspension is more similar to the velocity of the flow with respect to heavier materials. In this case, the parameters are estimated by fitting the experimental data. The best fitting is obtained with the next assumptions:

- the ratio C_L/C_D depends only on the Reynolds number and not on the density of the material, hence it is equal to the one estimated for sand ($C_L/C_D = 0.025$);

- the velocity of the particle close to the bed is scaled with the shear velocity ($c_u = 1$);

- the velocity of the particles crossing the section of measure is larger ($c_* = 4.8$) than the velocity at the instant of detachment. In particular, we would expect that c_* for the plastic material is much larger than the c_* for sand for two reasons:

  1. because of the small density, the particles move with a velocity which is of the same order of magnitude of the flow velocity;
  2. the jumps of suspended particles are larger than the jumps of sediments moving by saltation or rolling, and hence they are moved by a faster flow.

- also the limit for the detachment is changed, being $B_* = 0.12$.

Summarizing, the parameters adopted for the plastic material are:

$$\Delta = 0.05 \quad B_* = 0.12 \quad K = 0.05 \quad c_* = 4.8 \tag{5.33}$$

Figure 5.65 shows that the ballistic approach is in good agreement with the experimental results, also for the highest value of sediment transport, where the Einstein's theory fails. In addition, notwithstanding the ballistic approach was developed for being suitable to bed load, the model seems in good agreement also with the data obtained with the plastic material. This result is obtained by an empirical calibration of parameters in relation with the length and velocity of

displacement, even if for the plastic particles a part of transport is more similar to suspended load than to bed load. This does not mean that the approach can be considered a model valid also for the suspended load, but it is simply an extension of the bedload formula for this kind of material.

5.4.3 The ballistic approach applied to the vegetated reaches

In this section the experimental results obtained in the vegetated reaches of the channel are compared with the ballistic formulation for vegetated riverbeds:

$$\begin{cases} \Phi = K c_* \Delta (1 - \Omega_v) \Psi_v^{-3/2} \dfrac{p_1^{0.5}}{\ln (1/p_1)} \\ p_1 = \frac{1}{\sqrt{\pi}} \int_{B_* \Psi_v - 2}^{\infty} e^{-t^2} dt \\ \Psi_v = \Psi f_v \left(\Omega_v, h/d_p \right) \end{cases} \tag{5.34}$$

In eq. (5.34), Ψ_v is the flow intensity parameter related with vegetated beds and f_v is an empirical parameter depending on Ω_v and h/d_p, that has to be calibrated on the base of the experimental results. The other symbols have the same meanings as in the precedent section (Section 5.4.1). It is important to note that this formulation is valid both for vegetated and non-vegetated beds. Indeed, the condition of "non-vegetation" corresponds to assume $\Omega_v = 0$, that means $\Psi_v = \Psi$ and the first equation in eq. (5.34) becomes formally equal to the first equation in (5.27). Actually, the two equations are equal only if the parameters K and c_* are the same. This is equivalent to say that the parameters must depend only on the sediment characteristics. By using this last hypothesis, in the following figures are represented the results obtained in the vegetated reaches together with the results obtained in the non-vegetated reach.

In Figures 5.66 and 5.67 are reported the results obtainable considering the Einstein original definition of Ψ. The data for the non-vegetated reach for all the three materials are exactly the same shown in Figures 5.64 and 5.65 , since the parameters used are the same of the eq. (5.32) for the sands and of the eq. (5.33) for the plastic material.

The data for the vegetated reaches, on the contrary, are far from the theoretical curves, for both the materials (sands and plastic). Moreover, the departure of

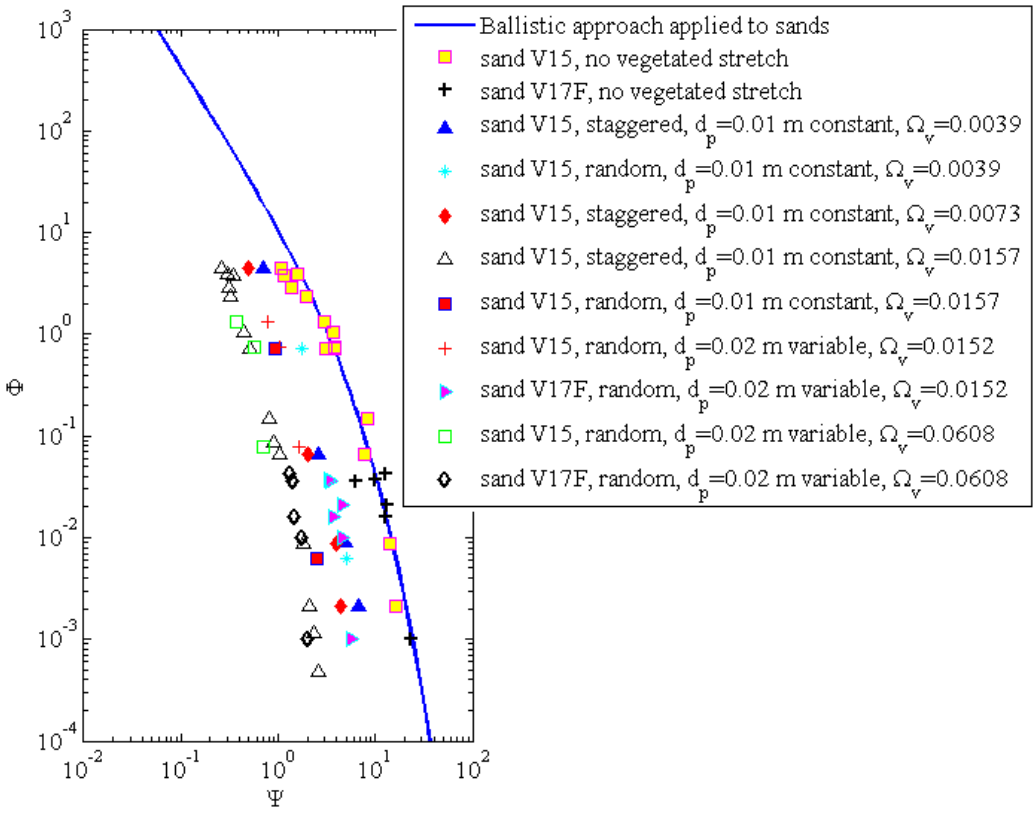

Figure 5.66: Comparison between the ballistic formulation and the experimental data calculated with the Einstein's definition of the mobility parameter

the data corresponding to the vegetated reaches increases with the increase of the vegetation density. This behavior seems to support our hypothesis that the ratio, for constant value of Φ, between the Ψ_v and the Ψ increases with the density of vegetation and the incumbrance of the plants. The ratio is expressed by the empirical function f_v, that depends on the density of vegetation and on h/d_p, which in general can be assumed as:

$$f_v = 1 + c\,\Omega_v \left(\frac{h}{d_p}\right)^{\alpha} \tag{5.35}$$

The parameters c and α must be calibrated by fitting the experimental data.

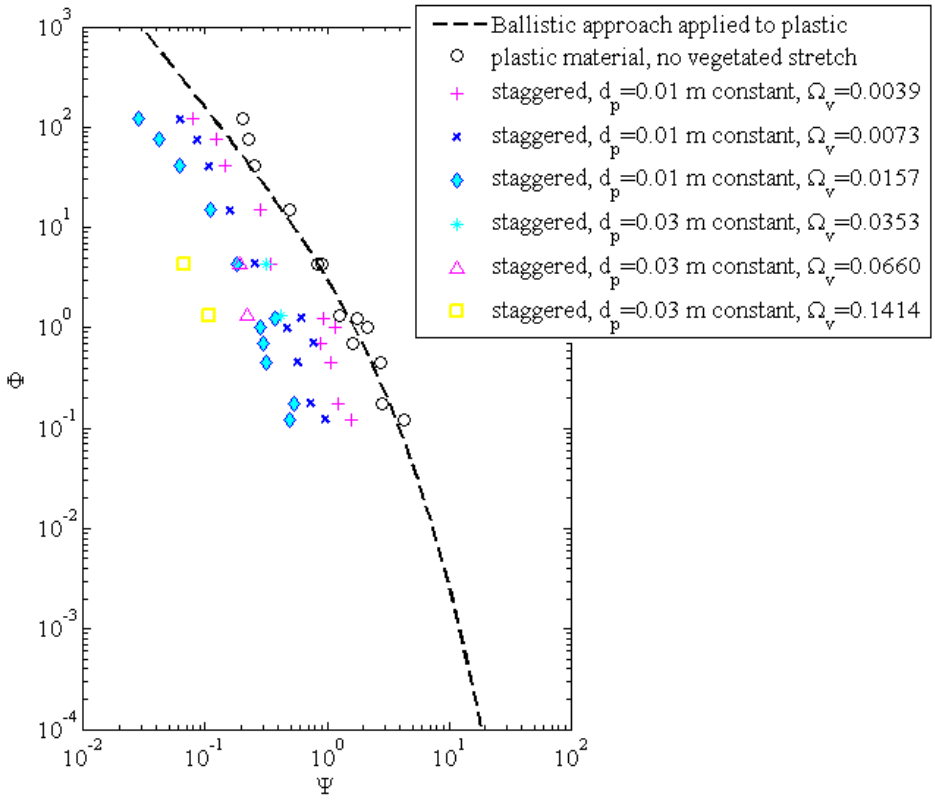

Figure 5.67: Comparison between the ballistic formulation and the experimental data calculated with the Einstein's definition of the flow intensity parameter

The best fitting of data gives $c = 25$ and $\alpha = 1$, that is:

$$\Psi_v = \Psi \left(1 + 25\,\Omega_v \frac{h}{d_p} \right) \tag{5.36}$$

Figures 5.68 and 5.69 show the data obtained by considering the new parameter Ψ_v.

In conclusion, the ballistic approach extended to vegetated reaches:

- is valid for both the sediment materials, with the calibration of the empirical parameters in f_v;

- considers the total resistance, given that the parameter Ψ_v is evaluated by using the shear velocity u_* related with the total shear stress. On the contrary, the Einstein parameter Ψ was calculated by considering the shear stress re-

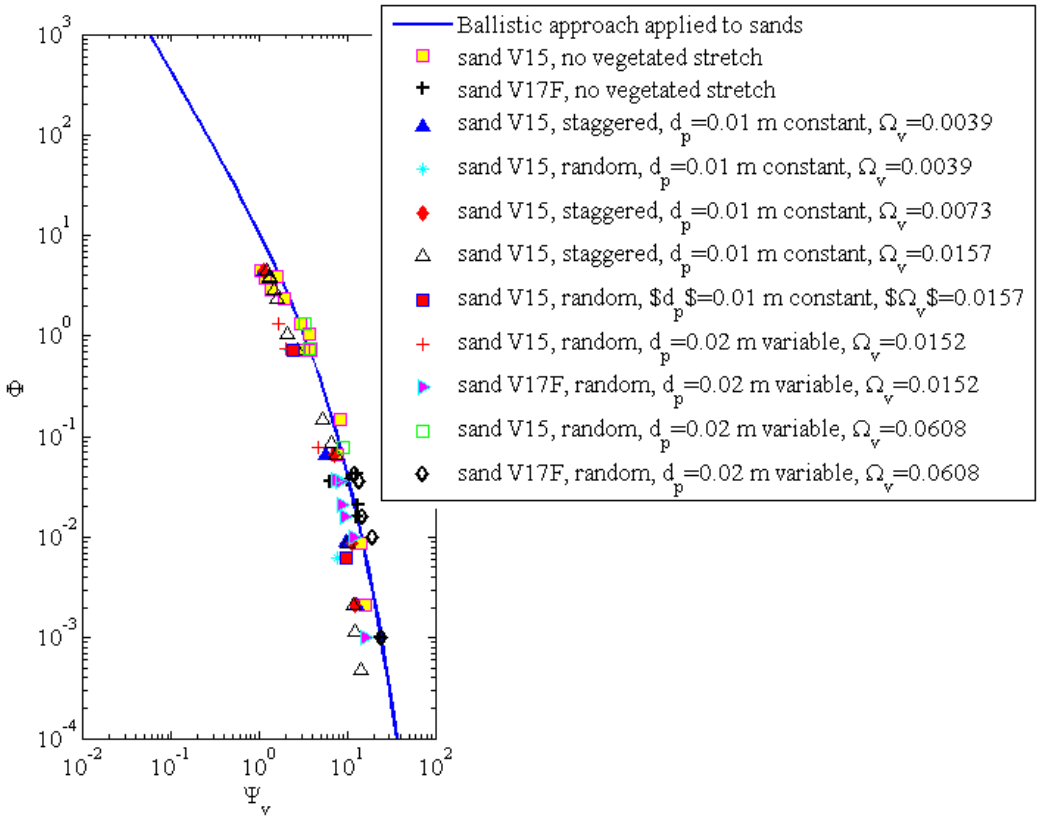

Figure 5.68: Comparison between the ballistic formulation and the experimental data calculated with the definition of the parameter of mobility Ψ_v

lated to the grain roughness u'_*;

- is valid for vegetated and unvegetated reaches.

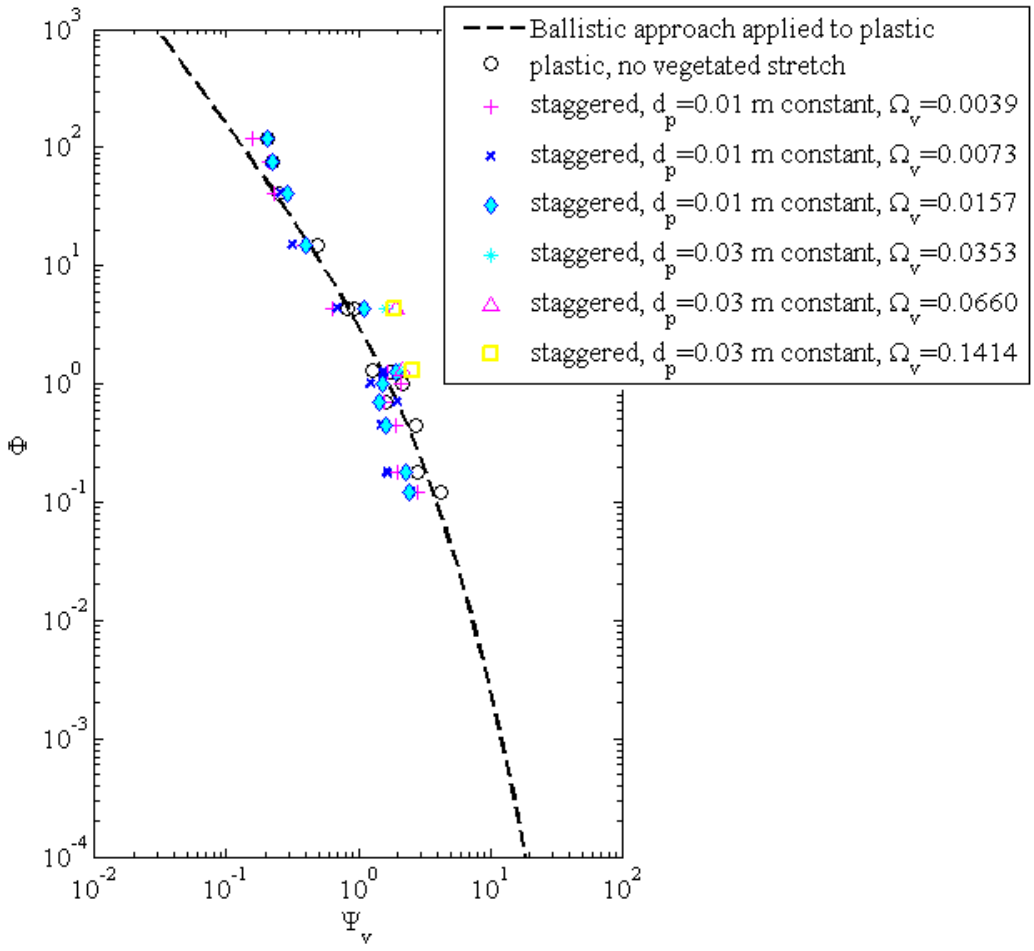

Figure 5.69: Comparison between the ballistic formulation and the experimental data calculated with the definition of the parameter of mobility Ψ_v

Chapter 6

Conclusions

As extensively described in the first part of the thesis, the role of the vegetation in riverbeds is fundamental for the improvement of the chemical, physical and biological quality of river systems. In this regards, the modifications to the flow field and turbulence structure, besides the influence on sediment transport and morphology must be thoroughly considered. On these problems there are many different approaches in the literature, not all adequately based on physical principles. The consequences of such abundant literature is a lack of clear criteria to correctly face the problem and correctly design the engineering measures on rivers. If fluvial engineers do not have the instruments for managing the vegetation, the benefits consequent to the use of vegetation might be nullified by an increase of hydraulic and flood hazards.

We have said that vegetation modifies flow field, sediment transport rate, flow resistance and morphology. Each of these effects is implicitly or explicitly related with the others. In order to define the design instruments, the scientific interest has to be focalized not only on the single effects due to vegetation, but also on the relationships among these effects. The main aim of the thesis was to put in relation some of these factors, and to define their influence on the sediment transport capacity. The analyzed factors related with sediment transport were the flow field through the stems, the bed forms at small scale and the flow resistance. Given the complexity of the topic, we have focused on rigid and emergent plants.

The thesis is based on an experimental approach coupled with theoretical anal-

ysis. Rigid stems were modeled by rigid circular cylinders in a laboratory channel. The width of the channel was divided into two parts. The left part was used for the tests on a mobile bed and in a condition of sediment transport; the right part of the channel had a fixed bed and was used for the measurements of drag force and flow field. The cylinders in the channel were fixed at the bottom and were always emergent. Their distribution, density and size were changed for obtaining the different test configurations. The tests with sediment transport were obtained also modifying the sediment characteristics (density and grain size).

In the thesis, an innovative rational approach, termed *ballistic approach*, for the prediction of sediment transport capacity was presented. The ballistic approach was developed for non-vegetated riverbeds and then its validity was extended also to vegetated beds. Both formulations contain some physical parameters that were calibrated. The calibration for unvegetated beds and sand sediment was done comparing the ballistic formula with some popular empirical formulas and with the data obtained in the channel with the sands. A different calibration was done for the data obtained with the material at lower density, for which a portion of grains was transported in suspension. The calibrated parameters were related with the velocity of particles at the instant of detachment from the bed and during the movement, besides with the ratio between the lift and drag coefficient correspondent to the incipient motion. Given their physical meaning, the calibrated parameters were analyzed and compared with literature results and nature of sediments and transport. The comparison with the empirical formulas and with the experimental results, in addition to the physical analysis of the empirical parameters, allows to affirm that the ballistic method overcomes the weakness points of other theoretical approaches, fits well the experimental results and is in a better agreement with the empirical formulas with respect to the other approaches (Einstein 1950; Yalin 1977).

The extension of the ballistic method to vegetated beds was done by considering the average incumbrance of plants and the modification to the structure of grain movements. In this case, other empirical parameters were obtained by calibrating the theoretical curve with the experimental data, both for sand and plastic material. In this case the results are satisfactory, but there is still room for improvement.

The part of the thesis focused on the drag force exerted by the plants on the flow was based on experimental measurements. The drag force was measured directly for different densities of vegetation and a staggered distribution. These measurements, carried out at a fixed bed, showed the tendency of the drag coefficient to assume a constant value for the Reynolds number of plants larger than $6000 \sim 8000$. This value seems partially dependent on the density of vegetation and on the shape of the wake formed downstream the cylinder. This dependence was put in evidence by means of the measurements of the flow field. It is evident, however, that the value assumed for high Reynolds numbers is dependent on the density of vegetation, but not linearly, as in other literature results. The linear dependence, indeed, compared with our data, failed for the highest vegetation density.

The direct measurements were compared also with the indirect measurements of the drag coefficient, that were obtained through the balance of momentum in a control volume at mobile bed. In this first part of the study, the hypothesis of considering as negligible the contribution due to bed forms was taken. This assumption is generally accepted in the studies related with drag coefficient and rigid stems. The comparison showed that the direct and indirect results are in good agreement, especially for the highest values of Reynolds numbers. For the smallest values of Reynolds numbers, at the contrary, the indirect measurements have given data rather spread. This seemed to be related with the assumption of neglecting the bed forms resistance in the momentum balance. In order to demonstrate this hypothesis, the vegetation bed forms among stems were analyzed.

From the analysis of results of tests with mobile bed we were able to say that the formation of bed forms is often forced by the presence of rigid stems. The experimental results have put in evidence that for a sufficiently high density of stems, the length of the vegetation bed forms is not influenced by the vegetation density, but only by the distance between the plants, whereas the height of the forms seems to not depend on the vegetation density, but it is more probably related with the characteristics of the flow field and with the sediment properties. In particular, the length of bed forms is equal on average to the distance between the stems for constant diameters of stems, and it is linearly dependent on the distance for variable diameter of stems. For sparse distribution of stems, the vegetation

bed forms are much more similar to the natural dunes in non-vegetated beds. The length of these bed forms results to be less influenced by the distance between cylinders. In fact, in some tests it was evident as both kinds of bed forms (vegetation forms and natural dunes) are contemporarily present, and they interacted mutually and overlapped.

With the measurements of bed forms in mobile bed for staggered and dense distribution of cylinders, a model of forms was made with rigid plastic. The model was obtained by averaging the bed forms lengths and heights for a range of data related with similar flow conditions. With this model, the direct measurements of drag coefficient were repeated. The results, compared with the drag coefficients in plane bed, put in doubt the common assumption to consider negligible the contribution of bed forms to drag coefficient. Indeed, the drag coefficient with plane bed and that with bed forms were similar, but not coincident. On the contrary, the drag coefficient of the cylinders in presence of bed resulted slightly but constantly larger than the drag coefficient without bed forms.

Other tests were carried out with the modeled bed forms in order to understand which is the real contribution of the bed forms resistance on the global resistance. For this purpose, some experiments without cylinders were done. The comparison between the equivalent shear stress of bed forms measured in this way (direct method) and that obtained by the balance of forces for a control volume containing also the cylinders (indirect method) showed that the bed forms resistance and the drag force due to the cylinders were of the same order of magnitude.

Finally, by using the PIV technique and uniform distribution of cylinders, the parameters of the classical theory of DAM were compared with local velocities. The PIV analysis has put in evidence that there is an area of the bed where the shear stress at the bottom results directed upstream, and hence where the sediments are upstream entrained and do not contribute to the sediment discharge, unless they reach a sufficient height to be transported by the flow. This height is as smaller as the sediment is far from the cylinder. This behavior has a direct relationship also with the presence of the scour around the cylinders and with the formation of bed forms. In addition, the mechanisms of sediment transport in vegetated rivers are different compared to the mechanisms of transport in unvegetated reaches, because different equilibria between detachment and transport have to be

considered. In particular, sediment movements are not everywhere in correlation with local values of shear stress at the bottom, as usually assumed in spatially homogeneous flows. The analysis showed that there are zones of active particle erosion but negligible downstream transport. These aspects were considered for the physical definition of the parameters in the ballistic approach extended to vegetated riverbeds.

In conclusion, our research was centered on the sediment transport related with the presence of stems and on a new rational approach to predict the sediment transport capacity both in vegetated and unvegetated beds. The research has allowed to relate the flow field through the stems with the mechanisms of sediment transport. Then we have verified that the bed forms size depends on the sediment transport and, contemporarily, on the distribution of stems. Finally, we have faced the relationship between bed forms and drag coefficient, and bed forms and global flow resistance.

In order to conclude the study, other aspects have to be considered. In particular, the direct dependence between flow field and drag force. This part was not proposed, because it needs a deeper analysis, specially because only one configuration of stems, as in the thesis, can not be sufficient to explain and generalize the results.

During the thesis we also began to develop a more rational expression for the ballistic approach for vegetated beds. In particular, we tried to consider in the ballistic approach not only the incumbrance of the cylinders, but also the bed forms geometry. Nevertheless, from the first results, we realized we need more tests, and also other arrangements of the stems and variabilities in the cylinder sizes.

References

Adrian, R.J. (1991). "Particle-imaging techniques for experimental fluid mechanics". In: *Annual review of fluid mechanics* 23.1, pp. 261–304.

Ancey, C. et al. (2006). "Statistical description of sediment transport experiments". In: *Physical Review E* 74.1, p. 011302.

Armanini, A. (1999). *Principi di idraulica fluviale*. Bios.

Armanini, A., V Cavedon, and M. Righetti (2010). "Sediment transport processes in vegetated streams". In: *Proceedings of the 1st European IAHR Congress, Edimburgh*.

Armanini, A. and C. Gregoretti (2005). "Incipient sediment motion at high slopes in uniform flow condition". In: *Water resources research* 41.12, W12431.

Ashida, K. (1972). "Study on hydraulic resistance and bed-load transport rate in alluvial streams". In: *Journal of Civil Engineering, Jpn Soc Civil Engineers* 206, pp. 59–69.

Babovic, V. and M. Keijzer (2000). "Genetic programming as a model induction engine". In: *Journal of Hydroinformatics* 2.1, pp. 35–60.

Bagnold, RA (1936). "The movement of desert sand". In: *Proceedings of the Royal Society of London. Series A, Mathematical and Physical Sciences* 157.892, pp. 594–620.

Baptist, MJ et al. (2007). "On inducing equations for vegetation resistance". In: *Journal of Hydraulic Research* 45.4, pp. 435–450.

Best, J. (1992). "On the entrainment of sediment and initiation of bed defects: insights from recent developments within turbulent boundary layer research". In: *Sedimentology* 39.5, pp. 797–811.

Blevins, R.D. (1984). "Applied fluid dynamics handbook". In: *New York, Van Nostrand Reinhold Co., 1984, 568 p.* 1.

Bravo-Espinosa, M., WR Osterkamp, and V.L. Lopes (2003). "Bedload transport in alluvial channels". In: *Journal of Hydraulic Engineering* 129, p. 783.

Brownlie, W.R. and N.H. Brooks (1981). *Compilation of alluvial channel data: laboratory and field*. California Institute of Technology, WM Keck Laboratory of Hydraulics and Water Resources.

Cao, Z., X. Zhang, and H. Xi (1996). "Turbulent bursting-based diffusion model for suspended sediment in open channel flows". In: *Journal of Hydraulic Research/Journal de Recherches Hydraulique* 34.4, pp. 457–472.

Carmo, BS et al. (2011). "Flow-induced vibration of a circular cylinder subjected to wake interference at low Reynolds number". In: *Journal of Fluids and Structures*.

Cavedon, V, M. Righetti, and A. Armanini (2012). "Characterization of the flow field through a staggered distribution of cylinders". In: *Submitted to 2nd European IAHR Congress, Munich*.

Chen, N.-S. (2007). "Power-law index for velocity profiles in open channel flows". In: *Advances in Water Resources* 30.1, pp. 1775–1784.

Coleman, N.L. (1970). "Flume studies of the sediment transfer coefficient". In: *Water Resources Research* 6.3, pp. 801–809.

Coleman, SE and VI Nikora (2008). "A unifying framework for particle entrainment". In: *Water resources research* 44.4, W04415.

Doebelin, E.O. (1990). *Measurement systems*. McGraw-Hill.

Drake, T.G. et al. (1988). "Bedload transport of fine gravel observed by motion-picture photography". In: *Journal of Fluid Mechanics* 192.1, pp. 193–217.

Einstein, HA (1950). "The bed-load function for sedimentation in open channel flows". In: *Sedimentation, edited by Shen HW, Colorado State University, Fort Collins, Colorado, USA*.

Einstein, H.A., N.L. Barbarossa, and American Society of Civil Engineers. Hydraulics Division (1951). "River channel roughness". In: American Society of Civil Engineers.

Elliot, A.H. (2000). "Settling of fine sediment in a channel with emergent vegetation". In: *Journal of the Hydraulics Engineering* 126, pp. 570–577.

Engelund, F. (1966). "Hydraulic resistance of alluvial streams". In: *Journal of the Hydraulics Division* 98, pp. 315–326.

Ettema, R., T. Nakato, and M. Muste (2008). "Estimation of scour depth at bridge abutment". In: *NCHRP Rep. No. 24* 20.

Fa, MaghadamM and N. Kouwen (1997). "Nonrigid Nonsubmerged Vegetative RoLIshness on Floodplains". In: *J. Hydr. Engrg.. ASCE* 123.1.

Fang, H.W. and G.Q. Wang (2000). "Three-dimensional mathematical model of suspended-sediment transport". In: *Journal of Hydraulic Engineering* 126, p. 578.

Finnigan, J. (2000). "Turbulence in plant canopies". In: *Annual Review of Fluid Mechanics* 32.1, pp. 519–571.

Furukawa, K., E. Wolanski, and H. Mueller (1997). "Currents and sediment transport in mangrove forests". In: *Estuarine, Coastal and Shelf Science* 44.3, pp. 301–310.

Ghisalberti, M. and H. Nepf (2009). "Shallow flows over a permeable medium: the hydrodynamics of submerged aquatic canopies". In: *Transport in porous media* 78.2, pp. 309–326.

Giménez-Curto, L.A. and M.A. Corniero (2009). "Entrainment threshold of cohesionless sediment grains under steady flow of air and water". In: *Sedimentology* 56.2, pp. 493–509.

Gran, K. and C. Paola (2001). "Riparian vegetation controls on braided stream dynamics". In: *Water Resources Research* 37.12, pp. 3275–3283.

Hardy, R.J. (2005). "Modelling granular sediment transport over water-worked gravels". In: *Earth Surface Processes and Landforms* 30.8, pp. 1069–1076.

Hayashi, T. and S. Ozaki (1980). "On the Saltation Heights and Step Lengths of Sediment Particles in the Bed-Load Layer". In: *International Symposium on River Sedimentation, Beijing, China*.

Hinze, JO (1959). "Turbulence, 1975". In: *New York*.

Hsieh, T. (1964). "Resistance of cylindrical piers in open-channel flow". In: *Jour. of Hyd. Div., proc., ASCE* 90, pp. 161–173.

Hu, C. and Q. Guo (2010). "Near-Bed Sediment Concentration Distribution and Basic Probability of Sediment Movement". In: *Journal of Hydraulic Engineering* 1, p. 207.

Ishikawa, Y., K. Mizuhara, and M. Ashida (2000a). “Drag force on multiple rows of cylinders in an open channel”. In: *Grant-in-aid research project report no. 10555176*.

Ishikawa, Y., K. Mizuhara, and S. Ashida (2000b). “Effect of density of trees on drag exerted on trees in river channels”. In: *Journal of Forest Research* 5.4, pp. 271–279.

Ishikawa, Y., T. Sakamoto, and K. Mizuhara (2003). “Effect of density of riparian vegetation on effective tractive force”. In: *Journal of Forest Research* 8.4, pp. 235–246.

Jackson, R.G. (1976). “Sedimentological and fluid-dynamic implications of the turbulent bursting phenomenon in geophysical flows”. In: *Journal of Fluid Mechanics* 77.03, pp. 531–560.

James, CS et al. (2004). “Flow resistance of emergent vegetation”. In: *Journal of Hydraulic Research* 42.4, pp. 390–398.

Järvelä, J. (2004). “Determination of flow resistance caused by non-submerged woody vegetation”. In: *International Journal of River Basin Management* 2.1, pp. 61–70.

Jarvela, J. (2005). “Effect of submerged flexible vegetation on flow structure and resistance”. In: *Journal of Hydrology* 307.1-4, pp. 233–241.

Jordanova, A.A. and CS James (2003). “Experimental study of bed load transport through emergent vegetation”. In: *Journal of Hydraulic Engineering* 129, p. 474.

Kalinske, A.A. (1942). *Criteria for determining sand transport by surface creep and saltation*.

Kirkil, G., SG Constantinescu, R. Ettema, et al. (2008). “Coherent structures in the flow field around a circular cylinder with scour hole”. In: *Journal of Hydraulic Engineering* 134, p. 572.

Kothyari, U.C., H. Hashimoto, and K. Hayashi (2009). “Effect of tall vegetation on sediment transport by channel flows”. In: *Journal of Hydraulic Research* 47.6, pp. 700–710.

Kothyari, UC, K. Hayashi, and H. Hashimoto (2010). “Drag coefficient of unsubmerged rigid vegetation stems in open channel flows”. In: *Journal of hydraulic research* 48.6, pp. 829–830.

Kouwen, N. (1988). “Field estimation of the biomechanical properties of grass”. In: *Journal of Hydraulic Research* 26.5, pp. 559–568.

Kuhnle, R.A. and J.B. Southard (1988). “Bed load transport fluctuations in a gravel bed laboratory channel”. In: *Water Resources Research* 24.2, pp. 247–260.

Lane, EW and AA Kalinske (1941). “Engineering calculations of suspended sediment”. In: *Trans. AGU* 22, pp. 603–607.

Lee, H. and S. Balachandar (2010). “Drag and lift forces on a spherical particle moving on a wall in a shear flow at finite Re”. In: *Journal of Fluid Mechanics* 657, pp. 89–125.

Li, CW and JF Xie (2011). “Numerical modeling of free surface flow over submerged and highly flexible vegetation”. In: *Advances in Water Resources*.

Li, R.M. and H.W. Shen (1973). “Effect of tall vegetations on flow and sediment”. In: *Journal of the Hydraulics Division* 99.5, pp. 793–814.

López, F. and M. García (1998). “Open-channel flow through simulated vegetation: Suspended sediment transport modeling”. In: *Water resources research* 34.9, pp. 2341–2352.

López, F. and M.H. García (2001). “Mean flow and turbulence structure of open-channel flow through non-emergent vegetation”. In: *Journal of Hydraulic Engineering* 127, p. 392.

Marchi, E. and A. Rubatta (1981). “Meccanica dei fluidi–Principi e applicazioni idrauliche”. In: *UTET Torino*.

Martin, Y. (2003). “Evaluation of bed load transport formulae using field evidence from the Vedder River, British Columbia”. In: *Geomorphology* 53.1-2, pp. 75–95.

Meyer-Peter, E. and R. Müller (1948). “Formulas for bed-load transport”. In: *Proceedings of the 2nd Meeting of the International Association for Hydraulic Structures Research*, pp. 39–64.

Nakagawa, H., T. Tsujimoto, and Y. Shimizu (1992). “Sediment transport in vegetated bed channel”. In: *Conference Proceedings of the 5th International Symposium on River Sedimentation, Karlsruhe*.

Nepf, H. and M. Ghisalberti (2008). “Flow and transport in channels with submerged vegetation”. In: *Acta Geophysica* 56.3, pp. 753–777.

Nepf, HM (1999). “Drag, turbulence, and diffusion in flow through emergent vegetation”. In: *Water resources research* 35.2, pp. 479–489.

Nepf, HM, JA Sullivan, and RA Zavistoski (1997). “A model for diffusion within emergent vegetation”. In: *Limnology and Oceanography*, pp. 1735–1745.

Nikora, V. (2004). “Spatial averaging concept for rough-bed open-channel and overland flows”. In: *Advances in Hydro-Science and Engineering, Proceedings of the 6th International Conference on Hydro-Science and Engineering, Brisbane, Australia*.

— (2010). “Hydrodynamics of aquatic ecosystems: an interface between ecology, biomechanics and environmental fluid mechanics”. In: *River Research and Applications* 26.4, pp. 367–384.

Nikora, V. et al. (2007). “Double-averaging concept for rough-bed open-channel and overland flows: Theoretical background”. In: *Journal of Hydraulic Engineering* 133, p. 873.

Nikora, V.I. and D.G. Goring (2002). “Fluctuations of suspended sediment concentration and turbulent sediment fluxes in an open-channel flow”. In: *Journal of Hydraulic Engineering* 128, p. 214.

Papanicolaou, AN et al. (2002). “Stochastic incipient motion criterion for spheres under various bed packing conditions”. In: *Journal of Hydraulic Engineering* 128, p. 369.

Parker, G. (1990). “Surface-based bedload transport relation for gravel rivers”. In: *Journal of Hydraulic Research JHYRAF,* 28.4.

Perucca, E., C. Camporeale, and L. Ridolfi (2007). “Significance of the riparian vegetation dynamics on meandering river morphodynamics”. In: *Water resources research* 43.3, W03430.

Poggi, D. et al. (2004). “The effect of vegetation density on canopy sub-layer turbulence”. In: *Boundary-Layer Meteorology* 111.3, pp. 565–587.

Prandtl, L. (1935). “The mechanics of viscous fluids”. In:

Raffel, M. and F. Kost (1998). “Investigation of aerodynamic effects of coolant ejection at the trailing edge of a turbine blade model by PIV and pressure measurements”. In: *Experiments in fluids* 24.5, pp. 447–461.

Righetti, M. (2008). “Flow analysis in a channel with flexible vegetation using double-averaging method”. In: *Acta Geophysica* 56.3, pp. 801–823.

Righetti, M. and A. Armanini (2002). "Flow resistance in open channel flows with sparsely distributed bushes". In: *Journal of Hydrology* 269.1-2, pp. 55–64.

Rouse, H. (1937). "Modern conceptions of the mechanics of fluid turbulence". In: *Trans. ASCE* 102, pp. 463–543.

Schlichting, H., K. Gersten, and K. Gersten (2000). *Boundary-layer theory*. Springer Verlag.

Shen, HW (1962). "Development of bed roughness in alluvial channels". In: *J. Hydraul. Div., Am. Soc. Civ. Eng* 88, pp. 45–58.

Shields, A., WP Ott, and JC Van Uchelen (1936). "Application of similarity principles and turbulence research to bed-load movement". In:

Shucksmith, JD, JB Boxall, and I. Guymer (2010). "Effects of emergent and submerged natural vegetation on longitudinal mixing in open channel flow". In: *Water Resources Research* 46.4, W04504.

Souliotis, D. and P. Panagiotis (2007). "3D numerical experiments on drag resistance in vegetated flows". In: *Proceedings of the Congress-International Association for Hydraulic Research*. Vol. 32. 1, p. 171.

Stamhuis, E. and J. Videler (1995). "Quantitative flow analysis around aquatic animals using laser sheet particle image velocimetry". In: *Journal of experimental biology* 198.2, p. 283.

Stanislas, M., J. Kompenhans, and J. Westerweel (2000). *Particle image velocimetry: Progress towards industrial application*. Kluwer Academic Publishers Dordrecht, The Netherlands:

Stephan, U. and D. Gutknecht (2002). "Hydraulic resistance of submerged flexible vegetation". In: *Journal of Hydrology* 269.1-2, pp. 27–43.

Stone, B.M. and T.S. Hung (2002). "Hydraulic resistance of flow in channels with cylindrical roughness". In: *Journal of Hydraulic Engineering* 128.5, pp. 500–506.

Strickler, A. (1923). *Beiträge zur Frage der Geschwindigkeitsformel und der Rauhigkeitszahlen für Ströme, Kanäle und geschlossene Leitungen*. Im Selbstverlag.

Takemura, T. and N. Tanaka (2007). "Flow structures and drag characteristics of a colony-type emergent roughness model mounted on a flat plate in uniform flow". In: *Fluid dynamics research* 39.9-10, pp. 694–710.

Tanino, Y. and H.M. Nepf (2008). "Laboratory investigation of mean drag in a random array of rigid, emergent cylinders". In: *Journal of Hydraulic Engineering* 134, p. 34.

Tsujimoto, T. (1999). "Fluvial processes in streams with vegetation". In: *Journal of Hydraulic Research* 37.6, pp. 789–803.

Van Rijn, L.C. (1984). "The prediction of sediment transport and alluvial roughness". In: *J.of Hydraulic Division* 110, pp. 1733–1757.

— (2007). "Unified view of sediment transport by currents and waves. II: Suspended transport". In: *Journal of Hydraulic Engineering* 133, p. 668.

Van Rijn, L.C. et al. (1993). *Principles of sediment transport in rivers, estuaries and coastal seas*.

Whitaker, S. (1999). *The method of volume averaging*. Vol. 13. Springer Netherlands.

White, B.L. and H.M. Nepf (2003). "Scalar transport in random cylinder arrays at moderate Reynolds number". In: *Journal of Fluid Mechanics* 487.25, pp. 43–79.

Wilcock, P.R. and B.W. McArdell (1993). "Surface-based fractional transport rates: Mobilization thresholds and partial transport of a sand-gravel sediment". In: *Water Resources Research* 29.4, pp. 1297–1312.

Wilson, C., T. Stoesser, and PD Bates (2005). "Modelling of open channel flow through vegetation". In: *Computational Fluid Dynamics*, pp. 395–428.

Wu, F.C., H.W. Shen, and Y.J. Chou (1999). "Variation of roughness coefficients for unsubmerged and submerged vegetation". In: *Journal of Hydraulic Engineering* 125.9, pp. 934–942.

Wu, W., W. Rodi, and T. Wenka (2000). "3D numerical modeling of flow and sediment transport in open channels". In: *Journal of Hydraulic Engineering* 126, p. 4.

Wu, W. et al. (2005). "A depth-averaged two-dimensional model for flow, sediment transport, and bed topography in curved channels with riparian vegetation". In: *Water Resources Research* 41.3, W03015.

Yalin, M.S. (1977). *Mechanics of sediment transport*. Pergamon.

Zedler, E.A. and R.L. Street (2001). “Large-eddy simulation of sediment transport: currents over ripples”. In: *Journal of Hydraulic Engineering* 127.6, pp. 444–452.

Zirbel, M.J., F. Veron, and M.I. Latz (2000). “The reversible effect of flow on the morphology of ceratocorys horrida (PERIDINIALES, DINOPHYTA)*”. In: *Journal of Phycology* 36.1, pp. 46–58.